RIGA TECHNICAL UNIVERSITY

Anda Barkāne

PHOTO-CURABLE VEGETABLE OIL-BASED ACRYLATE RESINS WITH LIGNOCELLULOSE COMPONENTS

Doctoral Thesis

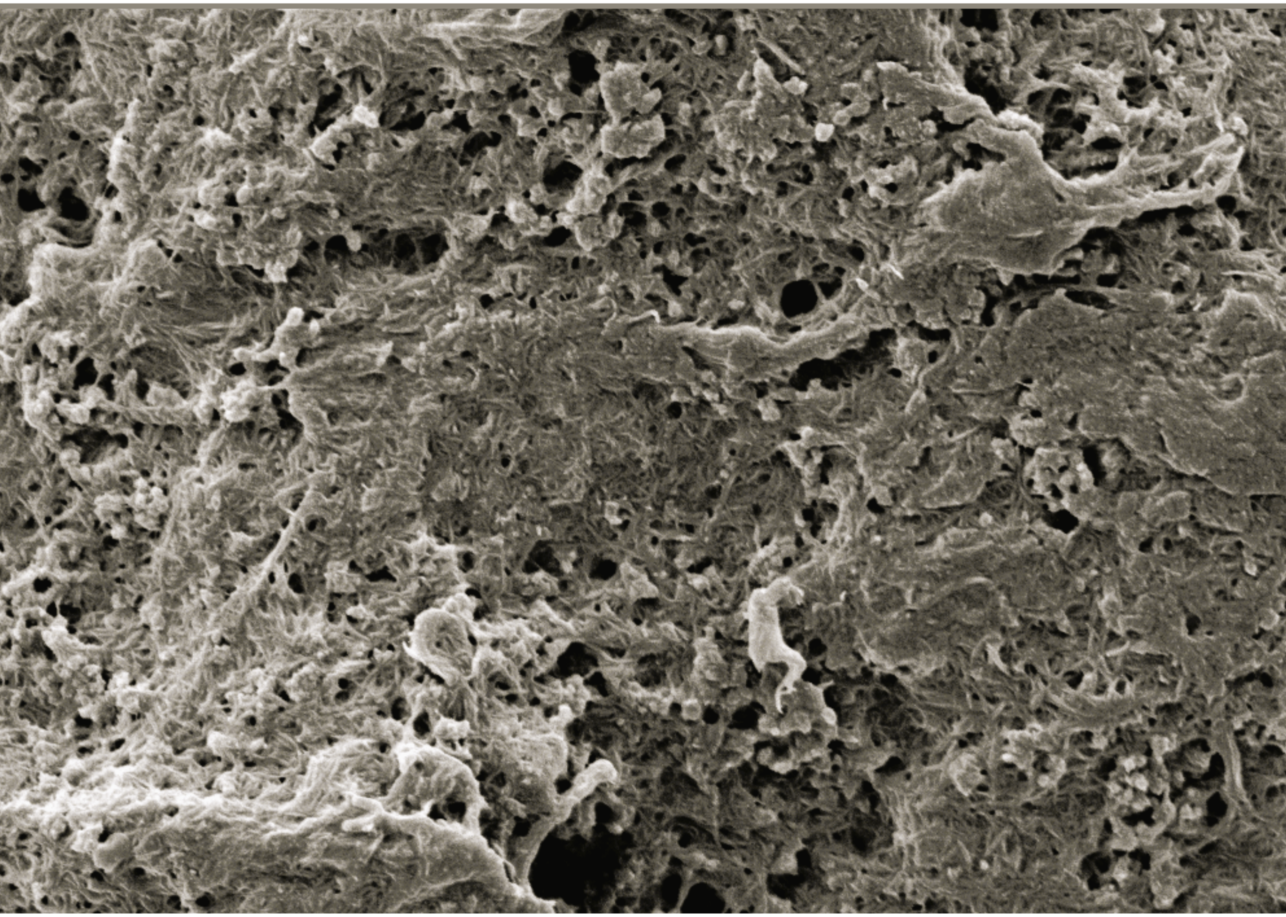

RTU Press
Riga 2024

RIGA TECHNICAL UNIVERSITY
Faculty of Natural Sciences and Technology
Institute of Chemistry and Chemical Technology

Anda Barkāne
Doctoral Student of the Study Programme “Chemistry, Materials Science and Engineering”

PHOTO-CURABLE VEGETABLE OIL-BASED ACRYLATE RESINS WITH LIGNOCELLULOSE COMPONENTS

Doctoral Thesis

Scientific supervisor
Professor Dr. sc. ing.
SERGEJS GAIDUKOVS

Riga 2024

Barkāne, A. Photo-curable Vegetable Oil-based Acrylate Resins with Lignocellulose Components. Summary of the Doctoral Thesis. Riga: RTU Press, 2024. – 174 p.

Published in accordance with the decision of the Promotion Council "P-02" of 13 February 2024, Minutes No. 04030-9.2.2/1.

The materials were investigated, prepared, and tested at Riga Technical University Institute of Chemistry and Chemical Technology.

This research was carried out within the scope of M-era.net 2017 project "3D Printable Innovative Biobased Materials for Wood Mimics", 3DPrintInn; No.1.1.1.5/ERANET/18/05 (State Education Development Agency Republic of Latvia (VIAA).

This research was supported by:

- the Riga Technical University project RTU No. MP2019/8 for strengthening scientific personnel capacity in 2019/2020;
- Riga Technical University's Doctoral Grant program;
- the European Social Fund within Project No. 8.2.2.0/20/I/008, "Strengthening of PhD students and academic personnel of Riga Technical University and BA School of Business and Finance in the strategic fields of specialization" of the Specific Objective 8.2.2 "To Strengthen Academic Staff of Higher Education Institutions in Strategic Specialization Areas" of the Operational Programme "Growth and Employment";
- the Latvian Council of Science project RealHLC No. lzp-2019/1-0390.

ACKNOWLEDGEMENTS

I express my deepest gratitude towards my wonderful family for their love, support, encouragement, and understanding.

I am incredibly grateful to my supervisor Professor Sergejs Gaidukovs, for his guidance, support, motivation, encouragement, and pushing forward. I would like to extend my sincere thanks to colleagues and students for participating and contributing to this work. I must also thank reviewers for their constructive assessment, suggestions, and guidance.

I am obliged to thank Riga Technical University and the Institute of Chemistry and Chemical Technology (Polymer Materials) for all the opportunities provided to me during my doctoral studies.

One step at a time is all it takes to get you there.
/*Emily Dickinson*/

DOCTORAL THESIS PROPOSED TO THE SCIENTIFIC DEGREE OF DOCTOR OF SCIENCE

To be granted the scientific degree of Doctor of Science (Ph. D.), the present Doctoral Thesis has been submitted for defence at the open meeting of RTU Promotion Council on 15 May 2024 13.00 at the Faculty of Natural Sciences and Technology of Riga Technical University, Paula Valdena 7 Street, Room 272.

SCIENTIFIC SUPERVISOR
Professor Dr. sc. ing. Sergejs Gaidukovs
Faculty of Materials Natural Sciences and Technology, Riga Technical University, Latvia

OFFICIAL REVIEWERS

Associate Professor Dr. Ingars Reinholds
University of Latvia, Latvia

Professor Dr. Alexander Bismarck
University of Vienna, Austria

Dr. Tobias Robert
Fraunhofer Institute for Wood Research, Germany

DECLARATION OF ACADEMIC INTEGRITY

I hereby declare that the Doctoral Thesis submitted for review to Riga Technical University for promotion to the scientific degree of Doctor of Science (Ph. D.) is my own. I confirm that this Doctoral Thesis has not been submitted to any other university for promotion to a scientific degree.

Anda Barkāne ……………………………. (signature)

Date: ………………………

The Doctoral Thesis has been written in English. It consists of an Introduction; Literature review; Materials and methods; Results and discussion; Conclusions; 51 figures; 12 tables, schematics 6, and the total number of pages is 174. The Bibliography contains 340 titles.

ANNOTATION

Keywords: UV-light curing resins, 3D printing, acrylated epoxidized soybean oil, nanocrystalline cellulose, nanofibrillated cellulose, hemicellulose, lignin, bio-based polymer, nanoparticle reinforcement, hydrogen bonding, aging.

Acrylated epoxidized soybean oil (AESO) is a chemical compound resulting from the acrylation of epoxidized soybean oil, a vegetable oil-based acrylate. The acrylation process involves the incorporation of acrylic or acrylate functional groups into the structure of epoxidized soybean oil. This modification enhances its reactivity and compatibility with other polymers and materials. AESO exhibits notable characteristics, such as improved adhesion, flexibility, and durability, making it a valuable constituent in various applications, including the formulation of bio-based coatings, adhesives, and composite materials. In particular, AESO composites incorporating lignocellulose components have gained significant attention within the scientific community. These composites leverage the inherent properties of AESO and combine them with the abundance and renewability of lignocellulose components, resulting in promising bio-based solutions for a wide range of applications in polymer chemistry and materials science.

The majority of commercially available acrylate resins employed in 3D printing are derived from petroleum-based acrylates, with those marketed as bio-based typically containing less than 50 wt% of bio-derived content. Despite nanocellulose's established efficacy as a robust reinforcing agent in diverse polymer composites encompassing both thermoset (photocured acrylates) and thermoplastic polymers, challenges persist. Notably pertaining to the agglomeration of nanocellulose, particularly in the case of nanofibrillated cellulose, and issues of compatibility at the interface between cellulose-polymer matrix. Moreover, not all constituents of lignocellulose, encompassing cellulose, hemicellulose, and lignin, have been systematically investigated in the context of acrylic photocurable resins. Consequently, this study employs AESO-based resin and investigates various resin formulations encompassing all lignocellulose components and incorporates surface functionalization of nanocellulose to address interface compatibility concerns. Bio-based acrylate resins, whether utilized in coatings, films, or 3D printing applications, necessitate customizable attributes, including mechanical and thermal robustness, as well as resilience to weathering for outdoor applications. This objective is attained through the utilization of lignocellulose components as singular and hybrid fillers in diverse combinations, in conjunction with nanocellulose surface functionalization.

The PhD thesis is a set of combined original articles. The results of the current work are presented into five parts which corresponds to 8 original publications:

Part 1 describes development of neat resin composition and its validation for films and 3D printing applications. The use of reactive diluents was explored to improve the thermomechanical performance as well as thermal stability. Further the photoinitiator concentrations were controlled in order to achieve highest double bond conversion rates. All

prepared resin formulations were tested for their double bond conversion rates achieved, thermomechanical performance and thermal stability.

Part 2 describes the development of AESO-based resin filled with lignocellulose components in multiple ratios up to 30 wt% and in hybrid compositions for film applications. Controlling the filler concentration and hybrid composition of the fillers allowed to control the cured films performance properties. Adjustable thermomechanical performance as well as controllable surface morphology was achieved without losing the thermal stability. This section demonstrates the great potential of using also hemicellulose and lignin in photocurable acrylate resins.

Part 3 describes the use of neat nanofibrillated cellulose reinforcement in AESO-based photocurable resin for 3D printing. Reducing the nanofibrillated cellulose concentration down to percolation threshold allowed to mitigate the extreme fiber tendency to agglomerate. Nanofibrillated cellulose effect on resins viscosity, printing accuracy, materials mechanical, thermomechanical and thermal properties was analysed in-depth. Ultra-low concentration of the nanofibrillated cellulose had no effect on thermal stability nor the printing accuracy. It was discovered that keeping the concentration of the nanofibrillated cellulose around the percolation threshold gives the best mechanical performance since particle agglomeration is reduced.

Part 4 describes the surface functionalization effect on improving the compatibility between the nanocellulose and AESO-based resin. Nanocellulose underwent two different surface functionalization’s to reduce its hydrophilic nature. In-depth analysis of reinforcement efficiency and adhesion between the particles and the matrix was performed. Exceptional mechanical performance of newly developed composite resins was achieved.

Part 5 describes the weathering investigations of neat nanofibrillated cellulose AESO-based composite resins. This section closed the gap of bulk properties changes during accelerated weathering in photocured materials. It was discovered that nanofibrillated cellulose introduction prevents the surface cracking and delays the yellowing of the samples. Surprising results showed that nanofibrillated cellulose even ensures some mechanical performance improvements during the weathering.

The Doctoral Theses has been written in English; it consists of 50 figures; 12 tables, 5 schematics, and the total number of pages is 174. The Bibliography contains 340 titles.

ANOTĀCIJA

Fotocietējoši augu eļļā bāzēti akrilātu sveķi ar lignocelulozes komponentiem

Atslēgas vārdi: UV gaismā polimerizējami sveķi, 3D druka, akrilēta epoksidēta sojas pupiņu eļļa, nanokristāliskā celuloze, nanofibrilēta celuloze, hemiceluloze, lignīns, biobāzēts polimērs, nanodaļiņu stiegrojums, ūdeņraža saišu mijiedarbība, novecošana.

Akrilētā epoksidētā sojas pupiņu eļļa (AESO) ir no augu eļļas bāzes izgatavots akrilāts, ko iegūst, akrilējot epoksidētu sojas pupiņu eļļu. Akrilēšanas process ietver akrila vai akrilāta funkcionālo grupu iekļaušanu epoksidētas sojas pupiņu eļļas struktūrā. Šī modifikācija uzlabo tās reaģētspēju un savietojamību ar citiem polimēriem un materiāliem. AESO piemīt izceļamas labas īpašības, piemēram, uzlabota adhēzija, elastība un izturība, padarot to par vērtīgu sastāvdaļu dažādos pielietojumos, tostarp biobāzētu pārklājumu, līmju un kompozītmateriālu veidošanā. Jo īpaši AESO kompozītmateriālos, kuros ir lignocelulozes komponentes, tie ir ieguvuši ievērojamu uzmanību zinātnieku aprindās. Šie kompozītmateriāli izmanto AESO raksturīgās īpašības un apvieno tās ar lignocelulozes komponenšu pārpilnību un atjaunojamību, kā rezultātā tiek iegūti daudzsološi biobāzēti risinājumi plašam pielietojumu klāstam polimēru ķīmijā un materiālu zinātnē.

Lielākā daļa komerciāli pieejamo akrilāta sveķu, ko izmanto 3D drukāšanā, ir iegūti no naftas bāzes akrilātiem, un tie, kas tiek tirgoti kā biobāzēti, parasti satur mazāk nekā 50 masas % biobāzētu sveķu. Neskatoties uz to, ka nanoceluloze ir iedarbīga kā spēcīgs stiegrojums dažādos polimēru kompozītmateriālos, kas ietver gan termoreaktīvos (fotopolimerizētus akrilātus), gan termoplastiskos polimērus, problēmas joprojām pastāv. Jo īpaši saistībā ar nanocelulozes aglomerāciju, sevišķi nanofibrilētas celulozes gadījumā, un saderības jautājumiem celulozes-polimēra matricas robežvirsmā. Turklāt ne visas lignocelulozes sastāvdaļas, tostarp celuloze, hemiceluloze un lignīns, ir sistemātiski pētītas akrilāta fotopolimerizējamu sveķu kontekstā. Līdz ar to šajā pētījumā tiek izmantoti AESO bāzes sveķi un tiek pētīti dažādi sveķu sastāvi, kas ietver visas lignocelulozes komponentes kā arī nanocelulozes virsmas funkcionalizāciju, lai risinātu robežvirsmas saderības problēmas. Biobāzēta akrilāta sveķiem neatkarīgi no tā, vai tos izmanto pārklājumos, plēvēs vai 3D drukāšanā, ir nepieciešamas pielāgojamas lietošanas īpašības, tostarp mehāniskā un termiskā noturība, kā arī noturība pret novecināšanu izmantošanai ārpus telpām. Šis mērķis tiek sasniegts, izmantojot lignocelulozes komponentes kā atsevišķas un hibrīdas pildvielas dažādās kombinācijās, kā arī ar nanocelulozes virsmas funkcionalizāciju.

Promocijas darbs ir apvienotu oriģinālu rakstu kopums. Pašreizējā darba rezultāti ir apkopoti piecās daļās, kas atbilst 8 oriģinālajām publikācijām:

1. daļā ir aprakstīta sveķu sastāva izstrāde un tā validācija plēvju un 3D drukāšanas pielietojumiem. Tika pētīta reaktīvo atšķaidītāju izmantošana, lai uzlabotu termomehānisko veiktspēju, kā arī termisko stabilitāti. Turklāt fotoiniciatora koncentrācijas tika kontrolētas, lai sasniegtu augstākos dubultās saites konversijas pakāpi. Visas sagatavotās sveķu formulācijas

tika pārbaudītas attiecībā uz sasniegto dubultsaišu konversijas pakāpi, termomehānisko veiktspēju un termisko stabilitāti.

2. daļā ir aprakstīta AESO bāzes sveķu izstrāde, kas pildīta ar lignocelulozes komponentēm vairākās koncentrācijās līdz 30 masas %, un hibrīdkompozīcijās plēvēm. Pildvielu koncentrācijas un pildvielu hibrīdā sastāva kontrole ļāva kontrolēt sacietējušo plēvju veiktspējas īpašības. Regulējama termomehāniskā veiktspēja, kā arī kontrolējama virsmas morfoloģija tika panākta, nezaudējot termisko stabilitāti. Šī sadaļa parāda lielas iespējas izmantot arī hemicelulozi un lignīnu fotopolimerizējamos akrilāta sveķos.

3. daļā ir aprakstīta nanofibrilētas celulozes stiegrojuma izmantošana AESO bāzes fotopolimerizējamos sveķos 3D drukāšanai. Nanofibrilētās celulozes koncentrācijas samazināšana līdz perkolācijas slieksnim ļāva mazināt šķiedru ārkārtējo tendenci aglomerēties. Tika padziļināti analizēta nanofibrilētās celulozes ietekme uz sveķu viskozitāti, drukas precizitāti, materiālu mehāniskajām, termomehāniskajām un termiskajām īpašībām. Īpaši zemā nanofibrilētās celulozes koncentrācija neietekmēja ne termisko stabilitāti, ne drukāšanas precizitāti. Tika atklāts, ka nanofibrilētās celulozes koncentrācijas saglabāšana ap perkolācijas slieksni nodrošina vislabāko mehānisko veiktspēju, jo tiek samazināta daļiņu aglomerācija.

4. daļā aprakstīta nanocelulozes virsmas funkcionalizācijas ietekme uz nanocellulozes-AESO bāzes sveķu savietojamības uzlabošanu. Nanoceluloze tika pakļauta divām dažādām virsmas funkcionalizācijām, lai samazinātu tās hidrofīlo raksturu. Tika veikta padziļināta stiegrojuma efektivitātes un daļiņu-matricas adhēzijas analīze. Jaunizstrādāto kompozītmateriālu sveķos tika sasniegta izcila mehāniskā veiktspēja.

5. daļā ir aprakstīti nanofibrilētas celulozes AESO bāzes kompozītmateriālu sveķu novecināšanas iedarbības pētījumi. Šī sadaļa aizpildīja pētījumu plaisu attiecībā uz tilpuma īpašību izmaiņām paātrinātas laikapstākļu novecināšanas ietekmē fotopolimerizējamos materiālos. Tika atklāts, ka nanofibrilētas celulozes ievadīšana novērš virsmas plaisāšanu un aizkavē paraugu dzeltēšanu. Pārsteidzoši rezultāti parādīja, ka nanofibrilētā celuloze pat nodrošina dažus mehāniskās veiktspējas uzlabojumus novecināšanas laikā.

Promocijas darbi ir uzrakstīti angļu valodā; tas sastāv no 174 lappusēm, 50 attēliem, 12 tabulām, 5 shēmām un 340 uzziņu avotiem.

TABLE OF CONTENTS

ABBREVIATIONS

A	Adhesion factor
AC	Acryloyl chloride
AESO	Acrylated epoxidized soybean oil
AFM	Atomic-force microscopy
AM	Additive manufacturing
ATR	Attenuated total reflectance
C	Nanocrystalline cellulose
C*	Filler-matrix stress efficiency transfer parameter
CNC	Computer numerical control
COD	Coefficient of determination
DBC%	Double bond conversion rate
DMA	Dynamic mechanical analysis
DMAc	N,N-dimethylacetamide
DMF	N,N-dimethylformamide
E'	Storage modulus
E'_c	Storage modulus for composite (95 °C)
E'_g	Storage modulus at glassy state (-45 °C)
E'_m	Storage modulus for polymer matrix (95 °C)
E'_v	Storage modulus at viscoelastic/rubbery state (95 °C)
E''	Loss modulus
F	Nanofibrillated cellulose
FESEM	Field emission scanning electron microscopy
FTIR	Fourier transform infrared spectroscopy
H	Hemicellulose
HNO_3	Nitric acid
HMDI	Hexamethylene diisocyanate
HDDA	1,6-hexanediol diacrylate
HCl	Hydrochloric acid
L	Lignin
LiCl	Lithium chloride
M_c	Molecular weight between crosslinks
N	Crosslinking density
NaOH	Natrium hydroxide
pC	Nanocrystaline cellulose from filter paper
pCI	Nanocrystaline cellulose from filter paper functionalized with isocyanate
PEGDA	Polyethylene glycol diacrylate
PI	Photoinitiator
pF	Nanofibrillated cellulose from filter paper
pFA	Acrylated nanofibrillated cellulose from filter paper
r	Reinforcement parameter

SEM	Scanning electron microscopy
SLA	Stereolithography apparatus
Tanδ	Loss factor
T_g	Glass transition temperature
TGA	Thermogravimetric analysis
TMPTA	Trimethylolpropane triacrylate
TPO	2,4,6-trimethylbenzoyldiphenylphosphine oxide
TPS	Thin plate spline
UV-Vis	Ultraviolet-visible light
VDA	Vanilin diacrylate
VDM	Vanilin dimethacrylate
V_f	Nanofiller volume fraction in the composite
VO	Vegetable oil-based composition without fillers
VOC5	Vegetable oil-based composition with nanocrystalline cellulose 5 wt%
VOC10	Vegetable oil-based composition with nanocrystalline cellulose 10 wt%
VOC20	Vegetable oil-based composition with nanocrystalline cellulose 20 wt%
VOC30	Vegetable oil-based composition with nanocrystalline cellulose 30 wt%
VOF5	Vegetable oil-based composition with nanofibrillated cellulose 5 wt%
VOF10	Vegetable oil-based composition with nanofibrillated cellulose 10 wt%
VOF20	Vegetable oil-based composition with nanofibrillated cellulose 20 wt%
VOF30	Vegetable oil-based composition with nanofibrillated cellulose 30 wt%
VOH5	Vegetable oil-based composition with hemicellulose 5 wt%
VOH10	Vegetable oil-based composition with hemicellulose 10 wt%
VOL5	Vegetable oil-based composition with lignin 5 wt%
VOL10	Vegetable oil-based composition with lignin 10 wt%
wt%	Weight percent
YI	Yellowing index

INTRODUCTION

In recent years, bio-based acrylates, especially those derived from vegetable oils, have gained prominence within polymer chemistry due to their renewability. These materials are increasingly recognized for their potential to reduce reliance on petroleum resources. However, there are still some performance properties challenges, such as mechanical and thermal durability, weathering resistance, and interface compatibility. These issues can be effectively addressed by incorporating lignocellulose components, such as nanocellulose, hemicellulose, and lignin. Surface functionalization of nanocellulose with hydrophilic groups is crucial for improving the compatibility with the hydrophobic acrylate matrix. This work highlights the significance of bio-based acrylates, emphasizing their role in modern markets and their ability to enhance performance characteristics through the strategic use of lignocellulose constituents and nanocellulose surface functionalization. Moreover, these bio-based acrylate lignocellulose composites hold promise in various applications, including film production, coatings, and UV-assisted 3D printing, aligning with the growing demand for bio-based materials across industrial sectors.

The doctoral thesis focuses on the development of lignocellulose composites using vegetable oil-based acrylate resins. As a reinforcing filler, it assesses various lignocellulose components, including nanocellulose, hemicellulose, lignin, and recycled cellulose. The thesis also explores the chemical surface functionalization of cellulose to address hydrophobicity issues. Notably, the transformation of cellulose into nanoscale particles demonstrates exceptional properties with promising applications, while maintaining precision in 3D printing. Mechanical testing reveals substantial improvements in performance due to nanocellulose reinforcement. Hemicellulose's potential as a nonreactive diluent is also highlighted. The extensive range of composite resin formulations developed in this study offers a versatile platform for systematic selection and optimization of performance properties.

Within the doctoral thesis, two distinct strategies are employed for preparing vegetable oil-based acrylate / lignocellulose composites: film curing for highly loaded compositions (up to 30 wt%) and UV-assisted 3D printing for lower loading (down to 0.1 wt%) compositions. The overall schematic of the presented Doctoral Thesis is depicted in Scheme 1. Both methods utilize UV-light curing, reducing the energy requirements for sample preparation. The thesis extensively examines the impact of lignocellulose fillers on mechanical and thermomechanical properties, thermal stability, and accelerated weathering endurance. Changes in double bond conversion rate and crosslinking degree are meticulously analyzed. The effectiveness of chemical surface functionalization of nanocellulose in enhancing the interface is investigated through mechanical performance and reinforcing efficiency analysis. Sample morphology and printing accuracy are evaluated using scanning electron microscopy and optical microscopy.

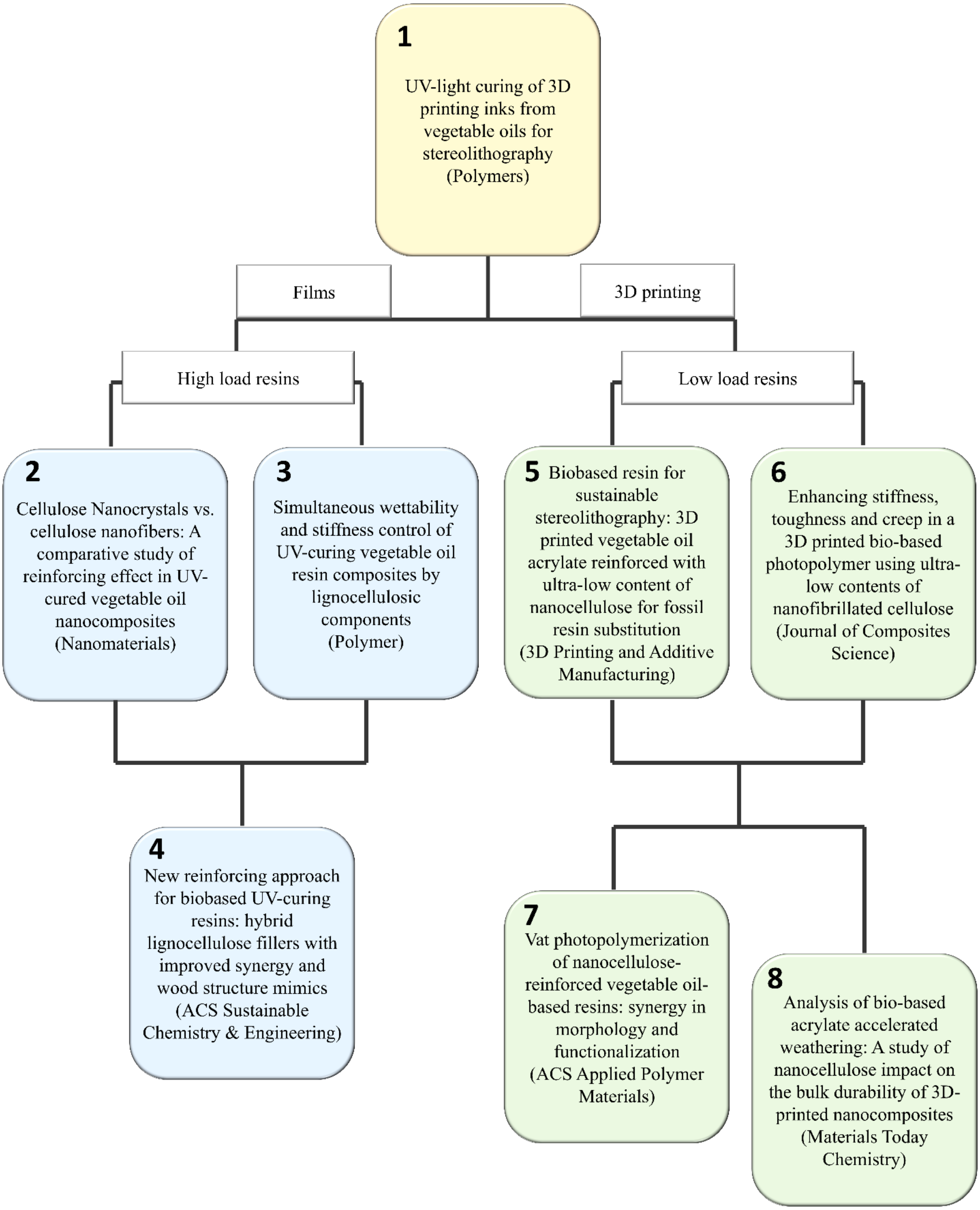

Scheme 1. The overall schematic of presented the Doctoral Thesis, (in brackets journals where papers are published).

Aim of the doctoral thesis

To utilize bio-based resources and UV-light assisted sustainable technologies to develop acrylated epoxidized soybean oil / lignocellulose nanocomposite resin materials with enhanced performance in comparison to other bio-based acrylate resin materials.

Tasks of the doctoral thesis

1. To formulate bio-based liquid resin from lignocellulose nanoparticles and bio-based acrylated epoxidized soybean oil (AESO) and reactive diluents, which are suitable for UV-light assisted curing of film / coating and 3D printing applications.
2. To assess AESO nanocomposite materials containing different contents of single and hybrid combinations of nanocrystalline cellulose, nanofibrillated cellulose, hemicellulose, and lignin.
3. To test resins’ processing properties like 3D printing accuracy and resolution, UV-light curing efficiency, and also cured materials performance properties like crosslinking degree, thermal, thermomechanical, and mechanical properties of the obtained resin materials for film and 3D printing processing.
4. To develop different nanocellulose surface functionalization methods to enhance the compatibility and interaction with the polymer matrix.
5. To evaluate the durability and accelerated weathering of obtained nanocellulose-polymer composites.

Thesis statements to be defended

1. The addition of reactive diluents (1,6-hexanediol diacrylate (HDDA) and trimethylolpropane triacrylate TMPTA) to acrylated epoxidized soybean oil (AESO) result in increased performance and UV-curable formulations have potential for coating / films and 3D printing applications.
2. The good processing and outstanding performance properties of AESO / lignocellulose resin materials are tuned up by using lignocellulose fillers to outperform other bio-based acrylate resins and hybrid combinations present significant advantages by reducing the total filler loading and benefitting the mechanical, thermal, wetting and durability performance characteristics.
3. Ultra-low loads of nanocellulose in AESO resin for 3D printing applications ensure their outstanding mechanical performance and long-term durability.
4. Surface functionalization of nanocellulose significantly enhances compatibility with the resin and improves composite materials' exploitation properties.
5. Introduction of nanofibrillated cellulose increased the durability and resistance to accelerated weathering of obtained nanocellulose-polymer composites.

Scientific novelty

1. Demonstration of novel bio-based composites as an alternative to fossil-based plastics for high-performance applications.
2. Demonstration of lignocellulose filler benefit for AESO resins UV-light processing and performance.
3. Development of a UV-light-assisted stereolithography 3D printing process for vegetable oil-based / nanocellulose composites.
4. Developments of different functionalization routes for nanocellulose crystals and fibrils to regulate the mechanical performance properties of the 3D printed composite materials.
5. In-depth analysis of accelerated weathering effect on UV-light cured AESO / nanocellulose composite materials.

Practical significance

1. Development of bio-based AESO resin with enhanced processing and performance properties for replacing petroleum-based acrylates used in photocuring applications.
2. Increase of mechanical performance with the introduction of lignocellulose components into the resin formulation.
3. Validation of the developed resin for 3D printing and film / coating production
4. Shown nanocellulose surface functionalization methods improve the nanocellulose reinforcement efficiency for bio-based acrylate resin.
5. Determinate the 3D printed materials' mechanical performance after weathering of the composite material.

Approbation of PhD thesis in Scopus and Web of Science indexed articles

Literature review

1. S. Briede, **A. Barkane**, M. Jurinovs, V. K. Thakur, S. Gaidukovs, Acrylation of biomass: A review of synthesis process: Know-how and future application directions. Current Opinion in Green and Sustainable Chemistry 35 (2022) 100626.
   Section 3.1.1.
2. **A. Barkane,** O. Platnieks, M. Jurinovs, S. Kasetaite, J. Ostrauskaite, S. Gaidukovs, Y. Habibi, UV-light curing of 3D printing inks from vegetable oils for stereolithography. Polymers 13 (2021) 1195, doi:10.3390/polym13081195
   Section 3.2.1.
3. **A. Barkane,** O. Platnieks, L. Grase, S. Gaidukovs, Simultaneous wettability and stiffness control of UV-curing vegetable oil resin composites by lignocellulosic components. Polymer 255 (2022) 125154, doi:10.1016/j.polymer.2022.125154
4. **A. Barkane,** E. Kampe, O. Platnieks, S. Gaidukovs, Cellulose Nanocrystals vs. cellulose nanofibers: A comparative study of reinforcing effect in UV-cured vegetable oil nanocomposites. Nanomaterials, 11 (2021) 1791, doi:10.3390/nano11071791

Section 3.2.2.

5. **A. Barkane,** E. Kampe, S. Gaidukovs, New reinforcing approach for biobased UV-curing resins: hybrid lignocellulose fillers with improved synergy and wood structure mimics. ACS Sustainable Chemistry & Engineering, 11 (17) (2023), 6578, doi:10.1021/acssuschemeng.2c07288
   Section 3.3.1.
6. **A. Barkane**, M. Jurinovs, O. Starkova, L. Grase, D. F. Schmidt, S. Gaidukovs, Enhancing stiffness, toughness and creep in a 3D printed bio-based photopolymer using ultra-low contents of nanofibrillated cellulose. Journal of Composites Science, 7 (10) (2023) 435, doi:10.3390/jcs7100435
7. **A. Barkane,** M. Jurinovs, S. Briede, O, Platnieks, P. Onufrijevs, Z. Zelca, S. Gaidukovs, Biobased resin for sustainable stereolithography: 3D printed vegetable oil acrylate reinforced with ultra-low content of nanocellulose for fossil resin substitution. 3D Printing and Additive Manufacturing, (2022) 1-16, doi:10.1089/3dp.2021.0294
   Section 3.4.1.
8. M. Jurinovs, **A. Barkane,** O, Platnieks, S. Beluns, L. Grase, R. Dieden, M. Strapolim D. F. Schmidt, S. Gaidukovs, Vat photopolymerization of nanocellulose-reinforced vegetable oil-based resins: synergy in morphology and functionalization. ACS Applied Polymer Materials, 5 (4) (2023), 3104, doi:10.1021/acssapm.3c00245
   Section 3.5.1.
9. **A. Barkane,** O. Platnieks, J. Vecstaudza, S. Gaidukovs, Analysis of bio-based acrylate accelerated weathering: A study of nanocellulose impact on the bulk durability of 3D-printed nanocomposites. Materials Today Chemistry, 33 (2023) 101737, doi:10.1016/j.mtchem.2023.101737

Other Publications on the Topic that are not included in PhD thesis

1. S. Briede, O. Platnieks, **A. Barkane**, I. Sivacovs, A. Leitans, J. Lungevics, S. Gaidukovs, Tailored biobased resins from acrylated vegetable oils for application in wood coatings. Coatings, 13 (2023)657, doi:10.3390/coatings13030657
2. **A. Barkane**, O. Platnieks, M. Jurinovs, S. Gaidukovs, Thermal stability of UV-cured vegetable oi epoxidized acrylate-based polymer system for 3D printing applications. Polymer Degradation and Stability 181 (2020) 109347, doi:10.1016/j.polymdegradstab.2020.109347

Dissemination in international scientific conferences

1. **A. Barkane,** O. Platnieks, S. Gaidukovs, Accelerated weathering of 3D-printed nanocomposites. RTU *64th International Scientific Conference - Materials Science and Applied Chemistry*, Riga, Latvia, 2023 October 6.
2. **A. Barkane,** S. Gaidukovs, New reinforcing approach for bio-based UV-curing resins: hybrid lignocellulose fillers with improved synergy and wood structure mimics. *38th*

International conference of the Polymer Processing Society, St. Gallen, Switzerland, 2023 May 22-26.

3. **A. Barkane,** S. Gaidukovs, Photo crosslinking kinetics for bio-based 3D printing resins: FTIR vs. photorheology. *Nordic Rheology conference*, Aarhus, Denmark, 2023 Apryl 12-14.
4. **A. Barkane,** O. Paltneiks, S. Gaidukovs, Comparison of Lignin, Hemicellulose and Nanocellulose as Green Additives to Reinforce Vegetable Oil Resins for UV Curing. *POLY-CHAR 2022 conference*, Online, 2022 May 22-25.
5. **A. Barkane,** M. Jurinovs, S. Gaidukovs, Bio-based, nanocellulose reinforced, UV-curable inks for additive manufacturing. *6th Green and Sustainable Chemistry Conference – Elsevier*, Online, 2021 November 16-18.
6. **A. Barkane,** S. Gaidukovs, Reinforcement Efficiency of Cellulose Nanofibers And Nanocrystal in UV-curable Vegetable Oil Polymer Matrix. *Riga Technical University 62nd International Scientific Conference - Materials Science and Applied Chemistry,* Riga, Latvia – Online, 2021 October 22.
7. **A. Barkane,** E. Kampe, M. Bleija, M. Jurinovs, Y. Habibi, S. Gaidukovs, Thermal properties of modified NFC bio-based photocurable polymer composites. *ACS Spring 2021 Macromolecular chemistry: The second century*, USA – online, 2021 Apryl 5-16.
8. **A. Barkane,** E. Kampe, M. Jurinovs, Y. Habibi, S. Gaidukovs, Bio-based polymer nanocomposite for photopolymerization applications. *1st Greenering international conference*, Online, 2021 February 15-17.
9. **A. Barkane,** M. Jurinovs, Z. Zelca, Y. Habibi, S. Gaidukovs, Nanocellulose filled acrylated epoxidized soybean oil inks for UV-assisted 3D printing. *Functional Materials and Nanotechnologies FM&NT-2020* Vilnius, Lithuania – online, 2020 November 23-26.
10. **A. Barkane,** E. Kampe, Y. Habibi, S. Gaidukovs, Photopolymerization of epoxidized soybean oil acrylate / lignocellulose biocomposites. *Materials Science and Applied Chemistry-2020,* Riga, Latvia – online, 2020, October 23.
11. E. Kampe, **A. Barkane,** S. gaidukovs, Y. Habibi, Photopolymerization of epoxidized soybean oil acrylate / lignocellulosic biocomposites. *Riga Technical University 61sd International Scientific Conference - Materials Science and Applied Chemistry*, Riga, Latvia, 2020 October 23.
12. **A. Barkane,** O. Platnieks, Y. Habibi, S. Gaidukovs, UV-assisted additive manufacturing of lignocellulosic nanomaterials. *ACS Fall 2020 Virtual Meeting & Expo – Moving chemistry from bench to market* online, USA, 2020 August 17-20.

1. LITERATURE OVERVIEW

1.1. Biomass acrylates

Publication:

- S. Briede, **A. Barkane**, M. Jurinovs, V. K. Thakur, S. Gaidukovs, Acrylation of biomass: A review of synthesis process: Know-how and future application directions. Current Opinion in Green and Sustainable Chemistry 35 (2022) 100626.

In the pursuit of a sustainable future, the polymer industry faces a significant challenge, given that approximately 99 % of the world's polymer production relies on fossil-based resources [1,2]. Over the years, eco-friendly raw biomass is being investigated to develop novel green monomer and oligomer components for sustainable polymer materials synthesis. The use of naturally obtained biomass can reduce the dependence on petrochemical suppliers and the impact of petroleum prices. Polymer materials obtained from biomass are a competitive alternative comparing with those made from petrochemicals. Notably, acrylic resins occupy a substantial portion of the resin market, accounting for 74 % of resin usage according to *SpecialChem's* 2020 market trend research [3]. In this context, vegetable oils emerge as a promising, abundant, renewable, and cost-effective resource, offering structural attributes that render them an attractive and sustainable foundation for various intermediates and products, including polymeric resins and composite materials [4,5]. Domestically and industrially used vegetable oil derivatives are considered widely available, while cellulose derivatives are the most abundant natural polymers. Modified vegetable oils, such as those derived from soybean, grapeseed, linseed, and rapeseed, have arisen as viable alternatives to fossil-based thermoset polymer resins [6,7]. Innovative technologies have been developed to convert these natural resources into novel monomers and polymers, resulting in industrial products with competitive properties akin to conventional petrochemical polymers [8-10]. Using acrylic derivatives of vegetable oils and cellulose as naturally obtained materials leads to long-lasting bio-based polymers with a wide range of high exploitation properties and applications. The characteristics of vegetable oil-based and cellulose-based acrylate resins of high bio-renewable carbon content are suitable for industrial application, while their role is still underestimated. A brief analysis of biomass-derived bio-based polymer resin compositions, properties, and applications are critically outlined herein.

1.1.1. Analysis of acrylated biomass derivatives

The number of applications of diverse polymeric materials continues to increase. The common polymers and polymer composites are derived from petroleum reserves, meaning an alternative source for these materials is still demanded [11]. To overcome the drawbacks of petroleum-based polymers, renewable bio-based resources, e.g., biomass, have begun to attract much attention. Figure 1.1 (a) from M. E. Fortuna et al. article lists the most relevant biomass sources are “Forestry, Agricultural, Industrial, Animal and Municipal Solid Waste and Sewage Sludge,” which ensure vast availability of the biomass [12]. Due to their broad availability and modification possibilities, the biomass of cellulose and natural oils from Forestry and Agricultural crops are of extra interest for the reviewed acrylation process. Cellulose is the most abundant biological macromolecule found in plants, marine animals, fungi, and algae, where it acts as the structural component in cell walls. Mainly cellulose consists of *D*-anhydroglucopyranose ($C_6H_{11}O_5$) linear, chemically polar chains with β-(1, 4)-glycosidic bonds, with polymerization of approximately 10 000. Although cellulose has been widely used in polymer acrylate matrix primarily as a reinforcing filler without additional modification [13], developing more sustainable cellulose-based biomaterial products requires novel ways to modify this renewable biomass. Vegetable oils are mainly triacylglycerols (92–98 %); the number of carbon atoms, double bonds (unsaturation), and functional groups differ in fatty acids. The consumption of seed oils has increased where saturated palmitic acid (16:0), stearic acid (18:0), monounsaturated oleic acid (18:1), the polyunsaturated linoleic (18:2) and α-linolenic (18:3) acids (x:y stands for chain carbon atoms: number of unsaturation) are the most used ones. The active groups in triacylglycerols are double bonds, allylic carbons, ester groups, and alpha to the ester group. The reactivity of various groups in the long chains is relatively low [14,15].

An intensive investigation has also been performed to develop sustainable polymer materials from vegetable oils in the last decade, considering the growing price of petroleum-based resources and environmental contamination [16]. Moreover, methods for obtaining polymers from vegetable oils meet the principles of “green chemistry,” such as design for degradation, pollution prevention, energy efficiency, and use of renewable feedstocks [17]. Using newly formed vegetable oils resins, bio-based polymers with a wide range of improved physical performance have been developed [18]. Photoinduced polymerization initiation triggered by light radiation occurs too slowly for the neat vegetable oils, and it is not suitable for commercial application to obtain any polymer materials. For this aim, the oils are being modified, introducing more active functional groups [19] and some formulations with more reactive comonomers are also investigated [20]. Modified vegetable oils can undergo radical polymerization, although polymerization can also occur via an ionic mechanism [21-24]. Acrylates and methacrylates are among the most reactive monomers suitable for UV-initiated photopolymerization [22-24]. Furthermore, acrylation or similar functionalization reactions are the most common means to introduce polymerizable groups to the vegetable oils molecules [25,26].

The number of articles reported from Scopus (Elsevier) and Web of Science (Clarivate Analytics) indexing databases of vegetable oil and cellulose acrylate polymer is represented in Figure 1.1 (b) (August 2021). The keywords used in the search were “cellulose, acrylate, polymer” for cellulose-based acrylates and “oil, acrylate, polymer” for vegetable oil-based acrylates. Nevertheless, the number of articles in 2016 reporting vegetable oil-based acrylic polymers and their derivatives are only 45 and 74 from Scopus and WOS databases, respectively, which mostly describe acrylated epoxidized soybean oil (AESO) and castor oil derivatives. In contrast, cellulose-based acrylic polymers are about 22 and 35, including acrylate-grafted cellulose. The total number of publications tends to increase every year, 2020 showed that the absolute number of publications doubled.

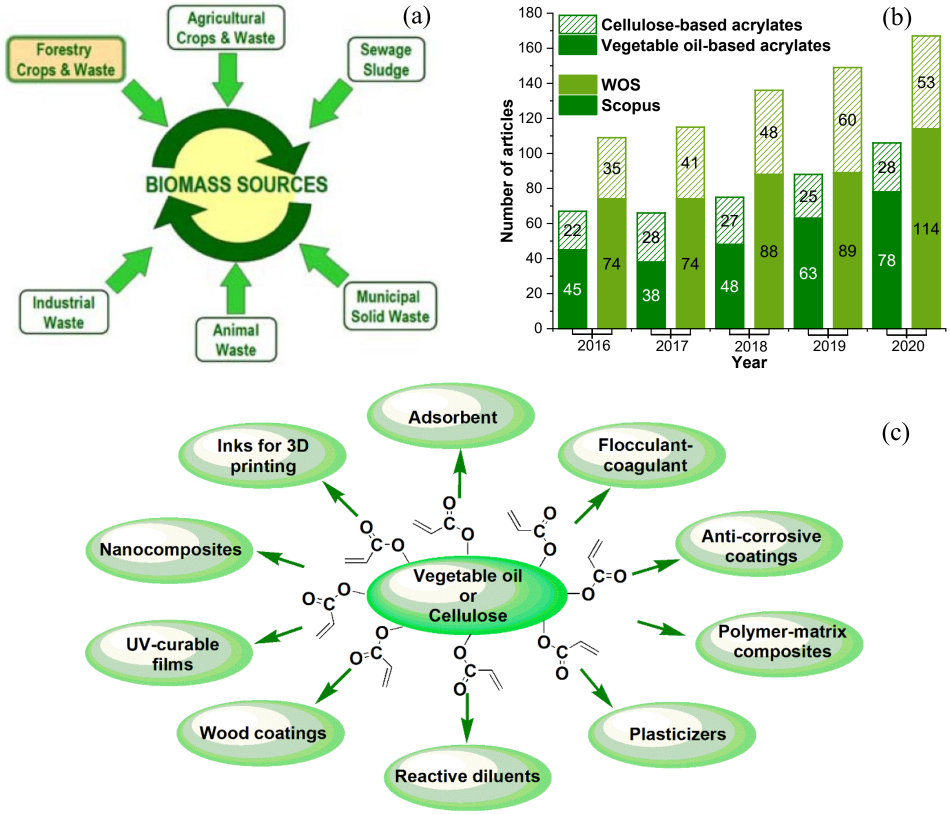

Figure 1.1. The most relevant sources of biomass (a) [12], the number of articles reporting bio-based acrylic polymers from 2016–2020 (b), application of vegetable oil- and cellulose-based polymers containing acrylate functionality (c).

1.1.2. Biomass acrylation

Figure 1.2 (a) (I) shows that acrylation of vegetable oils usually proceeds via a two-step process: (1) epoxidation of double bonds [27], followed by (2) oxirane ring-opening that has been extensively reported by the reaction of methacrylic acid with epoxidized soybean oil, linseed oil [28], sucrose soyate [29] etc. Lately, different vegetable oil-based acrylate prepolymers were obtained using one-step synthesis Figure 1.2 (a) (II) through the acrylation of vegetable oil with acrylic acid under the catalysis of $BF_3 \times Et_2O$, including palm oil, olive oil, peanut oil, rapeseed oil, corn oil, canola oil and grapeseed oil [6]. The advantages of the reaction are simple operation, mild conditions, and atom economy.

Acryloyl chloride (AC) is a popular reagent to obtain cellulose with acrylate entities, as shown in Figure 1.2 (b). The vinyl groups can be introduced via esterification between AC and hydroxyl groups of the cotton and jute cellulosic fibers [30]. Commonly, partly acrylation reaction conversion is received. The isocyanate is proposed to substitute the residual hydroxyl groups of cellulose, obtaining the cellulose esters [31]. The primary application of the modified cellulose is the filler for polymer biocomposites.

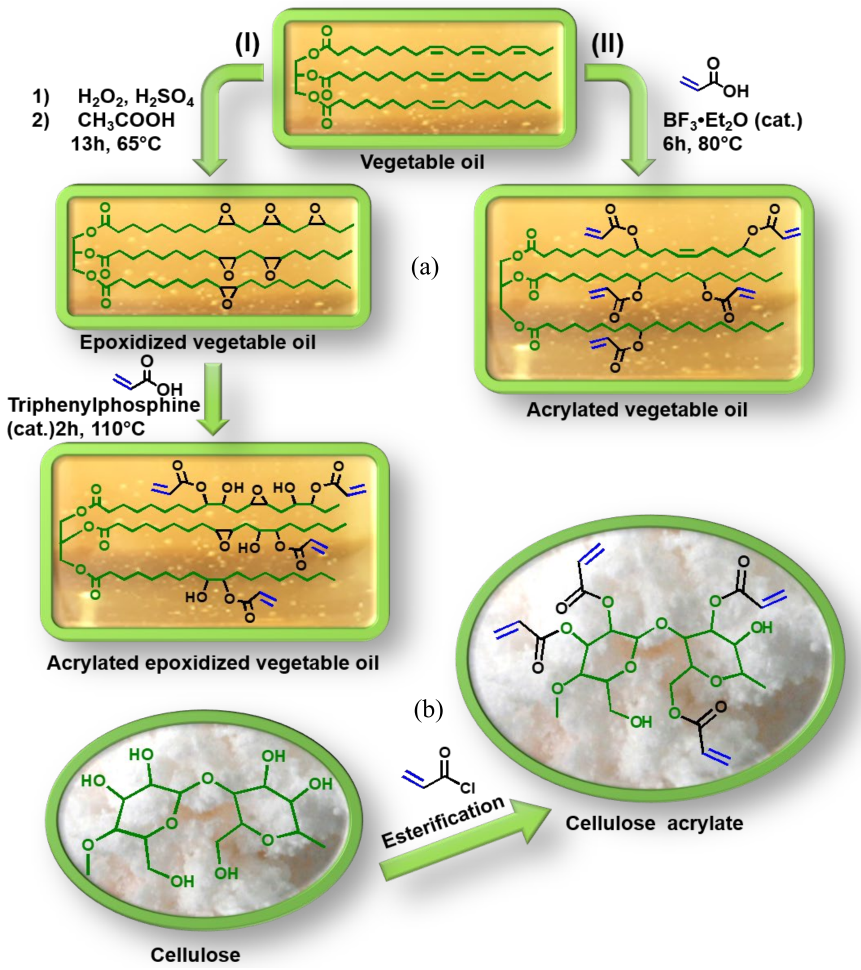

Figure 1.2. Vegetable oil acrylation via two-step (I) and one-step (II) synthesis methods (a), cellulose acrylation via esterification (b).

1.1.3. Applications of bio-based acrylates

Vegetable oils, when modified by acrylation, can be UV-light cured [6,32,33]. Bio-based resins demonstrate competitiveness with their petroleum-based counterparts in terms of performance [34-39]. These vegetable oil-based polymers find applications in adhesives [40], plasticizers [41], lubricants [42], resins [43], nanocomposites matrix [44,45] and coatings [46] (Figure 1.1 (c)). For example, wood protective modified vegetable oil coatings are being developed for physicochemical and fungal resistance [40,47]. The main advantages of these resources for polymeric materials are low costs and sustainability aspects – low ecotoxicity and low hazardous to humans [48]. Acrylation of plant oils yields highly reactive groups and additional oxygen atoms in their structure, rendering them suitable for thermoset polymer production [8]. Among these, acrylated epoxidized soybean oil (AESO) has been commercialized available under the trademark *Ebecryl 860* as a relatively competitive solution for coatings and UV-assisted additive manufacturing (AM) technology resins [32,49,50].

Such AESO-based polymers offer a competitive solution to replace petroleum-derived polymeric materials in the polymer industry. Mechanical characteristics of AESO polymer prepared by UV-light-assisted 3D printing technologies like stereolithography (SLA) and digital light processing methods (DLP) have been evaluated and compared with commercial 3D printing resin [50,51]. The synthesized polymers exhibited thermal decomposition temperature at the weight loss of 10 % above 300 ºC and showed very high tensile strength values. Interestingly, two similar polymeric resins, methacrylic ester AESO and tetrahydro furfuryl acrylate AESO, with the most deficient mechanical properties, also showed the highest biodegradability [52]. AESO-based UV-curable waterborne polyurethane pigment print adhesive is proposed for the textile industry considering the surprising increase of water absorption with the higher AESO content in the resin [53]. Nanocomposite containing AESO blended with 2-hydroxyethyl acrylate has excellent biocompatibility for bone tissue engineering applications [54]. Dai et al. developed a UV-curable coating based on AESO, delivering impressive adhesion and hardness properties [36]. Reported results showed the highest adhesion grade of 5 B and a pencil hardness of 5 H. These results are slightly lower than the 6 H reported by a commercial supplier for a protective coating for optical and outdoor applications [55].

Commonly oil component develops a polymer matrix, while cellulose is applied as a reinforcing filler [44,45]. In contrast, the modified cellulose can be also the matrix itself containing inorganic / organic nanofillers [44,45]. As acrylic functional groups are incorporated into cellulose molecules to obtain light reactivity properties and meet many applications. These monomers, oligomers, and polymer resins are widely applied due to their excellent ability to cure under ultraviolet (UV) and visible (Vis) lights by creating stable chemical crosslinks. UV-curable resin research and commercial application have expanded rapidly due to their advantages over traditional solvent evaporation and thermal two-component hardening methods, including very rapid curing, high-cost performance, energy-saving and friendliness to the environment [56].

Cellulose acrylate derivatives have found some applications to coat pharmaceutical dosage forms in textile, construction, electronic and automotive industries [57]. Derived cellulose crosslinking has been widely investigated and reported since 1961 and is highly important for progress in new material formulations [58]. Qian et al. extensively researched a novel solid-solid phase-changing material from cellulose acrylate and poly(*n*-alkyl acrylate) [59]. Synthesized material melting enthalpies and transition temperatures were sensitive to the molecular weight of the components, thus opening possibilities to tune for good thermal and shape stability. UV-curable formulations for coating application containing modified cellulose and AESO were prepared by Auclair et al. [60], who proposed modification reaction with AC, using a 1-methylimidazole catalyst and 1,4-dioxane solvent. Cellulose modification positively affected the mechanical properties of the coatings.

Acrylates formulated on soybean, linseed, and sesame oils are proposed extensively in UV-curable resins. In contrast, cellulose acrylates find their application as fillers. Applying acrylates as an additive in polymer composites technology can enhance the overall thermal stability, chemical resistance, and mechanical properties of the material for a specific application. Nevertheless, further research is needed to attain truly competitive bio-based polymer resins with customizable properties. In this context, enhancing resins with lignocellulosic additives for sustainability reasons becomes an appealing proposition. As a continuation of this bio-based approach, the need for tuneable properties in thermoset resins can be addressed by incorporating additives of sustainable origin, such as lignocellulosic components beyond cellulose. These biopolymer additives, when selected judiciously, offer the potential to significantly alter composite performance, impacting mechanical properties, visual aesthetics, surface morphology, and wetting characteristics [60-64].

1.1.4. Lignocellulose components prospects for vegetable oil-based acrylate resins

Lignin (L), cellulose, and hemicellulose are among the most prevalent naturally occurring polymers that contribute to specific structural and ancillary properties in plants and trees [65]. Lignocellulose, the most abundant biopolymer, is primarily composed of cellulose (40–50 %), hemicellulose (25–35 %), and L (15–20 %), with varying compositions based on plant species, origin, and growth conditions [66,67]. In hardwoods, the composition ranges from 40–50 % cellulose, 15–20 % hemicellulose, and 25–30 % L [68]. Given their wide availability, lignocellulosic components represent promising candidates for tailoring the properties of bio-based polymer resins. While hemicellulose has been primarily employed as a polymer matrix, nanocellulose has already demonstrated its effectiveness as an exceptional reinforcement agent [69-71]. Particularly, nanocellulose, owing to its properties comparable to synthetic fibers, holds substantial promise as a natural reinforcement in composite science [13]. Nanocrystalline cellulose (C) and cellulose nanofibrils (F) are the primary lignocellulosic fillers used for reinforcing acrylic resins [60,72-74]. The addition of neat C and F to acrylic resins in concentrations ranging from 0.1 to 50 wt% results in substantial improvements in tensile strength (up to 9-fold), stiffness (up to 1.25-fold), storage modulus (up to 6-fold), and thermal conductivity (up to 11 %) [60,75-77]. Wood furniture coating resins have shown improvements with the addition of C [78]. Incorporating 3 wt% C increased the stiffness of UV-curable coatings by nearly 25 % and enhanced the hardness index by up to 2 H.

Undoubtedly, nanocellulose has proven itself as an effective reinforcement in polymer composites, but hemicellulose and L have been underexplored in UV-curing resin composites. Hemicellulose, although unsuitable as a primary filler due to its tendency to form polymer blends rather than composites [71], should not be disregarded as a diluent for UV-curable polymer compositions. Its structural composition offers advantages such as tuneable barrier properties and the capacity to regulate compatibility between nanocellulose and the polymer matrix [79]. In plant structures, branched and amorphous hemicellulose molecules promote the dense packing of cellulose fibers and their linkage [80]. While hemicellulose has been extensively studied for applications in thermoplastic material-based additive manufacturing technologies and coatings [79,80], its potential in UV-curable resins remains largely unexplored. In contrast, LN, due to its properties of UV-light absorption, has been less explored for UV-curing resins [81]. However, L possesses unique attributes, including excellent water and UV-light barrier properties, as well as thermal stability. Its relatively hydrophobic nature contributes to strong interfacial adhesion with polymers [82]. Despite its UV-absorbing properties, there have been successful applications of functionalized L as an additive for UV-curable systems [83,84].

Hemicellulose and L are occasionally incorporated into acrylic resins but primarily in modified forms (acrylated, functionalized with tyramine, or other modifications), and they are less frequently used compared to C and F [75,83-87]. For example, Markstedt et al. investigated modified hemicellulose, incorporating tyramine and immersion in H_2O_2, as a cross-linkable matrix for additive manufacturing [86]. Moreover, hemicellulose and L have found more widespread utilization as raw materials for chemical synthesis, yielding furans, phenolics, glycerides, ethanol, various acids (itaconic, lactic, fumaric, etc.), and other compounds [87-90]. Consequently, investigations into the incorporation of neat hemicellulose and L in UV-curable resins are warranted to unlock their potential.

1.1.5. Hybrid lignocellulose components prospects for vegetable oil-based acrylate resins

The necessity to tune up AESO-based resins performance exists. Complementing sustainability, natural additives could be the solution for improving the mechanical performance and tunability of AESO-based resins [74]. Lignocellulose fillers are actively investigated for this purpose. As a result, improvements in mechanical performance, surface morphology, wettability, and visual appearance can be achieved for these materials [72,75,91].

The application possibilities are broad regardless of using neat or modified lignocellulose filler. C and F mainly provide beneficial light scattering in the matrix and reinforcement and enhancing mechanical properties [69-71,92]. However, C and F additions also increase the resin viscosity, often limiting UV-curable resins [93]. Although hemicellulose cannot be considered as a filler [71,75], it can provide tunable barrier properties, improved polymer matrix compatibility, and densification [79,80]. Due to its UV-light absorption properties [81], L is not a typical choice for UV-curing resins. However, if L's radical scavenging properties [94] could be mitigated without chemical modification, its beneficial properties, like thermal stability and enhanced hydrophobicity, could be advantaged in thermoset composites [95]. A very appealing prospect would be to create hybrid lignocellulosic fillers for UV-curable resins. Hybrid fillers would mitigate L UV-light absorbance properties by using nanocellulose, which provides additional light scattering and also reinforces the polymer matrix. Hemicellulose could act as a nonreactive diluent and reduce the resin's viscosity, benefiting UV-curing [75]. Hence, UV-curable resins could be adjustable as hybrid lignocellulose composites, and various new applications would arise.

Most commonly, thermoplastics are the first to be squeezed in the industry. However, thermosets provide their advantages as thermal stability, chemical resistance, and structural integrity [96,97]. Coatings and 3D printing resins based on AESO are being broadly investigated [32,49]. Amongst the available single-filler UV-curing resin composites, some clothes, furniture, and coatings applications are extensively researched [78,84,86]. Adding hybrid lignocellulose fillers could provide visual and structural wood-mimicking properties [13]. This could further benefit the investigations of wood-based composites. Meaning that not only regenerable wood-based composites, which are widely investigated [98,99], but also wood waste for lignocellulosic fillers would be utilized. Additionally, these kinds of wood-like material coatings would be much more easily renovated if damaged than the chemically modified wood surfaces used for UV-light resistance [100]. Wood-mimic properties are already widely investigated, and new applications arise daily. However, to the authors knowledge, hybrid lignocellulosic fillers for UV-curable resins have not been investigated, while this has been done in thermoplastics [101]. Amongst wood-mimic thermoset applications come mimic wood varnishes, design objects, furniture, automotive industry interior panels, 3D printed orthopedics and others [101,102]. Combining wood-mimicking properties with coating applications or 3D printing technologies that use UV-light gives endless opportunities for applications.

1.2. UV-light-assisted additive manufacturing

Additive manufacturing (AM), commonly known as 3D printing, has rapidly evolved as a groundbreaking technology, enabling the production of intricate and advanced geometric objects that are often challenging to achieve using traditional subtractive manufacturing methods [103,104]. This approach proves cost-effective, as it minimizes material wastage compared to conventional processes that involve milling and generate significant waste [105]. AM fabricates 3D structures by layering materials based on computer-aided design. AM allows for the freedom of complicated structures that would otherwise be impossible. AM also started the 4th industrial revolution, making AM an integral part of Industry 4.0 [106]. *IDTechEx* forecasts that the global market for 3D printing materials will be worth \$29.5 billion in 2032 [107]. AM market growth means broad use of 3D printing, meaning that demand for sustainable feedstocks and a reduction in the potential for waste and pollution will increase [108]. Various AM techniques, such as fused filament fabrication, selective laser sintering, laminated object manufacturing, and stereolithography (SLA), are available for polymers [109,110].

First 3D printing technique SLA was developed and then patented by Charles (Chuck) Hull et al. in 1984 [111]. SLA is a laser-assisted printing technique, and its basic schematic is shown in Figure 1.3. SLA contains a container filled with a liquid photopolymerizable resin, a platform, that lowers and a sweeper which evenly distributes a layer of the photopolymerizable resin [112]. It also contains a light source, which is used for selective curing and solidification of the liquid resin in a layer-by-layer process with an UV-light projector. The surface of the UV-light curable monomer bath is scrutinized into patterns [113] by UV or visible light that induces photopolymerization of a reactive resin. Considering that the main time consumer in SLA technology is the deposition of the new layer of photosensitive material, most important role for saving time in production is defined viscosity for liquid photopolymerizable resin. That is why typically reactive or nonreactive diluents are used to decrease the viscosity of the resin [114,115]. Photocured layer is formed within 2D cross sections, while the rest monomer, that was not exposed to photocuring, remains in the bath. Therefore, the printer needs to move only in the vertical direction [113].

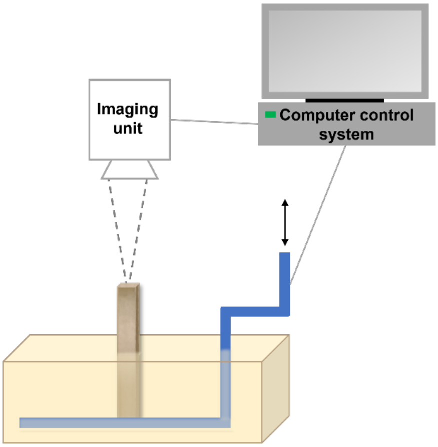

Figure 1.3. SLA schematic representation.

The spot size of focused laser beam provides SLA with high spatial resolution, which is one of these techniques main advantage. Light exposure is performed sequentially by scanning the laser beam within the plane on the surface, theoretically by controlling the laser intensity adjustments of exposure dose for every pixel separately, are allowed. By adding suitable absorbers to the photopolymer resin, vertical resolution can be controlled, based on its dependence on the light penetration depth. Vertical resolution is also affected by the curing depth, which depends on the exposure dose (light intensity and illumination time) [115]. Anisotropic bulk mechanical properties, part resolution, staircasing effect on curved or angle surfaces and built time are some of SLA challenges. Extent of staircasing effect is laid down by the thickness of the process slice and causes nonideal loss of part resolution. This can be countered by reduction of the slice thickness; however, it will increase built time significantly.

One of the reasons that stereolithography, as a 3D printing method, has develop is that it might be ten times as fast as CNC (computer numerical control) machining, therefore saving that much time of a prototyping cycle. [116] Moreover, SLA can produce a vast number of highly different 3D structures in a reproducible way with precise control over the final microstructure and geometry and even nonlinear scaffold geometries can be produced [114]. However, finding suitable bio-based material for SLA could be rather difficult since this technique is limited to photopolymerizable resins [117]. Even more so the physical properties of thermoset polymeric materials, which are used in SLA, are even more complicated than thermoplastics where morphology and anisotropy can be imparted as a function of the process. Complications comes from formation of molecular weight between crosslinks, and topology during the processing of the part and therefore intrinsic properties and part properties are inextricably entwined [118].

To broaden material options, there is a concerted effort to develop novel UV-curable resins suitable for SLA. While identifying bio-based feedstocks is important, there are equally important factors to consider, like the energy efficiency of the production process [119]. UV-light-assisted AM technologies have these advantages in terms of energy consumption, but they still lack the availability of a wide range of sustainable feedstocks [120,121].

1.2.1. Nanofibrillated cellulose as reinforcement in vegetable oil-based resins for additive manufacturing

Up until now discussed lignocellulose composite resins had considerably high filler loading that result in high viscosities which exclude them from UV-light-assisted AM technologies. For AM technologies that uses photocurable resins low viscosities are required. The bio-based photopolymer resin field is constrained by existing technologies and solutions, limiting the large-scale adoption of 3D printing [121]. Acrylates and epoxides are the most common polymer classes used in photocuring [122]. So far, vegetable oil-based resins have shown printing accuracy comparable to those of expensive, high-resolution commercial resins. However, even though AESO can be utilized for high-resolution 3D printing, the resulting mechanical properties can be considered relatively poor [123]. As established fiber reinforcement can improve mechanical performance because randomly distributed discontinuous fibers allow for crack bridging, providing "ductility" beyond the initial fracture event [96]. Meanwhile, sustainability can be maintained using natural fibers like cellulose, with its availability and excellent mechanical performance [96,101,124-127]. Fibers have to be sufficiently strong and well-bonded to the matrix material to carry significant stresses over a relatively wide range of strains, in spite of visible crack formation and growth [128]. Different cellulose fibers are already widely used as fillers in various polymer composites, including photocurable resins [124-127]. However, the nanocellulose is highly hydrophilic, which degrades reinforcing efficiency in many AM resins, bio-based and otherwise, given that they tend to be hydrophobic [126]. Nonetheless, progress has been made in the research and development of nanocellulose-reinforced photocurable AM resins [129-131]. Hence, competitive bio-based resins are needed. For this reason, while AESO is already used as a component of commercial vat photopolymerization resins, its content is generally limited to 50 wt% [132,133], with the other >50 wt% consisting of common petroleum-based acrylates. With that in mind, approaches to improve the performance of AESO are still needed.

Palaganas et al. incorporated 0.3 wt% of the C into a polyethylene glycol diacrylate (PEGDA) hydrogel resin and observed a 2-fold increase in tensile strength [129]. Meanwhile, Rosa et al. reported microcrystalline cellulose and C incorporation into a blend of AESO and PEGDA [130]. The authors demonstrated the advantages of higher aspect ratio C nanoparticles, obtaining an increase in tensile strength from 4.5 to 7 MPa and a decrease in strain at break from 25 % to 8 %. While these efforts show the potential of nanocellulose in photocurable resins for 3D printing, the use of neat Fs in this context has received very little attention. The authors are aware of only one report where Vidakis et al. studied F (0.5 to 2.0 wt%) to reinforce medical-grade *Formlabs* Biomed Clear resin and reported a 2-fold increase in tensile strength [131]. However, this commercial resin was not bio-based, highlighting the need for more work along these lines.

Due to the highly hydrophilic nature of cellulose and the high aspect ratios of F, their tendency to agglomerate is much more pronounced than that of C [134]. However, if agglomeration is overcome and adequate dispersion is achieved, the higher aspect ratios of Fs promise more significant reinforcement [134,135]. Nanocellulose has high stiffness and aspect ratios, and F has an even higher ratio than C, ensuring the ability to form a percolated filler network faster (~0.1 wt%) [136-138]. In addition, it can be argued that the production of Fs is more sustainable because it does not require treatment with strong acids or bases [139]. For these reasons, Fs represent a highly attractive option for the efficient reinforcement of bio-based photocurable resins and deserve further study around percolation threshold in particular due to decreases in nanoparticle agglomeration [131].

1.2.2. Nanocellulose surface functionalization for interphase improvements with AESO-based resins used for additive manufacturing

Mechanical performance can be enhanced by introducing additives such as nanofillers [131]. Borrowing this concept, a bio-based composition (vegetable oil-based resin) can be created with renewable nanocellulose fillers. Due to its excellent mechanical properties and natural prevalence, nanocellulose represents an attractive option [124]. The main challenges associated with development of the proposed compositions for 3D printing are filler dispersion, resin viscosity, and cure depth as a function of filler loading [140]. The hydrophilicity of nanocellulose fillers is a crucial factor that promotes their agglomeration [63]. Thanks to their high aspect ratio, F tends to agglomerate, resulting in large increases in resin viscosity as compared to C [134]; for this reason, C is often preferred in 3D printing resins due to easier processing. However, the larger aspect ratio of F also means that they should be able to provide higher levels of reinforcement if agglomeration is suppressed [134]. The functionalization of nanocellulose is considered a promising solution [60,141]. While nanocellulose has already been used as a filler for vat photopolymerization printing and UV-curable coatings, there are few publications describing the use of functionalized nanocellulose in this context. Auclair et al. described the functionalized C's influence on bio-based composite coatings' performance with concentrations of up to 2 wt% [60]. Coatings reinforced with acrylated C showed an increase of up to 60 % in elastic modulus, while hexadecyltrimethylammonium functionalization yielded an increase in tensile strength by 36 % and strain at break by 38 %. In the most recent study, Maturi et al. described C / commercial polylactic acid resin composites, where C was functionalized with modified fatty acids from safflower oil [142]. Vat photopolymerization resins with 0.25–5 wt% of modified and neat C’s were 3D printed. Unmodified C composites’ mechanical performance was lower than for the neat resin, while C-safflower oil / polylactic acid composites showed up-to 9 % increase in elastic modulus and 10 % increase in tensile strength for loadings below 1 wt%. The aforementioned research notwithstanding, there remains a need to create sustainable, high-performance replacements for commercial petroleum-based resins. At the same time, functionalization efforts to date have been focused mainly on C, with a relative lack of knowledge concerning the effects of F functionalization.

1.2.3. Accelerated weathering endurance of nanocellulose reinforced AESO-based resins used for additive manufacturing

The polymerization techniques employed in bio-based acrylate polymer synthesis are a subject of intense scientific investigation, as they allow for precise control over molecular weight, structure, and functionality, leading to tailored properties [20,143-146]. Moreover, developing novel catalysts and exploring innovative reaction conditions have further enhanced the efficiency and sustainability of acrylate polymerization processes [147,148]. The continuous advancements in this field contribute to the fundamental understanding of polymerization mechanisms and enable the design of novel bio-based acrylate polymers with superior properties. Understanding the aging behavior of bio-based acrylate polymers is paramount in various industries to ensure their adaptation, long-term performance, and durability. For this purpose, artificial weathering studies play a pivotal role in advancing scientific understanding and practical applications related to the degradation and performance of materials exposed to controlled and accelerated simulations of environmental conditions.

UV-light-assisted 3D printing resin research has gotten much attention as a means for developing bio-based resins to supplement and substitute commercial petroleum resins [149-152]. According to the authors knowledge, most of the studies have been devoted to improving the mechanical performance [63,93,153-156], while minimal efforts have been made toward understanding the developed resin weathering durability. Published research on the artificial weathering of UV-cured acrylate polymers has been devoted almost exclusively to coatings [157-160]. The investigations examined coating cracking, yellowing, gloss loss, and some chemical degradation processes occurring on the coating's surface. Bulk properties have not been investigated due to the small thickness of the layer. As a result, the researchers almost exclusively focused on the surface properties, while bulk properties affecting mechanical performance have not been investigated despite their extreme importance. Another aspect is that 3D printing introduces the concern of layer adhesion. In addition, the weathering of vegetable oil-based acrylic resins has not been investigated. However, vegetable oil-based acrylates, with their triglyceride form and ester bonds, are expected to act differently than widely investigated polyurethanes, epoxides, and systems with stabilizers [159,161,162].

At an accelerated rate, QUV accelerated weathering equipment allows the reproduction of sunlight, rain, and dew-caused damage in samples [163]. During this artificial weathering, photodegradation (including photooxidation) and hydrolysis must be considered. Vegetable oil triglycerides should be the most vulnerable to hydrolysis, releasing glycerol and fatty acids [164]. Photodegradation involves irreversible alterations in molecular structure, including photodissociation, which involves the fragmentation of molecules. Oxidation reactions are commonly observed during photodegradation processes, while the absence of oxygen leads to chain-breaking or crosslinking reactions [165]. Multiple factors can cause photodegradation, and two main factor groups are identified: internal and external impurities containing chromophoric groups [165]. UV-cured resins have been reported to have even lower photostability due to the residual amount of photoinitiator [160]. No acrylic resin can achieve a 100 % double bond conversion rate due to the viscosity increasing during crosslinking, which limits the radical transfer and free vinyl group mobility [166]. Theoretically, photodegradation-induced molecule fragmentation could set free uncured vinyl bonds and residual photoinitiators, allowing further photopolymerization to occur and counter the degradation process.

The presence of additives that enhance acrylate properties should be expected. For this reason, a sustainable and widely used nanofiller could be selected, i.e., nanocellulose. Several reports have identified nanocellulose as effective reinforcement for these bio-based acrylic resins [130,167,168]. Nanocellulose has also been reported to help photopolymerization via a light scattering control [92] in the vat photopolymerization approach. In addition, introduced nanocellulose could provide a bridging and strong network that limits crack propagation during the degradation [96]. However, nothing is without drawbacks, and with nanocellulose additional impurities are introduced in the matrix, contributing to photodegradation initiation. Introducing nanocellulose should increase water uptake, directly contributing to the hydrolysis [164,169]. To better understand and predict what will happen to bio-based nanocellulose reinforced resins during exploitation accelerated weathering testing is required.

1.2.4. Summary

2016–2020 literature analysis of biomass acrylates shows that the acrylic entities in vegetable oils primarily function as photocurable groups. Furthermore, fillers of cellulose-based acrylates can enormously enhance the developed bio-based polymers' hydrophobicity, mechanical, and thermal properties. However, despite the fact, that the end product of acrylation is obtained using biomass, the synthesis route primarily implies petroleum-based reagents, such as AC and acrylic acid. Almost all of those reagents and solvents used are far from being environmentally friendly and even present hazards for human health. Further investigations should focus on implementing and optimizing greener synthesis pathways for biomass acrylation, solving ecological and hazards concerns, e.g., the enzymatic catalysis paths. The next-generation biomass synthetic conversion pathways could reach high acrylation reaction conversions within mild process conditions and decrease commercial process costs and environmental impact.

Even though vegetable oil-based acrylate resins are yet to reach truly sustainable synthesis path, they are a considerable step forward in comparison to petroleum-based acrylate resins. Hence, investigations with vegetable oil-based acrylate resin formulations with various lignocellulosic fillers are of interest. The most interesting being the AESO-based resin formulations due to the commercial availability.

Research up until now has been divided in specific directions; focus has been towards bio-based UV-curable resin development. Main attention being given to mechanical performance improvements with mainly different reactive diluents and nanocrystalline cellulose. This has left a lot of holes to be explored in order to give broader understanding of bio-based resin future in replacing petroleum-based resins for UV-curing applications. There is a lack of investigations for all lignocellulose components for improving the performance of bio-based resins as well as filler-matrix interface improvements and durability investigations. These are the directions that were in the focus of this doctoral thesis research while other researchers focus on figuring out more sustainable synthesis paths for obtaining vegetable oil-based acrylates. This hopefully will allow accelerate the commercialization of the bio-based resins when more sustainable way of synthesizing them will be found.

2. MATERIALS AND METHODS

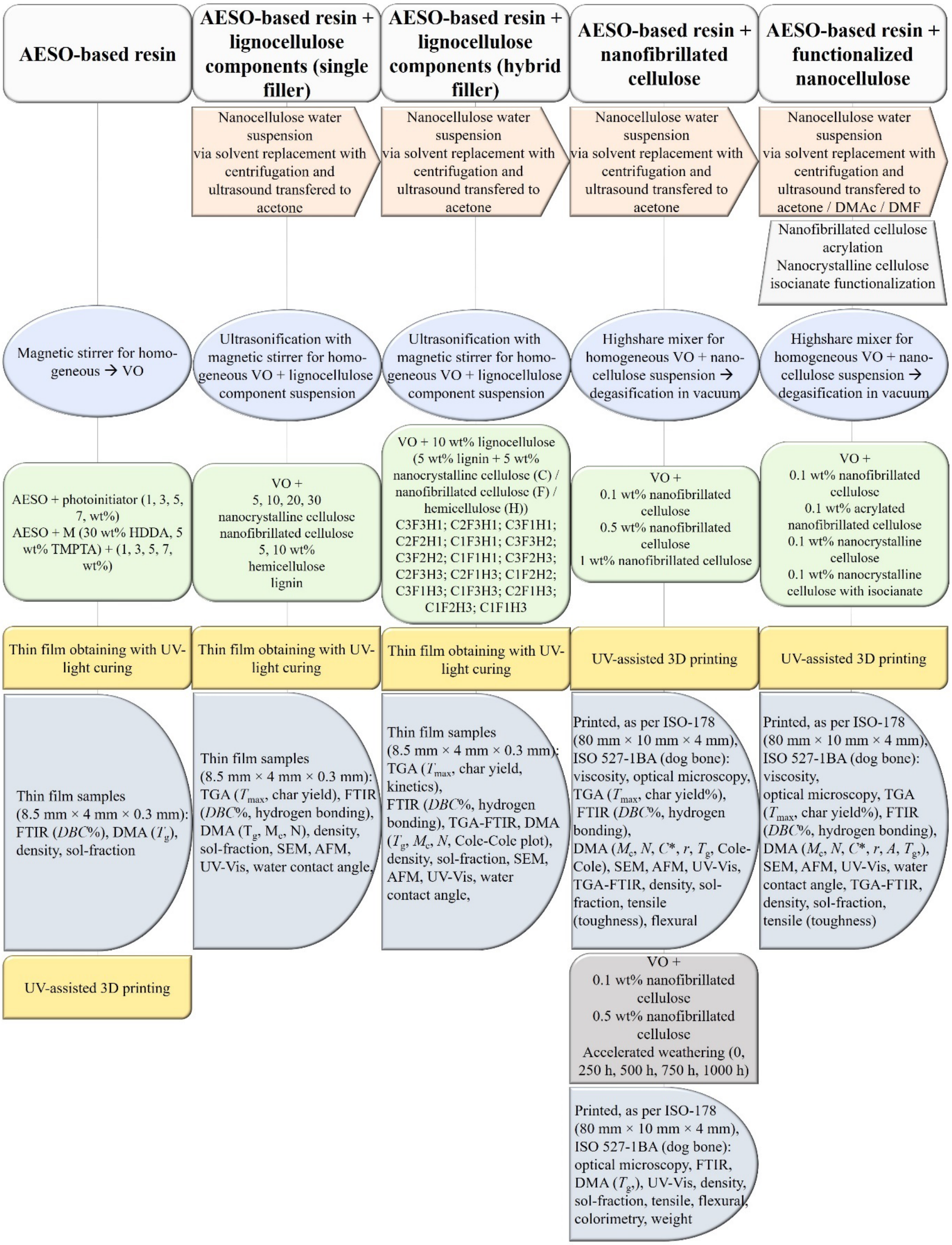

Scheme 2.1. The work schematics of the Doctoral Thesis.

2.1. Materials

2.1.1. Resin formulation

The neat resin was formulated from:

- acrylated epoxidized soybean oil (AESO) (specification: contains 4000 ppm monomethyl ether hydroquinone as inhibitor, viscosity 18,000–32,000 cps., and density 1.04 g/ml) purchased from Merck KGaA (Darmstadt, Germany);
- 1,6-hexanediol diacrylate-technical grade (HDDA) (specification: contains 100 ppm monomethyl ether hydroquinone as inhibitor, purity of > 77.5%, molecular weight 226.27 g/mol, density 1.01 g/ml) purchased from Merck KGaA (Darmstadt, Germany);
- trimethylolpropane triacrylate (TMPTA) (specification: contains 600 ppm monomethyl ether hydroquinone as inhibitor, purity of > 70.00 %, molecular weight 296.32 g/mol, density 1.10 g/ml) purchased from Merck KGaA (Darmstadt, Germany);
- 2,4,6-trimethylbenzoyldiphenylphosphine oxide (TPO) photoinitiator (PI) (specification: purity of 97.00 %, molecular weight 348.37 g/mol) obtained from Arkema Lambson (Wetherby, UK).

All chemicals were used as received without any additional purification.

2.1.2. Lignocellulose components for thin films

All lignocellulosic components used for thin film composite preparation were kindly provided by the Luxembourg Institute of Science and Technology (LIST) and used without any additional manipulations. Lignocellulosic components:

- Lignin (L), powder*;

- Hemicellulose (H), H_2O suspension (13.5 wt%)**;

- Nanocrystalline cellulose (C), H_2O suspension (3.0 wt%);

- Nanofibrillated cellulose (F), H_2O suspension (3.0 wt%).

** Sulphur free lignin extracted from a mixture of wheat straw and Sarkanda grass, contains 1.9 mmol/g of aliphatic hydroxyl groups and 3.3 mmol/g of phenolic hydroxyl groups and average molecular weight (Mn) of 1120 g/mol.*

*** Recovered from black liquor by precipitation in ethanol. Contains: xylose / Xylose-2-O-Glucuronic acid / Acetylated Xylose = 93% / 6% / <1%.*

2.1.3. Nanocellulose for 3D printing composites

Nanocellulose (C and F) used for 3D printing composite preparation was made in lab from filter paper. Briefly, the preparation of C from filter paper was as follows: Filter paper nanocrystalline cellulose (pC) – dry milling (ball mill) of cellulose and thermocatalytic degradation were applied to produce microcrystalline cellulose. Cellulose particles were then suspended in a 0.05 % hydrochloric acid solution for degradation of the amorphous phase, washed, and dried. Afterward, the dry powder was heated up to 110 °C to disrupt the cellulose structure slightly, and the powder was then milled for 15 h using JAR MILL 755RMV1 (US Stoneware, USA).

For C to prepare nanocellulose, a 1 wt% water suspension of microcellulose was processed using the high shear fluid processor LM 20 Microfluidizer (Microfluidics, USA). A Z-shaped chamber with a diameter of 200 µm was used to microfluidize the suspension for five cycles at 30 000 PSI.

Filter paper nanofibrillated cellulose (pF) production differed. Cellulose shredding was used to obtain microcrystalline cellulose using a Retsch SM300 with a sieve size of 2.00 mm for the first pass-through and a 0.25 mm sieve for the second pass-through. The mill rotation speed was 1500 RPM. To prepare nanocellulose, a 1 wt% water suspension of microcellulose was processed using the high shear fluid processor LM 20 Microfluidizer (Microfluidics, USA). A Z-shaped chamber with a diameter of 200 µm was used to microfluidize the suspension for five cycles at 30 000 PSI. The desired amount of prepared aqueous nanocellulose suspension was centrifuged for 15 min at 5000 RPM and the water was then replaced with acetone. The exchange process was repeated 4 times, after which the obtained nanocellulose / acetone suspension was stored in a refrigerator.

All used lignocellulose fillers and their abbreviations are combined in Table 2.1., their characterization was done with AFM and SEM (see Figure 2.1.) Lignocellulose components received from LIST have simple abbreviations like C, F, H, and L for nanocrystalline cellulose, nanofibrillated cellulose, hemicellulose, and lignin, respectively. Nanocelluloses prepared from filter paper have “p” before the same abbreviations as for LIST lignocellulose components and additional “I” or “A” for the appropriate functionalization.

Table 2.1.

Lignocellulose fillers used for further resin formulations

Source	Lignocellulose filler	Abbreviation	Length, nm	Width, nm
Luxembourg	Nanocrystalline cellulose	C	256 ± 44	47 ± 9
	Nanofibrillated cellulose	F	488 ± 142	70 ± 18
	Hemicellulose	H	-	-
	Lignin	L	-	74 ± 16
Filter paper	Nanocrystalline cellulose	pC	275 ± 70	50 ± 14
	Nanocrystalline cellulose + isocyanate	pCI	349 ± 91	150 ± 32
	Nanofibrillated cellulose	pF	-	58 ± 12
	Nanofibrillated cellulose + acrylation	pFA	-	-

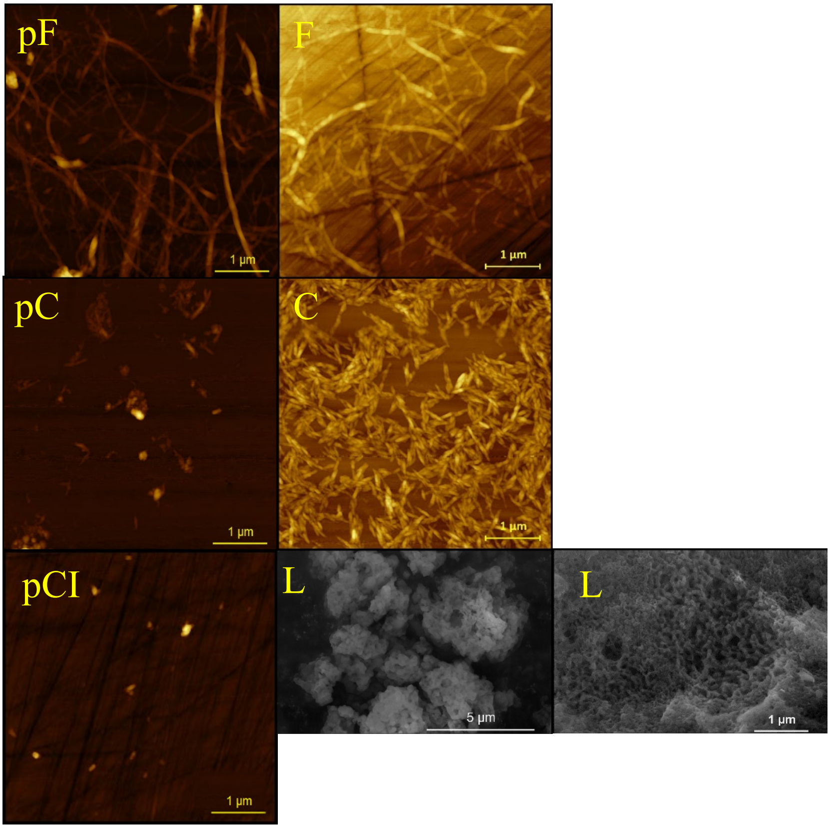

Figure 2.1. AFM images of used nanocelluloses and SEM image of used lignin (used abbreviations given in Table 2.1.).

2.1.4. Other chemicals

Acryloyl chloride (AC) (stabilized with phenothiazine), N,N-dimethylacetamide (DMAc) (anhydrous, purity 99.8 %), lithium chloride (LiCl) (analysis grade), N,N-dimethylformamide (DMF) (purity 99.8 %), hexamethylene diisocyanate (HMDI) (purity > 98 %), hydrochloric acid (ACS reagent, 37 %), ethanol (96.6 %) were purchased from Sigma Aldrich. The materials were used as received.

2.2. Sample preparation

2.2.1. Resin preparation

2.2.1.1. Neat resin formulation

The resin vegetable oil (VO) matrix was prepared as follows: photoinitiator dissolved in acetone and then HDDA and TMPTA as reactive diluents and mechanical performance enhancers [170-172] and AESO resin were added. The resin contains the following: 65, 30, and 5 wt% of AESO, HDDA, and TMPTA, respectively, with 3 wt% of TPO.

2.2.1.2. Lignocellulose component preparation

Acetone was used as a solvent replacement for H_2O suspensions (C, F, H). Acetone was added to water suspensions and sonicated (UIS250V, Hielscher, Germany) for 5 min and then centrifuged at 5000 RPM for 15 min for complete separation. This solvent replacement procedure has been repeated a total of 4 times. L powder was dispersed in acetone using a sonification procedure with no solvent replacement.

2.2.1.3. Functionalization of nanocellulose

Functionalization of nanocellulose. Nanocellulose functionalization was carried out via the processes shown in Scheme 2.2.

The nanocellulose acrylation was performed according to the scheme in Scheme 2.2 (a) by a widely adopted method described in the literature [59,173,174]. First, freeze-dried pF (1 g) was mixed with 20 ml of anhydrous dimethylacetamide (DMAc) at 120 °C for 1 h. After that, the mixture was cooled down to 100 °C, and LiCl (2.4 g) was added. The resulting mixture was stirred for another 30 min; then, the mixture was cooled down to room temperature and stored overnight. Next, acryloyl chloride (AC, 3 g) was added dropwise to the homogenous solution in an ice / water bath for 1 h. After the pFA were added, the solution was mixed for 3 h, heated to 50 °C, and mixed for another 3 h. Afterward, the solution was cooled to room temperature and the resulting product was precipitated in ethanol. The obtained acrylated pF (pFA) were vacuum filtered, thoroughly washed with ethanol for purification, and re-dispersed in acetone. The pFA were kept immersed in solvent during filtration to avoid drying.

The isocyanate functionalization method described by Gafurov et al. was used for pC (Scheme 2.2 (b)) [175]. pC was solvent exchanged to DMF in the same manner described above for pF. Next, pC (1 g) was suspended in a mixture of DMF (25 g) and HMDI (2.5 g). The suspension was heated to 110 °C and vigorously stirred for 4 h. Afterward, the mixture was cooled down to 20 °C, ethanol (25 g) was added, then the solution was mixed for 30 min and vacuum filtered. For further purification, the obtained powder was washed with ethanol, vacuum filtered, solvent exchanged with acetone, and stored as a suspension. As a result, isocyanate functionalized pC (pCI) was obtained. The isocyanate and acrylation chemical reactions are depicted in Scheme 2.2 (c).

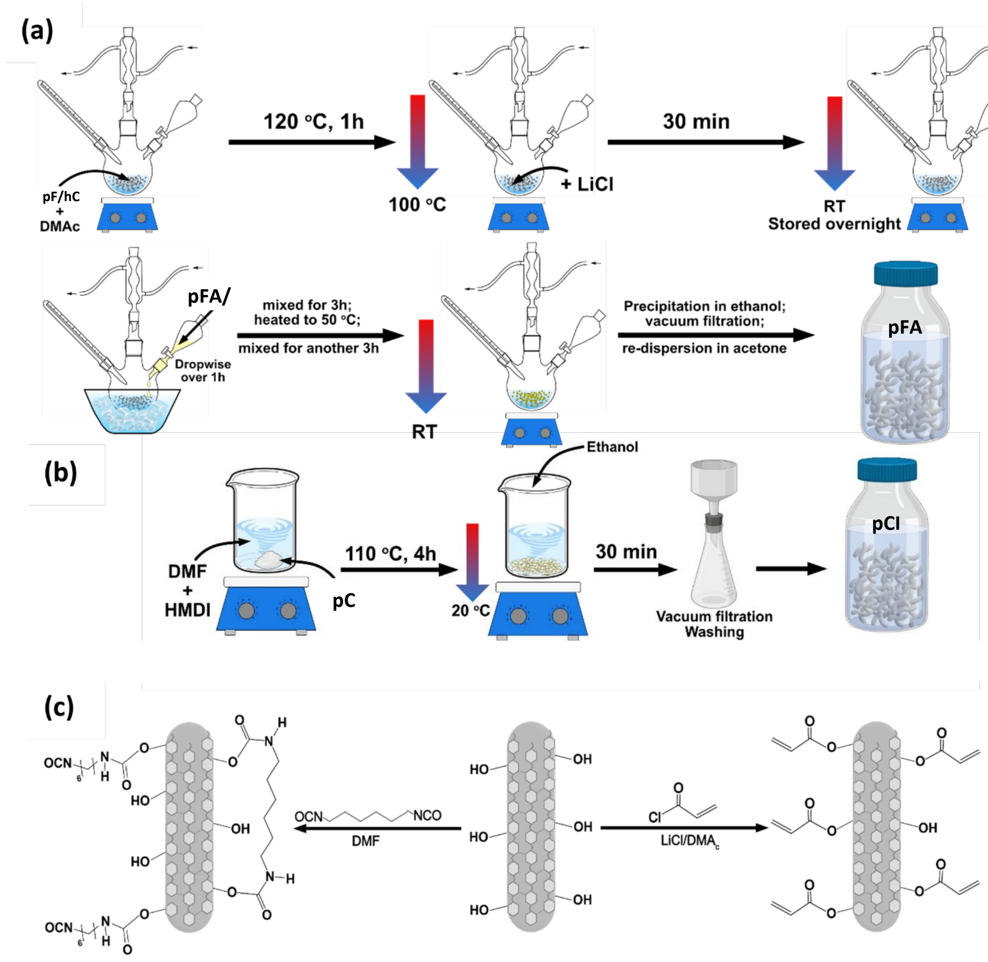

Scheme 2.2. Schematic representation of the functionalization route for pFA (a), pCI (b), and chemical reactions (c).

In the last step, the nanocellulose dispersion in acetone was added to the resin and mixed with a high-shear mixer for 5 min at 6000 RPM. Afterward, the resins were placed in a vacuum chamber at a vacuum of 1000 mbar for 2 h to remove all the excess air and remaining acetone. To prevent curing, prepared resins were stored in a dark environment.

2.2.2. Film curing

The prepared resins (neat and composite) were applied on a glass substrate using an applicator with a thickness of 200–250 µm. Resin curing was performed with a 5.5 W UV-LED lamp with a 405 nm wavelength at a 2.5 cm distance between the UV-light source and the applied resin on the substrate as showed in Scheme 2.3.

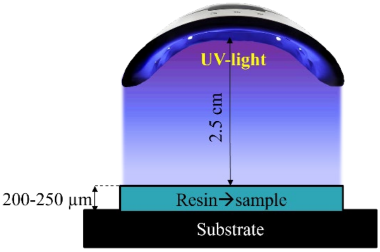

Scheme 2.3. Thin film curing scheme.

2.2.3. 3D printing

An Original PRUSA SL1 (PRUSA research, Czech Republic) 3D masked stereolithography 3D printer was used for all 3D printed sample preparation. To print samples from the CAD models shown in Scheme 2.4. (a), a PRUSA SL1 printer (Scheme 2.4. (c)) was used, with a 5.5' LCD mask and a 25 W LED with a UV wavelength of 405 nm. Briefly, the 3D printing process consists of four steps. Firstly, the desired CAD model (Scheme 2.4. (a)) is created using CAD software. In the next step, prepared CAD models must be sliced into layers of a certain height (a layer thickness of 50 μm was chosen as a good compromise between printing time and resolution) (Scheme 2.4. (b)). Then, sliced models are transferred to a 3D printer (Scheme 2.4. (c)), and the desired 3D objects are produced (Scheme 2.4. (d)). Finally, following printing, any remaining resin is washed off the printed part and then the part is post-cured. All resins were subject to an optimization process to achieve the optimal printing time without defects or failures. The single-layer UV-light irradiation time was increased in 1 s increments, starting at 3.5 s, until parts were printed with no defects. In this way, optimum layer printing times of 8 s for the neat resin formulation and 15 s for the composite resin formulations were found. The first 10 layers of each sample were printed at a constant time of 35 s to ensure adhesion to the printing platform. After printing, all parts were washed in isopropanol and post-cured in a Prusa Curing and Washing Machine (CW1). It is equipped with four 52.8 W UV-LED strips with a wavelength of 405 nm. The washing and drying time was 5 min, while the post-curing time was maintained at 3 min.

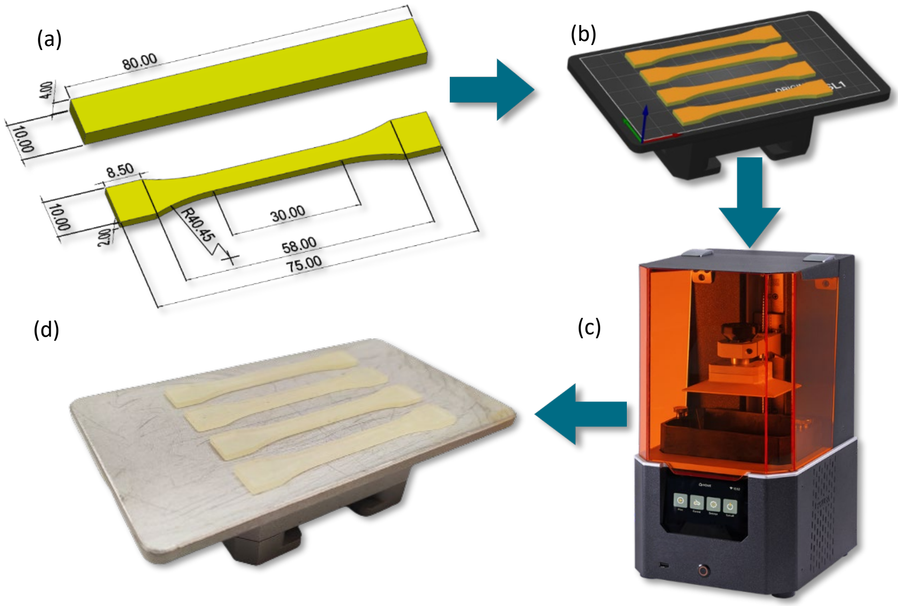

Scheme 2.4. Detailed 3D printing process scheme starting with CAD models of 3D printed ISO 178 (above) rectangular bars and ISO 527-1BA (below) dog bone specimens (a), continued with the slicing of CAD models (b), 3D printing (c) and an example of some of the resulting 3D printed specimens (d).

2.3. Testing methods

Fourier transform infrared spectroscopy performed in attenuated total reflectance mode

Photopolymerization kinetics was evaluated with a Nicolet 6700 (Thermo Scientific, Germany) Fourier transform infrared spectroscopy (FTIR) spectrometer as well as analysed the functionalization of the nanocellulose and the filler-matrix interactions. FTIR was measured using the attenuated total reflectance (ATR) method. Sixteen parallel measurements were taken with a 4 cm^{-1} resolution for each sample in the 400–4000 cm^{-1} range, and the average spectra were used.

Lignocellulose fillers were vacuum dried and measured by placing directly on the diamond prism. For printed samples, small pieces were shaved off the top and middle of the sample. Then, constant pressure was applied using a torque wrench supplied with the spectrometer.
Double bond conversion rate of the cured samples was calculated according to the equation (2.1) [20]:

$$DBC\% = \left(1 - (A_t \,/\, A_{ra}) \,/\, (A_0 \,/\, A_{rb})\right) \times 100\ \% \qquad (2.1)$$

…where A_0 and A_t are the absorption intensities of the C=C bond (at 810 cm^{-1}) before and after polymerization and A_{rb} and A_{ra} are the absorption intensities of the ester C=O bond (at 1722 cm^{-1}) before and after polymerization.

Theoretical spectra for filler-matrix interaction analysis were calculated using equation (2.2):

$$A_{Xf} = X \times A_f + (1 - X)A_{pol} \tag{2.2}$$

…where A_f and A_{pol} are the absorbances % for components in the composition spectra, lignocellulose component (f), and polymer matrix (pol), respectively, X = wt% of a lignocellulose component in specific composition.

Sol-fraction measurements

Curing efficiency was evaluated by sol-fraction measurements performed for 10 parallel samples using a manual Soxhlet extraction setup with acetone as the solvent. The extraction was conducted for 72 h. Samples were weighted before and after wrapping in filter paper and then again after Soxhlet extraction before and after unwrapping.

Thermogravimetric analysis

Thermal stability was evaluated with a Mettler TG50 instrument (Greifensee, Switzerland) on 10–15 mg samples, at a temperature range of 25–750 °C, with heating rates of 10, 15, 20, and 30 °C/min, under an inert atmosphere (N_2) with an 80 ml/min flow rate. Thermal degradation kinetics were calculated using the Friedman method [176,177]. The conversion (α) of the thermal decomposition process was calculated using the equation (2.3):

$$\alpha = \frac{m_i - m_t}{m_i - m_f} \tag{2.3}$$

…where α – conversion, m_i – sample weight mg before thermal degradation, m_t – sample weight mg at time t during thermal degradation and m_f – sample weight mg after thermal degradation, also known as char yield.

Values from characteristic data of the Ln(dα/dt) vs. 1/T, conversion rate vs. temperature and dα/dt vs. temperature at different heating rates are shown in Figure 3.23 (c) and Supplementary 11. Equation (2.4) was used to differentiate obtained values:

$$\frac{\mathrm{d}\alpha}{\mathrm{d}t} = \frac{\frac{\mathrm{d}m_t}{\mathrm{d}t}}{m_i - m_f} \tag{2.4}$$

were $\mathrm{d}m_t/\mathrm{d}t$ is the thermal degradation rate obtained from differential curves presented in Figure 3.23 (d), and Supplementary 11. The natural logarithm of equation (2.4) gives equation (2.5):

$$ln\frac{\mathrm{d}\alpha}{\mathrm{d}t} = -\frac{E}{RT} + ln[Af(\alpha)] \tag{2.5}$$

…where Af(α) is the pre-exponential factor s^{-1}, E is the activation energy J/mol, R is the universal gas constant, and T is the temperature K.

The thermal destruction products of the photopolymerized samples were analyzed with FTIR-ATR linked with TGA via the FTIR transfer line. The transfer line was set to 200 °C to avoid gas condensation. The exact amount (15 mg) of the sample was heated up to 750 °C with a heating rate of 10 °C/min. FTIR-ATR spectra of the gases were collected at a resolution of 4 cm^{-1} in the region of 400–4000 cm^{-1} with the same FTIR-ATR used for DBC%.

Hydrostatic density testing

The densities of prepared cured samples were determined by hydrostatic weighing. Samples were weighed using Sartorius MC-1 (Sartorius, Germany) analytical balance with a density measurement kit. For each sample 10 parallel sample measurements were performed. Each sample was weighed twice, first in air and then in ethanol. Equation (2.6) was then used to determine the density of each composite:

$$p = \frac{W_a \times (\rho_{ethanol} - 0.0012)}{0.99983 \times (W_a - W_{ethanol})} + 0.0012 \tag{2.6}$$

…where W_a and $W_{ethanol}$ are the sample weight in air and ethanol, respectively, and $\rho_{ethanol}$ is the experimentally determined density of ethanol.

Calculated theoretical density ρ_t, and the apparent polymer density ρ_{poly}^{a} were calculated by equations (2.7) and (2.8) [178].

$$\rho_t = \rho_{cel} \times \varphi_{cel} + \rho_{pol} \times (1 - \varphi_{cel}) \tag{2.7}$$

$$\rho_{poly}^{a} = (\rho - \rho_{cel} \times \varphi_{cel})/(1 - \varphi_{cel}) \tag{2.8}$$

…where ρ is the experimental density of the printed samples; ρ_{cel} the nanocellulose absolute density (1.6 g/cm^3) [179]; ρ_{poly} the 0% experimental density (1.1167 g/cm^3); and φ_{cel} the cellulose volume percent.

Dynamic mechanical analysis

Thermomechanical analysis was performed with a dynamic mechanical analyser Mettler DMA/SDTA861e (Mettler Toledo, USA) and storage modulus, loss modulus, and loss factor as a function of temperature were recorded.

Thin film samples with dimensions of 8.5 × 4 × 0.3 mm were tested attention mode with a 1 Hz frequency, a force of 10 N, and an elongation of 10 μm, in the temperature range from -70 to 100 °C and at a heating rate of 3 °C/min.

3D printed samples were tested at a dual cantilever deformation mode with a heating rate of 3 °C min^{-1}, applied force of 10 N, displacement of 20 μm, and at a frequency of 1 Hz from -70 to 100 °C. DMA samples were printed in a rectangular form, as per ISO-178 (80 × 10 × 4 mm). All samples, before the test, were stored in sealed plastic bags in a dark place, and tests were performed after 2 days from the moment the samples were printed.

Molecular weight between crosslinks (M_c) and crosslinking density (N) were calculated according to the theory of entropic rubber elasticity using equations (2.9) and (2.10) [180,181]:

$$M_c = \frac{3pRT}{E'} \tag{2.9}$$

$$N = \frac{p}{M_c} \tag{2.10}$$

…where, ρ is the density of composite, R is the gas constant, *E'* is the storage modulus at 95 °C, and T is the temperature at which E' is obtained.

The adhesion parameter A was calculated from tanδ at 20 °C via equation (2.11) [182]:

$$A = \frac{1}{1 - V_f} \frac{\tan\delta_{composite}}{\tan\delta_{matrix}} - 1 \tag{2.11}$$

To calculate the filler-matrix stress efficiency transfer parameter (C*), equation (2.12) was used [126]:

$$C* = \frac{(E'_g/E'_v)_{\text{composite}}}{(E'_g/E'_v)_{\text{matrix}}} \tag{2.12}$$

…where, E'_g and E'_v are glassy and rubbery storage modulus values measured at -45 °C and 95 °C, respectively.

For reinforcement parameter r calculations, equation (13) was used:

$$r = \frac{E'_c}{E'_m V_f} - \frac{1}{V_f} \tag{2.13}$$

…where E'_c and E'_m are storage modulus values at 95 °C for the composite and polymer matrix, respectively, and V_f is the nanofiller volume fraction in the composite.

Atomic-force microscope

Atomic force microscope (AFM) (Smena, NT-MDT, Russia) images of pristine and functionalised nanocrystalline cellulose and nanofibrillated cellulose were obtained using an HA_NC (ETALON) tip in semi-contact mode. To prepare AFM samples, highly diluted filler suspensions in analysis grade acetone with a concentration of 0.005 wt% were sonicated in an ultrasonic bath for 10 min and then dropwise applied on a clean Si substrate and dried overnight.

Scanning electron microscopy

Thin film surface morphology was evaluated by using the Tescan Vega II instrument (Brno, Czech Republic) with a magnification of 1000× and an accelerating voltage of 5 kV. Before the analyses, the samples were coated with gold.

Lignin particle characterization was done with Scanning electron microscopy (SEM) Hitachi Tabletop Microscope TM3000 (Japan). Dry lignin powder was applied on carbon tape to obtain an image with a voltage of 15 kV.

Nanofibrillated cellulose was characterised with an FEI Nova NanoSEM 650 Schottky field emission scanning electron microscope (FESEM) with an acceleration voltage of 10 kV. The measurements were performed using the STEM detector. The sample was obtained by placing a diluted F water suspension droplet on a copper grid and allowing the water to evaporate.

3D printed sample fracture surface was investigated with field emission scanning electron microscopy using a Nova NanoSEM 650 (FEI, USA) operated at an accelerating voltage of 3 kV. The sample fracture surfaces were obtained following freezing in liquid nitrogen.

Contact angle measurements

Contact angle measurements with sessile droplet distilled water (Crystal 10, Adrona, Latvia) were performed on Theta Lite optical tensiometer (Attention, China) to evaluate the functionalization effect on the hydrophobicity of the nanocellulose fillers and thin film composite surface.

For functionalised filler sample preparation, fillers were suspended in analysis grade acetone, sonicated in an ultrasonic bath for 10 min, applied dropwise and then dried on a glass substrate (3 layers).

For thin film sample preparation, Film surface was chemically etched with analytical grade acetone to remove sticky surface with unreacted resin and then left for drying.

All measurements were performed at room temperature on dried filler films; data were recorded after 10 s of contact.

Optical microscopy

3D printing accuracy was evaluated by optical microscopy using Leica 301-371.011 DMRBE, (Leica Microsystems, Germany) equipped with a 5× and 20× objective lenses and the Leica application suite software. Obtained the images of 3D printing object surfaces and fracture surfaces of the 3D printed composites. The sample fracture surfaces were obtained following freezing in liquid nitrogen.

UV-Vis spectroscopy analysis

Optical property changes were evaluated by a A SolidSpec3700 UV-VIS-NIR Shimadzu (Kyoto, Japan) spectrophotometer with a 60 mm diameter integration sphere and a wavelength precision of 0.5 nm in the wavelength range of 240–700 nm. Tests were performed on 200–250 μm thin films in transmittance mode and 3D printed samples with a width of 3 mm in transmittance and reflectance modes.

Viscosity measurements

The viscosity of the prepared resins was measured by the Viscolead One rotational viscometer (Fungilab, Spain) at various speeds in the range of 1 to 100 RPM at 25 °C temperature.

Spectrophotometry analysis

The prepared composition samples' changes in regards to used reinforcement and yellowing index (YI) were evaluated using the Ci7600 Sphere Benchtop Spectrophotometer (x-rite Pantone, Michigan, USA). Three parallel measurements were performed with a total transmittance aperture of 6 mm, a wavelength range of 360–750 nm, a photometric resolution of 0.01 %, and white paper as a background due to the transparency of the 3D printed samples.

Tensile testing

Mechanical performance of the 3D printed samples was evaluated by a tensile test using a 25ST universal testing machine (Tinius Olsen, United Kingdom) according to EN ISO 527-1BA. Testing speeds were 5 mm min^{-1} for stress and strain values and 1 mm min^{-1} for modulus values. The average values of elongation at break, elastic modulus, and tensile strength were obtained from parallel 5 samples. The area under the stress-strain curves was integrated to enable the calculation of composite toughness. Before testing, all samples were stored in sealed plastic bags in a dark place; tests were performed 2 days after the samples were printed.

Flexural testing

Three-point flexural tests were performed on 3D printed rectangular samples with dimensions of 80 × 10 × 4 mm^3, according to the EN ISO-178 standard. A Tinius Olsen 25ST universal testing machine (USA) was used, with testing speeds of 1 mm/min for flexural modulus and 5 mm/min for flexural strength, with 25 kN S-type load cell. Prepared specimens were stored in a sealed bag at room temperature in a dark place. Average flexural strain at break, flexural modulus and flexural strength values were obtained from the testing of 5 specimens. All flexural tests are performed two days after the printing of the specimens.

QUV accelerated weathering

A weathering test with a QUV accelerated weathering tester (Q-Panel Co., USA) equipped with fluorescent UVA-340 lamps (Q-Lab Co., USA) was performed to simulate outdoor conditions in accordance with the ISO 4892–3:2016 standard “Plastics-Methods of Exposure to Laboratory Light Source, Part 3: Fluorescent UV Lamp”. The test combines 3 cycles (12 h): ultraviolet sunlight (8 h) at black panel temperature 50 ± 3 °C and irradiance 0.75 W/m^2, spray (15 min), and condensation (3 h and 45 min at 50 °C). Each cycle of exposure occurs separately to simulate natural weathering conditions. The fluorescent UVA-340 lamps have a 295–365 nm (maximum at 340 nm) wavelength spectrum. UV light is responsible for most of the sunlight damage to polymer materials exposed outdoors [160,163]. In the condensation cycle, the water reservoir (bottom of the test chamber) is heated to produce vapor, reaching 100 % relative humidity, and forming the dew on the surface, responsible for most of the wetness outdoors. The water vapor continuously condensates on the test panels (which are kept at a lower temperature by room air flowing over the back surfaces of the specimens). Post-processed 3D printed samples were inserted into the QUV weathering chamber, removed, and tested after 0, 250, 500, 750, and 1000 h weathering exposures.

3. RESULTS AND DISCUSSION

3.1. Vegetable oil-based photocurable resins for films and additive manufacturing

3.1.1. Neat resin formulation: photoinitiator concentration selection

Publication:

- **A. Barkane**, O. Platnieks, M. Jurinovs, S. Kasetaite, J. Ostrauskaite, S. Gaidukovs, Y. Habibi, UV-light curing of 3D printing inks from vegetable oils for stereolithography. Polymers 13 (2021) 1195, doi:10.3390/polym13081195

Typical resins for UV-assisted additive manufacturing (AM) are prepared from petroleum-based materials and therefore do not contribute to the growing AM industry trend of converting to sustainable bio-based materials. To satisfy society and industry's demand for sustainability, renewable feedstocks must be explored; unfortunately, there are not many options that are applicable to photopolymerization. Nevertheless, some vegetable oils can be modified to be suitable for UV-assisted AM technologies. In this work, extended study, through FTIR measurements, of the UV-curing of acrylate epoxidized soybean oil (AESO)-based formulations have been performed to better understand the photopolymerization process. The study demonstrates that the addition of appropriate functional comonomers like trimethylolpropane triacrylate (TMPTA) and the adjusting of the concentration of photoinitiator from 1 to 7 wt% decrease the needed UV-irradiation time by up to 25 %. Under optimized conditions, the optimal curing time was about 4 s, leading to a double bond conversion rate (DBC%) up to 80 % and higher crosslinking density determined by the Flory–Rehner empirical approach. Thermal and mechanical properties were also investigated via TGA and DMA measurements that showed significant improvements of mechanical performances for all formulations. The properties were improved further upon the addition of the reactive diluents. After the thorough investigations, the prepared vegetable oil-based resin formulations containing reactive diluents were deemed suitable for UV-assisted AM, giving their appropriate viscosity. The validation was done by printing different objects with complex structures using a laser based stereolithography apparatus (SLA) printer.

**Sample abbreviation: AESO-1, AESO-3, AESO-5, AESO-7 – AESO resins with 1, 3, 5, and 7 wt% photoinitiator, respectively; M-AESO-1, M-AESO-3, M-AESO-5, M-AESO-7 – AESO resins with comonomers (30 wt% HDDA and 5 wt% TMPTA) and 1, 3, 5, and 7 wt% photoinitiator, respectively.*

3.1.1.1. Investigation of UV-Crosslinking Process

Soybean oil triglycerides contain mostly unsaturated fatty acids: linolenic acid (7–10 %), linoleic acid (51 %), and oleic acid (23 %). It also contains some saturated fatty acids such as stearic acid (4 %) and palmitic acid (10 %). It is made epoxidized and then acrylated to lower its viscosity and increase its reactivity toward UV-irradiation to be suitable for the SLA technique as it was used in the present study. Furthermore, HDDA and TMPTA were used as reactive diluents in order to further adjust the viscosity and increase the crosslinking density. The amounts of these reactive diluents were established based on literature research in order to maintain high bio-based AESO content. Indeed, previous studies have investigated the concentration of these reactive diluents and their effects on the performances of the final materials. TMPTA has been used in multiple cases where its concentration ranged from 2 wt% to 50 wt% [183-185]. As a trifunctional monomer, this monomer contributes to the increase of the crosslinking rate and density, but at too high concentration it can lead to unwanted stiffness [186-188]. HDDA as bifunctional linear monomer contributes to the increase of the mechanical properties [189]. The photoinitiator used in this study is diphenyl(2,4,6-trimethylbenzoyl)phosphine oxide (TPO) and belongs to the Norrish Type I PI [190], where absorption of visible and ultra-violet (UV) lights causes homolytic bondage cleavage and generates two highly reactive radical species, which then initiate the polymerization and irreversibly incorporate into the polymer matrix. In the present study, the ratio between AESO / TMPTA / HDDA was kept constant at 65 / 30 / 5, and the photoinitiator was loaded at different concentrations ranging from 1 wt% to 7 wt%. The formulations were then exposed to UV irradiation at various exposure times from 2 to 10 s. As there are many possible combinations in this system, the crosslinking can occur between the same molecules (a-a; b-b; c-c) and / or between different molecules (a-b; a-c; b-c; etc.) in more than one site of each molecule. Given the number of reactive sites, the later combination is supposed to be the most dominant. Moreover, AESO has five reactive sites, while TMPTA and HDDA have three and two reactive sites, respectively. Therefore, HDDA will more likely prolong the crosslinking of chains, which is expected to increase the elasticity of the material. On other hand, TMPTA with more reactive moieties will more likely increase the crosslinking speed and density [191].

The occurrence of the crosslinking was followed by Fourier-transform infrared spectroscopy (FTIR) analyses for all formulations (neat AESO and M-AESO). In the Figure 3.1, the spectra of AESO-3 and M-AESO-3 are given as examples.

All characteristic peaks of groups present in AESO corresponding to (-OH) stretching vibrations of (C=O) and (C-O) ester groups are present before and after the UV-light exposure in all spectra at 3462, 1733 and 1219, and 1271 cm^{-1}, respectively [192]. The bands corresponding to the asymmetric stretching of (O=C-O) at 1361 cm^{-1} [193,194] and stretching vibrations of ester (C-O-C) at 1158 cm^{-1} were also observed [192]. For AESO-3 resin, upon UV-irradiation, a decrease of the intensity is observed in (CH_2=CH-R) scissioning and (C=C) at 1406 and 1632 cm^{-1}, respectively. These decreases during the UV-irradiation happen because (C=C) bonds in acrylate groups are destroyed by the initiation of radicals and the occurrence of the crosslinking [172,193,195]. Additional conformation of acrylate polymer vinyl functionality is characterized by the (CH_2=CH (CO)-O-) vinyl group at 985 cm^{-1}, which also decreases upon UV-irradiation [193]. The decrease of the later peak affects also the peak at 1733 cm^{-1} related to the (C-O) of the ester groups, which is due to the electronic conjugation. Other characteristic peaks corresponding to asymmetric stretching vibrations and deformations of (C-H), (-CH_2-), and (-CH_3) groups were observed before and after the crosslinking at 1055, 2890, and 1449

cm^{-1}, respectively. It is worth noting that no characteristic peak of the TPO was observed even at the highest loading, probably due to the low concentrations compared to the amount of the resins, but also because of the overlapping with the peak of the resins.

Before the characterization of the formulations containing the reactive diluents, FTIR analyses of each of the used components before and after the UV-induced crosslinking were also performed to get preliminary insights on their interactions and crosslinking. The recorded spectra are provided in Supplementary 1. The spectra clearly show that both monomers are very similar from a chemical structure standpoint, but their crosslinking and physical properties aspects are different. Both reactive diluents as acrylates have similar characteristic peaks, also present in AESO, except for (-OH) band at 3462 cm^{-1}, which is not present, since none of the monomers have this group in their formula. After the irradiation, the spectra of the monomers consist of much more irregularities in peak intensities than AESO. The intensity of (C=C) band at 810 cm^{-1} does not decrease as much; on the other hand, (O=C-O) at 1361 cm^{-1} decreases until complete disappearance for both reactive diluents, in contrast to AESO resins.

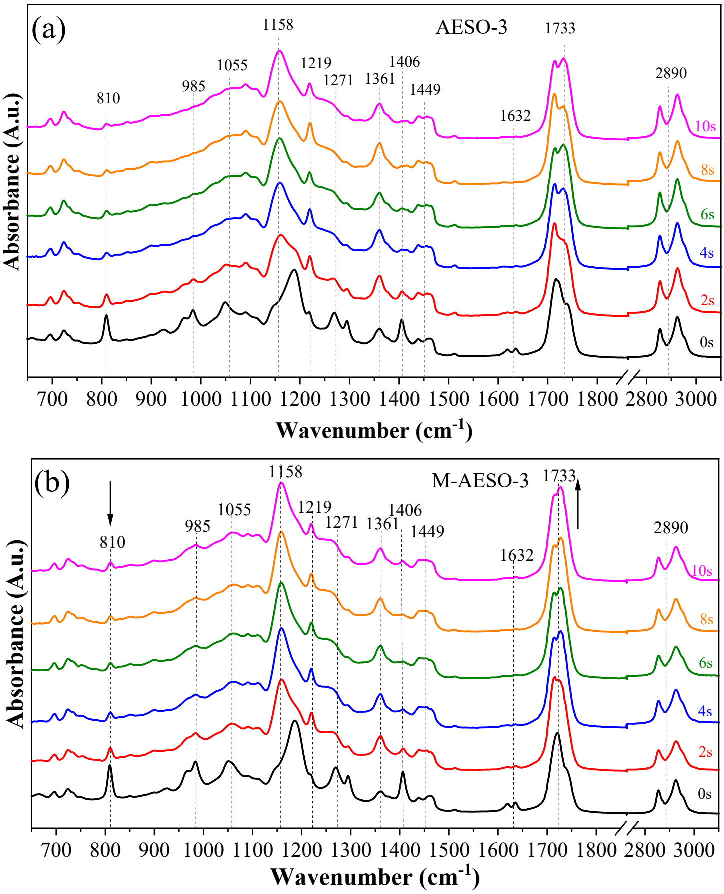

Figure 3.1. FTIR spectra of AESO-3 (a) and M-AESO-3 (b) resins before and after UV-curing at different exposure times.

M-AESO formulations were then analysed before and after the UV-curing at different exposure times. Similar characteristic peaks belonging to AESO, HDDA, and TMPTA were observed at different intensities depending on the curing times. One can observe a decrease of the peak corresponding to (CH_2=CH (CO)-O-) vinyl group at 985 cm^{-1} during the irradiation, which was not complete as in the case of neat AESO resin, which is related to the higher amount of (C=C) bonds from acrylate groups brought by the addition of reactive diluents in M-AESO formulations than in neat AESO for all formulations. Similar observation applies to the peak at 810 cm^{-1}.

FTIR measurements were used to evaluate the kinetic of the photopolymerization by following the intensities of the peaks at 810 and 1733 cm^{-1} corresponding to the (C=C) and (C=O) groups, respectively, for neat AESO resin and those containing reactive diluent M-AESO. The ratio of the two intensities I_{1733} / I_{810} cm^{-1} was used as the normalization means in order to eliminate possible errors that could arise from the differences in the thickness of the films. Figure 3.2 (a) shows the evolution of the calculated ratio I_{1733} / I_{810} cm^{-1} against the curing times for the formulation, having 3 wt% of TPO as an example. One can conclude that the onset optimal curing time is 3.3 s for AESO-3, while it is only about 2.4 s for M-AESO-3 resin, showing that the addition of the reactive diluents has increased the reactivity and hence decreasing the curing times. This applies to all loading of TPO. Indeed, the addition of the reactive diluents has decreased the curing time for all formulations regardless of the loading of the photoinitiator.

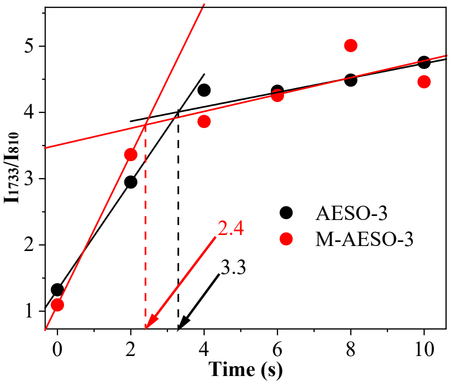

Figure 3.2. The variation of I_{1733} / I_{810} cm^{-1} with curing times of AESO and M-AESO resins at 3 wt% loading of the photoinitiator.

The mechanical properties of the resulting polymer materials are significantly dependent on the crosslinking density and hence on the conversion of functional groups [196]. Therefore, double bond conversion rate (DBC%) was calculated from the ratio of the intensity of the peak at 810 cm^{-1} related (C=C) groups against the intensity of the peak at 1361 cm^{-1} corresponding to (COO^-) groups, that is, unaffected by the photocrosslinking reaction, before and after the UV exposure at given time, using the Equation (2.1) [196,197]. Figure 3.3 depicts the variation of DBC% with curing time at different TPO loading, and the obtained curves confirm that the addition of polyfunctional comonomers increases the conversion degree by means of about 10

%, as the values of DBC% obtained for M-AESO are higher than those obtained for neat AESO. DBC% for neat AESO reaches around 77 % in 4 s in the case of 5 % TPO loading, while it was slightly below for the other loading of TPO. After 4 s irradiation time, the DBC% remains constant or drops. This high conversion rate achieved under UV-curing attests for the fast reactivity of the acrylated moieties, because when compared to thermally cured dimethacrylate, the same value of conversion rate can be reached only after 3000 s of curing [198]. In the case of M-AESO, the DCB% increases sharply after only 2 s of UV-irradiation and then continues to slowly increase after 4 s of UV irradiation, reaching 83 % of conversion after 8 s. When compared to other vegetable oil-based resins reported in the literature about UV-curing, prepared resin reached their highest conversion much faster. Indeed, in the case of acrylated epoxidized palm oil with no additional reactive diluents, DBC% was barely over 60 % after 8 s [199]. It is worth noting that the increase of the amount of the photoinitiator does not automatically lead to higher absolute conversion degree. This could be explained by the screening effect, where the crosslinking starts rapidly at the upper layer, causing a complete absorption of the UV-light and consequently obstructing its in-depth penetration into the materials [200,201].

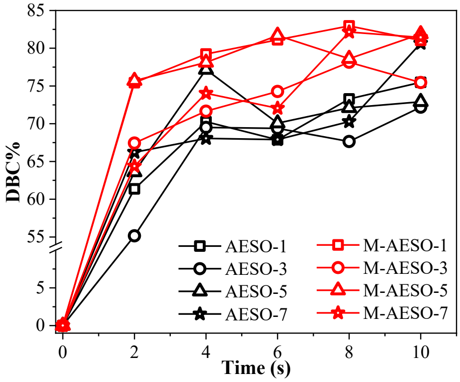

Figure 3.3. Double bond conversion (DBC%) rate as function of the UV-curing time for neat AESO and M-AESO for different loading of the photoinitiator.

Another parameter of interest in the case of crosslinked network is the crosslinking density (N) and the related molecular weight between crosslinks (M_c). These two parameters were calculated according to the empirical approach adopted by Flory–Rehner [202-204] (equation (2.9) and (2.10), respectively). The Table 3.1 gathers the calculated values of N and corresponding M_c for all fully UV-cured resins (cured at 4 s). According to this rubber elasticity theory [205], the highest rigidity of the thermoset polymer is obtained for the polymer chain network with dense crosslinking structures and short distance between chain crosslinks. Hence, the results show that in the case of the studied formulations, the UV-cured resins containing the functional monomers display almost 5-fold enhanced crosslinking density characteristics in comparison to the crosslinked neat AESO resin. For example, M-AESO-3 resin formulation exhibits $M_c = 45$ g/mol and $N = 73.9 \times 10^3$ mol/cc in comparison to cured AESO-3 resin, which has only M_c of 193 g/mol and N of 16.4×10^3 mol/cc, respectively.

Table 3.1.

Crosslinking density (N, mol/cc) and molecular weight (M_c, g/mol) obtained for different formulations cured at 4 s

Sample	M_c, g/mol	N, × 10^3, mol/cc
AESO-1	130	24.6
AESO-3	193	16.4
AESO-5	223	14.4
AESO-7	149	21.5
M-AESO-1	45	73.9
M-AESO-3	45	73.9
M-AESO-5	73	46.2
M-AESO-7	269	12.3

3.1.1.2. Thermomechanical Investigation of UV-Cured Materials

In general, thermal and mechanical properties of a polymer network can be directly linked to the crosslink density [206]. After being cured, the resulting polymer materials were investigated in terms of their thermal and mechanical properties. The thermal stability is directly linked to the crosslinking chain network density, where higher degradation temperatures are characteristic of more dense and less defective polymer chain network [195]. Thermogravimetric analysis (TGA) was used to investigate the thermal stability of the cured materials. Figure 3.4 (a) and (b) show the weight losses of the samples during the heating and the first derivative curve (DTG) T_{max} (temperature of maximums degradation rate), respectively. Both resins AESO and M-AESO exhibit closely similar degradation behaviours. Yet, the results show that the addition of the functional monomers in the case of M-AESO has increased the thermal stability by about 17–30 °C for each formulation having the same concentration of PI. Indeed, the main degradation temperature ranges from 387 to 400 °C for neat AESO, while it was around 420 °C for M-AESO. Moreover, the presence of the monomer induced a second degradation of the samples at around 460 °C, which could be attributed to the degradation of added reactive diluents. This degradation behaviour is likely to be attributed to TMPTA monomer, as has been suggested by other studies. Indeed, TMPTA monomer helps creating highly crosslinked density polymer network, which exhibits better heat-diffusion inhibition characteristics [172]. Overall, there is no significant weight loss until 250 °C (first 1 % weight loss detected at 249 °C for sample M-AESO-1), and even at this temperature, the loss is very limited, as it represents only 1–2 %, which could be related to the presence of incurable volatile components that degrade faster than cured network [199,207]. The main degradation takes place in the range of 300–500 °C, which is 50 °C higher compared to palm oil-based resin as reported in the Ashraf M. Salih et al. study [199]. Indeed, the main degradation of palm oil-based resin is reported between 250–550 °C. Additionally, 5 % of weight is lost at 277 or 308.5 °C, depending on the used photoinitiator, while in our case, AESO, even without additional monomers, loses its first 5 % at 339 °C, which is 30 °C higher compared to palm oil. Yet, in the present study, the char yields are 3–5 %, while for palm oils, the char was around 2.3 % [199]. The degradation results from random scission of the linear chains of the crosslinked system; therefore, branched systems with higher amounts of triacrylate monomer exhibit higher T_{max} values. A full investigation of the thermal stability of the produced resins was reported in a previous paper [176], where the kinetics of the thermal destruction were performed using Friedman method and revealed that the addition of the reactive comonomers increases the activation energy for thermal destruction by 10 %.

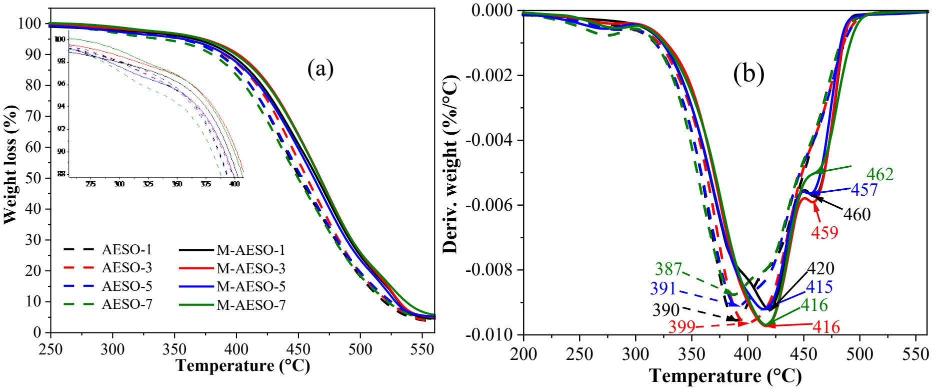

Figure 3.4. TGA thermograms (a) and the corresponding first derivatives (b) of AESO and M-AESO resins formulations cured at 4 s.

The mechanical properties of the studied resins were investigated by dynamic mechanical analysis (DMA) measurements. Figure 3.5 depicts the obtained DMA curves for neat AESO and M-AESO resin formulations loaded with different PI concentrations and UV-cured at 4 s. Table 3.2 gathers the extracted values of the storage modulus at different temperatures and the glass transition temperatures. For both formulations, the DMA profiles are typical of thermoset resins where the storage modulus decreases upon heating the materials due to phase transition from a glassy state to a rubbery state. For thermoset resins, the storage and loss modulus values are a direct indication of the crosslinking density, which can be compared in either a rubbery (viscoelastic) state or at the glass transition region; yet, the glassy state is mostly indifferent to crosslinking density. In addition, it is well known that higher crosslinking density yields higher glass transition temperature (Table 3.2), which is obtained from the damping factor (tanδ) peak (Figure 3.5 (c) and (d)).

In the case of neat AESO resins, the storage modulus and loss moduli values are similar at the glassy state regardless of the concentration of the PI and thus the crosslinking density. The glass transition in this case occurs in a very narrow temperature window ranging between 24 and 29 °C, and the profiles show only one well defined peak for each formulation. At the rubbery state, there is a slight decrease of the values of the storage modulus upon the increase of the loading of the PI confirming the differences yet slight in the crosslinking density of the material. The sample with 5 wt% initiator stands out with the best values of the storage modulus in the viscoelastic state and the highest T_g, and a relatively small difference was obtained for the sample with 1 wt% of added PI. The sample with 1 wt% PI shows the highest loss modulus peak values and thus indicates a less stiff response, which is induced from AESO ability to self-plasticize; this synergy results in almost the same performance as other concentrations [208,209].

The same DMA profiles are observed in the case of formulations containing reactive diluents. The values recorded at the glassy state are comparable to those of the neat AESO, demonstrating as expected that at this state the crosslinking density has no effect over the values of the storage modulus. The M-AESO-3 exhibits the highest loss modulus value, while the formulation M-AESO-7 has the lowest loss modulus. The storage modulus values are strongly enhanced with the addition of the functional monomers by means of 4-fold and 5-fold increase at room temperature and higher temperatures (80 °C), respectively.

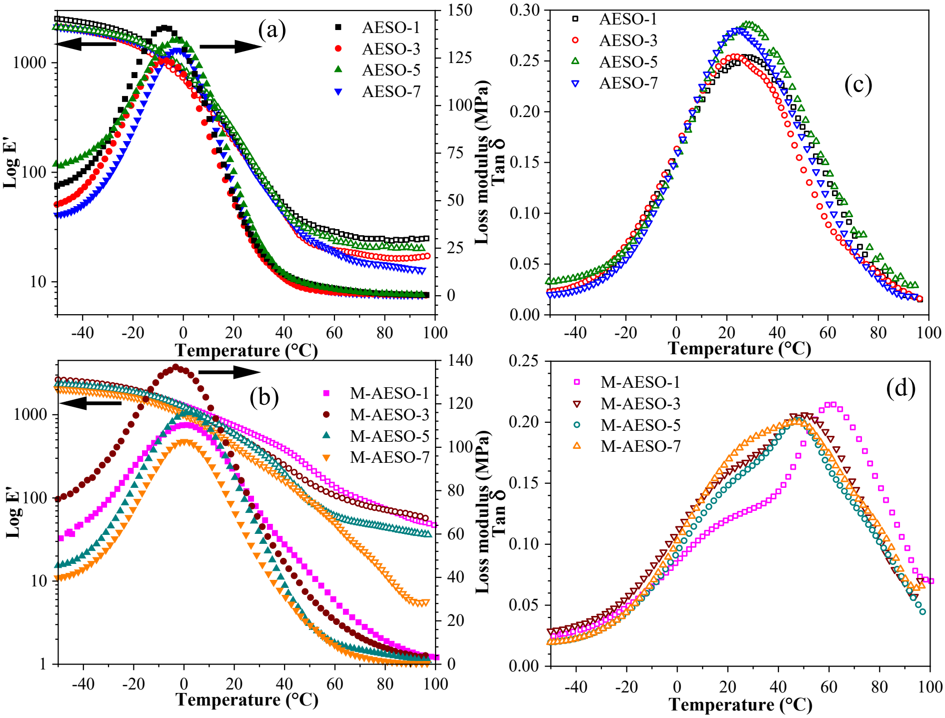

Figure 3.5. DMA curves for formulations cured at 4 s: (a) storage and loss modulus of AESO resins, (b) tanδ of AESO resins, (c) storage and loss modulus of M-AESO resins and (d) tan*δ* of M-AESO resins.

The glass transition occurs at higher temperatures compared to formulations without additives, attesting to a more rigid structure, hence increased crosslinking density. T_g values were 19–34 °C higher compared to those achieved for neat AESO samples. The damping factor (tanδ) peaks of all formulations were broader than those obtained for neat AESO resins, exhibiting a shoulder for which the intensity increases with the decrease of the PI loading. The presence of this shoulder is indicative of the presence of phase separation. The occurrence of this phase separation is probably the reason of the higher loss modulus values recorded after the glass transition compared to other samples. The segmental mobility of loosely connected AESO sections could reduce overall stiffness of M-AESO-1 and M-AESO-3 samples, while this also seems to create better energy storing capabilities.

Table 3.2.

Storage modulus values of AESO and M-AESO resin formulations cured at 4 s at different temperatures

Sample	Storage Modulus, MPa							T_g, °C
	-40 °C	-20 °C	0 °C	20 °C	40 °C	60 °C	80 °C	
AESO-1	2337	1754	821	213	50	29	24	28
AESO-3	1970	1489	721	196	44	19	16	24
AESO-5	1996	1591	805	204	42	18	14	29
AESO-7	2016	1627	879	233	45	23	21	24
M-AESO-1	2273	1890	1262	726	385	136	72	62
M-AESO-3	2500	2014	1210	572	245	108	72	50
M-AESO-5	2280	1849	1241	572	194	60	45	48
M-AESO-7	1942	1622	1004	416	156	51	12	47

3.1.1.3. Printability of the Materials

After the optimization of the formulations and their UV-curing, the formulated resins were validated as UV-sensitive. Yet, given the high viscosity of the formulations based on neat AESO (viscosity of the commercial AESO 18 000–32 000 CPS.), the printing of these resins was not possible with the used SLA printer, as it exceeded the operational range. Only formulations composed of AESO in combination with the reactive diluents were printable. Objects with more or less complex structures were then printed from all M-AESO formulations using SLA printers (Figure 3.6). These printed objects demonstrate complete layer fusion and accurate printing quality, as they were defect-free and exhibited high-resolution features and good mechanical properties, ensuring good stability without undergoing any shrinkage over the time.

Figure 3.6. Printed M-AESO-3 resin, transparent bar (a), owl (b), a Lego cube (c), and basket like bowl (d).

3.1.1.4. Summary

Acrylated epoxidized soybean oil was used alone or in combination with reactive diluents as the main component to formulate UV-curable resins. The effect of the photoinitiator and UV-light exposure time were studied to understand the curability of these vegetable oil-based formulations. Optimal curing time to achieve full curing was about 4 s, as determined by photorheological measurements. The addition of the reactive diluents not only decreased the viscosity of the resins, but also induced a decrease in the photopolymerization time by 25 % and an increase in the double bond conversion rate (DBC%) by 10 %. Thermal degradation analysis showed good thermal stability of both types of formulations, which was improved by the addition of reactive diluents reaching about 420 °C as a consequence of the increased crosslinking density. The mechanical properties of the cured resins improved with the crosslinking density for the same type of formulations, which was related the content of the photoinitiator. Similarly, these properties were also improved upon the addition of the reactive diluents. Indeed, the storage modulus improved by almost 4-fold at room temperature and 5-fold at 80 °C, reaching 726 and 72 MPa, respectively, for the formulations containing the reactive diluents (AESO-M compositions). Accordingly, the formulated sustainable bio-based resins containing the reactive diluents were deemed suitable for UV-assisted 3D printing, and thus they were successfully validated by printing different objects with complex structures with SLA printers. The formulated bio-based resins provided excellent printability showing a high promise for scalability toward commercial applications, yet further development and optimization are still needed.

For further investigations of UV-curable resins for films and 3D printing M-AESO-3 was chosen. Decision was based on the optimal properties of viscosity, crosslinking density, and thermomechanical properties that were not further improved with increasing PI concentration.

3.2 Lignocellulose filler loaded resins for films

3.2.1. Single lignocellulose filler loaded resins

Publications:

- **A. Barkane**, O. Platnieks, L. Grase, S. Gaidukovs, Simultaneous wettability and stiffness control of UV-curing vegetable oil resin composites by lignocellulosic components. Polymer 255 (2022) 125154, doi:10.1016/j.polymer.2022.125154
- **A. Barkane**, E. Kampe, O. Platnieks, S. Gaidukovs, Cellulose Nanocrystals vs. cellulose nanofibers: A comparative study of reinforcing effect in UV-cured vegetable oil nanocomposites. Nanomaterials, 11 (2021) 1791, doi:10.3390/nano11071791

Following green chemistry and environmental preservation trends, the demand for bio-based acrylic resins is growing. Vegetable oil-based resins have arisen to meet the present challenge. However, the performance and tuning of sustainable resin properties still need improvement. There is an opportunity to use lignocellulose as an efficient renewable filler for polymer composites. There have been many investigations to prove the reinforcement concept of different nanocellulose for thermoplastic and thermoset polymers. However, other lignocellulose components (hemicellulose and lignin) have not been investigated as much and almost at all in photocurable resins. Hence, we undertook this study to research tuneable vegetable oil-based UV-curing composite resins. This work reports on vegetable oil-based resin loaded with lignocellulosic components of nanocrystalline cellulose (C), nanofibrillated cellulose (F), hemicellulose (H), and lignin (LN). Chosen loading were 5 and 10 wt% for all four components and additional 20 and 30 wt% C and F components resin composites. The effects of lignocellulosic components on thermal stability, thermomechanical properties, transparency, surface morphology, and wettability were evaluated in detail. In addition, the interaction of lignocellulosic components with the polymer matrix and interface was thoroughly investigated. The intense interaction between lignocellulosic components and the polymer matrix helps to form a strong interface and creates a polymer composite with enhanced thermomechanical properties. The composite surface morphology and wettability can be tuned depending on the lignocellulosic component, i.e., with the addition of H, C, and F. Hydrophilic affinity is improved and water wetting angles as low as 8° can be achieved, but with L a value of 96° was observed, a slight increase in hydrophobicity compared to the vegetable oil (VO) matrix value of 90°. Adding H and C reduced transparency at 500 nm by 14 and 16 %, while adding L and F by 18 and 25 %, respectively. FTIR revealed strong interfacial interactions through the hydrogen bonding between C, F, H, and the VO polymer. Above the glass transition temperature at 80 °C, the storage modulus values increased 6-fold and 2-fold for the 30 wt% C and F nanocomposites, respectively. This work will shed light on the lignocellulose components' future role in UV-curing resin applications. It also broadens lignocellulose particles' application as reinforcing additives for UV-light sensitive polymeric resins. The obtained nanocomposites with enhanced properties show great potential for applications such as UV-light-processed coatings, adhesives, and additive manufacturing resins.

**Sample abbreviation: VO – vegetable oil-based composition without fillers; vegetable oil-based composition with lignocellulose components 5–30 wt% summarized in Table 3.3.*

Table 3.3.

Sample abbreviation

Filler	*Sample abbreviation in regard to filler loading, wt%*				
	0	*5*	*10*	*20*	*30*
None	*VO*	-	-	-	-
Nanocrystalline cellulose	-	*VOC5*	*VOC10*	*VOC20*	*VOC30*
Nanofibrillated cellulose	-	*VOF5*	*VOF10*	*VOF20*	*VOF30*
Hemicellulose	-	*VOH5*	*VOH10*	-	-
Lignin	-	*VOL5*	*VOL10*	-	-

3.2.1.1. Macromolecular chain network structure

The density, DBC%, molecular weight between crosslinks (M_c), and the crosslinking density (N) for 10 wt% compositions are summarized in Table 3.4. As one of the main characteristics of composite materials, density characterizes the homogeneity of the component mixing, dispersion quality, and structural defects [210]. Lignocellulosic component addition causes a slight density increase, as seen in Table 3.4. The increase is related to the absolute density of C and F (1.6 g/cm^3) [134], H (1.5 g/cm^3) [211], and L (1.4 g/cm^3) [211], which are higher than the experimentally determined VO density (1.1 g/cm^3). Theoretically calculated densities for VOC10, VOF10 and VOH10 compositions are 1.2 g/cm^3 and 1.1 g/cm^3 for VOL10. Theoretical and experimental densities overlap in the error range, so it can be concluded that no significant voids are present. The compositions could have homogenous dispersion. The 5 wt% compositions have similar observations and 20 and 30 wt% F and C compositions showed density increase by almost 6 and 9 %, respectively. The Cs and Fs had the same absolute density value of around 1.6 g/cm^3 [179,212]. The experimental density of C materials was higher than that of Fs, due to the denser stacking of crystalline short rod-like Cs than the entangled F nanofibers [134].

Sol-fraction measurements are frequently used to assess the effectiveness of crosslinking [172]. Data in Table 3.4 shows that 10 wt% composition sol fractions decrease by -0.51 % for VOC10 and increase by +3.1 % and +1.08 % for VOF10 and VOH10, respectively. VOC10 sol-fraction decrease indicates greater crosslinking than VO composition. This is explained by nanocellulose helping the light scattering, as reported by Schmocker et. al [92]. At the same time, an increase in viscosity has been reported to limit the movement and distribution of the free radicals [166], hence the sol-fraction increase for the VOF10 and VOH10 compositions. The VOL10 has a much more pronounced increase in the sol-fraction (+15.9 %) related to the L filler's UV-light blocking properties that interfere with forming free radicals and, therefore, the crosslinking process. UV-light blocking is mainly attributed to the phenolic groups and conjugated carboxyl groups in L [81]. Similar trend for data (with sol-fraction changes of -0.31 % for VOC5, -1.5 % for VOF5 and VOH5, and +3.28 % for VOL5 compositions) can be observed in Table 3.4. The observed incremental decrease in sol-fraction from 5 to 2 % for the VO, 30 wt% C and F compositions, correspondingly, relates to the observed DBC% remarkable drop after nanocellulose incorporation into the polymer matrix.

The Flory–Rehner equation [202] was proposed to calculate M_c and N (Table 3.4). M_c has significantly decreased for C, F, and H compositions with 5 and 10 wt% loading, while it has increased for L compositions. The decrease is explained by filler-matrix interaction; and the increase is due to the significantly higher sol-fraction. Accordingly, N increased for VOC10, VOF10, and VOH10 and decreased (-1.2-fold) for VOL10 composition. The highest increase of N was recorded for VOC10 composition (3.2-fold), indicating the most significant filler-matrix interaction. This is followed by a 2.3-fold and a 2-fold increase for VOH10 and VOF10 compositions, respectively. Milder N increases in F compositions are related to F's tendency to agglomerate, resulting in stronger filler-filler interaction than filler-matrix interaction [134]. The same tendency is observed for 5 wt% compositions in Table 3.4. (1.6, 1.3, 2.3, and -1.4-fold increase/decrease for VOC5, VOF5, VOH5, and VOL5, respectively). The UV-cured nanocomposite containing 30 wt% of Fs and Cs is characterized by the 2-fold and 6-fold-enhanced M_c compared to the VO sample.

Table 3.4.

Structural characteristics of the VO and lignocellulose compositions

Sample	Density, g/cm^3	Sol-fraction, %	DBC $\%_{max}$	M_c, g/mol	N, $\times 10^3$, mol/cm^3	Transmittance at 500 nm, %
VO	1.1197 ± 0.005	2.5	78	161	6.9	96
VOC5	1.1394 ± 0.003	2.2	80	100	11.4	90
VOC10	1.1583 ± 0.015	2.0	80	50	23.3	80
VOC20	1.1601 ± 0.007	1.3	71	29	40.0	-
VOC30	1.1711 ± 0.011	1.5	69	23	51.0	-
VOF5	1.1299 ± 0.003	1.0	68	127	8.9	83
VOF10	1.1339 ± 0.005	5.6	70	80	14.2	71
VOF20	1.1532 ± 0.002	2.1	67	76	15.2	-
VOF30	1.1585 ± 0.011	1.9	36	69	16.8	-
VOH5	1.1097 ± 0.010	1.0	75	69	16.2	91
VOH10	1.1457 ± 0.004	3.6	75	71	16.2	82
VOl5	1.1139 ± 0.000	5.7	55	225	5.0	86
VOL10	1.1347 ± 0.014	18.4	24	189	6.0	78

3.2.1.2. Morphological properties

The obtained compositions are shown in Figure 3.7. The VO composition is highly optically transparent, while the VOC10, VOF10, and VOH10 compositions are translucent with white colouring. In contrast, the VOL10 composition is brown. Translucence is confirmed by UV-

Vis measurements (Table 3.4), where VO shows the highest transmittance of 96 % at 500 nm, followed by VOH10, VOC10, VOL10, and VOF10 compositions with 82, 80, 78, and 71 % transmittance, respectively. Wetting of the composition surfaces can be observed in Figure 3.7, where H_2O droplet contact angles (θ) are displayed. Changes in wettability can be explained by surface morphology SEM images. In Figure 3.7, SEM magnification of 1 000× shows that the VO composition has a relatively smooth surface structure. VOC10 composition shows exceptionally homogeneous dispersion at the same magnification, resulting in a nanostructured surface with θ = 25 °. Only a few agglomerates were detected, demonstrating that the modified vegetable oil-based polymer matrix has excellent interaction and adhesion with C. While the VOF10 composition surface shows a much rougher surface structure than the VOC10 composition, it also shows the lowest θ = 8 °. F in the VO polymer matrix formed a mesh-like nanofibrille structure, similar to that demonstrated in Galland et al. research on the hyperbranched acrylate matrix with several loadings of nanofibrillated cellulose [213]. The contact angle of the VOH10 composition with a water droplet is 52 °, which is reduced compared to VO. This is due to the H polymer's hydrophilic nature, and the resulting blend has two polymer phases and a lower contact angle value [71]. At the same time, the VOL10 composition shows surface-wide particle distribution (2017 ± 736 nm from SEM), but a nanostructure pattern has not developed. Contact angle is nearly identical to the VO composition (96 and 90 °, respectively). The more hydrophobic surface of the VOL10 composition is related to the hydrophobic L nature [214].

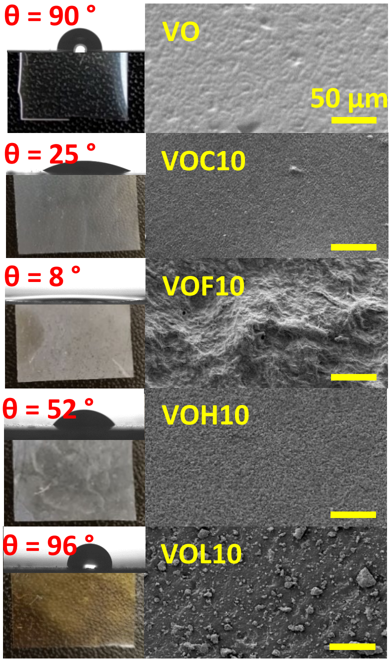

Figure 3.7. The prepared VO and 10 wt% compositions, SEM micrographs of the composite surface structure with 1 000× magnification, and water wetting (θ).

Figure 3.8 shows the optical images of the cured VO, VOC5, VOC10, VOC20, VOC30, and VOF5, VOF10, VOF20, and VOF30 with respective C and F wt% content. The obtained nonmonotonous changes in the transmittance values from the filler content could be explained by a mild nanocellulose agglomeration and segregation. Nevertheless, even at a load of 30 wt%, the translucency remained for C and F composites to some extent. The VOF30 sample had the lowest translucency.

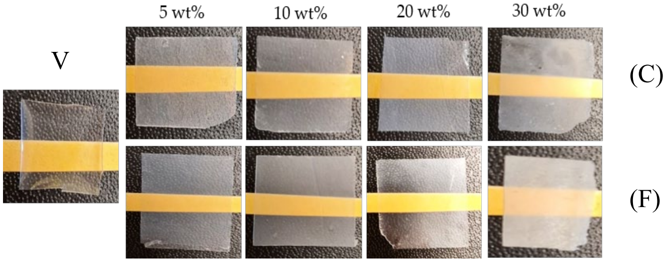

Figure 3.8. The cured VO, and the 5, 10, 20, and 30 wt% C and F composites.

3.2.1.3. Fourier-transform infrared spectroscopy

Resins, cured compositions, and lignocellulosic components were characterized with FTIR spectroscopy (VO, 10 wt% compositions in Figure 3.9, and VO, 5, 20, and 30 wt% compositions, and lignocellulose components in Supplementary 2 and 3). Crosslinking absorbance peaks at 810 cm^{-1} (CH_2=CH out of plane deformation [215]) and 1716 cm^{-1} (C=O stretching of carbonyl groups acrylates [49, 50]) in Figure 3.9 are highlighted in orange sectors I and II. Resins (dashed lines) and cured samples (solid lines) are plotted on top of each other, clearly showing CH_2=CH and C=O peak maximums decreasing and increasing after curing. When FTIR spectra of lignocellulosic components and VO cured composition are compared (Supplementary 3), it is seen that many absorption peaks overlap. Spectra in Figure 3.9 show no new absorption peaks, absent in VO and lignocellulosic component spectra. Therefore, it is concluded that no new covalent bonds between the polymer matrix and lignocellulosic components are formed. All characteristic absorption bands of the nanocellulose were assigned from FTIR measurements shown in Figure Supplementary 3. The broad peak from approximately 3000 to 3650 cm^{-1} is related to –OH stretching vibrations [216,217]; the peak at 2900 cm^{-1} is assigned to the C–H stretching vibration [218]; the peak at 1430 cm^{-1} represents CH_2 symmetric bending [218], while the peak at 1316 cm^{-1} is assigned to CH_2 wagging, and C–OH in-plane bending at C6 can be observed at 1204 cm^{-1} [216]. The band at 1160 cm^{-1} corresponds to C–O–C asymmetric stretching at the β-glycosidic linkage [216]. Other characteristic absorption peaks of C–O in cellulose can be observed approximately at 1055 cm^{-1} [217,219] and at 1028 cm^{-1}, and C–O-specific C6 stretching is represented by the band at 985 cm^{-1}. The signature peak at 897 cm^{-1} is assigned to C–O–C asymmetric stretching at β-glycosidic linkages of amorphous cellulose [216]. While there are peaks (Figure 3.9, 1175–1000 cm^{-1} range) attributed to C, F fillers, and H diluent absent from the VO spectra. Peaks with maximums at 1034 cm^{-1} coincide with C and F spectra; at 1111 cm^{-1} with C, F, H, and L spectra; and at 1513 cm^{-1} with L spectra in supplementary data Supplementary 3.

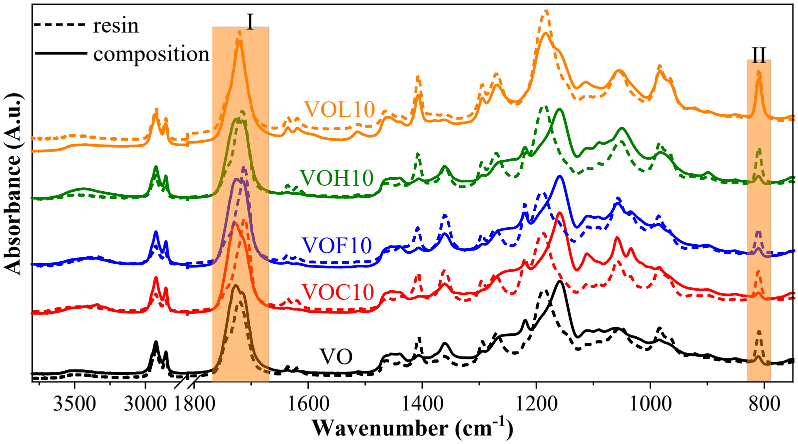

Figure 3.9. FTIR spectra of resins and cured VO and 10 wt% compositions. The curing time was 10 s.

The characteristic absorption peaks attributed to the polymer matrix were discussed in section 3.1 and lignocellulosic component structural groups are summarized in Supplementary 4. The lignocellulosic components in a polymer matrix create intermolecular bonding through hydrogen bonds, obstructing vinyl group conversion and lowering the light transmission [168]. This is confirmed by the calculated DBC%, representing the covalent bond crosslinking degree in Figure 3.10 for VO and 10 wt% samples (Supplementary 2: 5, 20, and 30 wt% samples). The Flory–Rehner calculations are represented in Table 3.5, while the DBC% calculation results from appropriate peak intensities (C=C and C=O) [20]. Curing trends for all prepared resins are similar. The primary curing occurs in the first 4 s, while the maximum DBC% was achieved at the 4 s mark.

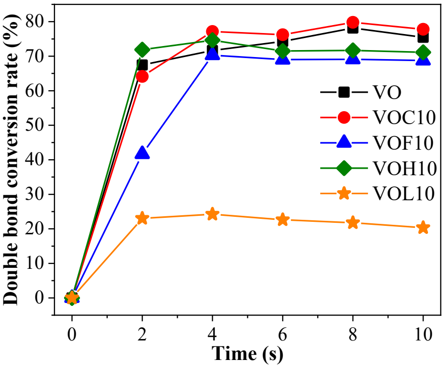

Figure 3.10. Double bond conversion rate % (DBC%) for VO and 10 wt% compositions.

Crosslinking evaluated by DBC% corresponds to sol-fraction data discussed before. The addition of nanocellulose, which aids in light scattering and increased viscosity, has resulted in observable inverted changes in sol-fraction and DBC% data for C and F compositions. Hence, compared to VO, a rise of DBC% for C compositions (+2 % for both VOC5 and VOC10) and a decrease for F compositions (-10 % and -8 % for VOF5 and VOF10, respectively) as improved light scattering and limited free radical movement produced these effects. Due to the previously mentioned UV-light blocking properties of L compositions, they have a much more significant drop in DBC% values (-23 % and -54 % for VOL5 and VOL10, respectively). An exception is H compositions with the second polymer phase, creating a slight decrease in DBC% values (-3 % for both 5 and 10 wt% compositions). The DBC% values are combined in Table 3.4. Similar tendencies are observed for 5 wt% compositions (Supplementary 5), with the lowest DBC% for VOL5 (55 %).

The steepest curing and the highest DBC% were received for the VO resin. After 2 s of irradiation, 67 % of the double bonds were converted, followed by the highest 78 % DBC% reached after 8 s. Herein, achieved curing time characteristics were considerably enhanced compared to the curing of poly(methyl methacrylate) and 1,6-hexanediol dimethacrylate formulations discussed by Zhang et al. [220], where after 5, 10, and 15 s of UV-light irradiation, the DBC% reached 18, 55, and 72 %, respectively. Steyrer et al. showed that the additional post-curing at elevating temperatures of the UV-light irradiation had increased DBC% by 2-fold [221]. Nevertheless, we report that we have reached a 1.35-fold higher DBC% than Steyrer et al. did without the additional post-curing at elevated temperatures. The C nanocomposites' curing with 70 % and 80 % of DBC% took place in the first 4 s indicated for 30 and 10 wt% content, respectively. The Fs had a more substantial impact on UV-light curing than the Cs did. A lower degree of DBC% was achieved for the F nanocomposites compared to the Cs. The curing process seemed to reach equilibrium after 2 s of irradiation for the F composites, where 36 and 41 % of DBC% correspond to 30 and 10 wt% content, respectively. In addition, 72 % of DBC% was received after 4 s of curing for the VOC30 sample. Other C and F samples showed a similar trend (Supplementary 5).

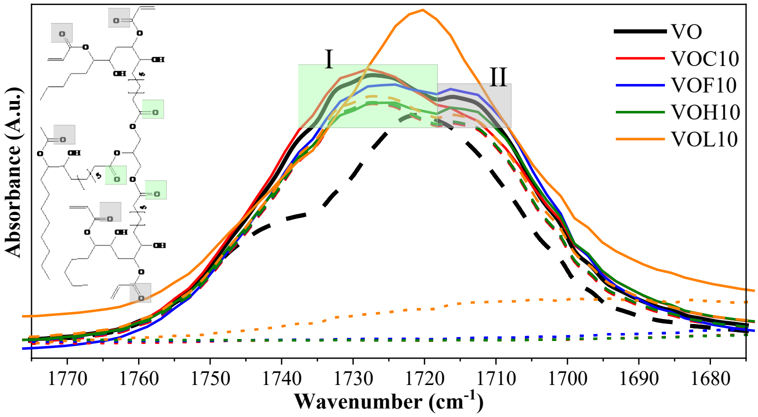

Figure 3.11. FTIR spectra of C=O group for VO resin (black dashed line) and cured composition (solid black line), 10 wt% cured compositions (dashed lines – theoretical spectra

obtained with Lambert-Beer's equation and solid lines – experimental spectra), and lignocellulosic component (dotted lines).

FTIR peak intensity shifts and changes can also determine the interactions between the lignocellulosic components and the VO polymer matrix. Like Liu et al., our previous research proposed an equation derived from Lambert-Beer's law to characterize the interaction between the F and the VO polymer matrix [192]. Theoretical lignocellulosic component composition spectra, according to equation (2.2), should be based mainly on polymer matrix spectra. This is confirmed by theoretical spectra (dashed lines) with increased and reduced peak intensities for C=O groups in Figure 3.11 for 10 wt% samples and Supplementary 6 for 5 compositions. However, experimental spectra do not overlap with theoretical spectra and show significant differences. At 1716 and 1727 cm^{-1}, two almost submerged peaks are attributed to acrylate and triglyceride carbonyl group stretching [215]. Changes to both peak intensities are attributed to lignocellulosic components' OH group interactions (forming hydrogen bonding) with the respective carbonyl groups of the polymer matrix [194]. VOC10 seems to have the most substantial interaction with the triglyceride's carbonyl group but limited with an acrylate carbonyl group. VOF10 has modified peak intensities for both carbonyl groups in comparison to VOC10 due to interactions of triglyceride and acrylate carbonyl groups, respectively. VOH10 only interacts with the acrylate carbonyl group (for the triglyceride carbonyl group, theoretical and experimental spectra overlap). Due to the reduced DBC%, the VOL10 resin interaction with L dominates over the cured compositions' interaction. They showed high interaction with the acrylic carbonyl group, which are more mobile than reacted counterparts (after crosslinking).

Even without calculations of theoretical spectra of the composite samples, these indications of hydrogen bonding can be observed. This was investigated for 30 wt% samples (Supplementary 6). The peak of the C–O bond at C6 stretching belonging to cellulose shifted from 1028 to 1033 cm^{-1}, while similarly, a shift in the second peak was observed from 1203 to 1219 cm^{-1}. These peaks were not observed for the neat resin, and they contributed to the developed cellulose–polymer interaction. Meanwhile, absorption bands attributed to nanocellulose at 1316 and 1430 cm^{-1} representing CH_2 wagging and C–H stretching vibrations could not be observed, due to the overlapping. Nonetheless, the separate peak applicable only to the nanocellulose fillers at 897 cm^{-1} related to C–O–C asymmetric stretching remained clear [192].

The VOF30 sample absorption bands, although in the same wavenumber ranges, were much more intensive compared to the VOC30. The higher content of nanocellulose contributed to the overall decrease in polymer resin characteristic absorption intensities. A similar explanation was reported by Yang et al. [194], who noted absorption intensity changes related to the development of the hydrogen bonding crosslinks between monomer's OH, C=O, and O=C–O groups and cellulose's –OH groups.

The –OH stretching vibration of the nanocellulose is revealed at 3342 cm^{-1} (Supplementary 3). The absorption was higher for F nanocomposites produced by their more elevated surface. Lui et al. suggested the current absorption band for H-bonding assessment between the hydroxyl groups of nanofibrillated cellulose [192]. The C=O absorption band at 1727 cm^{-1} of polymeric chains corresponds directly to the developed H-bonding (C=O ||| H–O) between the polymer matrix and nanofibrillated cellulose; then, H-bonding (H–O ||| H–O) between nanofibrillated cellulose was revealed at 3342 cm^{-1} in Supplementary 6. Ratios between C=O and O–H peak intensities (I_{1727}/I_{3342} and I_{1721}/I_{3342}) for 30 wt% C and F composites were 4.4 and 2.4, respectively. The almost 2-fold higher absorption intensity ratio for the Cs reflects the higher nanocellulose interaction with the polymer matrix than the Fs. Indeed, as shown in Supplementary 6, the C=O absorption band of the VOC30 shifted to longer wavenumber values, while the H–O absorption intensity strongly increased for nanocomposites compared to the uncured resins. Liu et al. attributed absorption bands shifts to the developed H-bonding interactions at the interface between cellulose particles and polymer matrix [192], which was more efficiently revealed for the C than the F nanocomposites. Attributed absorption bands shifted to the developed H-bonding interactions at the interface between the cellulose particles and polymer matrix [192], which were more efficiently revealed for VOC30 than for VOF30 samples.

3.2.1.4. Thermal stability

In previous research, the thermal stability of VO has been reported [176]. The AESO matrix and added reactive diluents (HDDA and TMPTA) are responsible for the high maximum destruction temperature T_{max2} (at 420 °C) and T_{max3} (at 462 °C). In Figure 3.12, the efficient derivative weight loss is estimated in the II-blue and III-green sectors, respectively. While T_{max1} (I-grey sector) peaks are present only for loaded compositions, they account for lignocellulosic components close to the composition surface where the polymer matrix does not provide protection [222]. The T_{max} values alongside the char yield wt% (leftover mass after thermal destruction) can be found in Table 3.5. Thermal destruction of used lignocellulosic components showed T_{max1} 174, 312, 273, and 328 °C for C, F, H, and LN, respectively (supplementary data Supplementary 7 and Table 3.5). Observing T_{max1} confirms higher thermal stability for L [223] and lower for C due to the more elevated surface providing greater exposure to heat [224]. T_{max1} values (increased by 104, 25, and 29 °C in comparison to filler T_{max1}) for 10 wt% compositions show that the matrix protects the lignocellulose component in VOC10, VOF10, and VOH10 compositions, respectively. Extreme protection (increase by 104 °C) for C in composition VOC10 confirms better filler-matrix interaction suggested in FTIR analysis. While T_{max1} for VOL10 has been lowered by 52 °C in comparison to LN, no significant mass loss can be observed in Figure 3.12. T_{max2} accounts for the main AESO matrix degradation. Adding lignocellulose components has not significantly affected the material's thermal stability; the biggest decrease from VO in T_{max2} is 18 °C for VOL10 composition. The lowest decrease of T_{max2} (2 °C) shows for VOC10 and VOF10 compositions due to their lower thermal stability – they have already burned out and therefore have a lower effect on the overall matrix thermal stability. VOH10 has a narrowed T_{max3} due to the H polymer nature confirmed by SEM, which dilutes the acrylate polymer matrix [71].

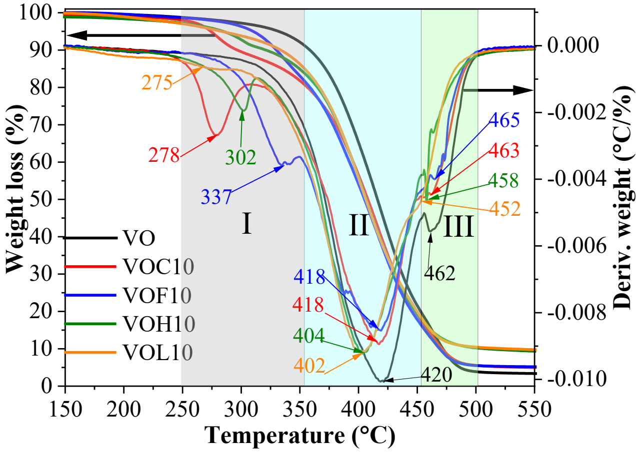

Figure 3.12. Thermal stability of the VO and 10 wt% compositions (weight loss and derivative weight).

The weight loss curves, and derivative curves of the VO and VOC, VOF nanocomposites, and C, F are shown in Supplementary 7. The cellulose composites are known for lower thermal stability than the neat polymer materials [225]. It was identified before that reactive diluent increases the thermal stability, and the thermal degradation maxima at 462 °C are attributable to reactive diluents. VOF samples, by themselves, have a higher thermal stability than VOC samples do, which is explained by the higher C surface area that provides larger exposure to the heat [169]. An enhanced nanoparticle–matrix interaction, observed with C nanocomposites via FTIR analysis, ensures better thermal protection by the polymer matrix [222]. In addition, 5% weight losses of the VO and VOF30 and VOC30 were observed at 332, 294, and 240 °C (Supplementary 7), correspondingly. The determined temperature at maximal degradation (T_{max}) was 313 and 175 °C, respectively, for Fs and Cs. However, it should be mentioned that above 320 °C, the thermal stability seemed to be higher for the Cs than for the Fs, as observed in Supplementary 7.

Supplementary 7 showed decreased thermal stability for the VOF and VOC nanocomposites, while the VOF samples thermally degraded at higher absolute temperatures than the VOC nanocomposites did. It was observed that when the nanocellulose content increased, the VOC and VOF nanocomposite thermal stability gradually decreased. It was found that the overall thermal stability, if measured by T_{max2}, did not suffer much compared to the poly(methyl methacrylate)/C nanocomposites reported in research by Sain et al., where T_{max2} dropped by 9 °C [226]. The tendency of the decrease in thermal stability, followed by increasing particle content, is compiled in Table 3.5. The VO sample had T_{max2} = 420 °C, and the VOF and VOC nanocomposites then showed a 2–5 °C decrease in T_{max2}, which depends on the nanocellulose and its content. The highest T_{max2} drop down to 415 °C was observed for the VOC20, VOF30, and VOC30 nanocomposites. T_{max2} dropped only by 1.2 %, but the first 10 % of weight loss was reached at 30.4 % and 10.0 % lower temperatures for VOC30 and VOF30 nanocomposites, respectively, as can be seen in Supplementary 7. As for char yields, nanocellulose increased the leftover char yield, but it seems that neither the Cs nor the Fs mattered. Both nanocelluloses char yields at 700 °C were around 30 %.

Table 3.5.

Weight loss at thermal degradation

Sample	T, °C when weight loss					T_{max1}, °C	T_{max2}, °C	T_{max3}, °C	Char yield, wt%
	10%	30%	50%	70%	90%				
VO	358	395	416	437	472	-	420	461	3
VOC5	349	391	414	436	473	285	418	466	4
VOC10	296	380	408	431	471	280	418	461	5
VOC20	275	365	399	426	467	266	418	465	7
VOC30	249	367	403	431	481	242	415	-	8
C	178	212	365	644	-	174	-	-	27
VOF5	336	383	407	430	469	341	418	460	4
VOF10	330	378	405	429	469	337	418	465	5
VOF20	325	366	401	429	478	345	415	455	6
VOF30	322	360	398	426	478	343	415	-	8
F	247	302	330	611	-	312	-	-	28
VOH5	339	388	411	435	487	305	408	463	8
VOH10	321	383	406	431	507	302	404	458	9
H	196	265	287	680	-	273	-	-	28
VOL5	351	389	411	433	467	-	414	463	3
VOL10	334	383	406	431	528	276	402	451	9
LN	248	346	549	-	-	328	-	-	42

The incorporation of nanocellulose can significantly increase the mechanical properties as interactions in the nanoscale directly impact the polymer interphase formation. Nanocomposites provide a different response to DMA continuous cyclic load depending on the nanocellulose content, dispersion degree, and formed interface adhesion between the reinforcement and polymer matrix. At lower nanocellulose loadings, the Fs would act as separate reinforcement nanofibers, but at higher loadings, the formation of a continuous entangled nanofibrille mesh-like network has been reported [134]. The Cs were observed as short rod-like nanoparticles (Figure 2.1); therefore, they were homogeneously dispersed in the polymer (Figure 3.7), while the good adhesion with the matrix remained.

3.2.1.5. Thermomechanical properties

The thermomechanical behaviour of compositions is characterized by storage modulus, loss modulus, and tanδ curves, visible in Figure 3.13. The increase in temperature contributes to decreased elastic response and the material's ability to store energy [227]. Components acting as reinforcement have a unique ability to store energy; thus, rigid C nanofillers yield a noticeable increase in stiffness [169]. Figure 3.15 shows the enhancement of storage modulus as a ratio between VO and lignocellulosic compositions’ values. This graph outlines the significant reinforcement achieved when the matrix undergoes the glass transition. VOC10 shows superior performance compared to the VOF10 composition by achieving up to a 3.5-fold increase in storage modulus values, compared to only a 2-fold improvement achieved with F filler over the VO. F can have issues with entanglement, which yields agglomerates and heterogeneous structures, thus lowering the compositions' mechanical properties [228]. This matches well with the observations from SEM micrographs of VOC10 and VOF10 (Figure 3.14). At 10 000× magnification, the VOC10 composition sustains homogeneous structures. The VOF10 composition shows a F tendency to form agglomerates and rougher structures than the VOC10 composition, revealing well-disposed nanoparticles. The SEM image testifies that the VOH10 composition has created a 2-phase nanostructured polymer blend. The VOL10 composition structure has the most exposed polymer matrix alongside micro-sized L particles and agglomerates.

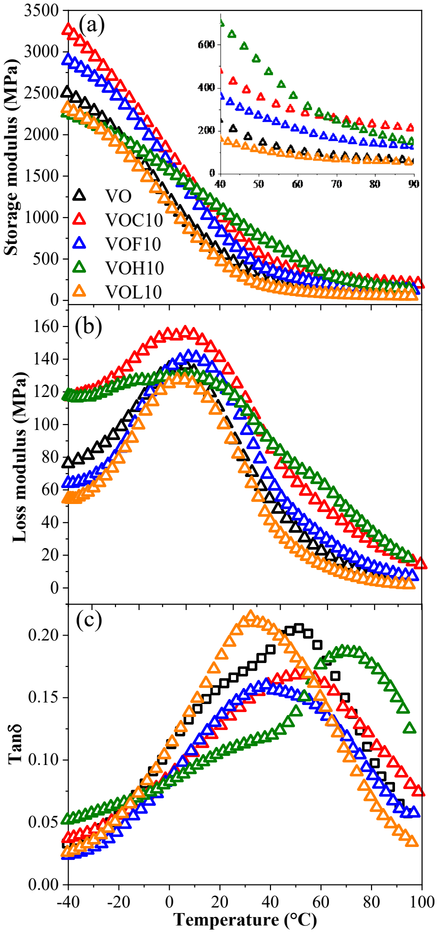

Figure 3.13. Storage modulus (a), loss modulus (b), and loss factor tanδ (c) curves of the VO and 10 wt% compositions.

L and H are not known for their ability to work as reinforcements. Adding H creates a polymer blend instead of the nanocomposite produced with nanocellulose [71]. It is important to note that neat H has relatively poor mechanical properties [229]. According to the literature, H could enhance the material's properties due to the densification of the structure by extensive hydrogen bonding [230,231]. In the case of VOH10, there is a very high increase in the storage modulus (Figure 3.13 (a)), showing a 3.5-fold improvement compared to VO. At the same time, adding too much H to a thermoset polymer like VO could yield a loss in mechanical performance due to the distribution of a crosslinked network. However, for L composition VOL10, there is a drop in properties compared to VO. It has been reported that the addition of L filler often results in reduced mechanical properties; therefore, it is often regarded as a filler that can increase the UV-light resistance of polymers [232]. L is therefore known for its radical scavenging ability [94]. Sol-fraction and DBC% (discussed above) show that L significantly limited the UV-curing process, which would be responsible for the decreased mechanical performance of VOL compositions.

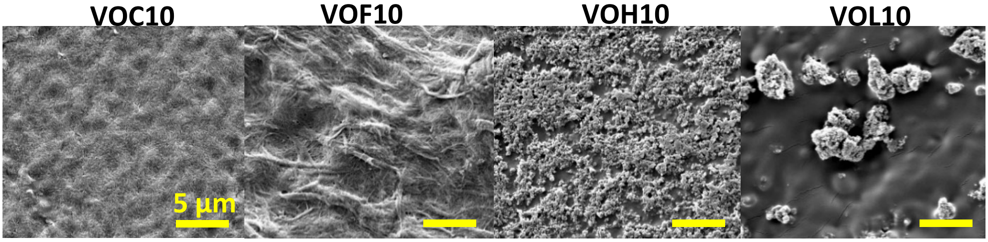

Figure 3.14. SEM micrographs of the prepared 10 wt% compositions at 10 000× magnification.

The loss modulus (Figure 3.13 (b)) shows that even at -40 °C, the compositions have relatively high viscous responses. The significant enhancement of loss modulus values is visible for VOC10 and VOH10. This is also visible above 30 °C, and VOC10 and VOH10 retain significantly higher values, indicating that these compositions have strong interactions with the VO matrix. Both VOC10 and VOH10 achieved a 3.5-fold improvement following a glassy to a viscoelastic state transition.

In tanδ curves (Figure 3.13 (c)), peak splitting can be seen for some of the compositions; the shoulder part of the VO peak could be related to more loosely packed regions or more elastomeric segments originating from the fatty acid composition [8]. An interesting observation can be made that compositions with fillers formed more uniform tanδ peaks, while blends with H made the shoulder part more pronounced. With peak deconvolution, two glass transition peaks were obtained for some compositions, and the obtained values can be seen in Table 3.6. VOL10 has a single glass transition peak that is 19 °C lower than the main peak of VO, indicating that L promoted chain mobility, which could be achieved by weak interaction with the matrix polymer [233]. VOH10 showed the opposite effect to VOL10 and shifted peaks to higher temperatures. The first peak (shoulder part) has a significantly lower tanδ value, but most notable was that the main peak was shifted by 22 °C to a higher temperature when compared to VO. This could be explained by polymer chains' restricted molecular thermal motions after incorporating H into the VO matrix [234]. This is assumed to be achieved by hydrogen bonding. The decrease in tanδ values matches well with the increase in storage modulus values and indicates a more rigid response of VOH10 compared to VO. In contrast, VOC10 and VOF10 remained similar to the initial VO curve, but their peaks were narrower and shifted by approximately 10 °C to a higher temperature.

Table 3.6.

T_g from tanδ of the VO and 10 wt% compositions

	T_{g1}, °C	T_{g2}, °C
VO	9	52
VOC10	9	51
VOF10	41	-
VOH10	23	74
VOL10	33	-

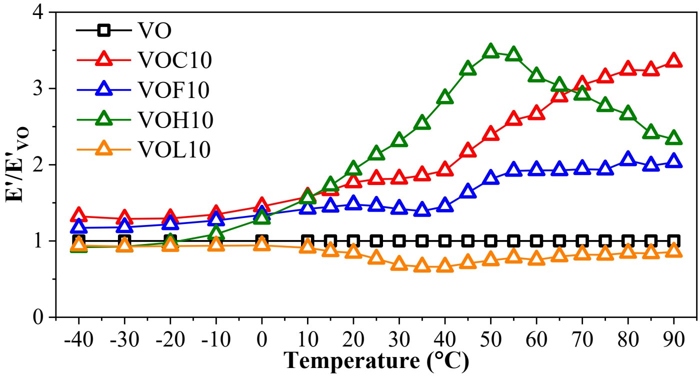

Figure 3.15. Storage modulus E'/E'$_{VO}$ ratio dependence on temperature for VO and 10 wt% compositions.

The data for VOC5, VOF5, VOH5, VOL5, VOC20, VOF20, VOC30, and VOF30 samples (Supplementary 8) shows a similar trend, with C and H being the best components that enhance thermomechanical properties. However, VOH5 provides a much higher increase in storage and loss modulus above 40 °C when compared to other compositions. The compositions with 10 wt% loadings showed superior thermomechanical properties to their 5 wt% counterparts. A significant storage and loss modulus increase was achieved for the nanocomposites with a nanocellulose load of 10–30 wt%, where a good reinforcement network was established, as indicated by the increased absolute values in both glassy and viscoelastic states (Supplementary 8). The shape differences of the nanocellulose are further expressed in the viscoelastic state, where Cs show significantly higher values than the Fs do. The 30 wt% loading of the nanocellulose produced a remarkable increase in the storage modulus at -40 °C – 1.9-fold and 1.3-fold, and at +80 °C – 6.2-fold and 2.1-fold, for the samples VOC30 and VOF30, accordingly. Wool et al. reported [235] reinforcement AESO with keratin fibers cured with a cumyl peroxide free-radical initiator. The modulus reached 2800 MPa at 0 °C with 30 wt% of the nanocellulose. Herein, higher performance was achieved for the VOC20.

A loss modulus increase was observed for highly loaded nanocomposites compared to the VO. In addition, 20–30 wt% loadings of the Cs and Fs significantly affect and restrict polymer segment motions; thus, the phase transition requires more energy, and subsequent slippage between the particles and matrix results in higher dissipated energy as heat [236]. If Cs and Fs are compared, then Cs present a gradual increase due to the particle nature, size, and geometry, but Fs do not follow the same trend. Polymer chain adsorption on F nanofibrilles is more restricted due to their morphology and entanglement [134]. Fs tend to agglomerate due to strongly developed hydrogen bonding between entangled nanofibrillated cellulose, as indicated by FTIR spectra.

The C and F effects on the damping properties are observed in Supplementary 8. Tanδ showed lower peak values for all nanocomposites than the VO. In this case, all samples followed a similar trend in line with the expected elastic response of the composite promoted by the addition of a rigid nanocellulose reinforcement, as reported by other authors [169]. The nanocellulose significantly affected the formation of the cured polymer chain network, which results in a higher rigidity and lower tanδ peak values for the C and F nanocomposites. The lowest tanδ values were observed for the 10 wt% compositions with values of 0.17 for the VOC10 and 0.16 for the VOF10. The 5–30 wt% Cs shifted the glass transition to a higher-temperature region, about 10–20 °C. The glass transition temperature, obtained from the tanδ peak maximum value, did not fully reflect the peak shifting trend; it could be explained by a relatively broad peak due to the formation of the crosslinked chain networks [237]. The tanδ peak shifts by 5–15 °C indicate significantly stronger interactions between the Cs and the polymer matrix than the Fs. These results coincide with the literature, where C addition to the thermoset matrix strongly increases the glass transition temperature [72].

3.2.1.6. Materials performance analysis

A radial plot of 10 wt% composition performance (storage modulus, thermal stability, and water wetting angle) ratio vs. vegetable oil composition is shown in Figure 3.16. All 10 wt% compositions show almost no changes in thermal stability, with a slight decrease for L and H compositions. The L composition is the only composition with an E'/E'_{VO} ratio of less than one, indicating that L filler, as previously discussed, blocks the UV-curing process, and reduces mechanical performance. Nevertheless, the 10 wt% composition of L is the only composition that shows an increased water contact angle. Therefore, L should not be disregarded as a filler, especially if hydrophobicity is desirable. 10 wt% compositions of C and F showed a significant increase in mechanical performance, where crystals are superior to fibres, although there is a considerable hydrophilicity increase. Unexpectedly, H composition shows the highest mechanical performance enhancement (at room temperature) and almost no thermal stability decrease. Hence, we were right not to neglect H as a diluent. Hence, our selection of H has been justified, and it shows tremendous potential as a diluent.

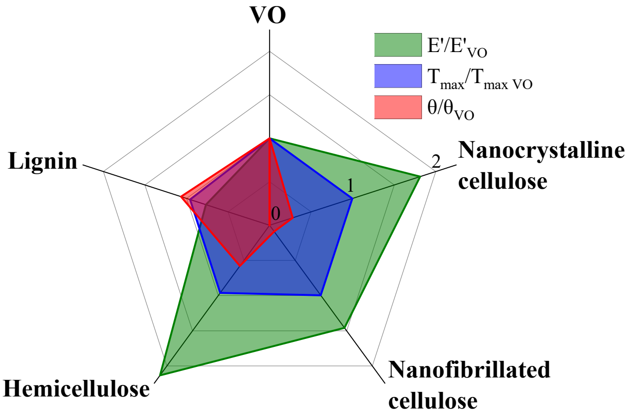

Figure 3.16. Relative changes of performance properties depending on 10 wt% compositions (at room temperature).

3.2.1.7. Summary

The present study investigates lignocellulose components' (nanocrystalline cellulose (C), nanofibrillated cellulose (F), hemicellulose (H), and lignin (L)) effects on vegetable oil-based UV-curable resin performance. 5 and 10 wt% loads of the lignocellulosic components and additional 20 and 30 wt% C and F components were introduced in vegetable oil-based resin (VO), emphasizing the 10 wt% compositions (VOC10, VOF10, VOH10, and VOL10 for C, F, H, and LN, respectively). The lignocellulose components and polymer matrix interaction and its effect on the curing degree, structural, thermal, and thermomechanical property changes were investigated. Transparency measurements showed a 14.6, 16.7, 18.8, and 26.0 % decrease in transparency for 10 wt% H, C, LN, and F compositions, respectively. Structural analysis showed a slight increase in density for all the compositions, increase by 2 % in curing efficiency (DBC%) for C 10 wt% composition and a decrease by 3, 8, and 54 % for H, F, and L 10 wt% compositions, respectively. Thermomechanical analysis shows no changes in glass transition temperature for 10 wt% C composition, a decrease for F (11 °C) and L (19 °C), and an increase for H (14 and 22 °C) composition, indicating lignocellulosic components' interaction with the matrix. DMA measurements for the 10 and 30 wt% C nanocomposites demonstrated superior stiffness performance compared to the F samples by remarkably increasing the storage and loss modulus values. The storage modulus was 3-fold and 6-fold at 30 °C and 80 °C for the 30 wt% C nanocomposites, respectively, while the 10 and 30 wt% F samples showed an increase of 1.5-fold and 2-fold, correspondingly. Thermal stability investigations revealed a 0.5 % drop in stability for 10 wt% C and F compositions and a 3.8 and 4.3 % drop for H and L compositions. Char yield increased by 2 % for C and F compositions and 6 % for H and L compositions. The incorporation of Fs proved to be preferable over Cs for the material's thermal stability because the 30 wt% F nanocomposite thermal degradation was 20 °C higher than those of the C samples. No covalent bonding between the lignocellulosic component and the polymer matrix was observed in Fourie-transform infrared spectroscopy. Nevertheless, the application of Lambert-

Beer’s law revealed strong interaction with the polymer matrix for C, F, and H components. C shows the strongest interaction with matrix triglyceride’s carbonyl group, F shows similar interaction with both carbonyl groups (triglycerides and acrylates), and H prefers to interact with the acrylate carbonyl groups. Meanwhile, the L composition appears to interact more in the resin form than in the cured composition, owing to the lower DBC%.

Although, until now, H and L in their unmodified form have been avoided in UV-curable compositions. We demonstrate significant results where both may bring exceptional property improvements necessary for a particular application involving hydrophobicity or 2-phase nanostructured polymer blends. Hence, we believe H has excellent potential to be a bio-based, nonreactive diluent for UV-curing resins. Furthermore, since L also has value, hybrid combinations of lignocellulosic components in UV-curing resins could be interesting for future investigations. Developed photocuring resins could be applicable as different coatings on wood or other surfaces; nonetheless, further investigations are still needed. Future research should also concentrate in creating hybrid filler systems in UV-curable resins therefore adapting nature based-systems.

3.2.2. Hybrid lignocellulose filler loaded resins

Publication:

- **A. Barkane**, E. Kampe, S. Gaidukovs, New reinforcing approach for biobased UV-curing resins: hybrid lignocellulose fillers with improved synergy and wood structure mimics. ACS Sustainable Chemistry & Engineering, 11 (17) (2023), 6578, doi:10.1021/acssuschemeng.2c07288

Lignocellulose fillers have been widely investigated for various polymer resin applications since they have great potential for using wood biomass and recycled plastics. However, besides nanocrystalline cellulose (C) and nanofibrillated cellulose (F), not much of the other lignocellulose has been used for UV-curing resins. Even more so, none in hybrid lignocellulose combination compositions. In the present work, the effects of hybrid lignocellulose fillers such as lignin (L) / C / F / hemicellulose (H) with ratio-varying compositions on UV-curing bio-based resins have been investigated for wood-mimic material coating applications. The hybrid filler effects on the macromolecular chain network, surface morphology, thermomechanical properties, and thermostability were carefully studied. A combination of scanning electron microscopy, DMA Cole-Cole plot, contact angle, etc., allowed getting a sense of hybrid filler distribution and interaction within the polymer matrix. It was identified that an increase in the H content of up to 38 % contributes to more even particle distribution and achieves a maximum double bond conversion rate of about 80 %. H also contributes to porous surface structure, while C smoothes surface morphology and, in turn, F increases defects. Thermomechanical testing revealed the unique benefit of hybrid reinforcement, showing higher results than single filler compositions despite the general decrease after incorporation of 5 wt% L. The storage modulus showed a 4-fold increase for 5 wt% L composition. The observed enormous property enhancement has been attributed to the benefits of hybrid fillers, which mitigate characteristic radical scavenging properties of LN, and strongly reduce general filler aggregation, allowing more even filler dispersion while also improving filler-matrix interface synergy. Seventeen different compositions clearly, in comparison to single fillers, show the benefit of hybrid lignocellulose reinforcement and testify the ability to precisely tune up material performance and achieve wood structure-mimicking coating materials.

**Sample abbreviations: 10 wt% of lignocellulose filler content, where 5 wt% was constant L content and 5 wt% was the C / F / H fillers. For example, C1F1H1 composition contains 33.33% of C, F, and H lignocellulosic components.*

3.2.2.1. Morphology properties

Hybrid composition morphology was characterized by SEM imaging at 10 000× magnification, presented in Figure 3.17. The green frame accounts for the hemicellulose (H) content decrease from top to bottom SEM image (Figure 3.17 (a) – (b)), and the red and blue for cellulose nanocrystal (C) (Figure 3.17 (d) – (b) – (e)) and nanofibrillated cellulose (F) (Figure 3.17 (f) – (b) – (g)) content decrease, accordingly. The micro-sized particles seen in the images are lignin (L) particles, evidently dispersed homogeneously [75]. The red-framed images in Figure 3.17 show that the decreasing C content results in a rougher structure. The highest C content shows the smoothest surface, with some evident agglomerates from F and L particles. F decreases in the blue frame images, which, on the contrary, show a more homogeneous structure with fewer F agglomerates. This contributes to the statement about the F content increase causing agglomerations and some defects in the material, resulting in a general density decrease discussed later. The surface porosity increases for the C3F1H3 (Figure 3.17 (g)), which is attributed to the H content increase (42.9 %), while the F decrease has no impact. In contrast, H is a nonreactive diluent in the composition that is chemically etched with acetone; increasing the H content results in increased porosity. This is revealed by the green-framed images, which show that surface porosity decreases by decreasing H. Composition C1F1H1 in Figure 3.17 (b) has the most homogeneous surface, with almost invisible separated L particle presence (encapsulated) on the surface due to equal C, F, and H content (33.3 %). Surface morphology can be tuned by adjusting the homogeneity of the lignocellulosic component and C and H's porosity changing content, respectively. F, even though beneficial for reinforcement, introduces agglomerates and defects. Water contact angle measurements support surface morphology adjustability by showing that hydrophobicity increased for C2F3H1, C1F1H1, and C2F1H3 compositions with increasing H content of 34, 54, and 55 °, respectively (Supplementary 9).

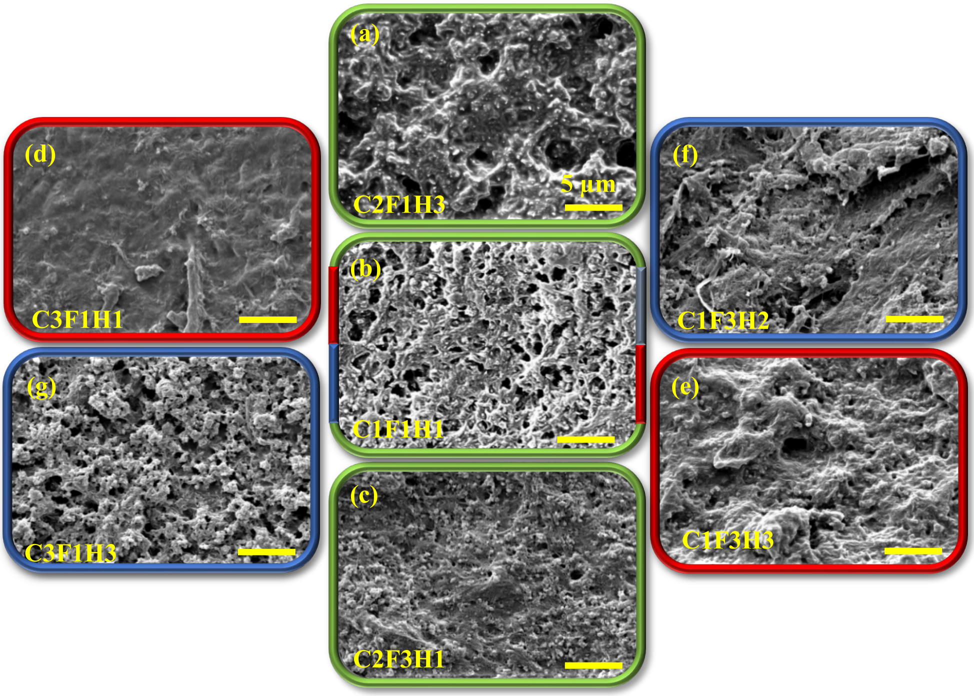

Figure 3.17. Surface morphology SEM images at 10 000× magnification of hybrid compositions where lignocellulose component content in 5 wt% decreases from top to bottom image H↓ (C2F1H3 (a)→C1F1H1 (b)→C2F3H1 (c)), C↓ (C3F1H1 (d)→C1F1H1 (b)→C1F3H3 (e)), and F↓ (C1F3H2 (f)→C1F1H1 (b)→C3F1H3 (g)).

3.2.2.2. Macromolecular chain network

The double bond conversion rate (DBC%) and sol-fraction (%) (presented in Figures 3.18 (a) and (b)) were used to assess photopolymerization efficiency. DBC% was calculated using equation (2.1) and the appropriate peak intensity of CH_2=CH out of plane deformation at 810 cm^{-1} [215] and C=O stretching of carbonyl group acrylates at 1716 cm^{-1} [168] from FTIR measurements. Figure 3.18 shows DBC% data over time (a); $DBC\%_{max}$ values (b), DBC% range from 62 % to 80 % for C3F3H1 and C3F2H3, respectively. It indicates that increasing H content up to 38 % from 5 wt% hybrid fillers is beneficial for achieving higher $DBC\%_{max}$ values. All the prepared hybrid resins are completely crosslinked approximately in 8 s under UV-light. L component 5 and 10 wt% loaded resins [75] (Table 3.7) reduced DBC% values from 78 % for the neat resin to 55 and 24 %, respectively. While the characteristic UV-light absorbing effect of L [81] has a lower impact for hybrid compositions with C, F, and H, and, in turn, higher $DBC\%_{max}$ values can be achieved. This demonstrates the benefit of C and F fillers, which aid in light scattering [92], while H is a nonreactive diluent that reduces viscosity and thus improves radical movement [75].

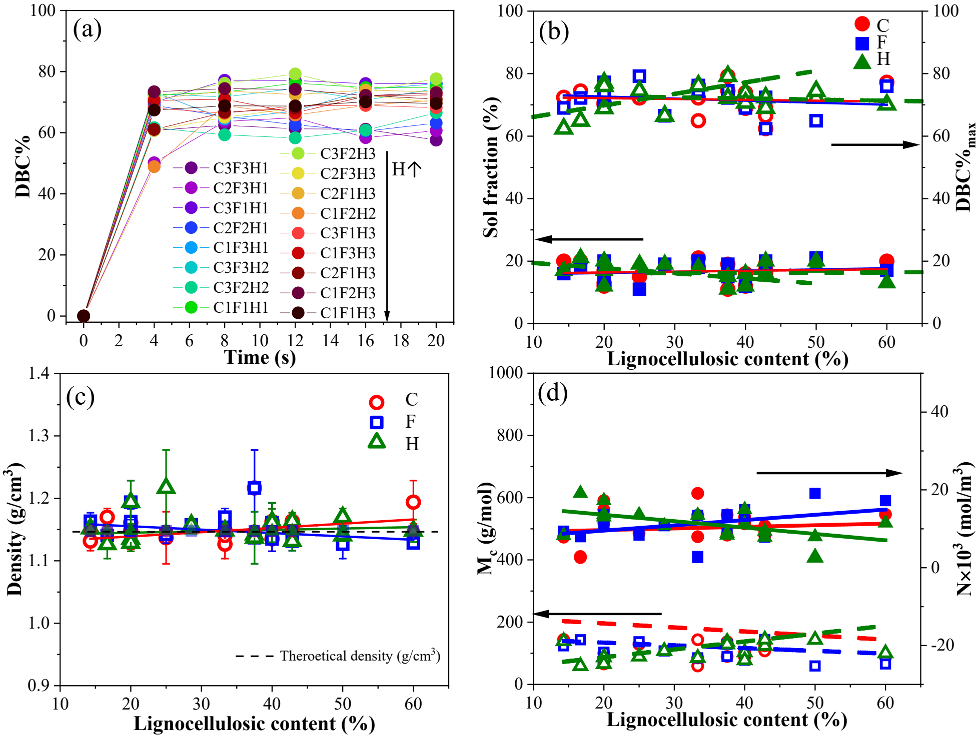

Figure 3.18. Double bond conversion rate (DBC%) vs. time (a), sol-fraction and maximum DBC% values ($DBC\%_{max}$) vs. content (b), experimental and theoretical densities (c), and crosslinking density and molecular weight between crosslinks (d) for hybrid lignocellulose nanocomposite resin photocuring.

A closer look at the impact of H content on DBC%$_{max}$ is presented in Figure 3.18 (b), which reveals that the optimal H content is 38 % in hybrid fillers for achieving the highest DBC% value of 80 %. Hence, it is evident that hybrid compositions help to overcome the negative effect of LN's loading on the photopolymerization process, increasing overall DBC%$_{max}$ values from 55 % up to 80 %. Sol-fraction data in Figure 3.18 (b) supports the DBC%$_{max}$ findings, revealing an insignificantly increasing sol fraction while C and F content increases, and decreases while H content is increased till 38 % and afterward, H content increase does not impact the sol-fraction. The sol-fraction data ranges 11–21 % for C3F2H3 and C2F3H1, respectively.

Filler content in UV-composite resins impacts the photopolymerization process, which raises composite homogeneity and structural defects [210]. Figure 3.18 (c) reveals that experimental densities vary 1.1–1.3 g/cm^3. However, experimental densities and theoretical densities have minimal deviations. Nevertheless, it is observed that C and H increase density while F causes a decrease in density. The higher C and H values could be attributed to the denser stacking of crystalline short rod-like Cs [126] and H densification [230]. While the density decrease in the case of Fs is related to long fibers' tendency to agglomerate, introducing some defects and voids into the matrix [126]. The polymer matrix density is known to be 1.12 g/cm^3, and since the absolute densities of the C and F, H, and L fillers were 1.6 g/cm^3 [134], 1.5 g/cm^3 [211], and 1.4 g/cm^3 [211], respectively, a general increase can be expected. However, when obtained data are compared to a density of 1.16 g/cm^3 for 10 wt% C composition [75], it is revealed that hybrid compositions provide higher density values.

While sol-fraction matches DBC%$_{max}$, crosslinking density N and molecular weight between crosslinks M_c, which are calculated with the Flory-Rehner equation and presented in Figure 3.18 (d). correspond to the experimental density data. Increasing N and decreasing M_c for samples C and H are shown in Figure 3.18 (d), while F content increase M_c. Increasing N for samples C and F is related to the profound matrix-filler interface crosslinking [75]. Compared to the VO matrix properties (Table 3.7), N for hybrid compositions has increased by 12 mol/cm^3 and M_c has decreased by 102 mol/cm^3. However, the highest N = 23.3 mol/cm^3 was achieved for C 10 wt% composition; while the highest N = 9.1 mol/cm^3 was achieved for hybrid composition C2F3H1, which is still 4.1-fold higher than for 5 wt% L sample. As a result, hybrid compositions achieve higher values of DBC%$_{max}$, offsetting the decrease caused by introducing L into the material.

3.2.2.3. Thermomechanical properties

The thermomechanical performance of the hybrid compositions, which are characterized by storage modulus (*E'*), loss modulus (*E''*), and loss factor (tanδ) curves, is presented in Figure 3.19. In paper [75] authors already concluded that 5 wt% L is known to lower the composites' ability to store energy (storage modulus), while 5 wt% of C, F, and H show some improvements in storage modulus values. Thermomechanical characterization below the glass transition temperature (T_g) is attributed to the glassy state polymer. Figure 3.19 (a) indeed shows that all hybrid compositions at low temperatures have enhanced storage modulus values in comparison to the 5 wt% LN. For example, the C1F3H1 sample showed $E'_{-45\ ^{\circ}C}$ 4250 MPa, which is a 2-fold increase than the 5 wt% L sample ($E'_{-45\ ^{\circ}C}$ = 1989 MPa). Half of the hybrid compositions show higher storage modulus values in comparison to sample 5 wt% H ($E'_{-45\ ^{\circ}C}$ = 2813 MPa) [75]. The C1F3H1, C3F1H1, and C2F3H1 compositions' storage modulus values are higher than 10 wt% of C compositions ($E'_{-45\ ^{\circ}C}$ = 3377 MPa). The C1F3H1 composition has 60 % and C2F3H1 has 50 % F. F is reported as the most mobile filler of the nanocellulose filler types, while C is more rigid [134]. This significantly increases the storage modulus in the polymer composites' glassy state. In other words, hybrid compositions with a lower H content and higher C / F content significantly outperform single filler materials. This corresponds to the reported strong filler's tendency to agglomerate above loadings of 2 wt% [126]. The threshold content for agglomeration is reduced when multiple fillers are introduced [238]. Therefore, a hybrid filler combination can be deployed more homogeneously in the resin.

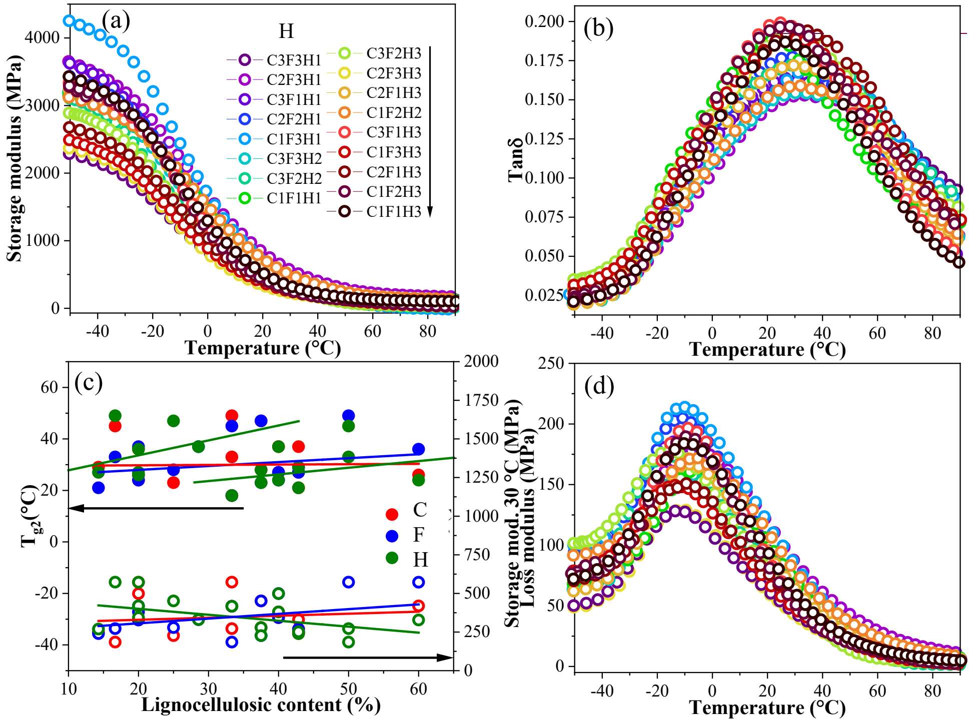

Figure 3.19. Storage modulus (a), loss modulus (b), loss factor tanδ (c), and glass transition temperature and storage modulus at 30 °C tendencies depending on lignocellulose component content (d).

Figure 3.19 (b) shows that increasing H and decreasing C / F content leads to a drop of tanδ absolute values, which is associated with material mechanical damping and attributed to the increasing overall stiffness of the hybrid compositions [169,239-241]. These tendencies are consistent with single filler compositions [75], where stiffness significantly increased for F and C and did not change for H and L compositions. Tanδ curves maximum can also be used to obtain glass transition temperatures. Deconvolution was performed on tanδ curves presented in Figure 3.19 (b) to assess single filler impact, and the calculated T_g were summarized in Table 3.7. The hybrid composition values revealed three T_g, in comparison to single filler compositions showed two. No single filler composition showed a T_{g1} below 0 °C related to the polymer matrix. T_g change is attributed to the primary VO matrix shifting to lower and higher temperatures depending on the composition. T_{g2} for the VO matrix is 52 and for the 5 wt% L composition – 37 °C (Supplementary 10); in turn, T_{g2} for hybrid compositions ranges 18–49 °C. Figure 3.19 (c) shows that T_{g2} increases with increasing H and F content, whereas increasing C content has no discernible effect on T_{g2}. This finding correlates with single filler compositions where adding H and F resulted in a T_{g2} increase while adding C had a minimal effect. T_{g3} is attributed to H influence because 10 wt% H increased significantly up to 74 °C.

Glass transition temperatures T_g loss can be obtained from the loss factor curve maximum [239]. When evaluating a homogeneous matrix, the loss factor gives a more precise T_g than the tanδ. Tanδ is better suited for complex resin systems and reinforced composites with strong effects [239,242]. T_g loss presented in Figure 3.19 (d), attributed to the matrix AESO -9 °C [20], is the closest to T_{g1} calculated from the tanδ deconvoluted peaks. Meanwhile, the loss modulus provides information on filler matrix interfacial interaction [75,240]. Single filler compositions [75] showed that fillers interact with the VO matrix (L was the only one that showed decreased loss modulus attributed to decreased DBC%). Hybrid compositions show an even higher viscous response at low temperatures than single-filler ones. Enhanced loss modulus values throughout the broad temperature range indicate strong filler-matrix interactions, making it harder to rearrange the structure. Consequently, when force is applied, the high-content hybrid compositions' loss modulus values correspond to lower H contents and higher reinforcement.

Table 3.7.

Glass transition temperatures from tanδ and loss modulus of the hybrid compositions

Sample	T_{g1}, °C	T_{g2}, °C	T_{g3}, °C	$T_{g,\ loss}$, °C
C3F3H1	-7	27	70	-12
C2F3H1	8	49	>100	-6
C3F1H1	-	26	-	-11
C2F2H1	-8	27	87	-11
C1F3H1	-7	36	>100	-11
C3F3H2	4	47	100	-10
C3F2H2	-7	37	>100	-17
C1F1H1	-15	18	76	-4
C3F2H3	-11	28	>100	-15
C2F3H3	-10	23	71	-13
C2F1H3	0	37	>100	-8
C1F2H2	-	24	60	-5
C3F1H3	-5	21	66	-8
C1F3H3	-9	29	>100	-14
C2F1H3	-8	33	>100	-10
C1F2H3	12	45	>100	-10
C1F1H3	-9	24	59	-9

The ratio of storage modulus L 5 wt% and the hybrid compositions is shown in Figure 3.20 (a). It reveals significant reinforcement enhancements as the polymer is heated above the glass transition. All hybrid compositions seem to have overcome the LN's ability to decrease the ability to store energy, as observed for the 5 wt% LN. Only three samples, C3F2H3, C1F2H3, and C1F3H3, have a ratio of less than one above 50 °C during testing. This demonstrates the beneficial effect of hybrid fillers in improving composite homogeneity, as evidenced by a ratio increase of up to 2-fold at the glassy state. The increases of the $E'/E'_{L\ 5wt\%}$ ratios overlap with T_g from Table 3.7; this shows that the transition to a viscoelastic state allows reinforcement to take some of the matrix load.

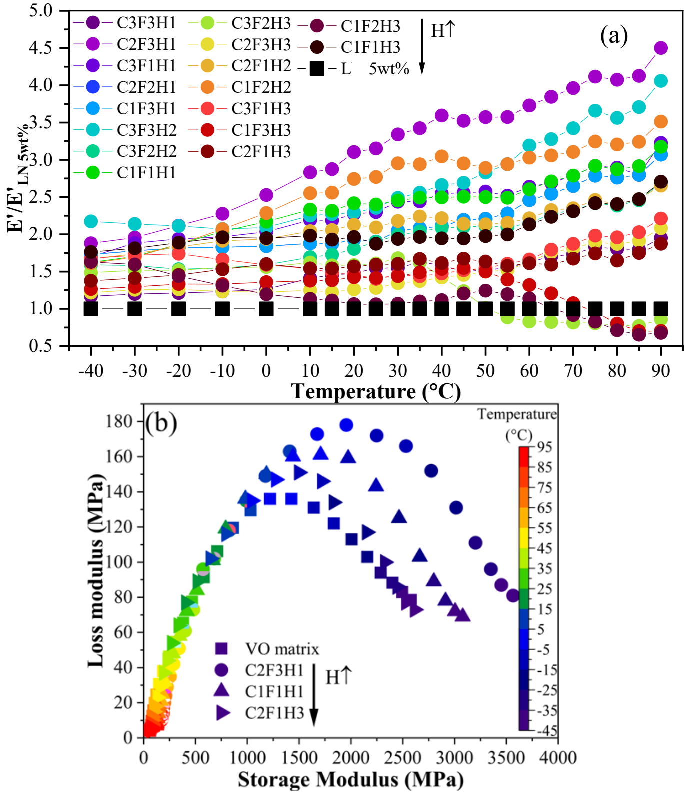

Figure 3.20. Storage modulus ratio $E'/E'_{L\ 5wt\%}$ vs. temperature for hybrid compositions (a) and Cole-Cole plot of hybrid compositions by increasing H content (b).

Cole-Cole plot obtained by plotting loss vs. storage modulus with each point corresponding to 1 (Hz) frequency throughout temperature changes is presented in Figure 3.20 (b). The Cole-Cole plot shows evident changes in crosslinked polymer structural properties [239,242,243]. Indications of the filler dispersion in the hybrid composite system. The semi-arch diagram describes a homogeneous polymeric system for an increased H content sample, whereas the elliptical path and irregular shape for an increased C / F content sample indicate phase segregation, heterogeneous system, and possible lignocellulose filler aggregation [239,242,244]. Totally, this indicates even filler distribution in resin as shown in SEM Figure 3.17 (a)–(c).

3.2.2.4. Lignocellulose filler synergy

Figure 3.21 shows two submerging FTIR absorption peaks of C=O groups attributed to acrylate and triglyceride carbonyl group stretching vibrations at 1716 and 1727 cm^{-1}, respectively [215]. Previous research has shown that shifts and changes in the intensity of these carbonyl group peaks indicate the interaction between lignocellulose components' OH groups and VO matrix C=O groups [75,194,245]. Previous research of similar materials showed that lignocellulose fillers do not have peaks around the 1760–1670 cm^{-1} range; hence, all changes in this region are attributed to developed hydrogen bonding. It is reported that C and F have a great tendency to interact (more substantial deviation of the C=O peak location and intensity) with triglyceride carbonyl groups. While H interacts with acrylate carbonyl groups [75]. In turn, L due to decreased DBC% in single filler compositions showed no significant impact on the polymer macromolecules. Hybrid composition spectra in Figure 3.21 show a similar tendency with increasing H content (decreasing C and F content), where triglyceride shows carbonyl group and acrylate group peaks shifts, respectively. Hence, one could adjust the interaction between fillers and matrix by modifying the C, F, H, and L ratios in the hybrid composite material.

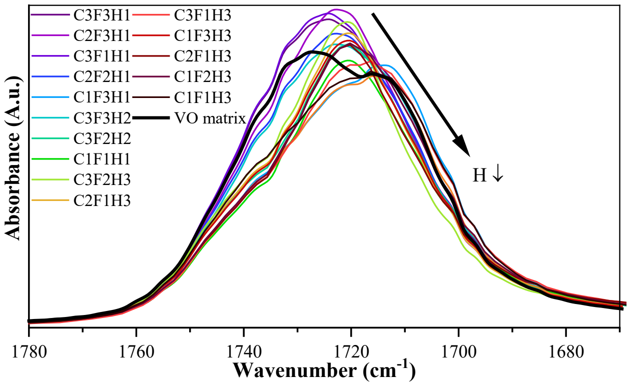

Figure 3.21. FTIR spectra of C=O group of hybrid compositions and VO matrix.

Color mapping supplemented with XYZ interpolation to smooth the contour plot using the Thin Plate Spline (TPS) algorithm in Origin with a smoothing parameter of < 0.01 is plotted in Figure 3.22. By variating C / F content, Figure 3.22 identifies DBC%$_{max}$ vs. T_{g2} (Figure 3.22 (a)), N vs. T_{g2} (Figure 3.22 (b)), filler content affects loss modulus vs. storage modulus at the glassy state at -45 °C (Figure 3.22 (c)), and viscoelastic state at 95 °C (Figure 3.22 (d)). DBC%$_{max}$ ranges 63–78 % with C / F reinforcement supremacy as red regions, as shown in Figure 3.22 (a). While all the polymer matrix's T_g temperatures are reachable at 18–45 °C. The dominance of H as blue regions appears to dictate average DBC%$_{max}$ values of 70–72 % and T_g of 22–42.5 °C. Compositions of equal ratios (C / F / H = 1 / 1 / 1, green regions) consider almost any desirable DBC%$_{max}$ and T_g values. Figure 3.22 (b) plotted to conclude the N affected by filler-matrix interactions and matrix double bond conversion rates. Here, higher reinforcement ensures higher N and higher T_g. High T_g is also observed with H supremacy, while N is lower. In the case of DBC%$_{max}$, the lowest values correspond to the most negligible H content. In turn, green regions of N relate to C / F / H = 1 / 1 / 1. H supremacy shows the lowest and average N values of 2 and 11 mol/m^3, respectively.

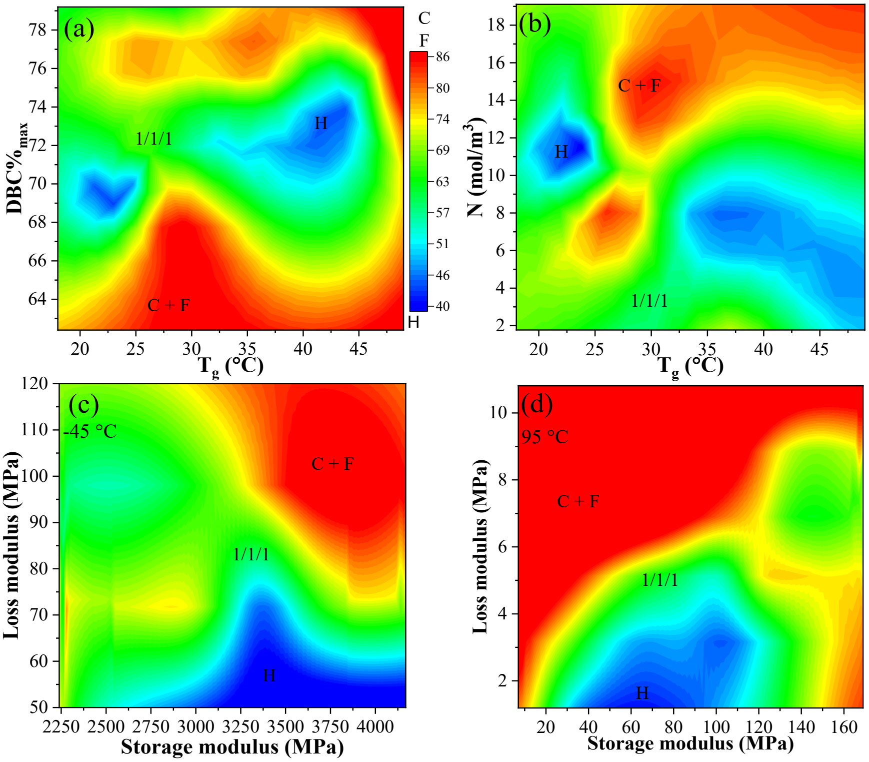

Figure 3.22. Color map plots of double bond conversion rate vs. T_{g2} (a), crosslinking density vs. T_{g2} (b), loss modulus vs. storage modulus for glassy state at -45 °C (c) and rubbery state at 95 °C (d) red – reinforcement of C / F dominates, green – C / F / H = 1 / 1 / 1, and blue – H content dominates.

H content dominance shown in the blue region ensures high storage modulus and low loss modulus in the glassy state (Figure 3.22 (c)). A 1 / 1 / 1 ratio of fillers dominates for all loss modulus values while storage modulus is lower; and when loss modulus varies 60–75 MPa, the highest storage modulus of 4250 MPa is ensured. Most C / F reinforcement compositions have shown the highest loss and storage moduli. At the viscoelastic state (Figure 3.22 (d)), the reinforcement dominance is attributed to the highest loss modulus with a lower storage modulus. H impact at glassy states gives the lowest loss modulus (50–70 MPa) and an average storage modulus. Naturally, since the structure rearranging is limited by filler matrix interfacial interaction more strongly than in the glassy state.

3.2.2.5. Thermal stability and decomposition

Thermal stability data from the thermogravimetric analysis are presented in Figure 3.23. The maximal destruction temperature (T_{max}) is read from the peaks in the derivative weight loss graph (Figure 3.23 (a)), which shows five-step thermal destruction at a standard heating rate of 10 °C/min. Previous investigations have discussed the thermal degradation steps of the VO matrix [176] and single filler compositions section 3.2.1. T_{max} attributed for degradation of the AESO main matrix and added comonomers HDDA and TMPTA in sectors IV and V (of Figure 3.23 (a) T_{max4} and T_{max5}, respectively). The 11 °C decrease of T_{max4} relates to the 5 wt% L and H content in the hybrid compositions. In turn single filler 10 wt% compositions with L and H showed an 18 and 16 °C decrease, respectively. For comparison, a special flame-retardant acrylic coating with graphite nanoplates and melamine polyphosphate showed T_{max} around 400 410 °C [246]. Destruction sectors I, II, and III (T_{max1}, T_{max2}, and T_{max3}, respectively) are assigned to C, H, and F filler. The hybrid structure and thermal protection by L at T_{max} 328 °C and the matrix at T_{max} 420 °C [75,222] are attributed to deviations of filler T_{max} of +35, +30, and +43 °C for C, H, and F, respectively, (Supplementary 10). The thermal destruction in sector VI has no significant weight loss changes. Figure 3.23 (b) shows T_{max4} at sector IV tendencies depending on the lignocellulose component content increase. The T_{max4} attributes to the main AESO matrix thermal destruction [176]. H content increase has two thermal stability tendencies: increasing, dropping and increasing again. F shows a slightly decreasing tendency, while C shows an increase of T_{max4}. The C's increase is related to more unstable Cs burning out faster, and therefore, when the temperature reaches sector IV, thermal destruction corresponds to the matrix.

Supplementary 11 and Figure 3.23 (d), show the thermal stability of C2F3H1, C1F1H1, and C2F1H3 by increasing H content at various heating rates 10, 15, 20, and 30 °C/min, which were used to calculate Friedman thermal degradation kinetics using equations (2.3–2.5) [247]. This demonstrates that increasing the heating rate causes thermographs to shift to higher temperatures due to reaction hysteresis with an increased temperature gradient [176,177]. The characteristic data of the Ln(d/dt) vs. 1/T from 5 % to 90 % (5 % step), conversion rate (α) vs. temperature $d\alpha/dt$ vs. temperature at different heating rates for the C1F1H1 composition are shown in Figure 3.23 (c), (d). Data for C2F3H1 and C2F1H3 compositions are provided in Supplementary 11. Figure 3.23 plots of intercepts ($Ln[Af(\alpha)]$) for each α were generated to fit regression lines with gained slopes E/R. The activation energy E was calculated from E/R slope values [176,177].

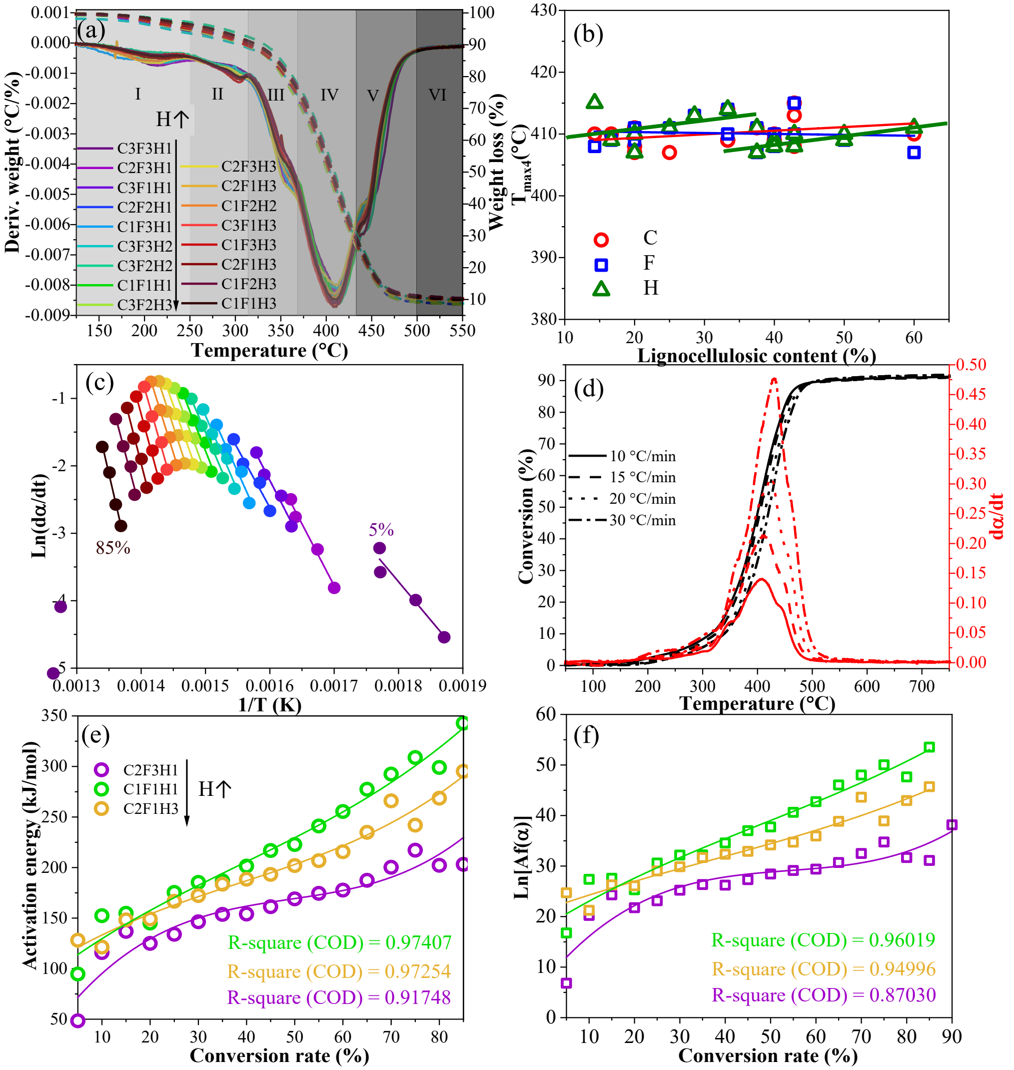

Figure 3.23. TGA curve of the hybrid compositions (a), T_{max4} tendencies depending on lignocellulose component content (b), and C1F1H1 composition plots of Ln(dα/dt) vs. 1/T from 5 % to 90 % (c), conversion rate vs. temperature and dα/dt vs. temperature at different heating rates (d), C2F3H1, C1F1H1, and C2F1H3 composition (increasing H content) plots of activation energy vs. conversion rate (e), and Ln[Af(α)] vs. conversion rate (f).

The E plotted in Figure 3.23 (e) confirms that increasing H content increases thermal stability. This is attributed to the increase in DBC%$_{max}$ by 13 %. Since the DBC%$_{max}$ of C2F1H3 has dropped by 1 % (in comparison), activation energy is also lower but still higher than for C2F3H1 composition. The cubic polynomial fit was used because previous studies reported it accurately [176,177]. The coefficient of determination (COD) R-square is almost equal to 1. The VO matrix E changes can be divided into 3 stages: clime until 35 %, then climb to 65 % of the α. 0 % > α > 35 % is attributed to the initial heating difficulty of volatilizing and decomposing crosslinked structures into low molecular substances. $35\ \% > \alpha > 65\ \%$ shows thermal degradation progression more easily, where those low molecular substances are decomposed and volatilized even further. At the same time, $65\ \% > \alpha$ is attributed to the destruction of the first two stages of destruction products (degradation residues) [176]. Since lignocellulose filler has lower thermal stability than the VO matrix, the E range is much broader than for the VO matrix. E values for C2F3H1, C1F1H1, and C2F1H3 were 50–225, 94–344, and 119–295 kJ/mol, respectively. The VO matrix spread ranged 132–268 kJ/mol. Hence, low α 5 % has dropped E significantly by 82, 38, and 13 kJ/mol, while for high α 90 %, E has dropped by 43 kJ/mol for the lowest H content and increased by 76 and 27 kJ/mol for C1F1H1 and C2F1H3 (increasing H content), respectively. Nonetheless, even though E values have changed, these hybrid composites could also be used for pyrolysis at the end of their lifespan to avoid landfilling. The obtained E values are lower and do not exceed the E ranges of other reported pyrolysis-capable plastic wastes such as polyvinyl chloride with pine wood with E values of 108–360 kJ/mol [248] and even coals 180–600 kJ/mol [249].

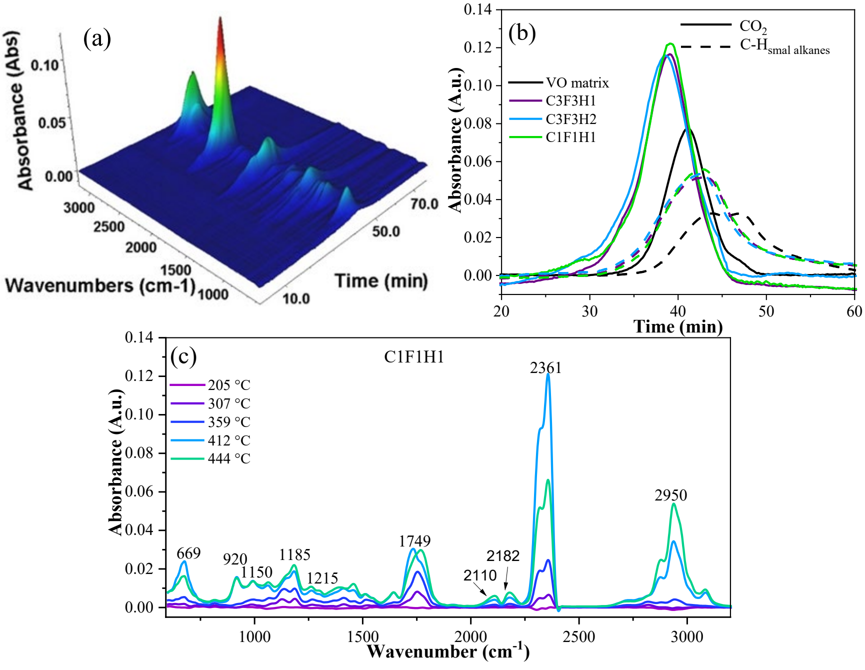

Figure 3.24. Thermal destruction 3D surface graph for the FTIR spectra of the evolved gases produced by C1F1H1 (a), CO_2 (solid lines) and C-H from small alkanes (dashed lines) emission during heating (b) with VO resin [176] and C1F1H1 spectra at different temperatures (c).

Information on volatile destruction products of prepared composite is essential when a polymer material is considered for pyrolysis [250]. Figure 3.24 depicts critical data on volatile products of thermal destruction from the linked system TGA-FTIR. VO matrix thermal destruction volatile products have been investigated in our previous investigations [176].

Compared to the volatiles released as shown in 3D surface graphs in Figure 3.24 (a) and Supplementary 12, they overlap with each other, differing only in intensities and release times. Considering no wt% changes of filler, this is not surprising. 3D surface graphs overlap with the previously investigated VO matrix, regardless of the 10 wt% of the lignocellulose fillers. Figure 3.24 (c) and Supplementary 12 show the FTIR graph of the emitted volatile products for C1F1H1, C3F3H1, and C3F3H2 samples. The highest intensity peak at 2361 cm^{-1} is attributed to CO_2, followed by a peak at 2950 cm^{-1} attributed to stretching vibrations of C-H from small alkane compounds [176,251]. Peaks at 2110 and 2182 cm^{-1} are attributed to the released CO gas. This indicated relatively nontoxic thermal decomposition [176]. Peaks at 669 and 1749 cm^{-1} are attributed to carbonyl-containing volatiles and C-H wagging vibration, respectively [251]. Peaks at 920, 1150, 1215, 1739, and 1365 cm^{-1} indicate vinyl functionality in acrylated polymers, as previously reported [170,176,194,199]. Figure 3.24 (b) provides a more in-depth look at CO_2 and alkane compound emissions. The addition of lignocellulosic filler accelerated thermal decomposition product release by ≈ 10 min at 100 °C, although maximum release has shifted only by 2 min at 20 °C. The absorbance intensity of decomposition products for hybrid samples increases. Consequently, it multiplies the release of CO_2 gas and small alkane compounds.

3.2.2.6. Summary

The present study investigates the benefits of hybrid lignocellulose components' of nanocrystalline cellulose (C), nanofibrillated cellulose (F), hemicellulose (H), and lignin (L) on the performance of vegetable oil-based (VO) UV-curable resins. 10 wt% of hybrid lignocellulose filler consisting of 5 wt% L and 5 wt% C / F / H ratios was introduced into the VO-based matrix, and a total of seventeen different hybrid compositions were prepared. The hybrid lignocellulose components affected morphology, curing degree, thermomechanical properties, thermal stability, and decomposition were studied. In addition, the hybrid composition's ability to mitigate L's UV absorption issues was determined. Scanning electron microscopy measurements revealed that by loading more H and C, low porosity and smooth surface could be achieved. Investigations revealed optimal H content of 38 % for the highest double bond conversion rate of 80 %. Thermomechanical investigations showed three different glass transition temperatures (T_g) and up to a 4.5-fold increase in storage modulus compared to a 5 wt% L single-filler composition. T_{g1} is assigned to the main AESO matrix -9 °C, T_{g2} by the lignocellulose components around 20–35 °C) and T_{g3} of interphase 70–90 °C. Tanδ curves benefit higher glass transition in H and F but do not affect T_{g2} in C. Thermal stability and decomposition studies revealed faster (by 10 min) and stronger CO_2 release at decomposing. Hybrid lignocellulose fillers mitigate L's UV-light absorption properties and provide beneficial synergies.

Until now, lignocellulose fillers for UV-curing resins have been investigated only in single filler compositions; this work sheds light on the novel role of hybrid lignocellulose reinforcement. The proposed hybrid lignocellulosic composite UV-curing resins could be used as various coatings with wood structure-mimic properties; however, more research is still needed for future application.

3.3. Nanocellulose reinforced AESO resins for stereolithography

3.3.1. Nanofibrillated cellulose reinforced AESO resins for stereolithography

Publications:

- **A. Barkane**, M. Jurinovs, O. Starkova, L. Grase, D. F. Schmidt, S. Gaidukovs, Enhancing stiffness, toughness and creep in a 3D printed bio-based photopolymer using ultra-low contents of nanofibrillated cellulose. Journal of Composites Science, 7 (10) (2023) 435, doi:10.3390/jcs7100435
- **A. Barkane**, M. Jurinovs, S. Briede, O, Platnieks, P. Onufrijevs, Z. Zelca, S. Gaidukovs, Biobased resin for sustainable stereolithography: 3D printed vegetable oil acrylate reinforced with ultra-low content of nanocellulose for fossil resin substitution. 3D Printing and Additive Manufacturing, (2022) 1-16, doi:10.1089/3dp.2021.0294

The use of bio-based materials in additive manufacturing (AM) is a promising long-term strategy for advancing the polymer industry toward a circular economy and reducing the environmental impact. In commercial 3D printing formulations, there is still a scarcity of efficient bio-based polymer resins. The present research proposes vegetable oils as bio-based components to formulate the stereolithography (SLA) resin. Application of nanocellulose filler, prepared from agricultural waste, remarkably improves the printed material's performance properties. The strong bonding of nanofibrillated celluloses' (Fs') matrix helps develop a strong interface and produce a polymer nanocomposite with enhanced thermal properties and dynamical mechanical characteristics. The ultra-low F content of 0.1 – 1.0 wt% (0.07–0.71 vol%) was examined in printed samples, with the lowest concentration yielding some of the most promising results. The developed SLA resins showed good printability, and the printing accuracy was not decreased by adding F. At the same time, an increase in the resin viscosity with higher filler loading was observed. Resins maintained high transparency in the 500–700 nm spectral region. The glass transition temperature for the 0.71 vol% composition increased by 28 °C when compared to the non-reinforced composition. The nanocomposite's stiffness has increased 5-fold for the 0.71 vol% composition. The incorporation of ultra-low concentrations of F produced disproportionate enhancements in mechanical performance. Noteworthy, a 2.3-fold increase in strain at the break and a 1.5-fold increase in impact strength were observed with only 0.1 wt% of F, while at 0.5 wt% a 2.7-fold increase in tensile modulus and a 6.2-fold increase in toughness were measured. This is in spite F agglomeration at even the lowest loadings as observed via examination of fracture surfaces and DMA Cole-Cole plot analysis. The thermal stability of printed compositions was retained after cellulose incorporation, and thermal conductivity was increased by 11 %. Strong interfacial interactions were observed between the cellulose and the polymer in the form of hydrogen bonding between hydroxyl and ester groups, which were confirmed by Fourier-transform infrared spectroscopy. The successful development of novel F / bio-based resin composites with enhanced mechanical highlights the potential of these composites to substitute petroleum-based resins in the context of AM resins.

***Sample abbreviations:** *all resin formulations were named in accordance with the filter paper nanofibrillated cellulose (pF) loading (wt%) as follows: 0%, pF0.1%, pF0.5%, and pF1%.*

3.3.1.1. Resin viscosity and printing parameters

The rheological properties, in particular the viscosity of the polymer, play a critical role in the resin composition formulation for SLA. It is suggested that the viscosity of resin should be in the range of 1–10 Pa×s [122,252]. The excellent resin printability has been described as having excellent flowability and spreadability while maintaining good reactivity [253]. The resin viscosity at room temperature was tested by a viscometer with rotation speeds of 1 to 100 RPM, as shown in Figure 3.25 (a). It reveals that effective viscosity absolute values strongly increase in all measured ranges correlating with higher filter paper nanofibrillated cellulose (pF) loading. The substantial alteration of the rheological properties of polymers filled with nanocellulose was discussed by Peterson et al [254]. The viscosity of 0% and pF1% resins at 1 RPM and 100 RPM slightly increases from 0.24 to 1.8 Pa×s and decreases from 38.0 to 3.8 Pa×s, respectively. The viscosities vs. rotation speed dependence indicate the non-Newtonian flow behavior of the resins [255]. Because different polymers have varying sensitivities to shear rate increases, power-law fluid can be used to characterize them [205]. The flow behavior index n is 1.09, 0.89, 0.56, and 0.52 for 0%, pF0.1%, pF0.5%, and pF1%, respectively. Observed $n < 1$ indicates pseudoplastic fluid shear thinning behavior for the pF-loaded resin compositions, related to pF orientation and phase separation [256]. In contrast $n > 1$ and shear thickening (0% resin) could respond to the oil resin behaving as dilatant fluid, which is attributed to overcoming the attraction of macromolecular chains [256]. The n value commonly decreases with increasing pF content [257]. Polymer resins with a low n would likely generate less heat with increasing shear rate through a viscous dissipation mechanism [205]. Thus, enhanced pseudoplastic behavior of the cellulose-loaded resins benefits SLA manufacturing.

In the beginning, the SLA printing process was optimized to receive the permanent non-defect printing quality of the developed pF reinforced resins. The appropriate irradiation and printing times for every resin were analyzed, considering the visual appearance of the printed part. Figure 3.25 (b) shows the printed owl prototypes using the neat polymer resin and pF loaded resin. The time step was 1 s, starting with the 2.5 s printing time previously determined as the optimal curing time for 0% resin under the UV lamp [20]. The first layer was printed at 35 s for all resins to ensure proper cured polymer material adhesion to the printing bed [20]. The curing time per layer was 7.5, and 15 s for 0% and pF loaded resin materials, respectively.

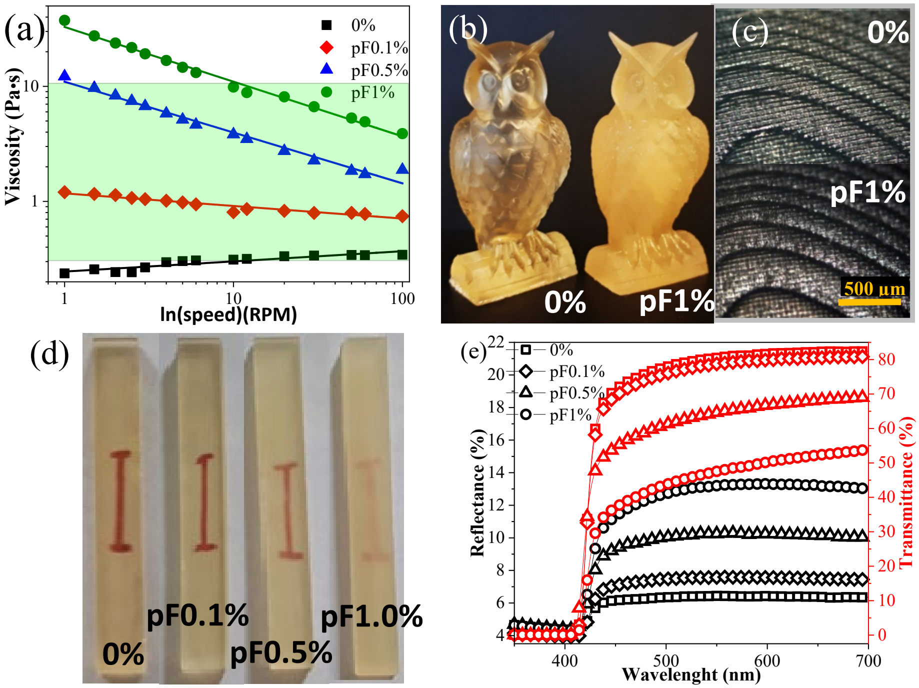

Figure 3.25. Resin viscosity curves (a), 3D printed owls with 0% and pF1% resins (b), owl's optical microscope images at 5× magnification (c), printed bars images (d), UV-Vis reflectance and transmittance spectra of printed resins (e).

The high printing accuracy for the owl model was obtained for 0%–pF1% resins, as shown in Figure 3.25 (b). The closer inspection of the printed objects at 5× magnification (Figure 3.25 (c)) by optical microscope revealed the excellent resin printing resolution. As shown in Figure 3.25 (d), the colors and the translucence of the printed objects have been strongly affected by pF loading. This allows UV-Vis spectroscopy to quantitatively measure the transparency and reflectance of the printed resin materials.

The samples were placed on a sheet of paper (Figure 3.25 (d)) on top of a red line for transparency observations, and they provided a good correlation with the UV-Vis transmittance spectroscopy measurements (Figure 3.25 (e) - red curves). Both show that the increase in pF loading leads to a decrease in transparency. Transmittance is decreased due to the scattering of visible light by pF particles, which can be explained in terms of the Rayleigh approximation and Mie theory [258].

Figure 3.25 (e) (black curves) reflectance spectra show minimal reflectance below the visible light, barely reaching 5 %. The reflectance increases with pF loading, thus yielding an opposing trend to the transmittance. Absolute values at 500 nm transmittance / reflectance for 0%, pF0.1%, pF0.5%, and pF1% samples are 78 % / 6 %, 76 % / 8 %, 61 % / 10 %, and 44 % / 13 %, respectively. The values of scattered visible light are 16 %, 16 %, 29 %, and 43 % for 0%, pF0.1%, pF0.5%, and pF1%, respectively. The increase in reflectance for the visible part of spectra corresponding with pF loading is explained by the backscattering of the incident light on pF particles in the resin [258]. As shown in Figure 3.26, there was a relatively small change in double bond conversion (DBC%). Therefore, the authors attributed the changes in UV-Vis spectra mainly to the introduction of pF filler.

3.3.1.2. Structure analysis

Density is one of the main intrinsic characteristics of composite materials; it identifies the homogeneity of the filler mixing, dispersion quality, and structural defects [210]. Figure 3.26 (a) represents the printed sample experimental density ρ, calculated theoretical density ρ_t, and the apparent polymer density ρ^a_{poly} calculated by equations (2.7) and (2.8) [178].

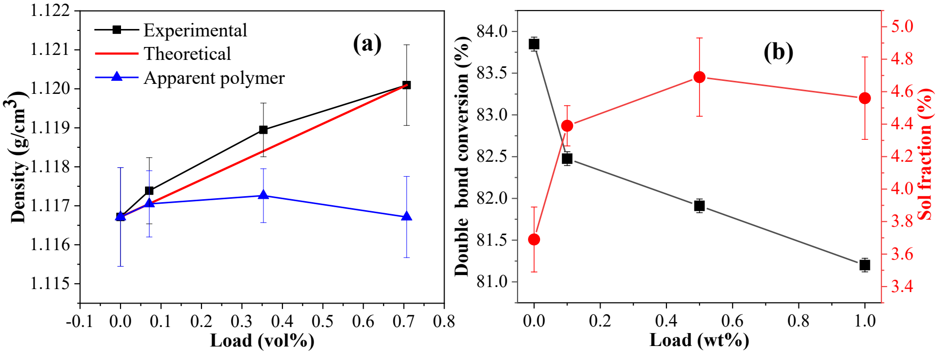

Figure 3.26. Experimental, apparent, and theoretical polymer densities (a) and double bond conversion rate and sol-fraction (b) for prepared, printed resins.

The composite theoretical density ρ_t was calculated using the rule of mixtures [178]. The increase in composite density value was expected because cellulose has a higher density than the polymer matrix. Figure 3.26 (a) shows that the composite experimental density ρ is within the margin of error compared to ρ_t. The higher ρ values are associated with denser stackings (structural packing) and fewer voids in the printed samples. DBC% (Figure 3.26 (b)) is calculated from FTIR measurement using a ratio from peak intensities ($C{=}C/COO^-$ at 810 and 1733 cm^{-1}, respectively) [20]. There is a slight decrease in DBC% values with higher pF loading in the resin, while the sol-fraction increases. These simultaneous changes in DBC% and sol-fraction absolute values indicate a minimal decrease in crosslinking degree. It has been reported that low pF content can benefit the scattering of UV-light, in which pF acts as a scattering particle, resulting in a more uniform distribution of UV-light [92]. The increase in viscosity limits the movement and distribution of free radicals; hence, it can lower the DBC% [166]. In our previous study, we demonstrated that high F loadings (up to 30 wt%) significantly increase viscosity and decrease DBC% (down to 30 %) [126]. Thus, the low nanofiller content, homogenization, and viscosity only slightly influenced the crosslinking reactions between polymer matrix forming components.

Table 3.8

Molecular Weight Between Crosslinks and Crosslinking Density

content, wt%	content, vol%	M_c, g/mol	N, 10^3 mol/m^3
0	0.000	1024	1.1
0.1	0.070	472	2.4
0.5	0.035	219	5.2
1	0.071	196	5.8

Table 3.8 summarizes the crosslinking density (N) and the molecular weight between crosslinks (M_c), calculated by the Flory–Rehner equation as the authors reported before [202]. Correspondingly, the mesh crosslinking density of the resins pF0.1%, pF0.5%, and pF1% has significantly increased by almost 2.4-fold, 5-fold, and 6-fold. These values have been influenced considerably by matrix-filler interaction. As values were calculated from the DMA data, hindered molecular mobility for polymer chains adsorbed to the surface of cellulose fibrils can be considered [259,260]. In addition, some authors have used molecular dynamics simulations to characterize interphase formation for thermoset polymer nanocomposites [261,262]. According to simulations, the mobilities of the atoms in the interphase regions are lower if strong interfacial bonding is provided, like hydrogen bonding.

3.3.1.3. Morphology

The morphology of the printed specimens was investigated by optical microscopy of cross-sections and scanning electron microscopy of freeze-fracture surfaces of 3D printed parts (Figure 3.27). Excellent printing accuracy (as judged by sample surface examination) was observed for all resins. However, surface quality decreased with increasing pF content (see cross sections in Figure 3.27 (a) with a 100 μm scale bar) when the printing accuracy was maintained using a constant layer thickness of 50 μm; this may be explained by pF agglomeration. Smooth surfaces are observed for the 0% sample, while with increasing pF content, fracture surfaces become rougher. In 10× optical microscopy images, black cracks are seen. According to the crack distribution, fibers agglomerate when the pF content exceeds 0.1 wt%, and overall homogeneity decreases as a consequence. Figure 3.27 (b) shows the SEM microscopy images; while similar fracture patterns are observed in all cases, changes in surface roughness are observed. The pF0.1% composite sample's fracture surface, while similar to that of the 0% sample, displays sharper fracture edges. Further increasing the pF content introduces a combination of smooth regions and sharp-edged fracture paths, consistent with increasing heterogeneity and indicative of significant changes in morphology and fracture mechanism.

Figure 3.27 (c) depicts the modified fracture mechanism with crack propagation in neat polymer matrices and reinforced composites for flexural and impact test specimens. When pF reinforcement is encountered crack deflection occurs [263,264]. This is confirmed by the visible cracks on the side of the rectangular samples after flexural testing as shown in the optical microscopy image of the pF1% composite sample (Figure 3.27 (d)). Again, crack deflection is observed, as well as bifurcation in some instances. No such cracks were observed in the 0% and pF0.1% samples. Nonetheless, black dashed lines (aligned with printing layers) show that these cracks develop perpendicular to the layers, not parallel to them, confirming a high level of interlayer adhesion.

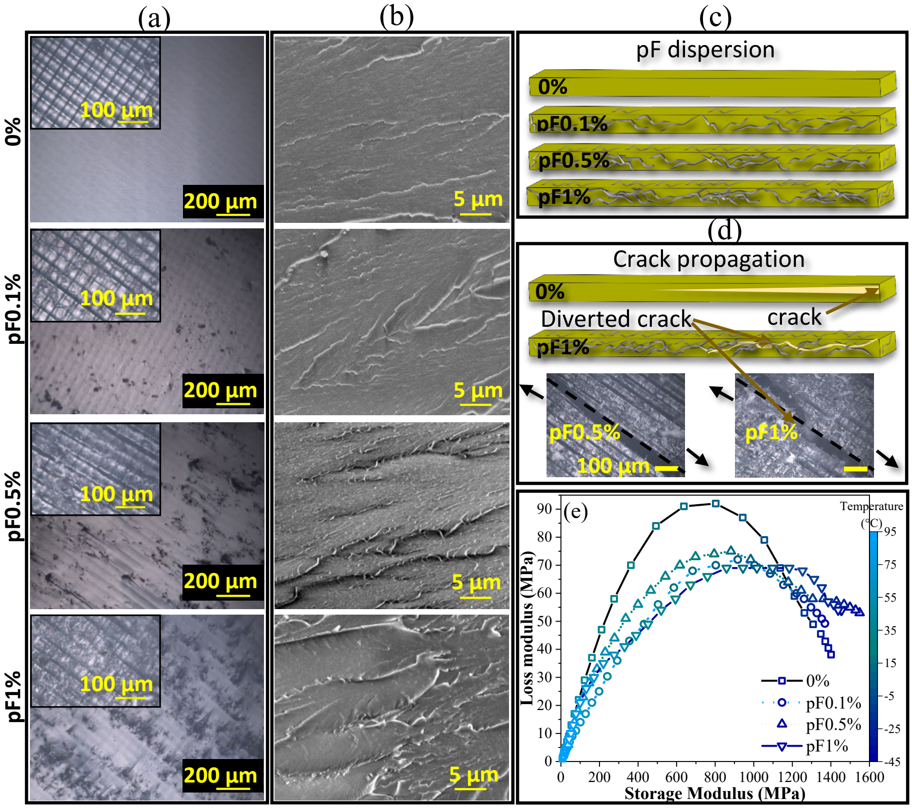

Figure 3.27. Morphology: optical microscope images of cross-sections (insets, 20× magnification) and freeze-fracture surfaces (10× magnification) (a), SEM micrographs of freeze-fracture surfaces (2 500× magnification) (b), schematic of possible pF distribution (c), illustrations and optical microscope images of crack propagation following tensile testing (20× magnification, tensile test direction indicated with the arrows) (d), and DMA Cole-Cole plots (e) of 3D printed neat (0%) and pF reinforced composite specimens.

The image shows that the most homogeneous specimen is the neat resin, followed by pF0.1%. In contrast, heterogeneity can be seen in the pF0.5% and pF1% samples, where cracks have separated smooth and rough black regions. F is known for its tendency to agglomerate [126,134], and increased loadings lead to a higher probability of agglomeration. Higher pF loads also increase the resulting viscosity of the composite resins [93], limiting the effectiveness of further homogenization. This effect is more pronounced if there are limitations in compatibility between the particles and the polymer matrix [168]. As it is known that AESO exhibits hydrophobic properties [263], it is not surprising that the resulting heterogeneity and surface roughness increases upon addition of increasing quantities of hydrophilic pF. This heterogeneity with increasing pF content is observed in Figure 3.27 (c), where nanocellulose distribution in the polymer matrix is shown.

The DMA Cole-Cole plot in Figure 3.27 (e) also confirms increasing heterogeneity with increased pF content, in line with previous studies involving the use of such plots to assess structural changes in crosslinked polymer composites [239,242,243]. Here, the DMA data appears in the form of Cole-Cole plots instead, where a semi-arch shape indicates a homogeneous polymer system while deviations from such a shape indicate the presence of heterogeneities such as phase separation and filler aggregation [239,242,244]. The Cole-Cole plots for the 0% and pF0.1% samples in Figure 3.27 (e) possess semi-arch shapes, while at lower temperatures the same plots for the pF0.5% and pF1% specimens show deviations from a semi-arch shape. This confirms optical microscopy and SEM results indicating that, when the pF content exceeds percolation threshold of ~ 0.1 wt%, pF tends to agglomerate in the resin, thereby creating a heterogeneous system.

3.3.1.4. Mechanical properties

The mechanical properties data show the largest increases in tensile and flexural stress, modulus, and flexural strain at 0.1 wt% pF; higher pF concentrations result in decreases (Figure 3.26). This further testifies to the structural heterogeneity of the pF0.5% and pF1% formulations. Particularly noteworthy here is the extent to which the mechanical properties were enhanced at the lowest pF concentration. The addition of 0.1 wt% pF resulted in 2.3-fold and 2.4-fold increases in tensile and flexural strength (Figure 3.26 (a) and (c), respectively). Tensile and flexural strains also show increases of 1.7-fold and 1.2-fold, as well as a 1.6-fold and 5 % increase in tensile and flexural moduli (Figure 3.26 (b) and (d), respectively). These results demonstrate pF's exceptional potential as a reinforcing filler in bio-based UV-curable 3D printing resins.

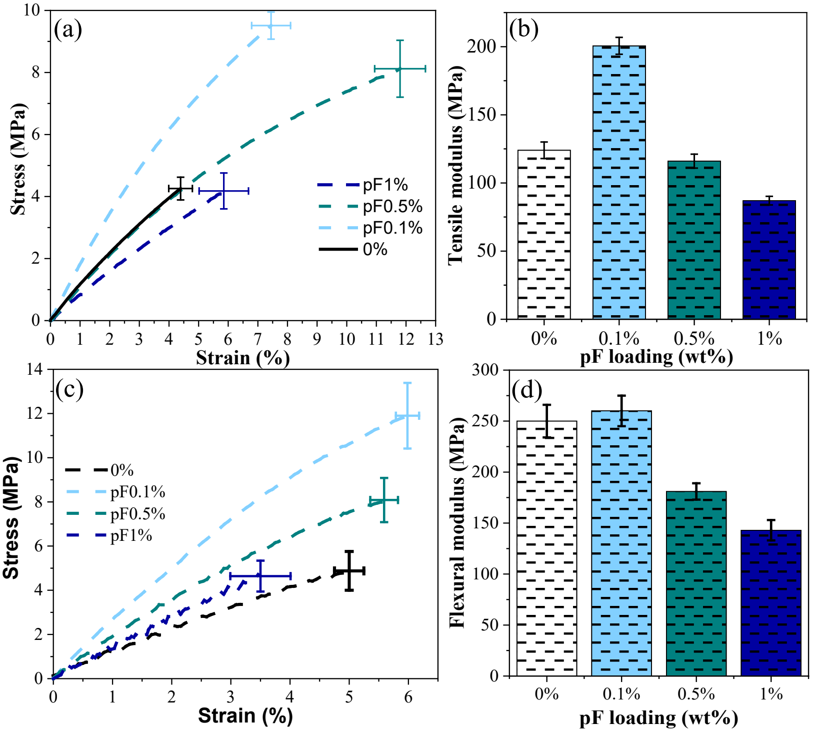

Figure 3.28. Tensile test results for neat and pF reinforced formulations: stress vs. strain (a), tensile modulus (b); flexural tests results: stress vs. strain (c), flexural modulus (d).

The pF0.5% composite also showed significant enhancements in tensile and flexural strength and strain vs. the neat material. In fact, for the tension test, the largest increase in strain at break (2.7-fold) was achieved at the 0.5 wt% pF content (vs. 0.1 wt% pF in the case of flexural testing). The increase in strain at break can be attributed to the friction energy dissipation during deformation between flexible Fs and a rigid polymer matrix [265]. On the other hand, the decrease in tensile strength when moving from 0.1 to 0.5 wt% pF is attributed to the system's increased heterogeneity, as revealed by the morphological analyses presented in Figure 3.27. Agglomeration of the hydrophilic pF and the weak adhesion with the polymer matrix may reduce the overall tensile strength [265,266]. The combination of these features leads to internal stress concentrations that result in points of failure in the material's structure. At the same time, the tensile strain at break for pF0.5% is 1.5-fold higher than for pF0.1% (Figure 3.28 (a)). This could be due to the fiber entanglements and spatial network developed by the long and flexible pF (known to increase the strain of polymer composites [267]). However, flexural strain at break in the pF0.5% composite shows a more limited (1.12-fold) increase vs. the neat resin, which is slightly lower than that observed for the pF0.1% composite. An increase in pF content to 1 wt% resulted in a decline in composite mechanical performance. Tensile and flexural strengths are similar, while modulus is reduced by 30 % and 42 %, compared to the neat resin, respectively. However, the tensile strain at the break still shows a 1.3-fold increase (Figure 3.28 (a)).

Material tensile toughness can be obtained by simply integrating the area below the stress-strain curve before fracture in tensile testing [268]. Figure 3.29 shows that introducing pF reinforcement increases the sample's ability to absorb energy per unit volume prior to fracture. This is evident from the toughness values, where the largest increase vs. the neat resin is observed at 0.5 wt% pF (6.2-fold). With 0.1 wt% pF, in contrast, a 3.1-fold increase is observed, and at 1 wt% pF the increase is only 1.4-fold, that is related to extreme heterogeneity of the sample.

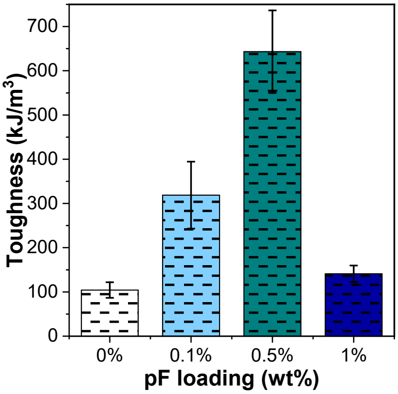

Figure 3.29. Toughness of neat and pF-reinforced samples.

3.3.1.5. Thermomechanical analysis

Temperature changes significantly influence the performance of studied 3D printed samples, as evidenced by the DMA analysis (Figure 3.30). They were indicated by the glass transition, with a start and end around 0 °C and 75 °C for 0% sample. The glass transition maximum for the 0% sample registers relatively close to the room temperature at 46 °C. Thermoset resin glass transition marks the transition from a rigid amorphous structure to a softer and more flexible amorphous structure with increased energy (heat movement). Reflected in storage modulus values (Figure 3.30 (a)), where 0% sample has 2.6-fold and 13.5-fold decrease at 30 °C and 50 °C compared to 0 °C. The introduction of the pF filler strongly influences the glass transition temperature (T_g), which is increased up to 82 °C (28 to 36 °C higher than 0%) see Figure 3.30 (b). An increase of the T_g indicates hindered mobility of the macromolecule due to the strong intermolecular bonding between filler and polymer [269]. This can also be explained as a decreased elastic response from cellulose surface adsorbed polymer chains, whose molecular thermal motions are restricted [270]. As transitions into a rubbery state occur, splitting of storage modulus curves (at 0 °C) appear. Split indicates that pF filler starts to work as a reinforcement. A sustained increase of the storage modulus absolute values in the rubbery state can indicate good filler distribution [271]. In this regard, all three compositions, pF0.1%, pF0.5%, and pF1%, achieved excellent reinforcement in the rubbery state. Storage modulus also distinguishes that the higher filler loading (pF1% sample) has a limited effect on the value increase. The optimum filler volume content from the storage modulus values is between 0.07 and 0.71 vol%. Crosslinking density (Table 3.8) increase is observed with higher pF loadings. However, this is achieved with increased intermolecular interface bonding between the filler and the matrix. The temperature rise reduces intermolecular bonding, but it cannot affect covalent bonding; thus, a critical threshold is observed.

The C* factor as a function of volume content is presented in Figure 3.30 (c). It is used to determine the reinforcement of composite materials. Generally, lower values of the C* factor indicate better reinforcement. At the same time, neat resin represents a value of 1 [272]. According to the literature, equations (2.12) and (2.13) were used for calculations [126]. The parameter C* was calculated from glassy (E_g') and viscoelastic (E_v') storage modulus values measured at -45 °C and 95 °C, correspondingly. The lowest values obtained are around 0.2 and are achieved by volume content 0.35 and 0.71 vol% samples (samples pF0.5% and pF1%, respectively), showing about 2-fold improvement compared to 0.07 vol% (sample pF0.1%). While the C* factor favors higher loadings, the reinforcement efficiency factor (*r*) does the opposite. The *r* value calculation considers the volume fraction of the filler. Theoretical percolation threshold (ν_{rc}) was calculated using aspect ratio of the particles (assuming used pF particles are rigid and homogeneous) [237]. The ν_{rc} for used pF is 0.07 vol% (calculated using equation (2.12)) which coincides with a pF0.1% sample. But in case of experimental results, it can be assumed that theoretical value will be lower than practical due to effects like clustering and agglomeration. Loading composites above the percolation threshold leads to greater stiffening, but interfacial adhesion suffers; thus, values like tensile strength need to be measured for in-depth analysis [273]. The reinforcement efficiency factor *r* was calculated from equation (2.13). Figure 3.30 (d) shows pF0.1% sample achieved *r* value 16.1, 1.5-fold and 2.5-fold higher than pF0.5% and pF1%, respectively. Thus, the C* factor shows that maximum stress transfer to reinforcement is achieved by the pF1% sample, while the strongest interaction between filler and polymer is observed for the pF0.1% sample (*r* value) [274]. The reinforcement dependence on the temperature was plotted in Figure 3.30 (e) using composite/polymer storage modulus ratio (E'_{comp}/E'_{pol}), where polymer values represent the neatly printed sample (0%). pF starts to reinforce the polymer matrix in the glass transition region. The lowest pF content sample, pF0.1%, formed sustained reinforcement from 30 °C, while higher contents from -20 °C. The reinforcement is pronounced after the transition into the rubbery state (around 50 °C), where higher loadings achieved about 2-fold improvement compared to the pF0.1% sample. Figure 3.30 (e) shows that the difference between pF0.5% and pF1% samples is relatively small.

It is considered that stiffness enhancement visible as increased storage modulus could be related to filler alignment, which could be achieved with liquid resin shear flow processing. The immersion of the printing bed in the resin bath can create pF particle orientation in a 2D plane, and selecting the correct printing plane significantly influences mechanical properties [275]. As discussed by Yunus et al. [276], particle orientation in one specific direction enhances the mechanical properties, and an increase of 28 % in tensile strength was gained with a 5 wt% loading, where orientation was achieved with the strong shear flow. According to reported data [277], in the absence of an induced orientation (shear, ultrasonic, magnetic, electric field, etc.), a perfect unidirectional alignment cannot be achieved. While SLA printer has a relatively small printing platform that does not provide remarkable resin flow, the obtained orientation effect of pF fibers could be negligible. The impact of pF filler orientation on the mechanical properties of the printed SLA resins needs more detailed investigations.

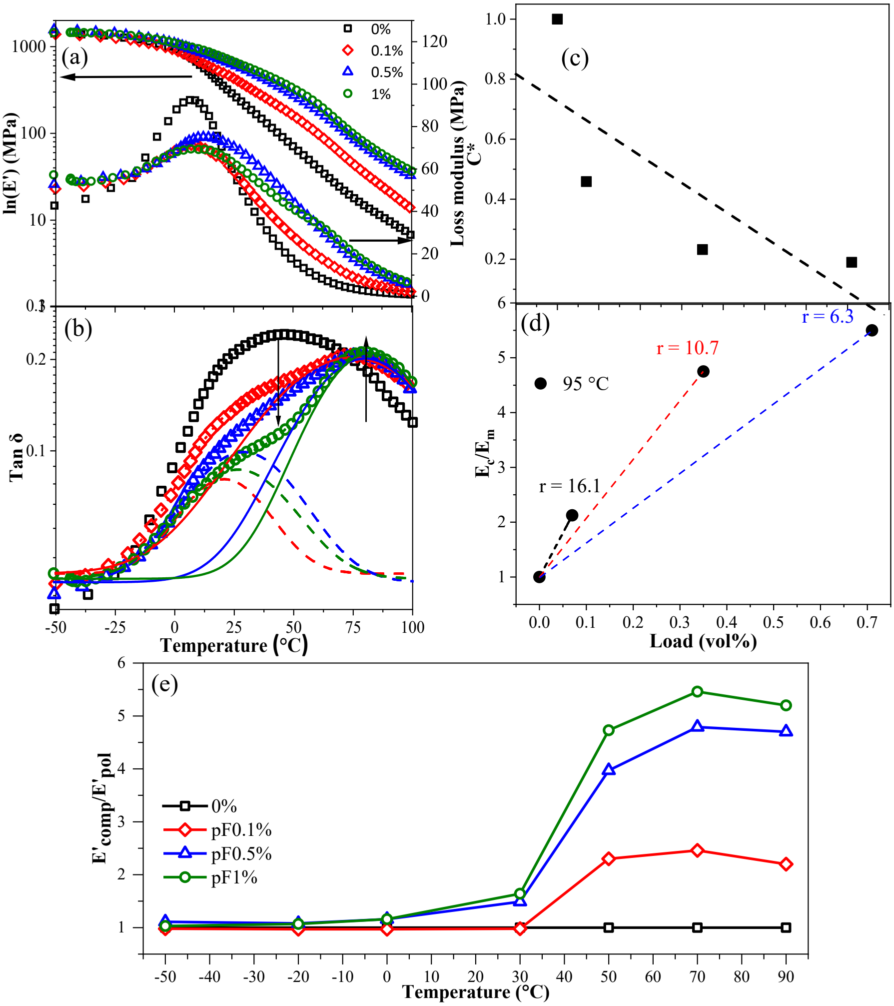

Figure 3.30. Storage and loss modulus (a) and tanδ (b) for the SLA printed resins. The C* factor (c) and the *r* factor as a function of volume content (d) for the SLA printed samples, storage modulus E'_{comp}/E'_{pol} ratio dependence on temperature (e).

Loss modulus curves show significant change with the introduction of the pF filler. Decreased values of the loss peak are associated with energy transfer and dissipation through the pF reinforcement [209]. The loss peak also shifts to higher temperatures, while increased loss modulus values where rubbery state registered for printed nanocomposites. Loss modulus shows particle slippage and interactions during structural rearrangements [236]. Thus, the increased values in the rubbery state of the loss modulus represent stronger interfacial interactions between the pF and polymer chains. This can be explained as the restricted molecular movements of the polymer matrix. This shift is visible in the splitting of the T_g peak, which moves to higher temperatures. Therefore, deconvolution was applied to the glass transition peaks (Figure 3.30 (b)). The first smaller peak matches more with the T_g of the 0% sample, and decreased dampening peak values were observed for all filled compositions, indicating a more rigid structure response [278]. While a new second peak is only observed for samples with the pF reinforcement. The first peak shows a polymer phase in the composite that acts similarly to the 0% sample. But the second peak at higher temperatures has a significantly higher intensity, indicating the formation of enhanced interphase with pF addition [279]. This structure (interphase) formation dominates the nanocomposites' design and has similar dampening peak values to the 0% resin. This is more pronounced with an increase in pF loading.

3.3.1.6. Thermal analysis

The printed resin's thermal stability has been reported in a previous paper on UV-curable vegetable oil resin thermal stability [176]. In summary, the second peak (circa 460 °C in Figure 3.31 (a)) is due to added comonomers. Cellulose fillers commonly lower the composite's thermal stability than the polymer matrix [225]. In Figure 3.31 (a), pF shows significantly lower thermal stability than the printed samples, with degradation maximums at 340 °C. However, pF loading up to 1 wt% does not cause a significant thermal stability decreases. Higher pF loading (5 wt% and more), as shown by previous investigations [126], leads to a three-step thermal degradation. An additional step observable around 340 °C is explained by an unprotected pF close to the composite surface. Although there is no significant effect on thermal stability, other thermal properties in Figure 3.31 shows some notable changes.

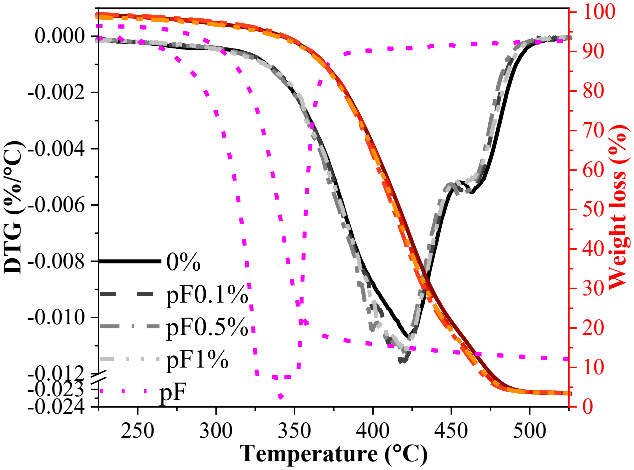

Figure 3.31. Thermal stability of prepared pF filler, 0% and pF0.1%, pF0.5% and pF1% samples.

3.3.1.7. pF-polymer interaction

Resin, pF filler, and printed samples were characterized with FTIR spectroscopy (Figure 3.32). Figure 3.32 (a) shows that some absorption peaks overlap between the matrix and pF filler. The characteristic peaks attributed to structural groups are summarized in Supplementary 4. Given the low filler content, there are no new peaks (Figure 3.32 (b)) that may be attributed to pF in printed samples.

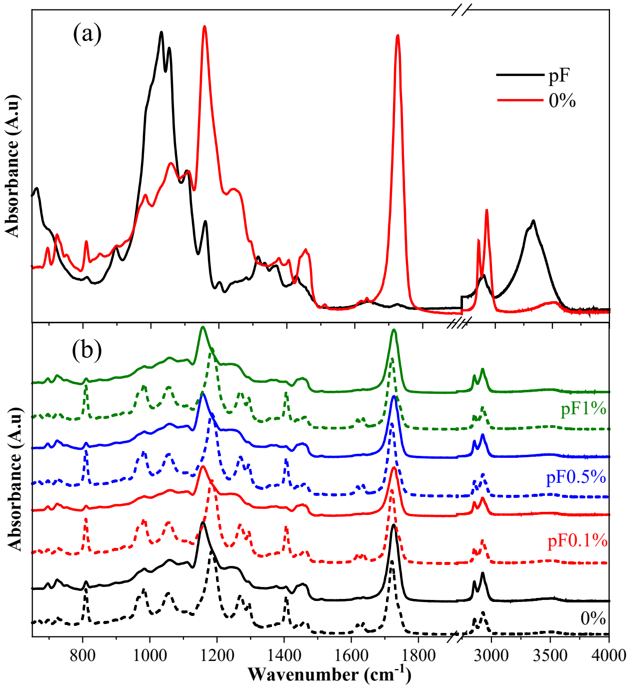

Figure 3.32. FTIR spectra of 0% printed sample and pF filler (a), spectra of resin (R) and printed samples (P) 0%, pF0.1%, pF0.5% and pF1% samples (b). Dashed lines – resin, solid lines –printed samples.

Peaks at 810, 981, 1409, and 1629 cm^{-1} were attributed to the vinyl bonds (C=C) in the acrylic groups [206] (Figure 3.32 (b)), which decrease in intensity or disappear from FTIR spectra after printing. The decrease of the vinyl group absorption at 810 cm^{-1} after printing suggests that all compositions achieved excellent polymerization. The pF in a polymer matrix creates its intermolecular bonding through hydrogen bonds, obstructing vinyl group conversion and lowering light transmission [168]. This is confirmed by DBC% calculation using a ratio from peak intensities ($C=C/COO^-$) [20] and Flory–Rehner equation, used for Figure 3.26 (b) and Table 3.8.

Intermolecular bonding between the filler and matrix has been proposed in other sections of the result analysis. These interactions for FTIR spectra are usually observed as peak shifts or changes in intensity. Liu et al. used an equation derived from Lambert-Beer's law to characterize the interaction between microcrystalline cellulose and AESO [192]. Using this equation (2.2). This equation was implemented to calculate the theoretical spectra for the C=O peak, as seen in Figure 3.33. Theoretical spectra would be based on the acrylate matrix because there is no pF absorption at 1727 cm^{-1}. However, the C=O peak intensity decreases significantly with the introduction of the pF filler. Thus, the significant decrease in peak intensity can identify the formation of strong hydrogen bonding between the pF and matrix. Similar observations are reported in the literature [192,194]. The pF0.1% printed sample shows the strongest pF interaction with the matrix. These findings are supported by data on the previously discussed reinforcement efficiency factor and thermal conductivity.

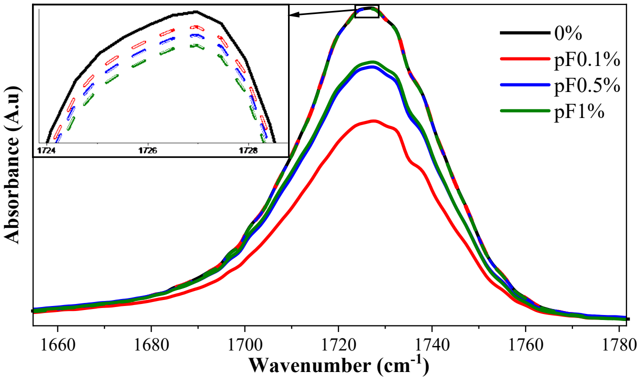

Figure 3.33. FTIR spectra of (C=O) at 1727 cm^{-1} for printed samples. Dashed lines – theoretical spectra obtained with Lambert-Beer's equation, solid lines – experimental spectra.

3.3.1.8. Summary

The present study demonstrates the viability of filter paper nanofibrillated cellulose (pF) as a reinforcing filler for UV-curable additive manufacturing (AM) of bio-based composite resins. Moreover, the importance of achieving a balance between agglomeration and filler network formation by utilizing filler loadings close to the percolation threshold is broadly discussed. pF volume concentration of 0.07, 0.35 and 0.71 vol% (0.1, 0.5, and 1 wt%, respectively) were introduced into the 0% resin. The printability of prepared composite resins and the structural, thermal, and thermomechanical property changes in response to the pF and polymer matrix interaction was investigated. Viscosity measurements of the prepared resins showed high viscosities for the pF0.5% and pF1% resins. Nevertheless, photos of printed objects complemented with optical microscopy images showed high printing quality. Even more so, pF content did not affect printing accuracy at all. UV-Vis measurements showed decreased transmittance (by 34 %) and increased light scattering (by 27 %) with an increase in the pF content. Structural analysis showed a slight increase in the printed sample's density and a minimal decrease in the curing efficiency (DBC% decreased by 3 % and sol-fraction increased by 1 %). The pF0.1% composite demonstrated the most significant improvements in overall mechanical performance, including enhanced tensile modulus (1.6-fold), strength (2.3-fold and 2.4-fold) and break strain (1.7-fold and 1.2-fold) in both tension and flexure, increased toughness (3-fold). Thermomechanical analysis shows a 34 °C increase in the glass transition temperature, indicating pF interacts with the polymer matrix. The splitting of the tanδ peak proved that the introduced pF acts as a reinforcement and leads to an excellent reinforcement in the rubbery state for all reinforced samples. C* factor (maximum stress transfer) showed a

2-fold increase of reinforcement for the pF0.5% and pF1% samples, but *r* (strongest pF interaction with matrix) showed a 1.5-fold and 2.5-fold increase for the pF0.1% in comparison to the pF0.5% and pF1%. There was no effect on thermal stability observed with the introduction of the pF reinforcement. Fourier-transform infrared spectroscopy showed no covalent bonding between the pF and polymer matrix. At the same time, applying Lambert-Beer's law allowed identifying stronger filler-matrix interaction for the pF0.1% sample. Stronger filler-filler interaction for the pF0.5% and pF1% samples (when an effective load was reached) reduces filler-matrix interaction.

All in all, this study shows that, by maintaining an ultra-low pF content (near the estimated percolation threshold), pF agglomeration can be minimized, and significant improvements in mechanical performance of the bio-based UV-curable composite AM resin can be realized as a result. This work indicates that carefully designed pF composite resins for vat photopolymerization AM technologies represent promising path for reaching sustainable alternatives to commercial petroleum-based resins. Further research should concentrate on improving the interphase between the hydrophilic filler and the hydrophobic polymer matrix to increase the reinforcement benefit.

3.4. Functionalized nanocellulose-reinforced AESO resins for stereolithography

3.4.1. Nanocellulose surface functionalisation for improved interface between reinforcement and AESO resin for stereolithography

Publication:

- M. Jurinovs, **A. Barkane**, O, Platnieks, S. Beluns, L. Grase, R. Dieden, M. Strapolim D. F. Schmidt, S. Gaidukovs, Vat photopolymerization of nanocellulose-reinforced vegetable oil-based resins: synergy in morphology and functionalization. ACS Applied Polymer Materials, 5 (4) (2023), 3104, doi:10.1021/acssapm.3c00245

With the advancement of additive manufacturing (AM) and the mass adoption of 3D printing technology, it is essential to shift focus to environmentally and economically sustainable materials. As the utilization of renewable feedstocks is quite limited in this context, the utilization of more bio-based raw materials in the ongoing development of AM represents an essential means of achieving this shift. In this work, vat photopolymerization 3D printing has been used to process vegetable oil-based (VO) resins with an ultra-low concentration of 0.07 vol% of nanofibrillated cellulose (F) and nanocrystalline cellulose (C). The developed nanocellulose containing bio-based vat photopolymerization resin shows excellent shelf stability, enabling high-resolution printing. Compatibilization of the nanocellulose with the polymer matrix was achieved through the introduction of isocyanate or acrylate groups via reactions of acryloyl chloride (AC) and hexamethylene diisocyanate (HMDI) with cellulose surface hydroxyls. Surface functionalization results in ~20–30 % increases in interfacial adhesion and stress transfer, yielding significant improvements in mechanical performance (4× higher toughness, 2.4× higher tensile strength, and 2× higher tensile strain) in 3D printed specimens. Fourier-transformation infrared (FTIR) spectroscopy study of the chemical structure of these materials as well. Tensile performance comparison with literature data on VO-based natural fiber-reinforced resins showed that this work brought bio-based resins one step closer to competing with petroleum-based resins. The prepared VO/nanocellulose resins are promising candidates for high-performance bio-based resins derived from completely renewable feedstocks.

**Sample abbreviations: filter paper nanofibrillated cellulose – pF; vegetable oil (VO) formulation – VO/pF; acrylated pF – pFA; VO formulation – VO/pFA; filter paper nanocrystalline cellulose – pC; VO formulation − VO/pC; and isocyanate-functionalized pC – pCI; VO formulation − VO/pCI.*

3.4.1.1. Characterization of nanocellulose fillers

Fourier transform infrared spectroscopy (FTIR) spectroscopy was used to investigate the chemical functionalization of the nanocellulose. Cellulose spectra before and after functionalization are shown in Figure 3.34. FTIR spectra in Figure 3.34 (a) shows the neat pC and functionalized pCI. The grafting of diisocyanate onto the pC surface occurs in two stages

[280]. In the first step, isocyanate groups react with hydroxyl groups on the surface of pC. As a result, absorbance peaks appear, assigned to coupled NH and CN bending vibrations at 1157 cm^{-1}, NH stretching and CN bending vibrations at 1530 cm^{-1}, and hydrogen bonded CO groups in the urethane at 1694 cm^{-1} [281]. When an excess HMDI is added, the urethane groups react with free isocyanate groups. This reaction forms a crosslinked polymer layer on the pC surface, as evidenced by the intense absorption maximum at 1651 cm^{-1} assigned to the carbonyl on the urea group [282]. The NCO peak also confirms the introduction of diisocyanate at 2264 cm^{-1}, as well as characteristic peaks at 1440 cm^{-1}, 2857, and 2933 assigned to CH bending vibrations and symmetric and antisymmetric CH_2 vibrations, respectively [280,281,283]. The peak at 2890 cm^{-1}, which overlaps with peaks at 2857 and 2933 cm^{-1}, is related to the CH stretching in the cellulose molecule [283]. The additional peaks at 1256, 1618, and 1580 cm^{-1} are introduced from amide, amide I, and amide II vibrations, respectively. Furthermore, at 3367 cm^{-1}, the characteristic NH stretching vibration peak can be seen, which can overlap with cellulose OH stretching vibration but appears as a sharper peak [284]. Figure 3.34 (b) represents the FTIR spectra of pF and pFA fillers. Before the functionalization, a broad absorption band at 3340 cm^{-1} corresponds to the stretching vibrations of OH groups in pF molecules. The OH groups in cellulose are replaced with acrylate groups that attach via an ester group. Consequently, the intensity of the OH bond peak is reduced, and additional sharp absorption peaks at 810, 982, 1184, 1407, 1631, and 1722 cm^{-1} have appeared. The peaks at 810, 982, 1407, and 1631 cm^{-1} are attributed to the stretching vibrations of vinyl bonds in acrylic groups; meanwhile, the peaks at 1184 and 1722 cm^{-1} belong to the stretching vibrations of the ester's carbonyl groups [59,285].

Alongside FTIR investigations, water contact angles (θ) of the nanocellulose were measured to assess the impact of functionalization on the hydrophobicity of the fillers. Suspensions of nanocellulose in acetone were applied dropwise on glass substrates and dried (3 layers) to produce homogeneous coatings for measurements. The neat nanocellulose was hydrophilic with the equilibrium $\theta = 0°$. The functionalized nanocelluloses gave θ of 69° and 63° for pCI and pFA, respectively. It was posited that this increase in hydrophobicity might help to further improve filler dispersion in the vegetable oil-based resin due to improved wetting. As it is known that the incorporation of cellulose filler in the polymer matrix can significantly affect the composites' overall thermal stability [169], a thermogravimetric analysis (TGA) of nanocellulose was performed (Figure 3.35). The TGA data shows that the thermal degradation process occurs in two stages for neat nanocellulose and three for functionalized nanocellulose. Initial weight loss is related to evaporation of absorbed water, which begins at around 80 °C. A reduction in water content is evident for functionalized nanocellulose. The functionalization process involves substituting OH groups in the cellulose molecules, which leads to decreased hydrophilicity.

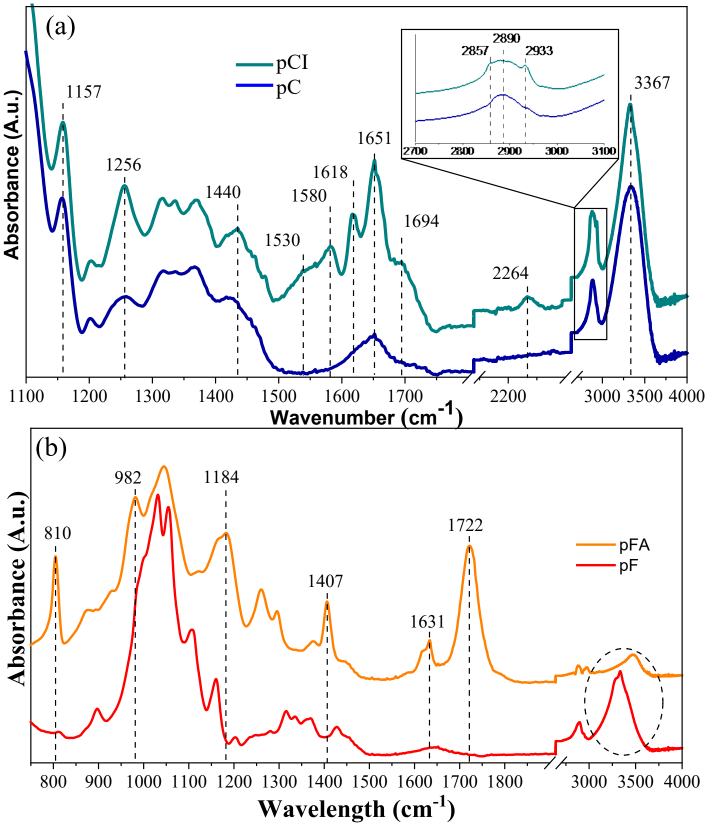

Figure 3.34. FTIR spectra of neat pC and isocyanate functionalized pC (pCI) (a) and neat pF and acrylated pFA (b).

Thermal degradation of the pF and pC begins at 230 °C and 210 °C, respectively. The rapid degradation of pFA starts at a significantly lower temperature of 200 °C. The shift to lower values for the pFA is explained by David et al. by the high instability of ester bonds [286]. In the derivative curve, pFA exhibits a broad degradation range from 360 °C to 520 °C. This may be due to self-crosslinking reactions which hinder molecular movement and prolong the degradation process [242], which could also help to explain the 9 % greater residue observed for pFA at 750 °C as compared to neat pF. The thermal degradation of the pCI started at 201 °C, a slight decrease compared to pC, but the temperature at which the degradation rate is a maximum is increased by 16 °C. The thermal stability of pCI is affected by the inclusion of HMDI-derived segments [287].

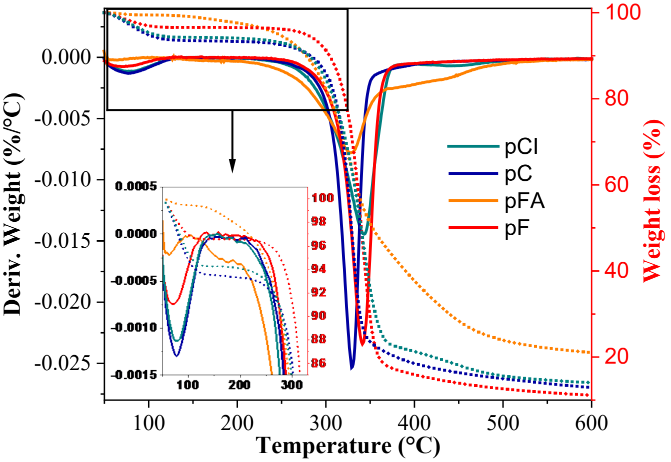

Figure 3.35. Weight loss (dotted lines) and first derivative (solid lines) curves of the filter paper nanofibrillated cellulose (pF), acrylated pF (pFA), filter paper nanocrystalline cellulose (pC), and isocyanate functionalized pC (pCI) fillers (in nitrogen).

3.4.1.2. Vat photopolymerization printability of bio-based resins.

The ability to achieve high print resolutions and reproduce fine details is commonly required in order to validate formulated resins. The SL1 standard calibration check models Petrin tower (Figure 3.36 (a) and a close up (b)) and Prusa clay army (Figure 3.36 (c) and a close up (d)) were printed using the developed nanocellulose / VO resin formulations. The bio-based vat photopolymerization resin gave very high printing resolution in the printed structures, as shown in Figure 3.36 (e–i). The measured layer height was constant at 50 µm, as set during the slicing process. At the same time, the Petrin tower calibration structure (Figure 3.36 (a) and (b)) demonstrates the possibility of printing high-quality, detailed objects with overhangs, no supports, and no missing parts. In tandem, the Prusa clay army models (Figure 3.36 (c) and (d)) show excellent resolution for small objects with especially fine details.

Using photography in conjunction with optical microscopy of printed samples provides an additional printability assessment. Polarized light optical microscope images at 20× magnifications were captured to assess the layer accuracy of the printed mechanical testing samples in the Z-axis direction perpendicular to the printing plane (Figure 3.36 (e–i)). Excellent printing precision is obtained for all prepared compositions. The best printing accuracy was observed for the VO and VO/pCI resins. In contrast, other nanocelluloses introduced surface defects into the layers, which consequently impacted the light transmittance properties, as revealed in Supplementary 13. Nontheless, printing layer thickness (50 µm, red lines in Figure 3.36 (e–i)) remains constant and, hence, printing accuracy is considered to be unchanged.

Supplementary 13 shows no color changes for any tensile bar samples. At the same time, UV-Vis transmission spectra reveal small but measurable changes in transparency following the incorporation of nanocellulose fillers into the vat photopolymerization resin (Supplementary 13). In particular most composite materials become translucent with some reduction in the UV-Vis light transparency. The visible light transmittance values calculated at 500 nm were 78, 76, 73, 83, and 84 % for VO, VO/pF, VO/pFA, VO/pC, and VO/pCI, respectively.

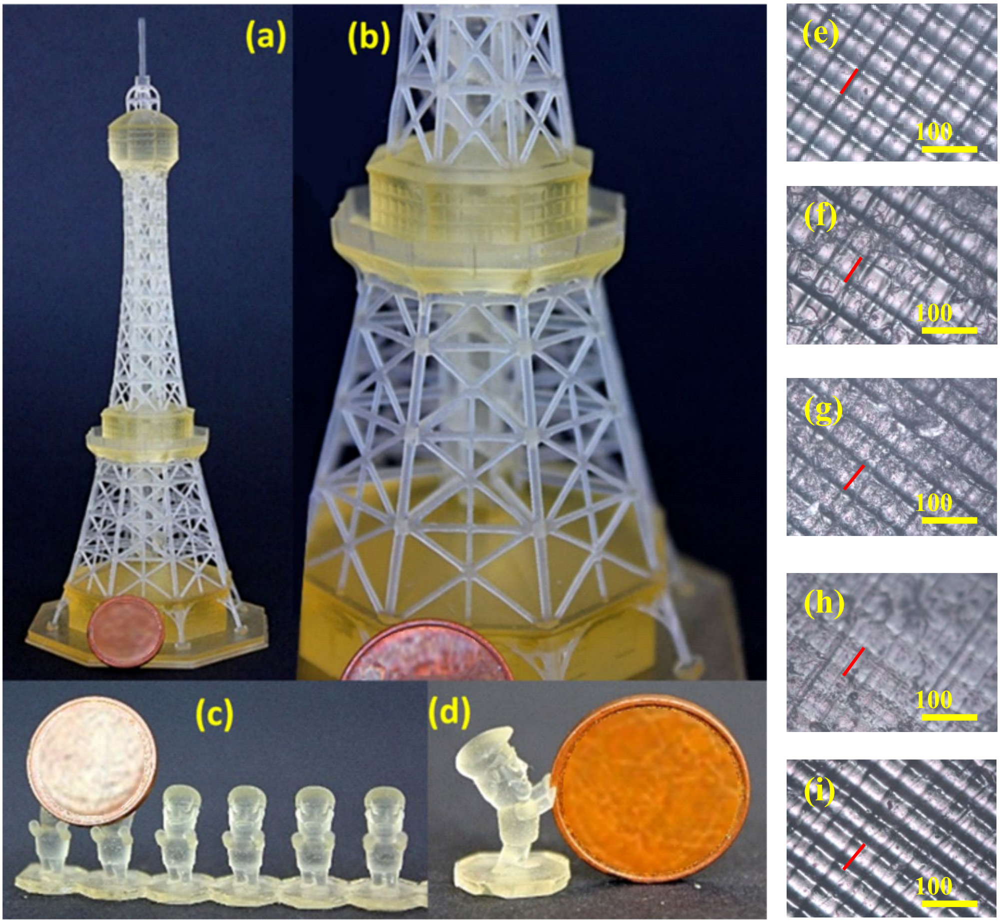

Figure 3.36. 3D printed SL1 standard calibration check models Petrin tower (a) and (b) and Prusa clay army (c) and (d) and optical microscope images of the 3D printed samples VO (e), VO/pF (f), VO/pFA (g), VO/pC (h), and VO/pCI (i).

Improved transmittance in the case of VO/pC and VO/pCI is likely due to homogeneous dispersion of single nanocellulose crystals in the matrix, given reports of similar results in the context of work on C films with up to 90 % UV transmittance [288]. pCI improves the interface between the polymer matrix and the filler, thus enhancing dispersion, enhancing print quality and reducing light scattering still further. In contrast, while pF can form thin translucent films, it is reported to have a tendency to form agglomerates, increasing light scattering and reducing overall transmittance [289]. Likewise, decreased light transmission of pFA composites may be due to increased agglomeration and heterogeneity [290]. This is best explained by the extremely high reactivity of the acrylate groups on the pFA surface coupled with the lack of stabilizers vs.

spontaneous polymerization, which is posited to lead to some level of inter-particle bond formation and irreversible aggregation during pFA precipitation in ethanol.

FTIR was used to analyze the UV-curing of SLA resins and the macromolecular network chemical structure of the polymer. FTIR is reported to be an effective and widely used technique to investigate the UV-curing reaction of polymer resins [19,242]. All FTIR spectra from uncured resin and printed samples are shown in supplementary data Supplementary 14. Peaks at 810, 980, 1409, and 1629 cm^{-1} indicate the vinyl bonds, which are characteristic of acrylic groups [291]. During the UV-light curing process, the vinyl moieties were consumed quickly by radically initiated polymerization reactions, developing a spatial network of macromolecular chains, and resulting in a noticeable drop in the characteristic spectral peak intensities, as shown in supplementary data Supplementary 14. The prepared resins display very high polymerization rates, with similar behavior reported elsewhere in the literature [93]. DBC% was calculated from the ratio of a vinyl bond at 810 cm^{-1} and a carbonyl group bond at 1731 cm^{-1} to evaluate the polymerization process according to equation (2.1). Calculated DBC% values are summarized in Table 3.9. Cellulose incorporation into VO resin can significantly modify DBC%, as other authors reported [292]. All composites show lower DBC% than VO (Table 3.9). The decrease for VO/pF and VO/pFA is 2 and 3 %. The observed DBC% decrease attributes to the increased resin viscosity [93] and reduced optical transmittance [290]. VO/pC and VO/pCI show even more significant decreases of 8 and 5 %. This could be explained by the work of Yang et al., where low C concentrations were observed to interfere with the photopolymerization of unreacted macroradicals and free hydroxyl groups were retained in the printed material [194]. In the case of surface-modified particles, fewer hydroxyl groups should be left to interfere with macroradicals, which could explain why VO/pCI achieved a higher DBC% than VO/pC. This correlation is also supported by increased covalent bonding / crosslinking between the VO matrix and pFA.

3.4.1.3. Macromolecular network structure

Table 3.9 provides basic physical properties data for the 3D printed polymers (density, sol-fraction) as well as the molecular weight between crosslinks (M_c) and crosslink density (N). These latter two values were calculated by applying the theory of entropic rubber elasticity to the rubbery plateau modulus as derived from the DMA data [180,181], and represent the sum of all types of crosslinks active in the system (chemical and physical). The N values of the composites all show significant increases compared to the VO (N_0). Given prior confirmation via FTIR of similar levels of double bond conversion in all cases, this result provides clear evidence of significant "physical crosslinking" (nanofiller reinforcement) even at the ultra-low nanofiller concentration of 0.07 vol%, and further confirms the importance of nanofiller aspect ratio as well, given that the higher aspect ratio pF consistently produces larger increases vs. the lower aspect ratio pC, regardless of surface chemistry. Furthermore, surface-modified nanofillers are shown to provide consistently higher crosslink densities than their unmodified counterparts. While the extremely low nanofiller concentration makes direct spectroscopic detection of interfacial interactions impractical, it is posited that this enhanced reinforcement may be at least partly due to covalent bond formation at the polymer / nanofiller interface, in addition to changes in dispersion state due to altered nanofiller compatibility with the polymer matrix.

Table 3.9.

Parameters of 3D printed samples

Sample	Density, g/cm^3	Sol-fraction, %	DBC%	M_c, g/mol	N, mmol/cm^3	$\Delta N/N_0$, %
VO	1.116 ± 0.0012	3.69 ± 0.20	84	1021	1.1	-
VO/pF	1.117 ± 0.0008	4.39 ± 0.12	82	464	2.4	+118
VO/pFA	1.118 ± 0.0017	5.12 ± 0.27	81	426	2.7	+145
VO/pC	1.119 ± 0.0013	4.10 ± 0.41	76	731	1.5	+36
VO/pCI	1.118 ± 0.0016	3.99 ± 0.40	79	568	2.0	+81

The thermogravimetric analyses are in Supplementary 15, while the char yield at 600 °C and temperature at 5 % mass loss ($T_{5\%}$) are summarized in Supplementary 16. Consistent with the very low nanofiller concentrations studied here, the obtained thermograms imply that the addition of cellulose does not significantly affect the degradation mechanism of 3D printed samples.

Figure 3.37 (a) compares the storage modulus of the VO to composites loaded with different nanocellulose types. At 20 °C, the stiffness of composites improves by 1.34 to 1.80-fold compared to the VO. This correlates well with the elastic modulus of the tensile test (Figure 3.38). In the glassy state, the matrix properties more strongly determine the achieved storage modulus, whereas a transition to a viscoelastic state yields a significant increase in values over the unfilled VO as the reinforcement begins to bear the load [126]. Figure 3.37 (a) compares the storage modulus of the VO to composites loaded with different nanocellulose types. At 20 °C, the stiffness of composites improves by 1.34 to 1.80-fold compared to the VO. This correlates well with the elastic modulus of the tensile test (Figure 3.38). In the glassy state, the matrix properties more strongly determine the achieved storage modulus, whereas a transition to a viscoelastic state yields a significant increase in values over the unfilled VO as the reinforcement begins to bear the load [126].

Figure 3.37 (b) shows the changes in loss modulus values after adding nanocellulose fillers. For all composites except VO/pFA, the loss modulus peak became narrower and weaker as compared to the pure VO. Above the glass transition, loss modulus values are higher for all composites vs. the VO. This suggests that at higher temperatures, the free movement of the polymer chains is restricted by nanocellulose fillers and high crosslink density. As for VO/pFA, an increase in the strength of the loss modulus peak indicates that the increased number of chain segments inhibits the relaxation process within the composite. A similar effect was reported by Maalihan R.D. et al. for methacrylate / acrylated chitosan C composites [242].

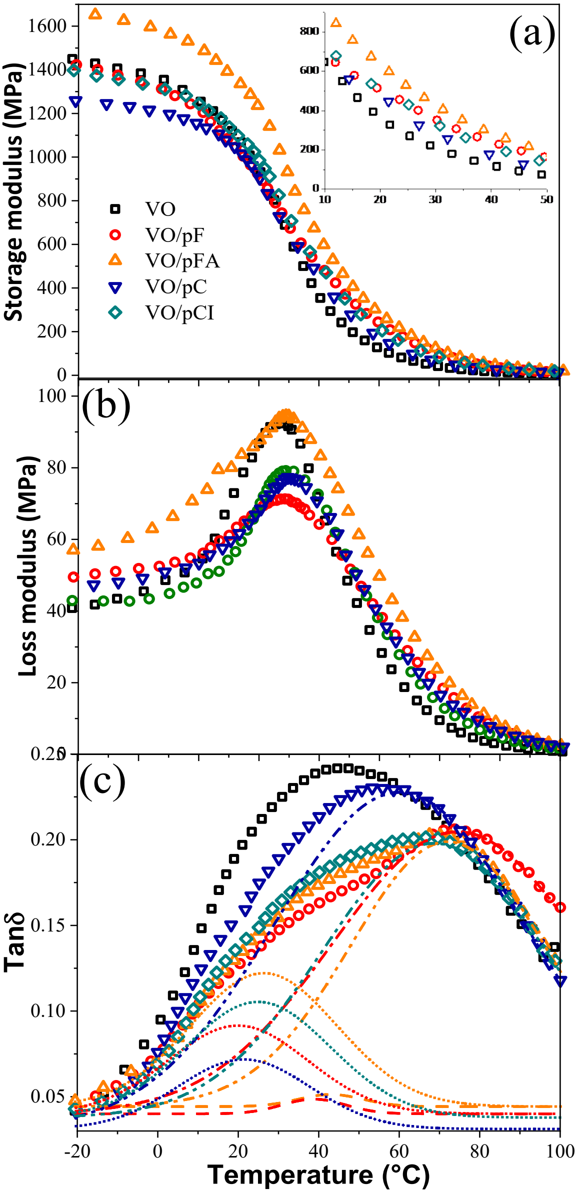

Figure 3.37. Storage (a), loss modulus (b), and tanδ (c) curves of 3D printed samples.

Figure 3.37 (c) presents tanδ curves, which represent damping properties and indicate the balance between the elastic and viscous phases in the composite [293]. In line with the observed increases in crosslink densities (Table 3.9), a clear decrease in tan δ around the glass transition was observed for all composites as compared to the VO. The peak of tanδ is commonly attributed to the glass transition temperature (T_{g3}) [294]. In order to compare the results with our previous work as well as the research literature more broadly, T_g was determined the same way.

The complex photocurable resin composition contributes to a relatively broad VO tanδ peak, which narrows for composites and shows a shoulder for some compositions. To better understand the shift in the composite's structure, deconvolution was applied to tanδ curves (Figure 3.37 (c)), and the resulting values are presented in Supplementary 17 as T_{g1} and T_{g2}. Our previous work examined the curing kinetics of neat AESO and VO resin compositions [20]. Compared to VO, a clear shift in the glass transition to higher temperatures was visible for all composites. Likewise, the observation of evidence of different phases highlights the heterogeneous nature of the polymer matrix in such systems [126]. In particular, the introduction of nanocellulose fillers results in the formation of an interphase between the cellulose surface and bulk matrix. The more crosslinked regions dominate the composite response as indicated by the shape of the tanδ peak. Likewise, the observed peak shoulders can be attributed to the phase separation of regions with differing crosslink densities (driven by local variations in composition and / or extent of reaction), where the resulting changes in chain mobility drive the appearance of additional transitions [93]. The fact that the soybean oil itself is a complex mixture of multiple components even before epoxidation, acrylation and polymerization further contribute to this heterogeneity.

The tensile strength, failure strain, and elastic modulus graphs can be found in Figure 3.38. The inclusion of nanocellulose fillers drastically improved the mechanical performance of all samples. All composite elastic modulus values increased nearly 2-fold. The stiffness of the VO/pC and VO/pCI composites was the highest, with an increase of up to 95 % compared to neat VO. Modulus values increased due to the highly rigid and crystalline needle-like C. VO/pC and VO/pCI modulus results are comparable within the margin of error. VO/pF and VO/pFA show modulus values that are ~60 % and ~70 % higher, respectively, as compared to VO. The greater stiffness enhancement in VO/pFA can be explained by covalent bond formation at the polymer-filler interface and more efficient stress transfer as a result.

It can be seen in Figure 3.38 (a) and (b) that the addition of nanocellulose had a significant impact on the tensile strength and failure strain of the composites. Compared to VO, the addition of pF led to a ~70 % increase in failure strain. In contrast with the rigidity of the pC particles, the fibrillar structure of pF can introduce a tremendous increase in the composite's flexibility. Long fibrils in VO/pF composites can entangle and intertwine, allowing them to form a reinforcing network [295]. Coupled with a flexible polymer matrix, these effects can lead to an increase in all tensile parameters. The functionalization of pF to form pFA resulted in a reduction in failure strain but no statistically significant changes in strength. It has been reported that an increase in chemical crosslink density tends to reduce failure strain values, and tensile strength only up to a certain point, beyond which brittle behavior is observed [296]. Maalihan R.D. et al. reported a similar observation for methacrylate composites with acrylated C (CA) obtained from chitosan. Up to 0.5 wt%, CA yielded an increase of strength and strain on CA vs. neat C, while addition of 1 wt% led to 4-fold decrease in properties [242,297]. Compared to the VO, VO/pCI showed 144 % and 52 % increases in tensile strength and strain, respectively. The chosen functionalization improves the wettability and adhesion between VO and pCI. Improved compatibility also results in a more uniform distribution of particles and a lower tendency to form agglomerates. Similar approach of improved compatibility was achieved with lignin coated pF with benefits observed in the methacrylate resin mechanical performance [298]. Lignin coating increases pF surface hydrophobicity resulting in increase of resin's strength and modulus. Figure 3.38 (d) displays the toughness of all samples. VO/pF and VO/pCI achieved an impressive toughness increase of ~30 J/m^3 (+300 %), consistent with a high resistance to deformation without failure of the material. Toughness is a desirable polymer material property, and it is evident that nanocellulose introduction led to at least a 2-fold increase in composite toughness compared to the VO.

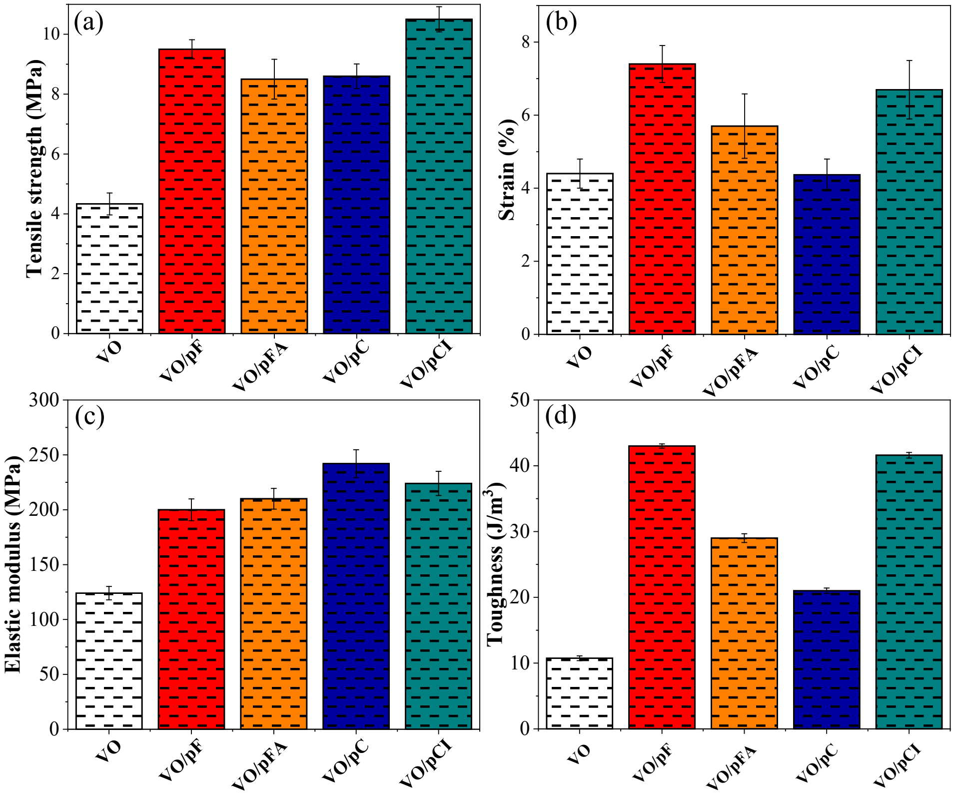

Figure 3.38. Tensile strength (a), failure strain (b), modulus (c) and toughness (d) graphs of 3D printed samples.

SEM images of fracture surfaces were taken to visualize the toughening effect of fillers on the polymer matrix [299]. Figure 3.39 shows SEM images of the fracture surfaces of printed samples fractured following exposure to liquid nitrogen. The images show that the fracture surface of the printed VO resin is smooth. This fracture type is characteristic of a brittle polymer material [300]. However, with the exception of VO/pCI, reinforced resins exhibit a significantly different fracture pattern. The roughness of the fracture surface increases dramatically after the nanocellulose fillers are incorporated into the VO matrix. The difference between VO and VO/pCI is less pronounced, but the pattern differs from the smooth fractures of the VO. The roughness is very similar for the VO/pF and VO/pC composites, while VO/pFA exhibits a more intense fracture surface roughness. The formation of a reinforcing filler network and the presence of covalent bonds at the polymer-nanoparticle interface could explain the drastic changes in fracture surfaces.

The formation of such a network leads to a delay in crack initiation and its further propagation because of the nanoparticle bridging effect in a polymer matrix [301,302]. This effect plays a crucial role in reinforcing polymer composites' mechanical performance by dissipating significant amounts of impact energy [303]. However, changes in the system's heterogeneity should also be considered based on the UV-Vis, DMA (broad tanδ peak with multiple shoulders), and tensile test results. The system's heterogeneity increases as soon as the filler is incorporated into the resin. Lower VO/pCI fractured surface roughness may be related to the matrix's pCI compatibility and bulk distribution. Simultaneously, introducing acrylate groups into pFA and developing covalent bonds with the polymer matrix might come at a cost if it results in local variations in crosslink density due to the high reactivity of pFA, thus rendering the sample more mechanically inhomogeneous than would be expected given high levels of dispersion.

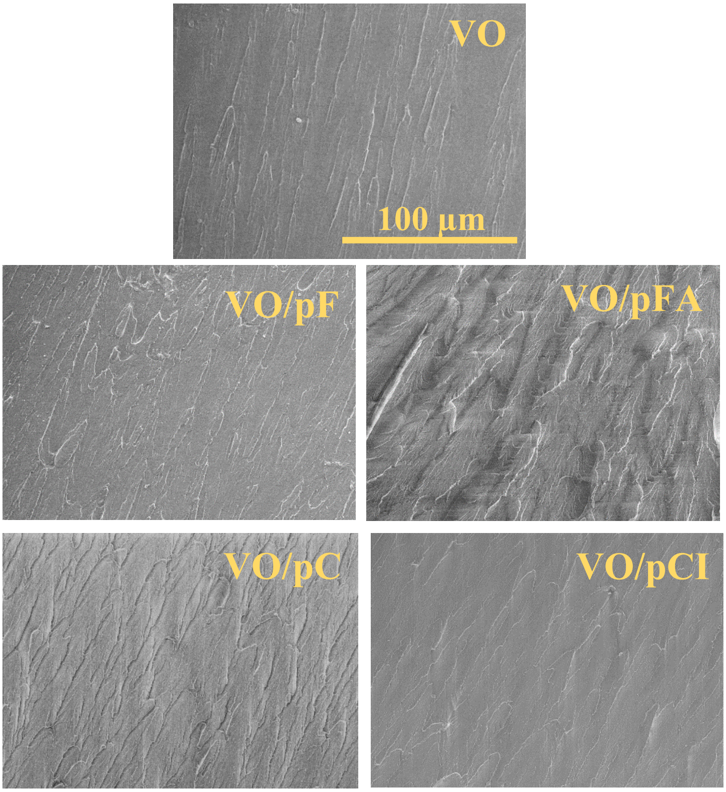

Figure 3.39. SEM micrographs of the fracture surface of 3D printed samples.

3.4.1.4. Reinforcement efficiency analysis

Understanding the filler-matrix interactions is critical for determining the reinforcement efficiency of the used filler. Strong filler-matrix interactions reduce polymer chain mobility at the interface and favor the ability of the filler to reinforce the composite more effectively. The developed interphase structure is proposed in Scheme 3.1. It shows both covalent bonding and physical interactions developing at the cellulose-polymer interface. The existence of such interactions can be detected via FTIR analysis, by following the C=O and OH peak shifts and changes in the shape and strength of these absorption bands due to hydrogen bond formation between filler OH groups and matrix C=O groups [93]. However, the low filler concentrations in this case make it impossible to directly detect both covalent bonds and the hydrogen bonding via conventional FTIR. Moreover, in case of pFA, FTIR absorption bands associated with the acrylate groups grafted to the pF surface and involved in network formation would appear in the same part of the spectrum as much stronger contributions from the polymer matrix [20,59,285]. Overall, there are at least three attractive forces that could contribute to filler-matrix interactions: hydrogen bonding (OH ||| O=C for all used fillers; NH ||| O=C for pCI), covalent bonds (pFA), and Van der Waals forces (pCI) (see Scheme 3.1). Figures in Scheme 3.1 (b) and (c) show that even after functionalization in VO/pCI and VO/pFA, respectively, that due to the likelihood of incomplete surface modification the potential for hydrogen bonding with the remaining OH groups of the cellulose remain. For this reason and regardless of modifications, all the fillers studied here are expected to possess the capacity to form OH ||| O=C hydrogen bonds with the polymer matrix. Additionally, in the case of pCI, hydrogen bonding is also possible between the NH moieties introduced thanks to HMDI modification and the carbonyls in the polymer matrix.

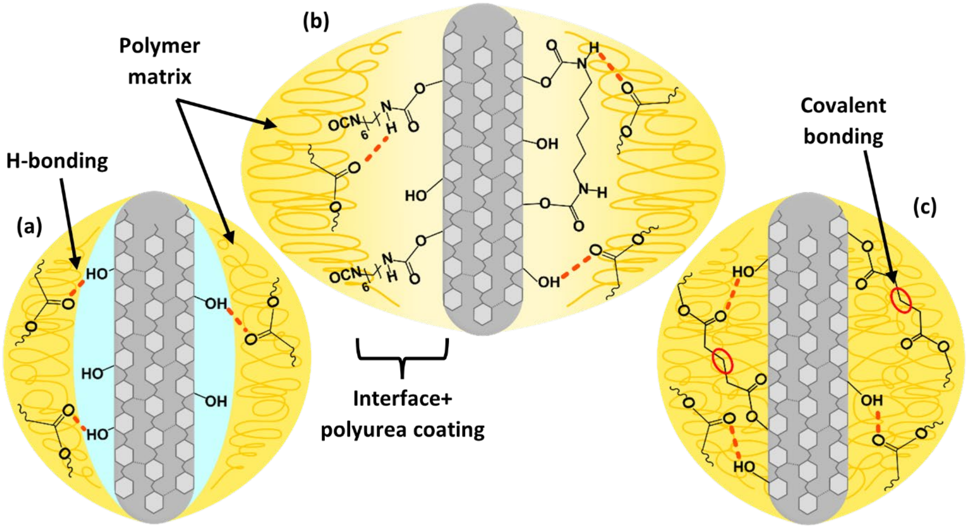

Scheme 3.1. Proposed filler-matrix interaction schematic representation for VO/pC and VO/pF (a), VO/pCI (b), and VO/pFA (c).

To further assess achieved reinforcement by different nanocellulose, the filler-matrix stress efficiency transfer parameter C*, adhesion factor A, and reinforcement efficiency parameter *r*, summarized in Table 3.10, were calculated according to equations (2.11), (2.12), and (2.13). The composite's ability to enter its glass transition region faster (characterized by a modulus drop with an increase in temperature) can be described by parameter C*, which is defined as C* = 1 for the neat polymer matrix and which should decrease with increasing levels of stress transfer in a reinforced system [126]. The incorporation of nanocellulose fillers results stress transfer from the polymer matrix to the nanocellulose, with values of C* ranging from 0.37 to 0.50. These significant reductions in C* imply excellent stress transfer from the polymer matrix to the nanocellulose fillers. Remarkably, the VO/pFA and VO/pCI composites show 25 % and 28 % lower C* parameter values than composites based on the analogous neat (unmodified) fillers, implying better filler effectiveness for composite reinforcement.

Coming now to interfacial adhesion, lower A values indicate stronger adhesion between the nanocellulose filler and the polymer matrix. The negative values of A are related to the heterogeneity of the composite and anisotropy of the filler orientation [182]. Filler functionalization increases adhesion with the VO matrix in both cases. This is consistent with the ability of pFA to form covalent bonds with the VO matrix (Scheme 3.1), as the A value for the VO/pFA composites is the lower compared to pF. It should be noted that the addition of pCI to the VO matrix resulted in an apparent decrease in the A parameter as well, again indicating a significant improvement in adhesion. As shown in Scheme 3.1, this effect is achieved through functionalization, resulting in increased wetting of pCI particles and forming an interface with the VO matrix.

Table 3.10.

The *r*, C*, and A parameters of 3D printed samples

Sample	*r*	C*	A
VO/pF	16.1	0.46	-0.313
VO/pFA	28.6	0.37	-0.339
VO/pC	10.7	0.50	-0.199
VO/pCI	21.4	0.39	-0.287

Finally, the increase in the *r* parameter shows improved filler-matrix reinforcement effectiveness. When judged by *r* values, pF appears to be more effective than pC in reinforcing the VO matrix, with the same tendency observed when comparing VO/pFA and VO/pCI. Surface functionalization approximately doubles reinforcement effectiveness, though the effect is slightly more pronounced in the case of VO/pCI. The lower C* and much higher *r* values in the case of pC in comparison with pF demonstrate that with such low concentrations, pF is a more suitable filler for the VO matrix. This further supports the idea that (at low concentrations) the higher aspect ratio of pF is beneficial to resin reinforcement, and that this is even more so in the case of the functionalized pFA given improved polymer-filler interactions. Higher aspect ratios facilitate the creation of a filler network, while in the VO/pFA composite, covalent bonding between the filler and the polymer matrix contributes even more to the filler's ability to reinforce the VO matrix.

3.4.1.5. Performance properties comparison.

Figure 3.40 (a) shows the storage modulus ratio between the VO and composites at different temperatures. This graph provides a straightforward means of assessing the reinforcement effect of the fillers as a function of temperature. The storage modulus ratio plot shows an increase at temperatures similar to those determined from the deconvolution of the tanδ peaks in Supplementary 17. It is seen that until about 20 °C, there is no significant reinforcement evidence for any of the obtained composites. The exception is VO/pFA because of the filler-matrix covalent bonding. The absence of any substantial effect relates to the T_g of the samples. Below the T_g, all segmental mobility is strictly limited, and fillers accept only minimal loads from the polymer matrix, as seen in Figure 3.40 (a). As temperatures approach the T_g, the segmental mobility of the polymer matrix increases. Hence, the structure becomes more mobile, allowing the filler to bear some of the applied load. As a result, all composites exhibit reinforcement at the T_{g1} temperature ranging from 20 to 26 °C, with the effect increasing until the T_{g3} is reached. As the segmental mobility of the polymer chains continues to rise as T_{g3} is exceeded, the reinforcement effects decrease with further temperature increases.

VO/pFA shows the highest storage modulus ratio across all temperature ranges, consistent with results obtained for C* and *r* parameters. However, some competition exists between the VO/pCI and VO/pF composites when it comes to the next best system. VO/pCI exhibits a higher relative modulus at temperatures ranging from -10 to 25 °C, which it maintains as the glass transition begins thanks to strong adhesion between the pCI and the VO matrix as a result of the surface functionalization of the filler. Nevertheless, as the temperature continues to increase, pF provides a greater relative modulus, presumably thanks to its higher aspect ratio and greater crosslink density.

The radial plot in Figure 3.40 (b) displays a summary of mechanical performance observations of 3D printed samples – strain at break, tensile strength, tensile modulus, tensile toughness, and temperature at 5 % mass loss. The relative changes in desired parameters for prepared composites are presented and referenced to VO. The tensile performance of VO/pF and VO/pCI was the highest of all printed composites. Incorporating pF and pCI into the VO matrix resulted in an almost 4-fold increase in toughness while substantially improving other parameters in tandem. VO/pC showed the highest 2-fold increase in tensile modulus of all 3D printed samples. The thermal stability of all composites remained similar to VO, with only minor differences in overall performance.

It should be stated that in the case of the VO/pFA system, underlying processes are more complicated. As discussed in the previous sections, it is clear that the combination of a high aspect ratio and a strong polymer / filler interface results in significant enhancements in stiffness in this system. At the same time, as noted in the context of the fracture surface analyses, there is evidence that these materials may actually be more heterogeneous due to the surface modification of the pF. In particular, these observations may be explained by a higher reactivity of the acrylate groups on the pF surface vs. those of the resin components. The end result of such a difference is an increased tendency to form strong covalent bonds between filler particles, favoring the formation of a strong filler network but increasing the heterogeneity of the system as a result. While such a strong network of high aspect ratio fillers favors high surf values, such heterogeneities tend to lead to stress concentrations and premature failure – thus explaining the observed combination of morphology and properties in this system. This is a highly significant outcome as it highlights just how important it is to match the reactivity of the filler surface and the surrounding resin matrix. However, further studies of such interactions and underlying processes should be done to broaden the available knowledge regarding this topic.

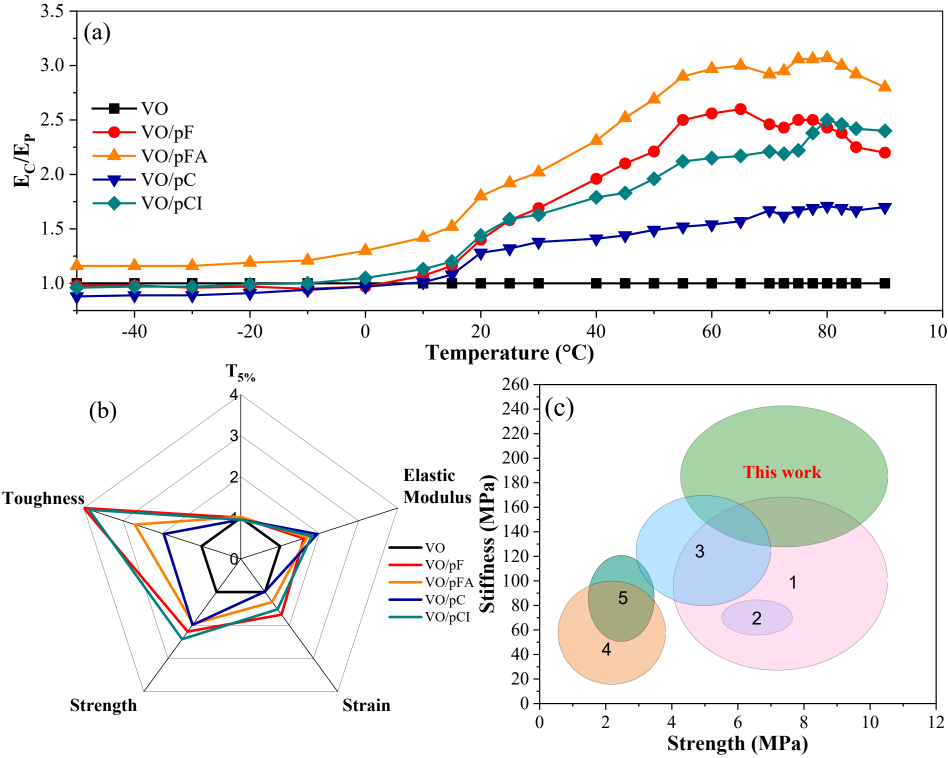

Figure 3.40. Ratio between composite (E_c) and VO (E_p) storage modulus values (a); Relative changes of performance properties for 3D printed samples. Value 1 represents the VO (at 20 °C) (b); Comparisons of tensile performance of AESO / cellulose composites from this work and the literature (c). (1) AESO/methyl acrylate functionalized cellulose 5–30 wt% (3D printed) [76], (2) AESO/acrylate or HDTMA functionalized C 1–2 wt% (films) [60], (3) AESO/micro- or nanocrystalline cellulose 0.15–2.4 wt% (3D printed) [130] 44(4) AESO/macadamia shell microcrystalline 1–10 wt% (3D printed) [304] (5) AESO/cellulose (1 mm particles) 5–10 wt% (cured composites) [305].

Overall, all composites' performance was improved compared to the VO. These results demonstrate the effectiveness of nanocellulose and its various functionalization methods for the reinforcement of 3D printed bio-based polymer resins. In addition, the variations observed as a function of filler type and surface functionalization provide the ability to tune composite performance for specific applications.

To better understand the mechanical performance of the prepared AESO-based composites with cellulose fillers, tensile test results were compared with those found in the literature and summarized in Figure 3.40 (c). It should be noted that the availability of scientific papers concerning such composites is minimal due to the various aforementioned difficulties in producing them. Liu et al. demonstrated syringe 3D printed AESO composites loaded with methyl acrylate functionalized cellulose range from 5 to 30 wt% [76] . Highly loaded composites showed increased tensile strength up to 11.5 MPa and modulus values of up to 167 MPa, against 4.3 and 27.4 MPa for neat AESO, respectively. Palucci Rosa et al. used two different cellulose sizes, microcrystalline cellulose and C, to prepare AESO-based composites for vat photopolymerization 3D printing [130]. A comparison of the influence of filler size on sample properties was carried out. The incorporation of fillers in the polymer matrix significantly enhanced mechanical properties. At low loadings, microcrystalline cellulose and C gave similar tensile strength values (~3 MPa), with further increases up to 4.5 MPa and 7 MPa, respectively, at higher concentrations. C addition to AESO-based resin also caused a 2-fold increase in the elongation at failure of a printed composite. At the same time, microcrystalline cellulose showed more than 2-fold higher modulus values (approaching 170 MPa) for loadings of 0.6 wt% and above. Noe et al. prepared biobased resins suitable for vat photopolymerization 3D printing using macadamia shell lignocellulosic waste with loadings ranging from 1 to 10 wt% [304]. 3D printed composites achieved remarkable printing quality with an increase in mechanical properties. Higher filler loadings increased strength from about 0.5 MPa to 2.5 MPa, and modulus from 3.8 to 100 MPa. Seabra et al. prepared thermosetting biodegradable composites by combining AESO-based resin with fragments of sisal rope (particle size about 1 mm) [305]. Variations in filler and hardener loadings were studied. The tensile test results revealed that increased filler loading adversely affected the composite strength and modulus values while increasing overall hardness. The tensile strength results ranged from approximately 3.25 MPa for unfilled samples to 1.75 MPa for samples containing 10 wt% filler as well as a higher hardener content. Overall, the formulation of neat resin combined with ultra-low loadings of nanofillers as represented in this paper appears to provide better mechanical performance than all prior attempts found by our team at the time of this writing.

3.4.1.6. Summary

This work successfully demonstrates additive manufacturing (AM) via vat photopolymerization of bio-based vegetable oil (VO) resins containing ultra-low concentrations of neat and functionalized nanocellulose with high printing resolution and favourable filler-matrix interactions. To the best of authors' knowledge, this report is the first to demonstrate the use of acrylate-functionalized pF as an efficient reinforcement in a 3D printing resin.

Functionalization, as well as the type of nanocellulose and its effects on the printing quality and performance of bio-based resins, were examined through various techniques. Notably, in addition to an in-depth FTIR analysis of the modified fillers. The introduction of nanofillers did not affect the printing quality. Concerning materials performance, the introduction of nanocellulose into VO resins provided up to 2.5-fold increase in strength and 4-fold increase in toughness of the 3D printed samples, with an even more pronounced effect for functionalized fillers. Functionalization of the fillers led to improved filler-matrix adhesion in the case of VO/pCI and chemical bonding for VO/pFA, a prerequisite condition for improving composite properties, with these results reflected in crosslink density calculations as well. While functionalization also induced changes in the thermal degradation of the functionalized fillers, the thermal stability of 3D printed samples was not significantly affected, and char yields were increased. Concerning reinforcement efficiency, VO/pFA showed 1.24-fold lower C and 1.77-fold higher r parameters than VO/pF. VO/pCI achieved a 1.28-fold lower C* and a 2-fold higher r than VO/pC. In addition to the significant increases in composite mechanical properties, these results highlight the improved reinforcement stemming from surface functionalization.

Overall, this work shows that the addition of ultra-low concentrations (0.07 vol%) of nanocellulose into a VO resin represents a promising means of strengthening sustainable vat photopolymerization resins. Even more so, more remarkable improvement can be achieved by using pF rather than pC at the ultra-low concentration. At the same time, the functionalization of fillers can help to overcome filler-matrix compatibility issues at the interface. As a result, well-designed VO-based composite resins could represent sustainable alternatives to conventional petroleum resins. Furthermore, the combination with nanocellulose fillers promises new types of reinforced materials, driving even greater adoption of UV-assisted AM techniques.

3.5. Accelerated weathering performance analysis of nanocellulose reinforced vegetable oil-based resins for stereolithography

3.5.1. Nanofibrillated cellulose effect on vegetable oil-based composite durability during QUV accelerated weathering

Publication:

- **A. Barkane**, O. Platnieks, J. Vecstaudza, S. Gaidukovs, Analysis of bio-based acrylate accelerated weathering: A study of nanocellulose impact on the bulk durability of 3D-printed nanocomposites. Materials Today Chemistry, 33 (2023) 101737, doi:10.1016/j.mtchem.2023.101737

Bio-based resins for UV-assisted photopolymerization vat 3D printing have received immense research interest. 3D printing has initiated the 4.0 industrial revolution and is expected to squeeze in more production industries, including making materials for outdoor applications. Weathering investigations have been devoted mainly to fossil acrylic polymers. This research aims to close the gap in understanding bio-based acrylic 3D-printed polymer weathering performance. QUV accelerated weathering was used on vegetable oil-based 3D-printed compositions with filter paper nanofibrillated cellulose (pF) as reinforcing filler. Discoloration, cracking, FTIR measurements of surface chemical degradation, and bulk properties evaluated by changes in mechanical performance were used to characterize materials performance during weathering. pF reinforcement delays the yellowing and cracking during 1000 h of weathering. After weathering, increased flexural stress and strain were achieved with 0.5 wt% pF loading. Chemical analysis reveals simultaneous photocleavage and additional crosslinking of the macromolecular chains. The glass transition temperature increased by up to 20 °C. pF introduction in bio-based polymers increased of weathering endurance and mechanical performance. The pF is compatible with and a perspective filler in bio-based acrylic resins for 3D printing applications.

**Sample abbreviations: all resin formulations were named in accordance with the filter paper nanofibrillated cellulose (pF) loading as follows: 0%, pF0.1%, and pF0.5%.*

3.5.1.1. Morphology

Visual examination in Figure 3.41 (a) clearly shows the yellowing of all samples already after 250 h in the UV weathering camera for all compositions, while precise quantitative colorimetric values are summarized in Figure 3.41 (b). Filter paper nanofibrillated cellulose (pF) addition (both concentrations of 0.1 and 0.5 wt%) has prevented surface cracking observed for 0% composition. This proves that the introduced pF increased ductility that in turn improved dimensional stability, resulting in enhanced weathering durability beyond mechanical performance enhancement. The weathering cycle transitions between intensive UV irradiation at elevated temperatures followed by spraying and condensation, introducing mobile water molecules that migrate into the structure [162]. Standard static testing, such as room temperature tensile tests, usually does not expose samples to these relatively extreme conditions for polymers, which mimic harsh outdoor environments [306].

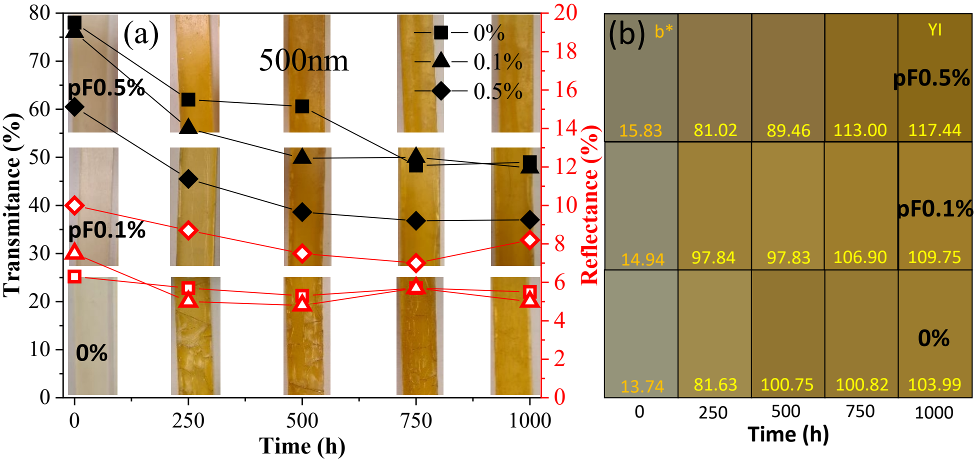

	0	250	500	750	1000
pF0.5%	15.83	81.02	89.46	113.00	117.44
pF0.1%	14.94	97.84	97.83	106.90	109.75
0%	13.74	81.63	100.75	100.82	103.99

Figure 3.41. Images of the sample surfaces during UV weathering with a UV-Vis 500 nm overlay tracking changes in transmittance and reflectance data (a) and colorimetry data (b).

Changes in optical properties, such as transmittance and reflectance, during UV weathering, were evaluated by UV-Vis spectroscopy measurements (in Figure 3.41 (a)). Data show that 0% composition has the highest transparency (78.0 %) at 500 nm, followed by pF0.1% and pF0.5% compositions (76.0 and 60.5 %, respectively). Full UV-Vis spectra data are available in Supplementary 18. For all compositions after 1000 h of UV weathering, transparency decreases to 49.0, 47.8, and 37.0 % for 0%, pF0.1%, and pF0.5% compositions. This shows that 0% and pF0.1% composition act similarly (transparency decreases by 29.0 and 28.2 %, respectively), while the pF0.5% sample's transparency decrease is less pronounced (23.5 %). Scattering calculated from transparency and reflectance (Supplementary 19) shows that pF0.5% composition has the highest values of 29.5 and 54.8 % at 0 h and 1000 h, respectively. Thus, photodegradation introduces an additional light scattering source, while the primary source is still the introduced pF filler [92]. Colorimetry images and the yellowing index (YI) with b* (attributes for yellow color) can be seen in Figure 3.41 (b). 0 h composition samples were used as a reference for yellowing evaluation during UV weathering; hence, the absolute values of b* are shown for these samples. pF introduction makes samples slightly more yellow, while the L* parameter (lightness / brightness) shows that pF makes the samples darker: 60.63, 56.90, and 51.68 for 0%, pF0.1%, and pF0.5% 0 h samples, respectively (visually, samples with pF are more matte). Samples during UV weathering are described with YI concerning the sample's value before weathering. 0%, pF0.1%, and pF0.5% samples get more yellow between 250 h and 1000 h by 27.39 %, 12.17 %, and 44.95 %, respectively. Also observed is that pF delays yellowing. 0% showed the most incredible jump between 250 and 500 h, while for 0.1%, there is almost no difference between 250 and 500 h, and a shift can be observed at 750 h. In turn, the pF0.5% sample shows a steady climb in yellowing throughout the weathering, which could relate to higher light scattering values. These YI changes show that pF can moderate or reduce the yellowing during the material's lifetime, also reported by Zhang et al. [307].

After flexural testing, additional visual investigations were performed with optical microscopy imaging at 200× magnification of the sample top and side surfaces. The obtained top and side images of the weathered samples can be seen in Figure 3.42. Optical microscopy confirms the conclusion of the visual examination analysis. The top surface of the 0% sample cracked during the weathering in the UV chamber, while pF0.1% and pF0.5% showed no cracks (cracking observed before flexural testing). There are no cracks for 0% sample top surfaces with 0 h exposure to UV weathering, but cracks are visible for samples after UV weathering. It is visible that flexural testing has introduced large cracks through the sample volume. The failure provides information about layer adhesion and crack propagation, which can be further analyzed [308].

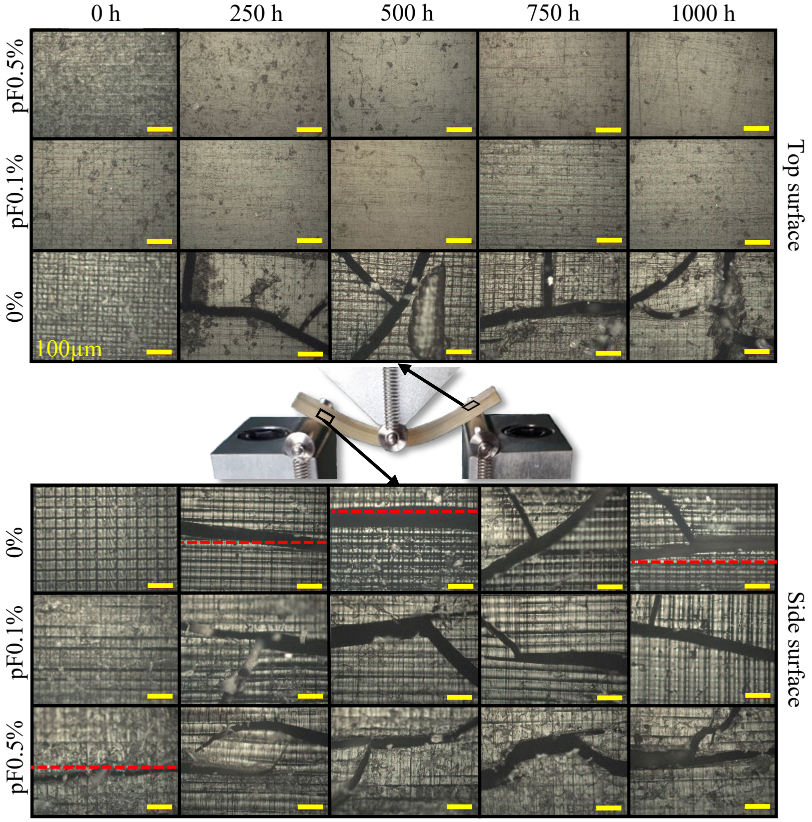

Figure 3.42. Optical microscopy images at magnification 200× of the prepared composition sample top and side surfaces during UV weathering after flexural testing are depicted in the middle of the image.

Figure 3.42 optical microscopy images of top and side surfaces show excellent printing accuracy; perfect pixel structure can be observed for all three prepared composition samples.

Surface appearance changes when pF is introduced, as pF particles can be left on the surface and partly outside the cured resin layer during post-processing washing. Proceeding with side surface analysis in Figure 3.42, 0% and pF0.1% samples show no cracks at 0 h exposure, while a pF0.5% sample shows a crack. Crack propagation for the 0 h pF0.5% sample and the rest of the samples during UV weathering happens crossing the printed layers. For better observation, red dotted lines in Figure 3.42 are provided where crack paths crossing the layers could be in question. The observed crack propagation paths testify excellent layer adhesion during the printing [308], which is not affected by UV weathering at all. Also, crack path sharp edges and direction changes can be observed with increased pF content, testifying to the reinforcement effect of the introduced pF causing crack deflection [131,263,264].

Weathering penetration depth was examined with methods that indicate volumetric changes, i.e., weight, sol-fraction, and density, as summarized in Figure 3.43. All samples show weight increases (Figure 3.43 (a)), which can be attributed to the absorbed water that fills the space between polymer molecules [309]. In addition, increasing hydrophilic pF content leads to a higher weight increase. Sol-fraction decreased (Figure 3.43 (b)) due to the additional UV-light exposure during weathering, acting as additional post-curing (sample preparation and post-processing included post-curing) that would reduce sol-fraction. Previous studies have demonstrated hydrogen bonding between the introduced pF and the polymer matrix, which is relevant to the absorbed water [93]. It could be expected that absorbed water removal would be difficult via simple Soxhlet extraction. Still, the low content of the introduced pF correlated with an increase in sample weight and density. It should be noted that the densities of the water and samples are close (1.00 and ≈ 1.12 g/cm^3 [93]) and relatively low, thus limiting the measurable effect.

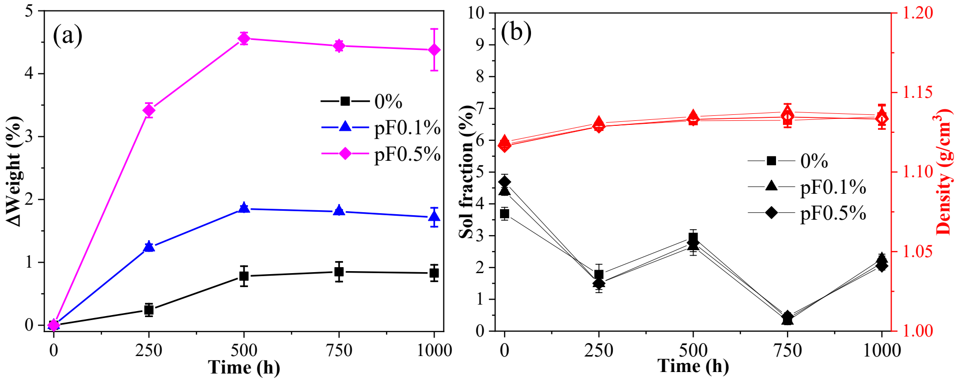

Figure 3.43. The prepared composition samples' weight changes (a), sol-fraction, and densities (b) during the UV weathering.

3.5.1.2. Chemical degradation processes

FTIR measurements were performed to characterize the chemical modifications imposed by UV weathering (Figure 3.44). A schematic representation of a crosslinked polymer network is shown in Figure 3.44 (a), where potential photodegradation locations are marked (circled ester bonds), and blue bonds show the crosslinks between monomers. When UV-light, heat, and oxygen are exposed, ester bonds can undergo photo-cleavage [310,311]. The reaction is represented in Figure 3.44 (b) and Figure 3.44 (c) [312]. Figure 3.44 (b) shows the ester bond cleavage in the middle of the chain network, while Figure 3.44 (c) shows the ester bond at a terminal, located close to the chain network end (terminal group).

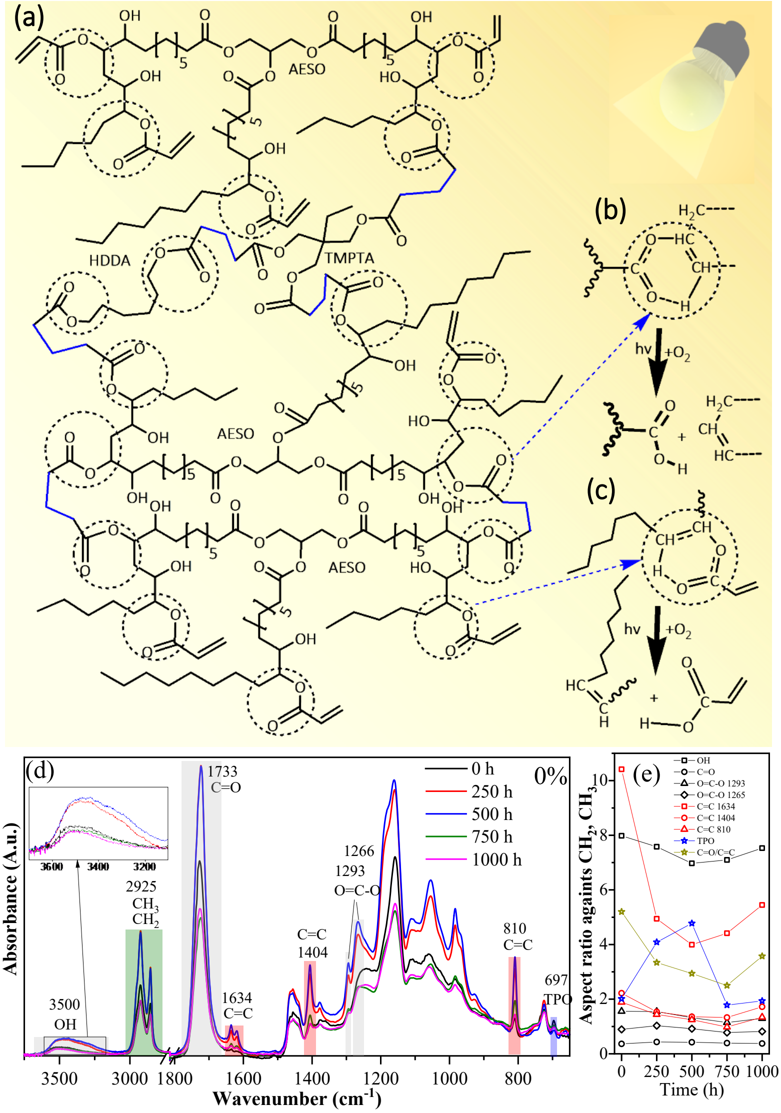

Figure 3.44. Crosslinked polymer matrix with dash circles marking possible degradation spots and blue bonds where monomers are crosslinked (a), photocleavage mechanisms and products at the crosslinked network (b), and close to terminal group (c), 0% sample FTIR spectra (d), and peak intensity ratios (e) during UV weathering.

FTIR spectra reveal a trend of increasing C=C bonds, marked red in Figure 3.44 (d). Simultaneously, the generated C=C bonds can be used in new crosslinks to form oligomers or to add chain length to the existing network. C=C bonds can occur because of crosslinking conversion limitations in the resin photopolymerization process [93]. The peak intensity ratio graph was created in Figure 3.44 (e) for better visualization of characteristic peak changes. As a reference peak, the 2925 cm^{-1} peak attributed to the CH_2 and CH_3 was chosen, and other appropriate intensities (attributed accordingly to C=C, OH, O=C-O, or TPO, as shown in Figure 3.44 (d)) were used to divide its intensity. The peak at 697 cm^{-1} was attributed to TPO using spectra from the uncured 0% resin spectra with and without TPO shown in Supplementary 20. Figure 3.44 (e), with the peak intensity ratios, shows that TPO content during UV weathering decreases while C=C increases, confirming the reported photo-cleavage [310]. Similar observations can be seen for the OH peak at 3500 cm^{-1}. The pF0.1% and pF0.5% photodegradation spectra, compared to 0%, show the same trends but are less pronounced (Supplementary 21). This indicates a lesser weathering impact on the samples, confirming the beneficial aspect of introducing pF. Although examples presented in Figure 3.44 (b) and (c) show photo-oxidation, it should be noted that similar photodegradation without O_2 present occurs in the bulk of the polymer as a chain cleavage [165]. The yellowing seen in the surface morphology analysis in Figure 3.41 (a) is attributed to the photooxidative degradation due to the formation of carboxy groups [313,314].

In parallel to photo-cleavage of the ester bonds during UV weathering (with H_2O and heat present), other degradation processes could also occur, like possible hydrolysis releasing glycerol and fatty acid chains [164]. Thermal oxidation, while with low likelihood due to relatively low temperatures (50 °C), could also occur at reactive sites δ^+ (CH_2 between O and CH-OH) and form new carbonyl groups, further developing the yellowing [315]. This would explain the slight peak intensity ratio increase after 750 h of exposure for O=C-O groups in Figure 3.44 (e).

High importance is assigned to mechanical property changes during UV weathering. While yellowing and surface cracking during weathering could be degradation limited to the sample surface, mechanical testing also shows bulk property changes [316]. Therefore, mechanical and thermomechanical performance changes were measured depending on weathering. DMA curves of samples before and after 250 and 1000 h weathering are shown in Figure 3.45. Significant structural changes are indicated by loss modulus curves depicting about a 20 °C increase in the glass transition temperature (the glass transition is taken from the peak of loss modulus [317,318]). For 0 h samples, the glass transitions temperature ranges from 6 to 7 °C, 250 h from 18 to 22 °C, and 1000 h from 23 to 26 °C. This indicates that initial UV exposure works as an additional post-curing of the acrylate matrix, while further UV exposure has a relatively limited effect. The follow-up increase in the glass transition could be explained by the structural changes induced by photooxidative degradation, which results in breaking the polymer chains, forming free radicals, and new crosslinks [319].

3.5.1.3. Thermomechanical properties

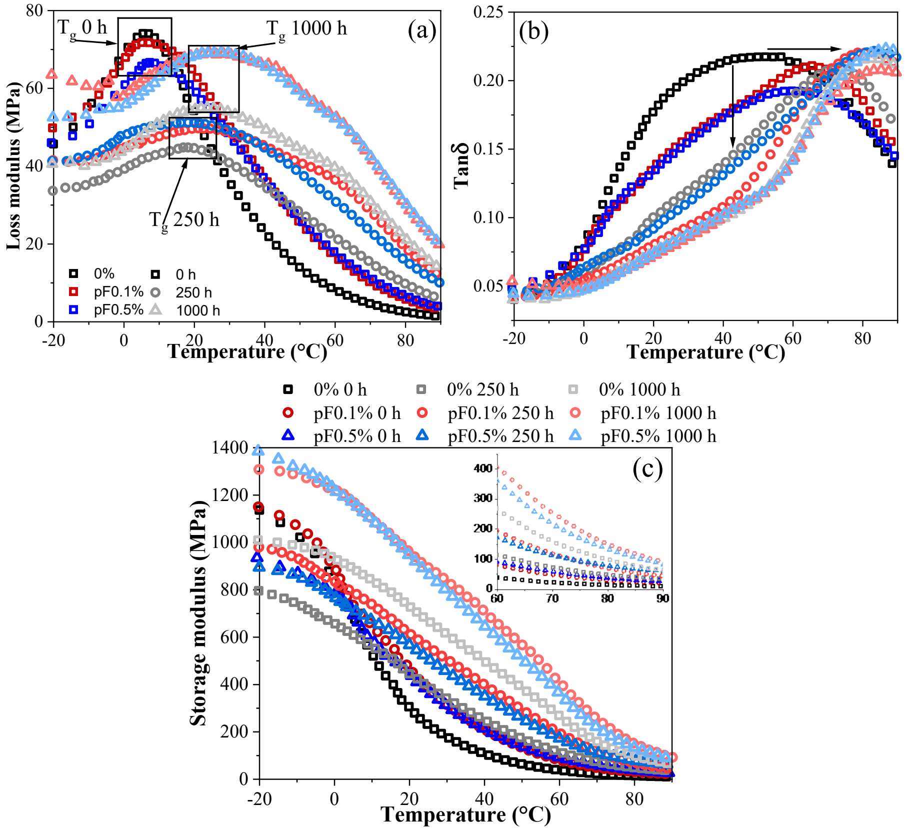

Figure 3.45. DMA measurement results: loss moduli (a), tanδ (b), and storage moduli (c) during UV weathering at 0, 250, and 1000 h.

Water's plasticizing and degrading properties lead to molecular relaxation at lower temperatures [320], which counteracts the UV-induced post-curing / crosslinking effects. By having a wider tanδ peak with a large shoulder at lower temperatures, it is clear that the degradation results in less uniform structures. The main peak of tanδ depicts the relaxation of the primary phase; the long trailing shoulder indicates the presence of lower molecular weight molecules and plasticizing effect of absorbed water [320,321]. Both loss modulus and tanδ peaks indicate that 1000 h samples are more crosslinked than 0 h and 250 h.

The intense interaction between vegetable oil acrylate matrix and pF filler has been shown to occur via an intermolecular bonding [75]. Storage modulus curves indicate that pF filler has not been compromised by the presence of water or photodegradation. In all three cases for 0 h, 250 h, and 1000 h above the glass transitions pF filled samples show significantly higher storage modulus values in the measured temperature range. The sustained increase in storage modulus values in the viscoelastic state indicates the presence of a reinforcement network that effectively supports the polymer matrix. The pF does not provide the reinforcement of composite in the glassy state. The increase of storage modulus at room temperature is up to 4-fold, which coincides well with an observed increase in the tensile and flexural moduli (discussed below). At the same time, it is visible that storage modulus values for pF0.1% and pF0.5% are close, and more often, pF0.1% shows higher values. DMA measurements were performed in tensile mode, which should be considered when compared with the results from tensile and flexural tests discussed in the next section.

3.5.1.4. Mechanical properties

Figure 3.46 depicts tensile and flexural testing results after weathering. The initial properties at 0 h of composites favor the 0.1% in tensile properties, while both pF loadings scale well with flexural properties.

The observed overall tendency for tensile strain is to decrease with increased exposure time. Tensile strain values shown in Figure 3.46 (a) reveal that ductility decreases after just 250 h for the 0% sample; however, pF0.1% and pF0.5% samples retain some of the ductility and see a more gradual decline before 1000 h weathering, where they reach similar values to that of 0%. The mechanical testing was performed at 20 °C, while DMA shows that during weathering, the glass transition significantly jumped from 6 up to 26 °C. This indicates that samples at 0 hare have higher segmental mobility and, thus, should have higher strain values. Surprisingly flexural strain in Figure 3.46 (a) shows somewhat different tendencies to those observed for the tensile strain before reaching 1000 h, where a notable drop occurs. Flexural strain increase seems to correlate with the absorbed water content, which relates to pF content, thus explaining the relatively large values observed for pF0.5%.

Sol-fraction data in Figure 3.42 (b) already indicated that UV weathering leads to additional post-curing. This observation matches the mechanical testing results, where both tensile Figure 3.46 (b) and flexural Figure 3.46 (c) moduli increase after weathering. The observed step of additional post-curing ensures higher double bond conversion rates, leading to higher crosslinking density and stiffer samples [313,314]. Table 3.11 shows all the modulus increase as folds compared to the neat 0 h sample. For the tensile moduli, the increase is higher than for flexural moduli, and the final values after weathering are within a margin of error for all compositions. In the case of flexural moduli, the values started to scale with pF loading from 250 h.

Figure 3.46 (d) with tensile and flexural stress values shows that for the 0% sample, tensile stress increases after 250 h of weathering and stays constant within the error bar range throughout the weathering. The stress bars for samples pF0.1% and pF0.5% increased to 750 h, but a sharp drop in performance was observed at 1000 h. This could be attributed to the competing processes of additional post-curing and degradation [157,162]. The degradation should not be limited to acrylate discussion and could significantly affect the nanocellulose [322]. This would explain the relatively constant values achieved by 0%. Multiple researchers have also reported that nanocellulose loses its beneficial reinforcing properties over time due to humidity and weakened interface [169,322]. It has been shown that UV-degradation affects cellulose structure significantly [323]. The already discussed increase in the glass transition temperature would indicate that at 1000 h, the properties should depend more on the matrix rather than reinforcement. Still, it can be observed that flexural stress values scaled with pF content even after 1000 h of exposure, and only tensile stress values were somewhat leveled. This again testifies to significant differences between mechanical load types concerning composites' failure [324]. The weathering shows that the appropriate pF content for tensile properties is 0.1 wt%, and for flexural properties is 0.5 wt%.

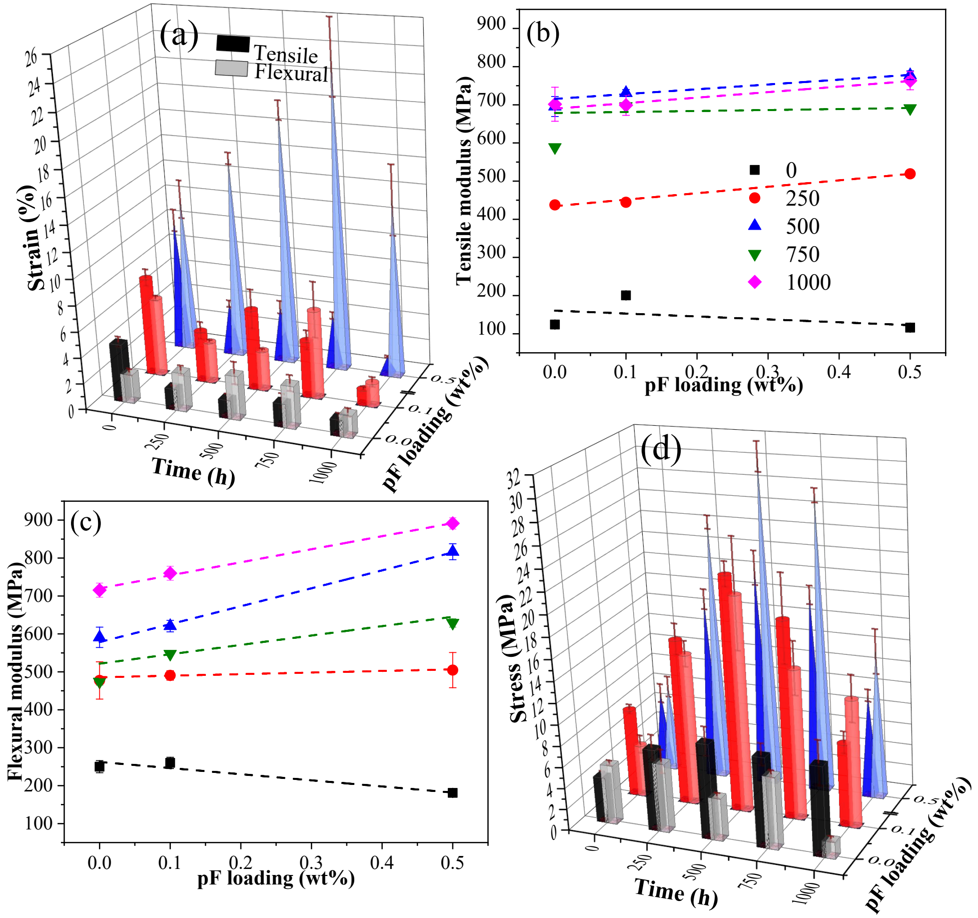

Figure 3.46. Tensile test results of the prepared composition samples during the UV weathering: tensile (left column) and flexural (right column) strain (a), tensile modulus (b), tensile (left column) and flexural (right column) stress (c), and flexural modulus (d).

Table 3.11.

Increase in mechanical moduli of the prepared composition samples after UV weathering

	0%		pF0.1%		pF0.5%	
Weathering time	Tensile (x-fold)	Flexural (x-fold)	Tensile (x-fold)	Flexural (x-fold)	Tensile (x-fold)	Flexural (x-fold)
250 h	2.5	0.91	1.22	0.88	3.47	1.78
500 h	4.6	1.36	2.65	1.38	5.70	3.51
750 h	3.75	0.90	2.48	1.10	4.96	2.47
1000 h	4.65	1.86	2.81	1.92	5.58	3.92

3.5.1.5. Summary

A bio-based acrylic resin for vat photopolymerization was prepared using acrylated epoxidized soybean oil and filter paper nanofibrillated cellulose (pF). The QUV accelerated weathering impact on 3D-printed rectangular-shape samples was examined to understand complex relationships between surface and bulk degradation processes. Morphology investigations showed that pF introduction delays the yellowing and prevents surface cracking of the samples. Chemical analysis with FTIR measurements proved simultaneous chain scission and other crosslinking processes during QUV weathering. The samples with pF reinforcement showed less pronounced chemical degradation than the reference sample. DMA measurements showed an increase in glass transition temperature of up to 20 °C after the weathering. Storage modulus revealed pF reinforcement preservation even after 1000 h of weathering. Introduced pF ensured ductility and retention of the flexural and tensile properties. Two pF loadings (pF0.1% and pF0.5%) were chosen to evaluate the effect on materials' performance during weathering. The 0.1 wt% loading showed optimal performance for tensile properties, while a higher loading of 0.5 wt% benefitted flexural properties. The introduction of pF also came with drawbacks. Increased water uptake correlated with introduced pF loading, showing a 5-fold increase for a pF0.5% loaded sample (water contributed to less than 5 wt% of the total sample weight) compared to 0% sample.

4. CONCLUSIONS

In the Doctoral Thesis research, 43 different UV-curable resin formulations were prepared with filler loading (0.1–30 wt%). Six different types of lignocellulose components (2 nanocrystalline cellulose, 2 nanofibrillated cellulose, hemicellulose, and lignin with variating biomass source, particle size, geometry, and surface functionalization) were successfully introduced into the vegetable oil-based resin formulation. Resin formulations were tested by coating/film photocuring processing and UV-light-assisted 3D printing fabrication. Single and hybrid filler approaches were evaluated. Acrylation and isocyanate (nanocellulose surface functionalization) were evaluated to improve matrix-filler interface interaction.

1. The addition of reactive diluents 1,6-hexanediol diacrylate and trimethylolpropane triacrylate into the soybean oil acrylate resin (AESO) resulted in increased double bond conversion rate (*DBC*%) by 10 %, increased thermal stability by 30 °C and storage modulus 4-fold at room temperature. Reactive diluents decreased viscosity, allowing the bio-based resin formulation to be validated for UV-assisted 3D printing showing excellent printing accuracy.
2. Performance properties improved further by introducing 5–30 wt% nanocrystalline cellulose, nanofibrillated cellulose, hemicellulose, and lignin as single and hybrid fillers. Hemicellulose increased glass transition temperature by 22 °C, and nanocrystalline cellulose most increased the storage modulus. Lignin reduced the *DBC*% down to 20 % and reduced surface hydrophilicity. Hybrid lignocellulose filler compositions, in turn, increased *DBC*%, reaching 80 % (resin with no fillers 82 %). Adjusting the hybrid filler composition allowed precise control of the sample surface morphology. Hybrid composition (C1F3H1, C3F1H1, and C2F3H1) showed higher storage modulus values than any of the 10 wt% single filler compositions. Adjusting the hybrid filler composition allowed precise control of the sample performance properties, surface morphology, etc.
3. Significant improvements in the overall mechanical performance of the 3D printed composite samples were observed with the introduction of ultra-low loading (down to 0.1 wt%) of nanofibrillated cellulose. The 0.1 wt% composite showed 1.6-fold, 2.4-fold, and 1.7-fold increases in tensile modulus, strength, and break strain, respectively. A 34 °C increase in glass transition indicated nanocellulose interaction with the polymer matrix. Additional FTIR analysis showed hydrogen bonding in the cured composite samples.
4. Nanocellulose surface functionalization improved filler-matrix compatibility – increased crosslinking density and interfacial adhesion. Functionalization resulted in a 1.77-fold and 2-fold reinforcement efficiency factor r increase in comparison to unfunctionalized nanofibrillated cellulose and nanocrystalline cellulose, respectively.
5. The introduction of nanofibrillated cellulose protected the 3D printed samples from cracking during the accelerated weathering. Nanocellulose reinforcement provided ductility and retention of the flexural and tensile properties after weathering.

REFERENCES

1. EU action to tackle the issue of plastic waste. Availabe online: https://www.eca.europa.eu/en/Pages/DocItem.aspx?did={B0EB7BF4-7786-4E45-B164-571968073A6D} (accessed on 2023 14 March).
2. The global bio-based polymer market in 2019 – A revised view. Availabe online: https://www.bioplasticsmagazine.com/en/news/meldungen/20200127-The-global-bio-based-polymer-market-in-2019-A-revised-view.php (accessed on 2023 14 Martch).
3. Market Trends on Bio-based and Plant-based Resins. Availabe online: https://coatings.specialchem.com/tech-library/article/market-trends-on-biobased-and-plant-based-resins (accessed on 2023 19 October).
4. Zhang, C.; Garrison, T.F.; Madbouly, S.A.; Kessler, M.R. Recent advances in vegetable oil-based polymers and their composites. *Progress in Polymer Science* **2017**, *71*, 91-143, doi:10.1016/j.progpolymsci.2016.12.009.
5. Meier, M.A.R.; Metzger, J.O.; Schubert, U.S. Plant oil renewable resources as green alternatives in polymer science. *Chemical Society Reviews* **2007**, *36*, 1788-1802, doi:10.1039/B703294C.
6. Su, Y.; Lin, H.; Zhang, S.; Yang, Z.; Yuan, T. One-Step Synthesis of Novel Renewable Vegetable Oil-Based Acrylate Prepolymers and Their Application in UV-Curable Coatings. *Polymers* **2020**, *12*, doi:10.3390/polym12051165.
7. Zhang, P.; Zhang, J. One-step acrylation of soybean oil (SO) for the preparation of SO-based macromonomers. *Green Chemistry* **2013**, *15*, 641-645, doi:10.1039/c3gc36961g.
8. Galià, M.; de Espinosa, L.M.; Ronda, J.C.; Lligadas, G.; Cádiz, V. Vegetable oil-based thermosetting polymers. *European Journal of Lipid Science and Technology* **2010**, *112*, 87-96, doi:10.1002/ejlt.200900096.
9. Mosiewicki, M.A.; Aranguren, M.I. A short review on novel biocomposites based on plant oil precursors. *European Polymer Journal* **2013**, *49*, 1243-1256, doi:10.1016/j.eurpolymj.2013.02.034.
10. Zhang, Y.; Li, Y.; Wang, L.; Gao, Z.; Kessler, M.R. Synthesis and Characterization of Methacrylated Eugenol as a Sustainable Reactive Diluent for a Maleinated Acrylated Epoxidized Soybean Oil Resin. *ACS Sustainable Chemistry & Engineering* **2017**, *5*, 8876-8883, doi:10.1021/acssuschemeng.7b01673.
11. Siracusa, V.; Blanco, I. Bio-Polyethylene (Bio-PE), Bio-Polypropylene (Bio-PP) and Bio-Poly(ethylene terephthalate) (Bio-PET): Recent Developments in Bio-Based Polymers Analogous to Petroleum-Derived Ones for Packaging and Engineering Applications. *Polymers* **2020**, *12*, doi:10.3390/polym12081641.
12. M. E. Fortuna, I.M.S., M. Gavrilescu. Assessment of sustainability based on lca case of woody biomass. *Cellulose Chemistry and Technology* **2012**, *46*, 493-510.
13. Gaidukovs, S.; Barkane, A. Chapter 16 Smart Wood-like Materials Based on Lignocellulose Nanoparticles. In *Cellulose Nanoparticles: Volume 1: Chemistry and Fundamentals*, The Royal Society of Chemistry: 2021; Vol. 1, pp. 402-423.
14. Li, Y.; Jiang, B.; Lou, Y.; Shi, Q.; Zhuang, R.; Zhan, Z.W. Molecular characterization of edible vegetable oils via free fatty acid and triacylglycerol fingerprints by electrospray ionization Fourier transform ion cyclotron resonance mass spectrometry. *International Journal of Food Science and Technology* **2019**, *55*, 165-174, doi:10.1111/ijfs.14258.
15. Silva, J.A.C., Grilo, L. M., Gandini, A., Lacerda, T. M. The Prospering of Macromolecular Materials Based on Plant Oils within the Blooming Field of Polymers from Renewable Resources. *Polymers (Basel)* **2021**, *13*, doi:10.3390/polym13111722.

16. Yuliati, F.; Hong, J.; Indriadi, K.S.; Picchioni, F.; Bose, R.K. Thermally Reversible Polymeric Networks from Vegetable Oils. *Polymers* **2020**, *12*, doi:10.3390/polym12081708.
17. Balart, R.; Montanes, N.; Dominici, F.; Boronat, T.; Torres-Giner, S. Environmentally Friendly Polymers and Polymer Composites. *Materials* **2020**, *13*, doi:10.3390/ma13214892.
18. Anusic, A.; Blößl, Y.; Oreski, G.; Resch-Fauster, K. High-performance thermoset with 100 % bio-based carbon content. *Polymer Degradation and Stability* **2020**, *181*, doi:10.1016/j.polymdegradstab.2020.109284.
19. Branciforti, D.S.; Lazzaroni, S.; Milanese, C.; Castiglioni, M.; Auricchio, F.; Pasini, D.; Dondi, D. Visible light 3D printing with epoxidized vegetable oils. *Additive Manufacturing* **2019**, *25*, 317-324, doi:10.1016/j.addma.2018.11.020.
20. Barkane, A.; Platnieks, O.; Jurinovs, M.; Kasetaite, S.; Ostrauskaite, J.; Gaidukovs, S.; Habibi, Y. Uv-light curing of 3d printing inks from vegetable oils for stereolithography. *Polymers* **2021**, *13*, doi:10.3390/polym13081195.
21. Ma, Y.; Ye, Y.; Wan, H.; Chen, L.; Zhou, H.; Chen, J. Chemical modification of graphene oxide to reinforce the corrosion protection performance of UV-curable polyurethane acrylate coating. *Progress in Organic Coatings* **2020**, *141*, doi:10.1016/j.porgcoat.2020.105547.
22. Fu, J.; Yu, H.; Wang, L.; Lin, L.; Khan, R.U. Preparation and properties of UV-curable hyperbranched polyurethane acrylate hard coatings. *Progress in Organic Coatings* **2020**, *144*, doi:10.1016/j.porgcoat.2020.105635.
23. Huang, M.; Liu, Y.; Klier, J.; Schiffman, J.D. High-Performance, UV-Curable Cross-Linked Films via Grafting of Hydroxyethyl Methacrylate Methylene Malonate. *Industrial & Engineering Chemistry Research* **2020**, *59*, 4542-4548, doi:10.1021/acs.iecr.9b06618.
24. Zhang, T.; Jiang, B.; Huang, Y. Combined use of methacrylate/epoxy functionalized silanes for tuning of hyperbranched polysiloxane structure. *Materials Chemistry and Physics* **2020**, *254*, doi:10.1016/j.matchemphys.2020.123525.
25. Stouten, J.; Vanpoucke, D.E.P.; Van Assche, G.; Bernaerts, K.V. UV-Curable Biobased Polyacrylates Based on a Multifunctional Monomer Derived from Furfural. *Macromolecules* **2020**, *53*, 1388-1404, doi:10.1021/acs.macromol.9b02659.
26. Tajau, R., Rohani, R., Alias, M. S., Mudri, N. H., Abdul Halim, K. A., Harun, M. H., Mat Isa, N., Che Ismail, R., Muhammad Faisal, S., Talib, M., Rawi Mohamed Zin, M., Izni Yusoff, I., Khairul Zaman, N., Asyila Ilias, I. Emergence of Polymeric Material Utilising Sustainable Radiation Curable Palm Oil-Based Products for Advanced Technology Applications. *Polymers (Basel)* **2021**, *13*, doi:10.3390/polym13111865.
27. Kousaalya, A.B.; Beyene, S.D.; Ayalew, B.; Pilla, S. Epoxidation Kinetics of High-Linolenic Triglyceride Catalyzed by Solid Acidic-Ion Exchange Resin. *Scientific Reports* **2019**, *9*, 1-12, doi:10.1038/s41598-019-45458-8.
28. Dean C . Webster, P.P.S., Zhigang Chen , Xiao Pan, Adlina Paramarta Highly functional epoxidized resins and coating. Aug. 15, 2019, 2019.
29. Yu, A.Z.; Sahouani, J.M.; Setien, R.A.; Webster, D.C. Effect of nature and extent of functional group modification on properties of thermosets from methacrylated epoxidized sucrose soyate. *Reactive and Functional Polymers* **2018**, *128*, 29-39, doi:10.1016/j.reactfunctpolym.2018.05.003.
30. Bao, X.; Dong, F.; Yu, Y.; Wang, Q.; Wang, P.; Fan, X.; Yuan, J. Green modification of cellulose-based natural materials by HRP-initiated controlled “graft from” polymerization. *International Journal of Biological Macromolecules* **2020**, *164*, 1237-1245, doi:10.1016/j.ijbiomac.2020.07.248.

31. Yin, C.; Chen, W.; Zhang, J.; Zhang, M.; Zhang, J. A facile and efficient method to fabricate high-resolution immobilized cellulose-based chiral stationary phases via thiol-ene click chemistry. *Separation and Purification Technology* **2019**, *210*, 175-181, doi:10.1016/j.seppur.2018.08.002.
32. Ma, S.; Jiang, Y.; Liu, X.; Fan, L.; Zhu, J. Bio-based tetrafunctional crosslink agent from gallic acid and its enhanced soybean oil-based UV-cured coatings with high performance. *RSC Advances* **2014**, *4*, 7, doi:10.1039/c4ra01311e.
33. Di Mauro, C.; Malburet, S.; Genua, A.; Graillot, A.; Mija, A. Sustainable Series of New Epoxidized Vegetable Oil-Based Thermosets with Chemical Recycling Properties. *Biomacromolecules* **2020**, *21*, 3923-3935, doi:10.1021/acs.biomac.0c01059.
34. Alam, M.; Akram, D.; Sharmin, E.; Zafar, F.; Ahmad, S. Vegetable oil based eco-friendly coating materials: A review article. *Arabian Journal of Chemistry* **2014**, *7*, 469-479, doi:10.1016/j.arabjc.2013.12.023.
35. Hermens, J.G.H.; Freese, T.; van den Berg, K.J.; van Gemert, R.; Feringa, B.L. A coating from nature. *Sci Adv* **2020**, *6*, doi:10.1126/sciadv.abe0026.
36. Dai, J.; Ma, S.; Wu, Y.; Zhu, J.; Liu, X. High bio-based content waterborne UV-curable coatings with excellent adhesion and flexibility. *Progress in Organic Coatings* **2015**, *87*, 197-203, doi:10.1016/j.porgcoat.2015.05.030.
37. Zhu, G.; Zhang, J.; Huang, J.; Yu, X.; Cheng, J.; Shang, Q.; Hu, Y.; Liu, C.; Hu, L.; Zhou, Y. High-performance 3D printing UV-curable resins derived from soybean oil and gallic acid. *Green Chemistry* **2021**, *23*, 5911-5923, doi:10.1039/D1GC01934A.
38. Standard SLA, DLP & LCD photopolymer resins for General Purpose applications. Availabe online: https://www.3dresyns.com/pages/standard-sla-dlp-lcd-photopolymer-resins-for-general-purpose-applications (accessed on 2023 15 March).
39. The toughest 3D-printing resins available. Availabe online: https://www.liqcreate.com/supportarticles/the-tough-3d-printing-resin-sla-dlp-lcd-msla/ (accessed on 2023 15 March).
40. Addis, C.C.; Koh, R.S.; Gordon, M.B. Preparation and characterization of a bio-based polymeric wood adhesive derived from linseed oil. *International Journal of Adhesion and Adhesives* **2020**, *102*, doi:10.1016/j.ijadhadh.2020.102655.
41. Tan, J.; Liu, B.; Fu, Q.; Wang, L.; Xin, J.; Zhu, X. Role of the Oxethyl Unit in the Structure of Vegetable Oil-Based Plasticizer for PVC: An Efficient Strategy to Enhance Compatibility and Plasticization. *Polymers* **2019**, *11*, doi:10.3390/polym11050779.
42. Singh, Y.; Sharma, A.; Singla, A. Non-edible vegetable oil-based feedstocks capable of bio-lubricant production for automotive sector applications-a review. *Environmental Science and Pollution Research* **2019**, *26*, 14867-14882, doi:10.1007/s11356-019-05000-9.
43. Volison-Klimentiev, A.; Cullari, L.; Shachar-Michaely, G.; Dor, S.; Peretz-Damari, S.; Afik, N.; Regev, O. Vegetable-Oil-Based Intelligent Ink for Oxygen Sensing. *ACS Sensors* **2020**, *5*, 3274-3280, doi:10.1021/acssensors.0c01777.
44. Rincón-Iglesias, M.; Lizundia, E.; Lanceros-Méndez, S. Water-Soluble Cellulose Derivatives as Suitable Matrices for Multifunctional Materials. *Biomacromolecules* **2019**, *20*, 2786-2795, doi:10.1021/acs.biomac.9b00574.
45. Hegde, M.B.; Mohana, K.N. A Sustainable and Eco-Friendly Polymer Based Graphene Oxide Nanocomposite Anti-Corrosion Coating on Mild Steel. *ChemistrySelect* **2020**, *5*, 1506-1515, doi:10.1002/slct.201904534.
46. Rosu, L.; Varganici, C.D.; Mustata, F.; Rosu, D.; Rosca, I.; Rusu, T. Epoxy Coatings Based on Modified Vegetable Oils for Wood Surface Protection against Fungal

Degradation. *ACS Applied Materials & Interfaces* **2020**, *12*, 14443-14458, doi:10.1021/acsami.0c00682.

47. Sahoo, S.K.; Khandelwal, V.; Manik, G. Synthesis and characterization of low viscous and highly acrylated epoxidized methyl ester based green adhesives derived from linseed oil. *International Journal of Adhesion and Adhesives* **2019**, *89*, 174-177, doi:10.1016/j.ijadhadh.2019.01.007.
48. Veith, C., iot-Néant, Florian, Miller, Stephen A., Allais, Florent. Synthesis and polymerization of bio-based acrylates: a review. *Polymer Chemistry* **2020**, *11*, 7452-7470, doi:10.1039/d0py01222j.
49. Kousaalya, A.B. Sustainable Photo-curable Polymers in Additive Manufacturing Arena: A Review. In *Sustainability & Green Polymer Chemistry Volume 1: Green Products and Processes*, H. N. Cheng, Gross, R.A., Eds. American Chemical Society: 2020; Vol. 1, pp. 89-98.
50. Khot, S.N.; Lascala, J.J.; Can, E.; Morye, S.S.; Williams, G.I.; Palmese, G.R.; Kusefoglu, S.H.; Wool, R.P. Development and application of triglyceride-based polymers and composites. *Journal of Applied Polymer Science* **2001**, *82*, 703-723, doi:https://doi.org/10.1002/app.1897.
51. G. Rosace, R.P.R., R. Arrigo, G. Malucelli. Photosensitive acrylates containing bio-based epoxy-acrylate soybean oil for 3D printing application. *Journal of Applied Polymer Science* **2021**, *138*, 51292-51303, doi:10.1002/app.51292.
52. Lebedevaite, M.; Talacka, V.; Ostrauskaite, J. High biorenewable content acrylate photocurable resins for DLP 3D printing. *Journal of Applied Polymer Science* **2020**, *138*, doi:10.1002/app.50233.
53. Li, C.; Xiao, H.; Wang, X.; Zhao, T. Development of green waterborne UV-curable vegetable oil-based urethane acrylate pigment prints adhesive: Preparation and application. *Journal of Cleaner Production* **2018**, *180*, 272-279, doi:10.1016/j.jclepro.2018.01.193.
54. Mondal, D.; Srinivasan, A.; Comeau, P.; Toh, Y.C.; Willett, T.L. Acrylated epoxidized soybean oil/hydroxyapatite-based nanocomposite scaffolds prepared by additive manufacturing for bone tissue engineering. *Mater Sci Eng C Mater Biol Appl* **2021**, *118*, 111400, doi:10.1016/j.msec.2020.111400.
55. UV curable resin for protective coatings, optical, and outdoor applications. Availabe online: https://www.sigmaaldrich.com/LV/en/product/aldrich/900156 (accessed on 2023 15 March).
56. Mendes-Felipe, C.; Oliveira, J.; Etxebarria, I.; Vilas-Vilela, J.L.; Lanceros-Mendez, S. State-of-the-Art and Future Challenges of UV Curable Polymer-Based Smart Materials for Printing Technologies. *Advanced Materials Technologies* **2019**, *4*, doi:10.1002/admt.201800618.
57. Melilli, G.; Carmagnola, I.; Tonda-Turo, C.; Pirri, F.; Ciardelli, G.; Sangermano, M.; Hakkarainen, M.; Chiappone, A. DLP 3D Printing Meets Lignocellulosic Biopolymers: Carboxymethyl Cellulose Inks for 3D Biocompatible Hydrogels. *Polymers* **2020**, *12*, doi:10.3390/polym12081655.
58. L., G.J.; R., S. Some Theoretical Considerations of Cellulose Cross-Lnking. *Textile Research Journal* **1961**, *31*, 160-171.
59. Qian, Y.Q.; Han, N.; Bo, Y.W.; Tan, L.L.; Zhang, L.F.; Zhang, X.X. Homogeneous synthesis of cellulose acrylate-g-poly (n-alkyl acrylate) solid-solid phase change materials via free radical polymerization. *Carbohydr Polym* **2018**, *193*, 129-136, doi:10.1016/j.carbpol.2018.03.057.
60. Auclair, N.; Kaboorani, A.; Riedl, B.; Landry, V.; Hosseinaei, O.; Wang, S. Influence of modified cellulose nanocrystals (CNC) on performance of bionanocomposite

coatings. *Progress in Organic Coatings* **2018**, *123*, 27-34, doi:10.1016/j.porgcoat.2018.05.027.

61. Kaboorani, A.; Auclair, N.; Riedl, B.; Hosseinaei, O.; Wang, S. Cellulose nanocrystal (CNC)-based nanocomposites for UV curable high-solid coating systems. *Journal of Coatings Technology and Research* **2017**, *14*, 1137-1145, doi:10.1007/s11998-017-9929-2.
62. Zarna, C.; Opedal, M.T.; Echtermeyer, A.T.; Chinga-Carrasco, G. Reinforcement ability of lignocellulosic components in biocomposites and their 3D printed applications – A review. *Composites Part C: Open Access* **2021**, *6*, doi:10.1016/j.jcomc.2021.100171.
63. Wang, B.; Ding, G.; Chen, K.; Jia, S.; Wei, J.; Wang, Y.; He, R.; Shao, Z. A physical and chemical double enhancement strategy for 3D printing of cellulose reinforced nanocomposite. *Journal of Applied Polymer Science* **2020**, *137*, doi:10.1002/app.49164.
64. Ambone, T.; Torris, A.; Shanmuganathan, K. Enhancing the mechanical properties of 3D printed polylactic acid using nanocellulose. *Polymer Engineering & Science* **2020**, *60*, 1842-1855, doi:10.1002/pen.25421.
65. Nishimura, H.; Kamiya, A.; Nagata, T.; Katahira, M.; Watanabe, T. Direct evidence for alpha ether linkage between lignin and carbohydrates in wood cell walls. *Sci Rep* **2018**, *8*, 6538, doi:10.1038/s41598-018-24328-9.
66. Chandra, M.R.G.S.; Madakka, M. Comparative Biochemistry and Kinetics of Microbial Lignocellulolytic Enzymes. In *Recent Developments in Applied Microbiology and Biochemistry*, 2019; 10.1016/b978-0-12-816328-3.00011-8pp. 147-159.
67. Khan, M.U.; Usman, M.; Ashraf, M.A.; Dutta, N.; Luo, G.; Zhang, S. A review of recent advancements in pretreatment techniques of lignocellulosic materials for biogas production: Opportunities and Limitations. *Chemical Engineering Journal Advances* **2022**, *10*, 100263-100278, doi:10.1016/j.ceja.2022.100263.
68. Li, S.; Li, Z.-J.; Yu, H.; Sytu, M.R.; Wang, Y.; Beeri, D.; Zheng, W.; Sherman, B.D.; Yoo, C.G.; Leem, G. Solar-Driven Lignin Oxidation via Hydrogen Atom Transfer with a Dye-Sensitized TiO2 Photoanode. *ACS Energy Letters* **2019**, *5*, 777-784, doi:10.1021/acsenergylett.9b02391.
69. Hu, L.; Fang, X.; Du, M.; Luo, F.; Guo, S. Hemicellulose-Based Polymers Processing and Application. *American Journal of Plant Sciences* **2020**, *11*, 2066-2079, doi:10.4236/ajps.2020.1112146.
70. Balli, B.; Calimli, M.H.; Kuyuldar, E.; Sen, F. Synthesis, Characterization, and Applications of Hemicellulose Based Eco-friendly Polymer Composites. In *Sustainable Polymer Composites and Nanocomposites*, 2019; 10.1007/978-3-030-05399-4_10pp. 293-311.
71. Li, X.; Zhang, X.; Yao, S.; Chang, H.; Wang, Y.; Zhang, Z. UV-blocking, transparent and hazy cellulose nanopaper with superior strength based on varied components of poplar mechanical pulp. *Cellulose* **2020**, *27*, 6563-6576, doi:10.1007/s10570-020-03236-0.
72. Auclair, N.; Kaboorani, A.; Riedl, B.; Landry, V. Effects of surface modification of cellulose nanocrystals (CNCs) on curing behavior, optical, and thermal properties of soybean oil bio-nanocomposite. *Journal of Coatings Technology and Research* **2019**, *17*, 57-67, doi:10.1007/s11998-019-00237-y.
73. Liu, Z.; Tisserat, B.H. Coating applications to natural fiber composites to improve their physical, surface and water absorption characters. *Industrial Crops and Products* **2018**, *112*, 196-199, doi:10.1016/j.indcrop.2017.12.002.

74. Poothanari, M.A.; Schreier, A.; Missoum, K.; Bras, J.; Leterrier, Y. Photocured Nanocellulose Composites: Recent Advances. *ACS Sustainable Chemistry & Engineering* **2022**, *10*, 3131-3149, doi:10.1021/acssuschemeng.1c07631.
75. Barkane, A.; Platnieks, O.; Grase, L.; Gaidukovs, S. Simultaneous wettability and stiffness control of UV-curing vegetable oil resin composites by lignocellulosic components. *Polymer* **2022**, *255*, 125154-125164, doi:10.1016/j.polymer.2022.125154.
76. Liu, Z.; Knetzer, D.A.; Wang, J.; Chu, F.; Lu, C.; Calvert, P.D. 3D printing acrylated epoxidized soybean oil reinforced with functionalized cellulose by UV curing. *Journal of Applied Polymer Science* **2021**, *139*, 51561-51571, doi:10.1002/app.51561.
77. Wang, B.; Zhou, J.; Wang, Z.; Mu, S.; Wu, R.; Wang, Z. Cellulose nanocrystal/plant oil polymer composites with hydrophobicity, humidity-sensitivity, and high wet strength. *Carbohydr Polym* **2020**, *231*, 115739-115748, doi:10.1016/j.carbpol.2019.115739.
78. Kaboorani, A.; Auclair, N.; Riedl, B.; Landry, V. Mechanical properties of UV-cured cellulose nanocrystal (CNC) nanocomposite coating for wood furniture. *Progress in Organic Coatings* **2017**, *104*, 91-96, doi:10.1016/j.porgcoat.2016.11.031.
79. Emmert, K.; Amberg-Schwab, S.; Braca, F.; Bazzichi, A.; Cecchi, A.; Somorowsky, F. bioORMOCER((R))-Compostable Functional Barrier Coatings for Food Packaging. *Polymers (Basel)* **2021**, *13*, 1257-1279, doi:10.3390/polym13081257.
80. Yang, J.; An, X.; Liu, L.; Tang, S.; Cao, H.; Xu, Q.; Liu, H. Cellulose, hemicellulose, lignin, and their derivatives as multi-components of bio-based feedstocks for 3D printing. *Carbohydr Polym* **2020**, *250*, 116881-116897, doi:10.1016/j.carbpol.2020.116881.
81. Espinosa, E.; Bascon-Villegas, I.; Rosal, A.; Perez-Rodriguez, F.; Chinga-Carrasco, G.; Rodriguez, A. PVA/(ligno)nanocellulose biocomposite films. Effect of residual lignin content on structural, mechanical, barrier and antioxidant properties. *Int J Biol Macromol* **2019**, *141*, 197-206, doi:10.1016/j.ijbiomac.2019.08.262.
82. Mohamad Aini, N.A.; Othman, N.; Hussin, M.H.; Sahakaro, K.; Hayeemasae, N. Lignin as Alternative Reinforcing Filler in the Rubber Industry: A Review. *Frontiers in Materials* **2020**, *6*, doi:10.3389/fmats.2019.00329.
83. Sutton, J.T.; Rajan, K.; Harper, D.P.; Chmely, S.C. Improving UV Curing in Organosolv Lignin-Containing Photopolymers for Stereolithography by Reduction and Acylation. *Polymers (Basel)* **2021**, *13*, 3473-3486, doi:10.3390/polym13203473.
84. Pezzana, L.; Malmstrom, E.; Johansson, M.; Sangermano, M. UV-Curable Bio-Based Polymers Derived from Industrial Pulp and Paper Processes. *Polymers (Basel)* **2021**, *13*, 1530-1556, doi:10.3390/polym13091530.
85. Goliszek, M.; Podkoscielna, B.; Klepka, T.; Sevastyanova, O. Preparation, Thermal, and Mechanical Characterization of UV-Cured Polymer Biocomposites with Lignin. *Polymers (Basel)* **2020**, *12*, 1159-1178, doi:10.3390/polym12051159.
86. Markstedt, K.; Escalante, A.; Toriz, G.; Gatenholm, P. Biomimetic Inks Based on Cellulose Nanofibrils and Cross-Linkable Xylans for 3D Printing. *ACS Appl Mater Interfaces* **2017**, *9*, 40878-40886, doi:10.1021/acsami.7b13400.
87. O'Dea, R.M.; Willie, J.A.; Epps, T.H., 3rd. 100th Anniversary of Macromolecular Science Viewpoint: Polymers from Lignocellulosic Biomass. Current Challenges and Future Opportunities. *ACS Macro Lett* **2020**, *9*, 476-493, doi:10.1021/acsmacrolett.0c00024.
88. Lucas, F.W.S.; Grim, R.G.; Tacey, S.A.; Downes, C.A.; Hasse, J.; Roman, A.M.; Farberow, C.A.; Schaidle, J.A.; Holewinski, A. Electrochemical Routes for the Valorization of Biomass-Derived Feedstocks: From Chemistry to Application. *ACS*

Energy Letters **2021**, 10.1021/acsenergylett.0c02692, 1205-1270, doi:10.1021/acsenergylett.0c02692.

89. Kerssemakers, A.A.J.; Doménech, P.; Cassano, M.; Yamakawa, C.K.; Dragone, G.; Mussatto, S.I. Production of Itaconic Acid from Cellulose Pulp: Feedstock Feasibility and Process Strategies for an Efficient Microbial Performance. *Energies* **2020**, *13*, 1654-1666, doi:10.3390/en13071654.
90. Xu, Y.; Li, N.; Wang, G.; Wang, C.; Chu, F. Synthesis of Lignin-Based MMA-co-BA Hybrid Resins from Cornstalk Residue via RAFT Miniemulsion Polymerization and Their Characteristics. *Polymers (Basel)* **2021**, *13*, 968-982, doi:10.3390/polym13060968.
91. Satyanarayana, K.G.; Arizaga, G.G.C.; Wypych, F. Biodegradable composites based on lignocellulosic fibers—An overview. *Progress in Polymer Science* **2009**, *34*, 982-1021, doi:10.1016/j.progpolymsci.2008.12.002.
92. Schmocker, A.; Khoushabi, A.; Schizas, C.; Bourban, P.E.; Pioletti, D.P.; Moser, C. Miniature probe for the delivery and monitoring of a photopolymerizable material. *J Biomed Opt* **2015**, *20*, 127001-127011, doi:10.1117/1.JBO.20.12.127001.
93. Barkane, A.; Jurinovs, M.; Briede, S.; Platnieks, O.; Onufrijevs, P.; Zelca, Z.; S., G. Biobased Resin for Sustainable Stereolithography: 3D Printed Vegetable Oil Acrylate Reinforced with Ultra-Low Content of Nanocellulose for Fossil Resin Substitution. *3D Printing and Additive Manufacturing* **2022**, *10*, 1272-1286, doi:https://doi.org/10.1089/3dp.2021.0294.
94. Collins, M.N.; Nechifor, M.; Tanasă, F.; Zănoagă, M.; McLoughlin, A.; Stróżyk, M.A.; Culebras, M.; Teacă, C.-A. Valorization of lignin in polymer and composite systems for advanced engineering applications – A review. *Int. J. Biol. Macromol.* **2019**, *131*, 828-849, doi:https://doi.org/10.1016/j.ijbiomac.2019.03.069.
95. Ridho, M.R.; Agustiany, E.A.; Rahmi Dn, M.; Madyaratri, E.W.; Ghozali, M.; Restu, W.K.; Falah, F.; Rahandi Lubis, M.A.; Syamani, F.A.; Nurhamiyah, Y., et al. Lignin as Green Filler in Polymer Composites: Development Methods, Characteristics, and Potential Applications. *Advances in Materials Science and Engineering* **2022**, *2022*, 1-33, doi:10.1155/2022/1363481.
96. Liu, W.; Chen, T.; Fei, M.-e.; Qiu, R.; Yu, D.; Fu, T.; Qiu, J. Properties of natural fiber-reinforced biobased thermoset biocomposites: Effects of fiber type and resin composition. *Composites Part B: Engineering* **2019**, *171*, 87-95, doi:10.1016/j.compositesb.2019.04.048.
97. Maddodi, B.S.; A, L.U.; Devesh, S.; Rao, A.U.; Shenoy, G.B.; Wijerathne, H.T.; Sooriyaperkasam, N.; M, P.K. Repurposing Plastic Wastes in Non-conventional Engineered Wood Building Bricks for Constructional Application – A Mechanical Characterization using Experimental and Statistical Analys. *Engineered Science* **2022**, 10.30919/es8d696, 329–336, doi:10.30919/es8d696.
98. Lian, M.; Huang, Y.; Liu, Y.; Jiang, D.; Wu, Z.; Li, B.; Xu, Q.; Murugadoss, V.; Jiang, Q.; Huang, M., et al. An overview of regenerable wood-based composites: preparation and applications for flame retardancy, enhanced mechanical properties, biomimicry, and transparency energy saving. *Advanced Composites and Hybrid Materials* **2022**, *5*, 1612-1657, doi:10.1007/s42114-022-00475-6.
99. Chu, T.; Gao, Y.; Yi, L.; Fan, C.; Yan, L.; Ding, C.; Liu, C.; Huang, Q.; Wang, Z. Highly fire-retardant optical wood enabled by transparent fireproof coatings. *Advanced Composites and Hybrid Materials* **2022**, *5*, 1821-1829, doi:10.1007/s42114-022-00440-3.
100. Yuan, B.; Guo, M.; Murugadoss, V.; Song, G.; Guo, Z. Immobilization of graphitic carbon nitride on wood surface via chemical crosslinking method for UV resistance

and self-cleaning. *Advanced Composites and Hybrid Materials* **2021**, *4*, 286-293, doi:10.1007/s42114-021-00235-y.

101. Kamarudin, S.H.; Mohd Basri, M.S.; Rayung, M.; Abu, F.; Ahmad, S.; Norizan, M.N.; Osman, S.; Sarifuddin, N.; Desa, M.; Abdullah, U.H., et al. A Review on Natural Fiber Reinforced Polymer Composites (NFRPC) for Sustainable Industrial Applications. *Polymers (Basel)* **2022**, *14*, 3698-3734, doi:10.3390/polym14173698.
102. Kumar, L.; Haleem, A.; Javaid, M. Impact of three dimensional printing in orthopedics. *Global Health Journal* **2021**, *5*, 178-182, doi:10.1016/j.glohj.2021.11.009.
103. Ngo, T.D.; Kashani, A.; Imbalzano, G.; Nguyen, K.T.Q.; Hui, D. Additive manufacturing (3D printing): A review of materials, methods, applications and challenges. *Composites Part B: Engineering* **2018**, *143*, 172-196, doi:https://doi.org/10.1016/j.compositesb.2018.02.012.
104. Jiménez, M.; Romero, L.; Domínguez, I.A.; Espinosa, M.d.M.; Domínguez, M. Additive Manufacturing Technologies: An Overview about 3D Printing Methods and Future Prospects. *Complexity* **2019**, *2019*, 9656938, doi:10.1155/2019/9656938.
105. Niaki, M.K.; Torabi, S.A.; Nonino, F. Why manufacturers adopt additive manufacturing technologies: The role of sustainability. *Journal of Cleaner Production* **2019**, *222*, 381-392, doi:https://doi.org/10.1016/j.jclepro.2019.03.019.
106. Prashar, G.; Vasudev, H.; Bhuddhi, D. Additive manufacturing: expanding 3D printing horizon in industry 4.0. *International Journal on Interactive Design and Manufacturing (IJIDeM)* **2022**, 10.1007/s12008-022-00956-4, doi:10.1007/s12008-022-00956-4.
107. Dadhania, S. *3D Printing Materials Market 2022-2032*; IDTechEx: 2022.
108. Rodriguez-Hernandez, A.G.; Chiodoni, A.; Bocchini, S.; Vazquez-Duhalt, R. 3D printer waste, a new source of nanoplastic pollutants. *Environ Pollut* **2020**, *267*, 115609, doi:10.1016/j.envpol.2020.115609.
109. Calignano, F.; Manfredi, D.; Ambrosio, E.P.; Biamino, S.; Lombardi, M.; Atzeni, E.; Salmi, A.; Minetola, P.; Iuliano, L.; Fino, P. Overview on Additive Manufacturing Technologies. *Proceedings of the IEEE* **2017**, *105*, 593-612, doi:10.1109/JPROC.2016.2625098.
110. Ligon, S.C.; Liska, R.; Stampfl, J.; Gurr, M.; Mülhaupt, R. Polymers for 3D Printing and Customized Additive Manufacturing. *Chemical Reviews* **2017**, *117*, 10212-10290, doi:10.1021/acs.chemrev.7b00074.
111. Hull, C.W.; Arcadia, C. United States Patent (19) Hull (54) (75) (73) 21) 22 (51) 52) (58) (56) APPARATUS FOR PRODUCTION OF THREE-DMENSONAL OBJECTS BY STEREO THOGRAPHY. **1984**, US005485919A, doi:US005485919A.
112. van Wijk, A.; van Wijk, I. 3D printing with biomaterials: Towards a sustainable and circular economy. *3D Printing with Biomaterials: Towards a Sustainable and Circular Economy* **2015**, 10.3233/978-1-61499-486-2-i, 1-85, doi:10.3233/978-1-61499-486-2-i.
113. Xu, W.; Wang, X.; Sandler, N.; Willför, S.; Xu, C. Three-Dimensional Printing of Wood-Derived Biopolymers: A Review Focused on Biomedical Applications. In *ACS Sustainable Chemistry and Engineering*, 2018; Vol. 6, pp 5663-5680.
114. Li, X.; Cui, R.; Sun, L.; Aifantis, K.E.; Fan, Y.; Feng, Q.; Cui, F.; Watari, F.; Xiaoming, L.; Rongrong, C., et al. 3D-Printed Biopolymers for Tissue Engineering Application. *International Journal of Polymer Science* **2014**, *2014*, 1-13, doi:10.1155/2014/829145.

115. Ligon, S.C.; Liska, R.; Stampfl, J.; Gurr, M.; Mülhaupt, R. Polymers for 3D Printing and Customized Additive Manufacturing. In *Chemical Reviews*, American Chemical Society: 2017; Vol. 117, pp 10212-10290.
116. Smith, P.G. The business of rapid prototyping. *Rapid Prototyping Journal* **1999**, *5*, 179-186, doi:10.1108/13552549910295550.
117. Chaunier, L.; Guessasma, S.; Belhabib, S.; Della Valle, G.; Lourdin, D.; Leroy, E. Material extrusion of plant biopolymers: Opportunities & challenges for 3D printing. *Additive Manufacturing* **2018**, *21*, 220-233, doi:10.1016/j.addma.2018.03.016.
118. Janusziewicz, R.; Tumbleston, J.R.; Quintanilla, A.L.; Mecham, S.J.; DeSimone, J.M. Layerless fabrication with continuous liquid interface production. *Proceedings of the National Academy of Sciences of the United States of America* **2016**, *113*, 11703-11708, doi:10.1073/pnas.1605271113.
119. Hopkins, N.; Jiang, L.; Brooks, H. Energy consumption of common desktop additive manufacturing technologies. *Cleaner Engineering and Technology* **2021**, *2*, doi:10.1016/j.clet.2021.100068.
120. Lawrence, W.H.; Bass, G.E.; Purcell, W.P.; Autian, J. Use of Mathematical Models in the Study of Structure-Toxicity Relationships of Dental Compounds: I. Esters of Acrylic and Methacrylic Acids. *Journal of Dental Research* **1972**, *51*, 526-535, doi:10.1177/00220345720510024701.
121. Voet, V.S.D.; Guit, J.; Loos, K. Sustainable Photopolymers in 3D Printing: A Review on Biobased, Biodegradable, and Recyclable Alternatives. *Macromol Rapid Commun* **2021**, *42*, e2000475, doi:10.1002/marc.202000475.
122. Taormina, G.; Sciancalepore, C.; Messori, M.; Bondioli, F. 3D printing processes for photocurable polymeric materials: technologies, materials, and future trends. *J Appl Biomater Funct Mater* **2018**, *16*, 151-160, doi:10.1177/2280800018764770.
123. Maines, E.M.; Porwal, M.K.; Ellison, C.J.; Reineke, T.M. Sustainable advances in SLA/DLP 3D printing materials and processes. *Green Chemistry* **2021**, *23*, 6863-6897, doi:10.1039/D1GC01489G.
124. Piras, C.C.; Fernandez-Prieto, S.; De Borggraeve, W.M. Nanocellulosic materials as bioinks for 3D bioprinting. *Biomater Sci* **2017**, *5*, 1988-1992, doi:10.1039/c7bm00510e.
125. Glaskova-Kuzmina, T.; Starkova, O.; Gaidukovs, S.; Platnieks, O.; Gaidukova, G. Durability of Biodegradable Polymer Nanocomposites. *Polymers (Basel)* **2021**, *13*, doi:10.3390/polym13193375.
126. Barkane, A.; Kampe, E.; Platnieks, O.; Gaidukovs, S. Cellulose Nanocrystals vs. Cellulose Nanofibers: A Comparative Study of Reinforcing Effects in UV-Cured Vegetable Oil Nanocomposites. *Nanomaterials* **2021**, *11*, 1791-1809, doi:10.3390/nano11071791.
127. Starkova, O.; Platnieks, O.; Sabalina, A.; Gaidukovs, S. Hydrothermal Ageing Effect on Reinforcement Efficiency of Nanofibrillated Cellulose/Biobased Poly(butylene succinate) Composites. *Polymers (Basel)* **2022**, *14*, doi:10.3390/polym14020221.
128. Lusis, V.; Kononova, O.; Macanovskis, A.; Stonys, R.; Lasenko, I.; Krasnikovs, A. Experimental Investigation and Modelling of the Layered Concrete with Different Concentration of Short Fibers in the Layers. *Fibers* **2021**, *9*, doi:10.3390/fib9120076.
129. Palaganas, N.B.; Mangadlao, J.D.; de Leon, A.C.C.; Palaganas, J.O.; Pangilinan, K.D.; Lee, Y.J.; Advincula, R.C. 3D Printing of Photocurable Cellulose Nanocrystal Composite for Fabrication of Complex Architectures via Stereolithography. *ACS Applied Materials & Interfaces* **2017**, *9*, 34314-34324, doi:10.1021/acsami.7b09223.

130. Palucci Rosa, R.; Rosace, G.; Arrigo, R.; Malucelli, G. Preparation and Characterization of 3D-Printed Biobased Composites Containing Micro- or Nanocrystalline Cellulose. *Polymers (Basel)* **2022**, *14*, doi:10.3390/polym14091886.
131. Vidakis, N.; Petousis, M.; Michailidis, N.; Kechagias, J.D.; Mountakis, N.; Argyros, A.; Boura, O.; Grammatikos, S. High-performance medical-grade resin radically reinforced with cellulose nanofibers for 3D printing. *Journal of the Mechanical Behavior of Biomedical Materials* **2022**, *134*, doi:10.1016/j.jmbbm.2022.105408.
132. Anycubic. Anycubic Plant-based UV Resin. Availabe online: anycubic.com/products/anycubic-plant-based-uv-resin (accessed on 15.08).
133. Elegoo. ELEGOO PLANT-BASED RAPID UV-CURING RESIN FOR LCD 3D PRINTERS. Availabe online: elegoo.com/collections/resin/products/elegoo-plant-based-rapid-resin?variant=39469352484912 (accessed on 15.08).
134. Xu, X.; Liu, F.; Jiang, L.; Zhu, J.Y.; Haagenson, D.; Wiesenborn, D.P. Cellulose Nanocrystals vs. Cellulose Nanofibrils: A Comparative Study on Their Microstructures and Effects as Polymer Reinforcing Agents. *ACS Applied Materials & Interfaces* **2013**, *5*, 2999-3009, doi:10.1021/am302624t.
135. Hakimi, N.M.F.; Lee, S.H.; Lum, W.C.; Mohamad, S.F.; Osman Al Edrus, S.S.; Park, B.D.; Azmi, A. Surface Modified Nanocellulose and Its Reinforcement in Natural Rubber Matrix Nanocomposites: A Review. *Polymers (Basel)* **2021**, *13*, doi:10.3390/polym13193241.
136. Lasenko, I.; Grauda, D.; Butkauskas, D.; Sanchaniya, J.V.; Viluma-Gudmona, A.; Lusis, V. Testing the Physical and Mechanical Properties of Polyacrylonitrile Nanofibers Reinforced with Succinite and Silicon Dioxide Nanoparticles. *Textiles* **2022**, *2*, 162-173, doi:10.3390/textiles2010009.
137. Zwawi, M. A Review on Natural Fiber Bio-Composites, Surface Modifications and Applications. *Molecules (Basel, Switzerland)* **2021**, *26*, 404, doi:10.3390/molecules26020404.
138. Redondo, A.; Mortensen, N.; Djeghdi, K.; Jang, D.; Ortuso, R.D.; Weder, C.; Korley, L.T.J.; Steiner, U.; Gunkel, I. Comparing Percolation and Alignment of Cellulose Nanocrystals for the Reinforcement of Polyurethane Nanocomposites. *ACS Applied Materials & Interfaces* **2022**, *14*, 7270-7282, doi:10.1021/acsami.1c21656.
139. Giri;, J.; ;, R.A. A Brief review on extraction of nanocellulose and its application. *BIBECHANA* **2012**, *9*, 81-87, doi:doi.org/10.3126/bibechana.v9i0.7179.
140. de Leon, A.C.; Chen, Q.; Palaganas, N.B.; Palaganas, J.O.; Manapat, J.; Advincula, R.C. High performance polymer nanocomposites for additive manufacturing applications. *Reactive and Functional Polymers* **2016**, *103*, 141-155, doi:10.1016/j.reactfunctpolym.2016.04.010.
141. Mekonnen, T.H.; Haile, T.; Ly, M. Hydrophobic functionalization of cellulose nanocrystals for enhanced corrosion resistance of polyurethane nanocomposite coatings. *Appl. Surf. Sci.* **2021**, *540*, 148299, doi:https://doi.org/10.1016/j.apsusc.2020.148299.
142. Maturi, M.; Spanu, C.; Fernández-Delgado, N.; Molina, S.I.; Comes Franchini, M.; Locatelli, E.; Sanz de León, A. Fatty acid – functionalized cellulose nanocomposites for vat photopolymerization. *Addit. Manuf.* **2023**, *61*, 103342, doi:https://doi.org/10.1016/j.addma.2022.103342.
143. Fei, M.; Liu, T.; Zhao, B.; Otero, A.; Chang, Y.-C.; Zhang, J. From Glassy Plastic to Ductile Elastomer: Vegetable Oil-Based UV-Curable Vitrimers and Their Potential Use in 3D Printing. *ACS Applied Polymer Materials* **2021**, *3*, 2470-2479, doi:10.1021/acsapm.1c00063.

144. Gastaldi, M.; Cardano, F.; Zanetti, M.; Viscardi, G.; Barolo, C.; Bordiga, S.; Magdassi, S.; Fin, A.; Roppolo, I. Functional Dyes in Polymeric 3D Printing: Applications and Perspectives. *ACS Materials Letters* **2020**, *3*, 1-17, doi:10.1021/acsmaterialslett.0c00455.
145. Xu, W.; Zhang, X.; Yang, P.; Langvik, O.; Wang, X.; Zhang, Y.; Cheng, F.; Osterberg, M.; Willfor, S.; Xu, C. Surface Engineered Biomimetic Inks Based on UV Cross-Linkable Wood Biopolymers for 3D Printing. *ACS Appl Mater Interfaces* **2019**, *11*, 12389-12400, doi:10.1021/acsami.9b03442.
146. Lee, S.; Kim, Y.; Park, D.; Kim, J. The thermal properties of a UV curable acrylate composite prepared by digital light processing 3D printing. *Composites Communications* **2021**, *26*, doi:10.1016/j.coco.2021.100796.
147. Tomal, W.; Ortyl, J. Water-Soluble Photoinitiators in Biomedical Applications. *Polymers (Basel)* **2020**, *12*, doi:10.3390/polym12051073.
148. Abdul-Monem, M.M. Naturally Derived Photoinitiators for Dental and Biomaterials Applications. *European Dental Research and Biomaterials Journal* **2021**, *1*, 72-78, doi:10.1055/s-0040-1721313.
149. Ma, Q.; Mohawk, D.; Jahani, B.; Wang, X.; Chen, Y.; Mahoney, A.; Zhu, J.Y.; Jiang, L. UV-Curable Cellulose Nanofiber-Reinforced Soy Protein Resins for 3D Printing and Conventional Molding. *ACS Applied Polymer Materials* **2020**, *2*, 4666-4676, doi:10.1021/acsapm.0c00717.
150. Navaruckiene, A.; Bridziuviene, D.; Raudoniene, V.; Rainosalo, E.; Ostrauskaite, J. Influence of Vanillin Acrylate-Based Resin Composition on Resin Photocuring Kinetics and Antimicrobial Properties of the Resulting Polymers. *Materials (Basel)* **2021**, *14*, doi:10.3390/ma14030653.
151. Alarcon, R.T.; Gaglieri, C.; Lamb, K.J.; Cavalheiro, É.T.G.; North, M.; Bannach, G. A new acrylated monomer from macaw vegetable oil that polymerizes without external photoinitiators. *Journal of Polymer Research* **2021**, *28*, doi:10.1007/s10965-021-02787-5.
152. Hu, Y.; Zhu, G.; Zhang, J.; Huang, J.; Yu, X.; Shang, Q.; An, R.; Liu, C.; Hu, L.; Zhou, Y. Rubber Seed Oil-Based UV-Curable Polyurethane Acrylate Resins for Digital Light Processing (DLP) 3D Printing. *Molecules* **2021**, *26*, doi:10.3390/molecules26185455.
153. Jurinovs, M.; Barkane, A.; Platnieks, O.; Beluns, S.; Grase, L.; Dieden, R.; Staropoli, M.; Schmidt, D.F.; Gaidukovs, S. Vat Photopolymerization of Nanocellulose-Reinforced Vegetable Oil-Based Resins: Synergy in Morphology and Functionalization. *ACS Applied Polymer Materials* **2023**, 10.1021/acsapm.3c00245, doi:10.1021/acsapm.3c00245.
154. Boquillon, N. Use of an epoxidized oil-based resin as matrix in vegetable fibers-reinforced composites. *Journal of Applied Polymer Science* **2006**, *101*, 4037-4043, doi:10.1002/app.23133.
155. Weng, Z.; Zhou, Y.; Lin, W.; Senthil, T.; Wu, L. Structure-property relationship of nano enhanced stereolithography resin for desktop SLA 3D printer. *Composites Part A: Applied Science and Manufacturing* **2016**, *88*, 234-242, doi:10.1016/j.compositesa.2016.05.035.
156. Sutton, J.T.; Rajan, K.; Harper, D.P.; Chmely, S.C. Lignin-Containing Photoactive Resins for 3D Printing by Stereolithography. *ACS Appl Mater Interfaces* **2018**, *10*, 36456-36463, doi:10.1021/acsami.8b13031.
157. Chiantore, O.; Trossarelli, L.; Lazzari, M. Photooxidative degradation of acrylic and methacrylic polymers. *Polymer* **2000**, *41*, 1657-1668, doi:10.1016/S0032-3861(99)00349-3.

158. Decker, C.; Zahouily, K.; Valet, A. Weathering Performance of Thermoset And Photoset Acrylate Coatings. *Journal of Coatings Technology* **2002**, *74*, 87-92, doi:10.1007/BF02720154.
159. Nowrouzi, Z.; Mohebby, B.; Ebrahimi, M.; Petrič, M. Weathering performance of thermally modified wood coated with polyacrylate containing olive leaf extract as a bio-based additive. *European Journal of Wood and Wood Products* **2021**, *79*, 1551-1562, doi:10.1007/s00107-021-01712-3.
160. Decker, C.; Zahouily, K. Photodegradation and photooxidation of thermoset and UV-cured acrylate polymers. *Polymer Degradation and Stability* **1999**, *64*, 293-304, doi:10.1016/S0141-3910(98)00205-5.
161. Sung, L.-P.; Jasmin, J.; Gu, X.; Nguyen, T.; Martin, J.W. Use of laser scanning confocal microscopy for characterizing changes in film thickness and local surface morphology of UV-exposed polymer coatings. *Journal of Coatings Technology and Research* **2004**, *1*, 267-276, doi:10.1007/s11998-004-0029-8.
162. Decker, C.; Masson, F.; Schwalm, R. Weathering resistance of waterbased UV-cured polyurethane-acrylate coatings. *Polymer Degradation and Stability* **2004**, *83*, 309-320, doi:10.1016/s0141-3910(03)00276-3.
163. Q-Lab. QUV. Corporation, Q.-L., Ed. 2022.
164. Tenbohlen, S.; Koch, M. Aging Performance and Moisture Solubility of Vegetable Oils for Power Transformers. *IEEE Transactions on Power Delivery* **2010**, *25*, 825-830, doi:10.1109/tpwrd.2009.2034747.
165. Yousif, E.; Haddad, R. Photodegradation and photostabilization of polymers, especially polystyrene: review. *SpringerPlus* **2013**, *2*, 32, doi:10.1186/2193-1801-2-398.
166. Marina Di Francescantonio; Thaiane Rodrigues Aguiar; César Augusto Galvão Arrais; Andrea Nóbrega Cavalcanti; Celso Ulysses Davanzo; Giannini, M. Influence of viscosity and curing mode on degree of conversion of dual-cured resin cements. *European Journal of Dentistry* **2013**, *7*, 5.
167. Wang, Q.; Liu, X.; Qiang, Z.; Hu, Z.; Cui, X.; Wei, H.; Hu, J.; Xia, Y.; Huang, S.; Zhang, J., et al. Cellulose nanocrystal enhanced, high dielectric 3D printing composite resin for energy applications. *Composites Science and Technology* **2022**, *227*, doi:10.1016/j.compscitech.2022.109601.
168. Mohan, D.; Sajab, M.S.; Kaco, H.; Bakarudin, S.B.; Noor, A.M. 3D Printing of UV-Curable Polyurethane Incorporated with Surface-Grafted Nanocellulose. *Nanomaterials (Basel)* **2019**, *9*, 1726-1741, doi:10.3390/nano9121726.
169. Gan, P.G.; Sam, S.T.; Abdullah, M.F.b.; Omar, M.F. Thermal properties of nanocellulose-reinforced composites: A review. *Journal of Applied Polymer Science* **2019**, *137*, 48544-48558, doi:10.1002/app.48544.
170. Firdous, H.; Madhu, B.; Habib, F.; Bajpai, M.; Firdous, H.; Madhu, B. Synthesis and Characterization of Acrylated Epoxidized Soybean Oil for UV Cured Coatings. *Chemistry & Chemical Technology* **2011**, *5*, 1-10.
171. Tehfe, M.; Louradour, F.; Lalevée, J.; Fouassier, J.-P. Photopolymerization Reactions: On the Way to a Green and Sustainable Chemistry. *Applied Sciences* **2013**, *3*, 490-514, doi:10.3390/app3020490.
172. Kunwong, D.; Sumanochitraporn, N.; Kaewpirom, S. Curing behavior of a UV-curable coating based on urethane acrylate oligomer: The influence of reactive monomers. *Songklanakarin Journal of Science and Technology* **2011**, *33*, 201-207.
173. Bojanić, V., Jovanović, S., Tabaković, R., Tabaković, I. Synthesis and electrochemistry of grafted copolymers of cellulose with 4-vinylpyridine, 1-vinylimidazole, 1-vinyl-2-pyrrolidinone, and 9-vinylcarbazole. *J. Appl. Polym. Sci.*

1996, *60*, 1719-1725, doi:10.1002/(sici)1097-4628(19960606)60:10<1719::aid-app24>3.0.co;2-y.

174. Chen, Z.; Xiao, P.; Zhang, J.; Tian, W.; Jia, R.; Nawaz, H.; Jin, K.; Zhang, J. A facile strategy to fabricate cellulose-based, flame-retardant, transparent and anti-dripping protective coatings. *Chemical Engineering Journal* **2020**, *379*, doi:10.1016/j.cej.2019.122270.
175. Gafurov, T.G.; Pilosov, M.Y.; Adylov, A.; Mannanova, D.; Suvorova, Y.V.; Tashpulatov, Y.T.; Nikonovich, G.V.; Usmanov, K.U. The reaction of cellulose with hexamethylene diisocyanate. *Polym. Sci. U.S.S.R.* **1970**, *12*, 2848-2853, doi:https://doi.org/10.1016/0032-3950(70)90430-2.
176. Barkane, A.; Platnieks, O.; Jurinovs, M.; Gaidukovs, S. Thermal stability of UV-cured vegetable oil epoxidized acrylate-based polymer system for 3D printing application. *Polymer Degradation and Stability* **2020**, *181*, 109347-109357, doi:10.1016/j.polymdegradstab.2020.109347.
177. Cui, H.-W.; Jiu, J.-T.; Sugahara, T.; Nagao, S.; Suganuma, K.; Uchida, H.; Schroder, K.A. Using the Friedman method to study the thermal degradation kinetics of photonically cured electrically conductive adhesives. *Journal of Thermal Analysis and Calorimetry* **2014**, *119*, 425-433, doi:10.1007/s10973-014-4195-3.
178. Gaidukovs, S.; Zukulis, E.; Bochkov, I.; Vaivodiss, R.; Gaidukova, G. Enhanced mechanical, conductivity, and dielectric characteristics of ethylene vinyl acetate copolymer composite filled with carbon nanotubes. *Journal of Thermoplastic Composite Materials* **2017**, *31*, 1161-1180, doi:10.1177/0892705717734603.
179. Sharma, A.; Thakur, M.; Bhattacharya, M.; Mandal, T.; Goswami, S. Commercial application of cellulose nano-composites - A review. *Biotechnol Rep (Amst)* **2019**, *21*, e00316, doi:10.1016/j.btre.2019.e00316.
180. Kong, D.; Meng, Y.; McKenna, G.B. Determination of the molecular weight between cross-links for different ambers: Viscoelastic measurements of the rubbery plateau*. *Polym. Eng. Sci.* **2022**, *62*, 1023-1040, doi:https://doi.org/10.1002/pen.25903.
181. Pelletier, H.; Belgacem, N.; Gandini, A. Acrylated vegetable oils as photocrosslinkable materials. *Journal of Applied Polymer Science* **2006**, *99*, 3218-3221, doi:https://doi.org/10.1002/app.22322.
182. Mysiukiewicz, O.; Kosmela, P.; Barczewski, M.; Hejna, A. Mechanical, Thermal and Rheological Properties of Polyethylene-Based Composites Filled with Micrometric Aluminum Powder. *Materials* **2020**, *13*, 1242.
183. Bail, R.; Hong, J.Y.; Chin, B.D. Effect of a red-shifted benzotriazole UV absorber on curing depth and kinetics in visible light initiated photopolymer resins for 3D printing. *Journal of Industrial and Engineering Chemistry* **2016**, *38*, 141-145, doi:10.1016/j.jiec.2016.04.017.
184. Lantean, S.; Roppolo, I.; Sangermano, M.; Pirri, C.; Chiappone, A. Development of New Hybrid Acrylic/Epoxy DLP-3D Printable Materials. *Inventions* **2018**, *3*, doi:10.3390/inventions3020029.
185. Bajpai, M.; Shukla, V.; Habib, F. Development of a heat resistant UV-curable epoxy coating. *Progress in Organic Coatings* **2005**, *53*, 239-245, doi:10.1016/j.porgcoat.2004.12.010.
186. Omonov, T.S.; Curtis, J.M. Plant Oil-Based Epoxy Intermediates for Polymers. In *Bio-Based Plant Oil Polymers and Composites*, 2016; 10.1016/b978-0-323-35833-0.00007-4pp. 99-125.
187. Black, M.; Rawlins, J.W. Thiol-ene UV-curable coatings using vegetable oil macromonomers. *European Polymer Journal* **2009**, *45*, 1433-1441, doi:10.1016/j.eurpolymj.2009.02.007.

188. M. Khalid, A.S., C. T. Ratnam, C. A. Luqman Effect of trimethylolpropane triacrylate (TMPTA) on the mechanical properties of palm fiber empty fruit bunch and cellulose fiber biocomposite. *Journal of Engineering Science and Technology* **2008**, *3*, 10.
189. Yun HU, P.J., Qianqian SHANG, Meng ZHANG, Guodong FENG, Chengguo LIU, Yonghong ZHOU. Synthesis and Application of UV-curable Phosphorous-containing Acrylated Epoxidized Soybean Oil-based Resins. *Journal of Bioresources and Bioproducts* **2019**, *4*, 9, doi:10.12162/jbb.v4i3.007.
190. Ley, C.; Carré, C.; Ibrahim, A.; Allonas, X. Application of High Performance Photoinitiating Systems for Holographic Grating Recording. In *Holographic Materials and Optical Systems*, 2017; 10.5772/66073.
191. Kaewpirom, S.; Kunwong, D. Curing behavior and cured film performance of easy-to-clean UV-curable coatings based on hybrid urethane acrylate oligomers. *Journal of Polymer Research* **2012**, *19*, doi:10.1007/s10965-012-9995-1.
192. Liu, W.; Fei, M.e.; Ban, Y.; Jia, A.; Qiu, R. Preparation and evaluation of green composites from microcrystalline cellulose and a soybean-oil derivative. *Polymers* **2017**, *9*, doi:10.3390/polym9100541.
193. Lai, W.; Li, X.; Liu, H.; Han, L.; Zhao, Y.; Li, X. Interfacial Polycondensation Synthesis of Optically Sensitive Polyurea Microcapsule. *Journal of Chemistry* **2014**, *2014*, 1-6, doi:10.1155/2014/597578.
194. Yang, Z.; Wu, G.; Wang, S.; Xu, M.; Feng, X. Dynamic postpolymerization of 3D-printed photopolymer nanocomposites: Effect of cellulose nanocrystal and postcure temperature. *Journal of Polymer Science, Part B: Polymer Physics* **2018**, *56*, 935-946, doi:10.1002/polb.24610.
195. Kayode Adekunle, D.A., Mikael Skrifvars Synthesis of reactive soybean oils for use as a biobased thermoset resins in structural natural fiber composites. *Journal of Applied Polymer Science* **2010**, *115*, 3137-3145, doi:10.1002/app.31411.
196. Li, Z.; Chen, H.; Wang, C.; Chen, L.; Liu, J.; Liu, R. Efficient photopolymerization of thick pigmented systems using upconversion nanoparticles-assisted photochemistry. *Journal of Polymer Science Part A: Polymer Chemistry* **2018**, *56*, 994-1002, doi:10.1002/pola.28969.
197. Loginos, P.; Patsidis, A.; Georgakilas, V. UV-Cured Poly(Ethylene Glycol) Diacrylate/Carbon Nanostructure Thin Films. Preparation, Characterization, and Electrical Properties. *Journal of Composites Science* **2020**, *4*, doi:10.3390/jcs4010004.
198. Fernandez-Francos, X.; Kazarian, S.G.; Ramis, X.; Serra, A. Simultaneous monitoring of curing shrinkage and degree of cure of thermosets by attenuated total reflection Fourier transform infrared (ATR FT-IR) spectroscopy. *Applied Spectroscopy* **2013**, *67*, 1427-1436, doi:10.1366/13-07169.
199. Salih, A.M.; Ahmad, M.B.; Ibrahim, N.A.; HjMohd Dahlan, K.Z.; Tajau, R.; Mahmood, M.H.; Yunus, W.M.Z.W. Synthesis of radiation curable palm oil-based epoxy acrylate: NMR and FTIR spectroscopic investigations. *Molecules* **2015**, *20*, 14191-14211, doi:10.3390/molecules200814191.
200. Navaruckiene, A.; Skliutas, E.; Kasetaite, S.; Rekstyte, S.; Raudoniene, V.; Bridziuviene, D.; Malinauskas, M.; Ostrauskaite, J. Vanillin Acrylate-Based Resins for Optical 3D Printing. *Polymers* **2020**, *12*, doi:10.3390/polym12020397.
201. Asmussen, S.; Vallo, C. Light absorbing products during polymerization of methacrylate monomers photoinitiated with phenyl-1,2-propanedione/amine. *Journal of Photochemistry and Photobiology A: Chemistry* **2009**, *202*, 228-234, doi:10.1016/j.jphotochem.2008.12.007.

202. Flory, P.J.; Jr., J.R. Statistical Mechanics of Cross-Linked Polymer Networks I. Rubberlike Elasticity. *The Journal of Chemical Physics* **1943**, *11*, 512-520, doi:10.1063/1.1723791.

203. Gaidukovs, S.; Medvids, A.; Onufrijevs, P.; Grase, L. UV-light-induced curing of branched epoxy novolac resin for coatings. *Express Polymer Letters* **2018**, *12*, 918-929, doi:10.3144/expresspolymlett.2018.78.

204. Bandyopadhyay, A.; Valavala, P.K.; Clancy, T.C.; Wise, K.E.; Odegard, G.M. Molecular modeling of crosslinked epoxy polymers: The effect of crosslink density on thermomechanical properties. *Polymer* **2011**, *52*, 2445-2452, doi:https://doi.org/10.1016/j.polymer.2011.03.052.

205. Treloar, L.R.G. *The Physics of Rubber Elasticity*; Oxford University Press, USA: 1975.

206. Rengasamy, S.; Mannari, V. Development of soy-based UV-curable acrylate oligomers and study of their film properties. *Progress in Organic Coatings* **2013**, *76*, 78-85, doi:10.1016/j.porgcoat.2012.08.012.

207. Lebedevaite, M.; Ostrauskaite, J.; Skliutas, E.; Malinauskas, M. Photoinitiator free resins composed of plant-derived monomers for the optical μ-3D printing of thermosets. *Polymers* **2019**, *11*, doi:10.3390/polym11010116.

208. Lu, J.; Khot, S.; Wool, R.P. New sheet molding compound resins from soybean oil. I. Synthesis and characterization. *Polymer* **2005**, *46*, 71-80, doi:10.1016/j.polymer.2004.10.060.

209. Ahmad, F.; Yuvaraj, N.; Bajpai, P.K. Influence of reinforcement architecture on static and dynamic mechanical properties of flax/epoxy composites for structural applications. *Composite Structures* **2021**, *255*, doi:10.1016/j.compstruct.2020.112955.

210. Rizal, S.; Mustapha, A.; Owolabi, F.A.T.; Abdul Khalil, H.P.S.; Tye, Y.Y.; Fizree, H.M.; Abdullah, C.K.; Seeta Uthaya Kumar, U.; Paridah, M.T. Enhancement of the Physical, Mechanical, and Thermal Properties of Epoxy-based Bamboo Nanofiber Nanocomposites. *BioRes.* **2018**, *13*, 7709-7725.

211. Essien, C.; Via, B.K.; Cheng, Q.; Gallagher, T.; McDonald, T.; Wang, X.; Eckhardt, L.G. Multivariate modeling of acoustomechanical response of 14-year-old suppressed loblolly pine (Pinus taeda) to variation in wood chemistry, microfibril angle and density. *Wood Science and Technology* **2017**, *51*, 475-492, doi:10.1007/s00226-017-0894-9.

212. Moon, R.J.; Martini, A.; Nairn, J.; Simonsen, J.; Youngblood, J. Cellulose nanomaterials review: structure, properties and nanocomposites. *Chem Soc Rev* **2011**, *40*, 3941-3994, doi:10.1039/c0cs00108b.

213. Galland, S.; Leterrier, Y.; Nardi, T.; Plummer, C.J.G.; Månson, J.A.E.; Berglund, L.A. UV-cured cellulose nanofiber composites with moisture durable oxygen barrier properties. *Journal of Applied Polymer Science* **2014**, *131*, doi:10.1002/app.40604.

214. Nakasone, K.; Kobayashi, T. Cytocompatible cellulose hydrogels containing trace lignin. *Mater Sci Eng C Mater Biol Appl* **2016**, *64*, 269-277, doi:10.1016/j.msec.2016.03.108.

215. Sung, J.; Sun, X.S. Cardanol modified fatty acids from camelina oils for flexible bio-based acrylates coatings. *Progress in Organic Coatings* **2018**, *123*, 242-253, doi:10.1016/j.porgcoat.2018.02.008.

216. Han, J.; Zhou, C.; Wu, Y.; Liu, F.; Wu, Q. Self-assembling behavior of cellulose nanoparticles during freeze-drying: effect of suspension concentration, particle size, crystal structure, and surface charge. *Biomacromolecules* **2013**, *14*, 1529-1540, doi:10.1021/bm4001734.

217. Wang, Z.; Ding, Y.; Wang, J. Novel Polyvinyl Alcohol (PVA)/Cellulose Nanocrystal (CNC) Supramolecular Composite Hydrogels: Preparation and Application as Soil Conditioners. *Nanomaterials (Basel)* **2019**, *9*, doi:10.3390/nano9101397.
218. Jayaramudu, T.; Ko, H.U.; Kim, H.C.; Kim, J.W.; Muthoka, R.M.; Kim, J. Electroactive Hydrogels Made with Polyvinyl Alcohol/Cellulose Nanocrystals. *Materials (Basel)* **2018**, *11*, doi:10.3390/ma11091615.
219. Lim, L.S.; Rosli, N.A.; Ahmad, I.; Mat Lazim, A.; Mohd Amin, M.C.I. Synthesis and Swelling Behavior of pH-Sensitive Semi-IPN Superabsorbent Hydrogels Based on Poly(acrylic acid) Reinforced with Cellulose Nanocrystals. *Nanomaterials (Basel)* **2017**, *7*, doi:10.3390/nano7110399.
220. Zhang, H.; Nie, J.; Muhyodin, G.; Zhu, X. The effect of solvent on postcuring in free radical photopolymerization. *Journal of Applied Polymer Science* **2017**, *134*, doi:10.1002/app.44223.
221. Steyrer, B.; Busetti, B.; Harakály, G.; Liska, R.; Stampfl, J. Hot Lithography vs. room temperature DLP 3D-printing of a dimethacrylate. *Additive Manufacturing* **2018**, *21*, 209-214, doi:10.1016/j.addma.2018.03.013.
222. Abdellaoui, H.; Bouhfid, R.; Qaiss, A.E.K. Lignocellulosic Fibres Reinforced Thermoset Composites: Preparation, Characterization, Mechanical and Rheological Properties. In *Lignocellulosic Composite Materials*, 2018; 10.1007/978-3-319-68696-7_5pp. 215-270.
223. Zhang, N.; Tao, P.; Lu, Y.; Nie, S. Effect of lignin on the thermal stability of cellulose nanofibrils produced from bagasse pulp. *Cellulose* **2019**, *26*, 7823-7835, doi:10.1007/s10570-019-02657-w.
224. Trache, D.; Tarchoun, A.F.; Derradji, M.; Hamidon, T.S.; Masruchin, N.; Brosse, N.; Hussin, M.H. Nanocellulose: From Fundamentals to Advanced Applications. *Front Chem* **2020**, *8*, 392, doi:10.3389/fchem.2020.00392.
225. Ouarhim, W.; Zari, N.; Bouhfid, R.; Qaiss, A.e.k. Mechanical performance of natural fibers–based thermosetting composites. In *Mechanical and Physical Testing of Biocomposites, Fibre-Reinforced Composites and Hybrid Composites*, 2019; 10.1016/b978-0-08-102292-4.00003-5pp. 43-60.
226. Sain, S.; Ray, D.; Mukhopadhyay, A.; Sengupta, S.; Kar, T.; Ennis, C.J.; Rahman, P.K.S.M. Synthesis and characterization of PMMA-cellulose nanocomposites by in situ polymerization technique. *Journal of Applied Polymer Science* **2012**, *126*, doi:10.1002/app.36723.
227. Izabela M. Barszczewska-Rybarek, A.K.-W., Malgorzata Kurcok, Grzegorz Chladek, Jacek Kasperski. DMA analysis of the structure of crosslinked poly(methyl methacrylate)s. *Acta of Bioengineering and Biomechanics* **2017**, *19*, doi:10.5277/ABB-00590-2016-01.
228. Lee, K.-Y.; Aitomäki, Y.; Berglund, L.A.; Oksman, K.; Bismarck, A. On the use of nanocellulose as reinforcement in polymer matrix composites. *Composites Science and Technology* **2014**, *105*, 15-27, doi:10.1016/j.compscitech.2014.08.032.
229. Abdulkhani, A.; Najd Mazhar, A.; Hedjazi, S.; Hamzeh, Y. Preparation of xylan bio-composite films reinforced with oxidized carboxymethyl cellulose and nanocellulose. *Polym. Bull.* **2020**, *77*, 6227-6239, doi:10.1007/s00289-019-03075-5.
230. Naidu, D.S.; Hlangothi, S.P.; John, M.J. Bio-based products from xylan: A review. *Carbohydr. Polym.* **2018**, *179*, 28-41, doi:https://doi.org/10.1016/j.carbpol.2017.09.064.
231. Berglund, J.; Mikkelsen, D.; Flanagan, B.M.; Dhital, S.; Gaunitz, S.; Henriksson, G.; Lindström, M.E.; Yakubov, G.E.; Gidley, M.J.; Vilaplana, F. Wood hemicelluloses

exert distinct biomechanical contributions to cellulose fibrillar networks. *Nature Communications* **2020**, *11*, 4692, doi:10.1038/s41467-020-18390-z.

232. Sadeghifar, H.; Ragauskas, A. Lignin as a UV Light Blocker—A Review. *Polymers* **2020**, *12*, doi:10.3390/polym12051134.
233. Wang, X.; Jia, Y.; Liu, Z.; Miao, J. Influence of the Lignin Content on the Properties of Poly(Lactic Acid)/lignin-Containing Cellulose Nanofibrils Composite Films. *Polymers* **2018**, *10*, doi:10.3390/polym10091013.
234. Beluns, S.; Platnieks, O.; Gaidukovs, S.; Starkova, O.; Sabalina, A.; Grase, L.; Thakur, V.K.; Gaidukova, G. Lignin and Xylan as Interface Engineering Additives for Improved Environmental Durability of Sustainable Cellulose Nanopapers. *Int. J. Mol. Sci.* **2021**, *22*, doi:10.3390/ijms222312939.
235. Wool, R.P. Bio-based composites from soybean oil and chicken feathers. In *Bio-Based Polymers and Composites*, Richard P. Wool, X.S.S., Ed. 2005; 10.1016/B978-012763952-9/50013-7pp. 411-447.
236. Boparai, K.S.; Singh, R. Thermoplastic Composites for Fused Deposition Modeling Filament: Challenges and Applications. In *Reference Module in Materials Science and Materials Engineering*, Elsevier: 2018; https://doi.org/10.1016/B978-0-12-803581-8.11409-2.
237. Kargarzadeh, H.; Mariano, M.; Huang, J.; Lin, N.; Ahmad, I.; Dufresne, A.; Thomas, S. Recent developments on nanocellulose reinforced polymer nanocomposites: A review. *Polymer* **2017**, *132*, 368-393, doi:10.1016/j.polymer.2017.09.043.
238. Nagaprasad, N.; Vignesh, V.; Karthik Babu, N.B.; Manimaran, P.; Stalin, B.; Ramaswamy, K. Effect of green hybrid fillers loading on mechanical and thermal properties of vinyl ester composites. *Polymer Composites* **2022**, 10.1002/pc.26925, 1-12, doi:10.1002/pc.26925.
239. Jesuarockiam, N.; Jawaid, M.; Zainudin, E.S.; Thariq Hameed Sultan, M.; Yahaya, R. Enhanced Thermal and Dynamic Mechanical Properties of Synthetic/Natural Hybrid Composites with Graphene Nanoplateletes. *Polymers (Basel)* **2019**, *11*, 1085-1103, doi:10.3390/polym11071085.
240. Naveen, J.; Jawaid, M.; Zainudin, E.S.; Sultan, M.T.H.; Yahaya, R.; Abdul Majid, M.S. Thermal degradation and viscoelastic properties of Kevlar/Cocos nucifera sheath reinforced epoxy hybrid composites. *Composite Structures* **2019**, *219*, 194-202, doi:10.1016/j.compstruct.2019.03.079.
241. Garcia Filho, F.d.C.; Luz, F.S.d.; Oliveira, M.S.; Pereira, A.C.; Costa, U.O.; Monteiro, S.N. Thermal behavior of graphene oxide-coated piassava fiber and their epoxy composites. *Journal of Materials Research and Technology* **2020**, *9*, 5343-5351, doi:10.1016/j.jmrt.2020.03.060.
242. Maalihan, R.D.; Chen, Q.; Tamura, H.; Sta. Agueda, J.R.H.; Pajarito, B.B.; Caldona, E.B.; Advincula, R.C. Mechanically and Thermally Enhanced 3D-Printed Photocurable Polymer Nanocomposites Containing Functionalized Chitin Nanowhiskers by Stereolithography. *ACS Applied Polymer Materials* **2022**, *4*, 2513-2526, doi:10.1021/acsapm.1c01816.
243. Jyoti, J.; Singh, B.P.; Arya, A.K.; Dhakate, S.R. Dynamic mechanical properties of multiwall carbon nanotube reinforced ABS composites and their correlation with entanglement density, adhesion, reinforcement and C factor. *RSC Advances* **2016**, *6*, 3997-4006, doi:10.1039/c5ra25561a.
244. Balakrishnan, P.; Geethamma, V.G.; Gopi, S.; Thomas, M.G.; Kunaver, M.; Huskic, M.; Kalarikkal, N.; Volova, T.; Rouxel, D.; Thomas, S. Thermal, biodegradation and theoretical perspectives on nanoscale confinement in starch/cellulose nanocomposite

modified via green crosslinker. *Int J Biol Macromol* **2019**, *134*, 781-790, doi:10.1016/j.ijbiomac.2019.05.088.

245. Ryu, I.S.; Liu, X.; Jin, Y.; Sun, J.; Lee, Y.J. Stoichiometric analysis of competing intermolecular hydrogen bonds using infrared spectroscopy. *RSC Adv* **2018**, *8*, 23481-23488, doi:10.1039/c8ra02919a.
246. Liang, C.; Du, Y.; Wang, Y.; Ma, A.; Huang, S.; Ma, Z. Intumescent fire-retardant coatings for ancient wooden architectures with ideal electromagnetic interference shielding. *Advanced Composites and Hybrid Materials* **2021**, *4*, 979-988, doi:10.1007/s42114-021-00274-5.
247. Friedman, H.L. Kinetics of Thermal Degradation of Char-Forming Plastics from Thermogravimetry. Application to a Phenolic Plastic. *Journal of Polymer Science Part C: Polymer Symposia* **1964**, *6*, 183-195, doi:10.1002/polc.5070060121.
248. Han, B.; Chen, Y.; Wu, Y.; Hua, D.; Chen, Z.; Feng, W.; Yang, M.; Xie, Q. Co-pyrolysis behaviors and kinetics of plastics–biomass blends through thermogravimetric analysis. *Journal of Thermal Analysis and Calorimetry* **2013**, *115*, 227-235, doi:10.1007/s10973-013-3228-7.
249. Yan, J.; Yang, Q.; Zhang, L.; Lei, Z.; Li, Z.; Wang, Z.; Ren, S.; Kang, S.; Shui, H. Investigation of kinetic and thermodynamic parameters of coal pyrolysis with model-free fitting methods. *Carbon Resources Conversion* **2020**, *3*, 173-181, doi:10.1016/j.crcon.2020.11.002.
250. Qian, X.; Tai, Q.; Song, L.; Yuen, R. Thermal degradation and flame-retardant properties of epoxy acrylate resins modified with a novel flame retardant containing phosphorous and nitrogen. *Fire Safety Science* **2014**, *11*, 883-894, doi:10.3801/iafss.fss.11-883.
251. Xing, W.; Jie, G.; Song, L.; Hu, S.; Lv, X.; Wang, X.; Hu, Y. Flame retardancy and thermal degradation of cotton textiles based on UV-curable flame retardant coatings. *Thermochimica Acta* **2011**, *513*, 75-82, doi:10.1016/j.tca.2010.11.014.
252. Kuhnt, T.; Morgan, F.L.C.; Baker, M.B.; Moroni, L. An efficient and easily adjustable heating stage for digital light processing set-ups. *Additive Manufacturing* **2021**, *46*, doi:10.1016/j.addma.2021.102102.
253. Xu, W.; Jambhulkar, S.; Zhu, Y.; Ravichandran, D.; Kakarla, M.; Vernon, B.; Lott, D.G.; Cornella, J.L.; Shefi, O.; Miquelard-Garnier, G., et al. 3D printing for polymer/particle-based processing: A review. *Composites Part B: Engineering* **2021**, *223*, doi:10.1016/j.compositesb.2021.109102.
254. Peterson, A.; Östergren, I.; Lotsari, A.; Venkatesh, A.; Thunberg, J.; Ström, A.; Rojas, R.; Andersson, M.; Berglund, L.A.; Boldizar, A., et al. Dynamic Nanocellulose Networks for Thermoset-like yet Recyclable Plastics with a High Melt Stiffness and Creep Resistance. *Biomacromolecules* **2019**, *20*, 3924-3932, doi:10.1021/acs.biomac.9b00993.
255. Vahid, S.; Burattini, V.; Afshinjavid, S.; Dashtkar, A. Comparison of Rheological Behaviour of Bio-Based and Synthetic Epoxy Resins for Making Ecocomposites. *Fluids* **2021**, *6*, doi:10.3390/fluids6010038.
256. Du, L.; Zhong, T.; Wolcott, M.P.; Zhang, Y.; Qi, C.; Zhao, B.; Wang, J.; Yu, Z. Dispersing and stabilizing cellulose nanoparticles in acrylic resin dispersions with unreduced transparency and changed rheological property. *Cellulose* **2018**, *25*, 2435-2450, doi:10.1007/s10570-018-1739-x.
257. Lasseuguette, E.; Roux, D.; Nishiyama, Y. Rheological properties of microfibrillar suspension of TEMPO-oxidized pulp. *Cellulose* **2007**, *15*, 425-433, doi:10.1007/s10570-007-9184-2.

258. Chaker, A.; Mutje, P.; Vilaseca, F.; Boufi, S. Reinforcing potential of nanofibrillated cellulose from nonwoody plants. *Polymer Composites* **2013**, *34*, 1999-2007, doi:10.1002/pc.22607.
259. Litvinov, V.M.; Orza, R.A.; Klüppel, M.; van Duin, M.; Magusin, P.C.M.M. Rubber–Filler Interactions and Network Structure in Relation to Stress–Strain Behavior of Vulcanized, Carbon Black Filled EPDM. *Macromolecules* **2011**, *44*, 4887-4900, doi:10.1021/ma2007255.
260. Sarvestani, A.S.; Picu, C.R. Network model for the viscoelastic behavior of polymer nanocomposites. *Polymer* **2004**, *45*, 7779-7790, doi:10.1016/j.polymer.2004.08.060.
261. Li, K.; Li, Y.; Lian, Q.; Cheng, J.; Zhang, J. Influence of cross-linking density on the structure and properties of the interphase within supported ultrathin epoxy films. *Journal of Materials Science* **2016**, *51*, 9019-9030, doi:10.1007/s10853-016-0155-6.
262. Hadden, C.M.; Jensen, B.D.; Bandyopadhyay, A.; Odegard, G.M.; Koo, A.; Liang, R. Molecular modeling of EPON-862/graphite composites: Interfacial characteristics for multiple crosslink densities. *Composites Science and Technology* **2013**, *76*, 92-99, doi:10.1016/j.compscitech.2013.01.002.
263. Meng, L.; Li, S.; Yang, W.; Simons, R.; Yu, L.; Liu, H.; Chen, L. Improvement of Interfacial Interaction between Hydrophilic Starch Film and Hydrophobic Biodegradable Coating. *ACS Sustainable Chemistry & Engineering* **2019**, *7*, 9506-9514, doi:10.1021/acssuschemeng.9b00909.
264. Lamm, M.E.; Wang, L.; Kishore, V.; Tekinalp, H.; Kunc, V.; Wang, J.; Gardner, D.J.; Ozcan, S. Material Extrusion Additive Manufacturing of Wood and Lignocellulosic Filled Composites. *Polymers* **2020**, *12*, doi:10.3390/polym12092115.
265. Tian, Y.; Kim, W.; Kiziltas, A.; Mielewski, D.; Argento, A. Effects of interfacial dynamics on the damping of biocomposites. *Sci Rep* **2022**, *12*, 20042, doi:10.1038/s41598-022-23355-x.
266. Ferreira, F.; Pinheiro, I.; de Souza, S.; Mei, L.; Lona, L. Polymer Composites Reinforced with Natural Fibers and Nanocellulose in the Automotive Industry: A Short Review. *Journal of Composites Science* **2019**, *3*, doi:10.3390/jcs3020051.
267. Nair, S.; Dartiailh, C.; Levin, D.; Yan, N. Highly Toughened and Transparent Biobased Epoxy Composites Reinforced with Cellulose Nanofibrils. *Polymers* **2019**, *11*, doi:10.3390/polym11040612.
268. Kovačič, S.; Žagar, E.; Slugovc, C. Strength versus toughness of emulsion templated Poly(Dicyclopentadiene) foams. *Polymer* **2019**, *169*, 58-65, doi:10.1016/j.polymer.2019.02.045.
269. Gan, P.G.; Sam, S.T.; Abdullah, M.F.b.; Omar, M.F. Thermal properties of nanocellulose-reinforced composites: A review. *Journal of Applied Polymer Science* **2020**, *137*, 48544, doi:https://doi.org/10.1002/app.48544.
270. Salleh, E.M.; Razali, N.A.M.; Ya'acob, W.M.H.W.; Aziz, F.A. Dynamic mechanical analysis of epoxy reinforced by nanocellulose rice straw composite.
271. Šupová, M.; Martynková, G.S.; Barabaszová, K. Effect of Nanofillers Dispersion in Polymer Matrices: A Review. *Science of Advanced Materials* **2011**, *3*, 1-25, doi:10.1166/sam.2011.1136.
272. Jyoti, J.; Babal, A.S.; Sharma, S.; Dhakate, S.R.; Singh, B.P. Significant improvement in static and dynamic mechanical properties of graphene oxide–carbon nanotube acrylonitrile butadiene styrene hybrid composites. *Journal of Materials Science* **2017**, *53*, 2520-2536, doi:10.1007/s10853-017-1592-6.
273. Zare, Y.; Rhee, K.Y. Evaluation of Mechanical Properties in Nanocomposites Containing Carbon Nanotubes Below and Above Percolation Threshold. *Jom* **2017**, *69*, 2762-2767, doi:10.1007/s11837-017-2294-x.

274. Panwar, V.; Pal, K. Dynamic Mechanical Analysis of Clay–Polymer Nanocomposites. In *Clay-Polymer Nanocomposites*, 2017; 10.1016/b978-0-323-46153-5.00012-4pp. 413-441.
275. Xu, W.; Jambhulkar, S.; Ravichandran, D.; Zhu, Y.; Kakarla, M.; Nian, Q.; Azeredo, B.; Chen, X.; Jin, K.; Vernon, B., et al. 3D Printing-Enabled Nanoparticle Alignment: A Review of Mechanisms and Applications. *Small* **2021**, *17*, e2100817, doi:10.1002/smll.202100817.
276. Yunus, D.E.; Shi, W.; Sohrabi, S.; Liu, Y. Shear induced alignment of short nanofibers in 3D printed polymer composites. *Nanotechnology* **2016**, *27*, 495302, doi:10.1088/0957-4484/27/49/495302.
277. Elder, B.; Neupane, R.; Tokita, E.; Ghosh, U.; Hales, S.; Kong, Y.L. Nanomaterial Patterning in 3D Printing. *Adv Mater* **2020**, *32*, e1907142, doi:10.1002/adma.201907142.
278. Saba, N.; Jawaid, M.; Alothman, O.Y.; Paridah, M.T. A review on dynamic mechanical properties of natural fibre reinforced polymer composites. *Construction and Building Materials* **2016**, *106*, 149-159, doi:10.1016/j.conbuildmat.2015.12.075.
279. Huang, J.; Zhou, J.; Liu, M. Interphase in Polymer Nanocomposites. *JACS Au* **2022**, 10.1021/jacsau.1c00430, doi:10.1021/jacsau.1c00430.
280. Stenstad, P.; Andresen, M.; Tanem, B.S.; Stenius, P. Chemical surface modifications of microfibrillated cellulose. *Cellulose* **2008**, *15*, 35-45, doi:10.1007/s10570-007-9143-y.
281. Verdolotti, L.; Stanzione, M.; Khlebnikov, O.; Silant'ev, V.; Postnova, I.; Lavorgna, M.; Shchipunov, Y. Dimensionally Stable Cellulose Aerogel Strengthened by Polyurethane Synthesized In Situ. *Macromolecular Chemistry and Physics* **2019**, *220*, 1800372, doi:https://doi.org/10.1002/macp.201800372.
282. Shen, Z.; Zheng, L.; Song, D.; Liu, Y.; Li, C.; Liu, J.; Xiao, Y.; Wu, S.; Zhou, T.; Zhang, B., et al. A Non-Isocyanate Route to Poly(Ether Urethane): Synthesis and Effect of Chemical Structures of Hard Segment. *Polymers* **2022**, *14*, 2039.
283. Stern, T. Side-reactions in diisocyanate-derived bulk polyurea synthesis. *J. Appl. Polym. Sci.* **2020**, *137*, 49034, doi:https://doi.org/10.1002/app.49034.
284. Tenorio-Alfonso, A.; Sánchez, M.C.; Franco, J.M. Preparation, Characterization and Mechanical Properties of Bio-Based Polyurethane Adhesives from Isocyanate-Functionalized Cellulose Acetate and Castor Oil for Bonding Wood. *Polymers* **2017**, *9*, 132.
285. Fareghi, A.R.; Moghadam, P.N.; Khalafy, J.; Bahram, M.; Moghtader, M. Preparation of a new molecularly imprinted polymer based on self-crosslinkable cellulose acrylate in aqueous solution: A drug delivery system for furosemide. *J. Appl. Polym. Sci.* **2017**, *134*, 45581, doi:10.1002/app.45581.
286. David, G.; Gontard, N.; Guerin, D.; Heux, L.; Lecomte, J.; Molina-Boisseau, S.; Angellier-Coussy, H. Exploring the potential of gas-phase esterification to hydrophobize the surface of micrometric cellulose particles. *Eur. Polym. J.* **2019**, *115*, 138-146, doi:https://doi.org/10.1016/j.eurpolymj.2019.03.002.
287. Gallego, R.; Arteaga, J.F.; Valencia, C.; Franco, J.M. Rheology and thermal degradation of isocyanate-functionalized methyl cellulose-based oleogels. *Carbohydr. Polym.* **2013**, *98 1*, 152-160.
288. Du, L.; Yu, H.; Zhang, B.; Tang, R.; Zhang, Y.; Qi, C.; Wolcott, M.P.; Yu, Z.; Wang, J. Transparent oxygen barrier nanocellulose composite films with a sandwich structure. *Carbohydr. Polym.* **2021**, *268*, 118206, doi:https://doi.org/10.1016/j.carbpol.2021.118206.

289. Shrestha, S.; Chowdhury, R.A.; Toomey, M.D.; Betancourt, D.; Montes, F.; Youngblood, J.P. Surface hydrophobization of TEMPO-oxidized cellulose nanofibrils (CNFs) using a facile, aqueous modification process and its effect on properties of epoxy nanocomposites. *Cellulose* **2019**, *26*, 9631-9643, doi:10.1007/s10570-019-02762-w.
290. Anžlovar, A.; Huskić, M.; Žagar, E. Modification of nanocrystalline cellulose for application as a reinforcing nanofiller in PMMA composites. *Cellulose* **2016**, *23*, 505-518, doi:10.1007/s10570-015-0786-9.
291. Rosace, G.; Palucci Rosa, R.; Arrigo, R.; Malucelli, G. Photosensitive acrylates containing bio-based epoxy-acrylate soybean oil for 3D printing application. *J. Appl. Polym. Sci.* **2021**, *138*, 51292, doi:https://doi.org/10.1002/app.51292.
292. Guven, M.N.; Seckin Altuncu, M.; Demir Duman, F.; Eren, T.N.; Yagci Acar, H.; Avci, D. Bisphosphonate-functionalized poly(β-amino ester) network polymers. *J. Biomed. Mater. Res., Part A* **2017**, *105*, 1412-1421, doi:https://doi.org/10.1002/jbm.a.36026.
293. Akil, H.; Zamri, M.H. 12 - Performance of natural fiber composites under dynamic loading. In *Natural Fibre Composites*, Hodzic, A., Shanks, R., Eds. Woodhead Publishing: 2014; https://doi.org/10.1533/9780857099228.3.323pp. 323-344.
294. Kletetschka, K.; Rimstidt, J.D.; Long, T.E.; Michel, F.M. Suitability of 3D-Printed devices for low-temperature geochemical experiments. *Appl. Geochem.* **2018**, *98*, 121-126, doi:https://doi.org/10.1016/j.apgeochem.2018.08.012.
295. Abitbol, T.; Rivkin, A.; Cao, Y.; Nevo, Y.; Abraham, E.; Ben-Shalom, T.; Lapidot, S.; Shoseyov, O. Nanocellulose, a tiny fiber with huge applications. *Curr. Opin. Biotechnol.* **2016**, *39*, 76-88, doi:10.1016/j.copbio.2016.01.002.
296. Nielsen, L.E. Cross-Linking–Effect on Physical Properties of Polymers. *J. Macromol. Sci., Polym. Rev.* **1969**, *3*, 69-103, doi:10.1080/15583726908545897.
297. Maalihan, R.D.; Pajarito, B.B.; Advincula, R.C. 3D-printing methacrylate/chitin nanowhiskers composites via stereolithography: Mechanical and thermal properties. *Mater. Today: Proc.* **2020**, *33*, 1819-1824, doi:https://doi.org/10.1016/j.matpr.2020.05.063.
298. Feng, X.; Yang, Z.; Wang, S.; Wu, Z. The reinforcing effect of lignin-containing cellulose nanofibrils in the methacrylate composites produced by stereolithography. *Polym. Eng. Sci.* **2022**, *62*, 2968-2976, doi:https://doi.org/10.1002/pen.26077.
299. Tee, Y.L.; Tran, P.; Leary, M.; Pille, P.; Brandt, M. 3D Printing of polymer composites with material jetting: Mechanical and fractographic analysis. *Addit. Manuf.* **2020**, *36*, 101558, doi:https://doi.org/10.1016/j.addma.2020.101558.
300. Yaragalla, S.; Zahid, M.; Panda, J.; Tsagarakis, N.; Cingolani, R.; Athanassiou, A. Comprehensive Enhancement in Thermomechanical Performance of Melt-Extruded PEEK Filaments by Graphene Incorporation. *Polymers* **2021**, *13*, 1425, doi:10.3390/polym13091425.
301. Padmanathan, H.R.; Federico, C.E.; Addiego, F.; Rommel, R.; Kotecky, O.; Westermann, S.; Fleming, Y. Influence of Silica Specific Surface Area on the Viscoelastic and Fatigue Behaviors of Silica-Filled SBR Composites. *Polymers (Basel)* **2021**, *13*, 3094, doi:10.3390/polym13183094.
302. Shao, Y.; Yashiro, T.; Okubo, K.; Fujii, T. Effect of cellulose nano fiber (CNF) on fatigue performance of carbon fiber fabric composites. *Composites, Part A* **2015**, *76*, 244-254, doi:https://doi.org/10.1016/j.compositesa.2015.05.033.
303. Zhang, J.; Zhang, D.; Zhang, A.; Jia, Z.; Jia, D. Poly (methyl methacrylate) grafted halloysite nanotubes and its epoxy acrylate composites by ultraviolet curing method. *J. Reinf. Plast. Compos.* **2013**, *32*, 713-725, doi:10.1177/0731684412472745.

304. Noè, C.; Cosola, A.; Tonda-Turo, C.; Sesana, R.; Delprete, C.; Chiappone, A.; Hakkarainen, M.; Sangermano, M. DLP-printable fully biobased soybean oil composites. *Polymer* **2022**, *247*, 124779, doi:10.1016/j.polymer.2022.124779.
305. Seabra, C.P.; Sousa, A.C.; Bragança, I.M.F.; Silva, C.M.A.; Robalo, M.P.; Loja, M.A.R.; Martins, P.A.F. On the Performance and Recyclability of a Green Composite Based on AESO Resin. *J. Manuf. Mater. Process.* **2020**, *4*, 65, doi:10.3390/jmmp4030065.
306. Philip, M.; Al-Azzawi, F. Effects of Natural and Artificial Weathering on the Physical Properties of Recycled Poly(ethylene terephthalate). *Journal of Polymers and the Environment* **2018**, *26*, 3139-3148, doi:10.1007/s10924-018-1191-x.
307. Zhang, H.; Chen, H.; She, Y.; Zheng, X.; Pu, J. Anti-Yellowing Property of Polyurethane Improved by the Use of Surface-Modified Nanocrystalline Cellulose. *BioResources* **2014**, *9*, 673-684.
308. Gojzewski, H.; Guo, Z.; Grzelachowska, W.; Ridwan, M.G.; Hempenius, M.A.; Grijpma, D.W.; Vancso, G.J. Layer-by-Layer Printing of Photopolymers in 3D: How Weak is the Interface? *ACS Appl Mater Interfaces* **2020**, *12*, 8908-8914, doi:10.1021/acsami.9b22272.
309. Briede, S.; Barkane, A.; Jurinovs, M.; Thakur, V.K.; Gaidukovs, S. Acrylation of biomass: a review of synthesis process – know how and future application directions. *Current Opinion in Green and Sustainable Chemistry* **2022**, 10.1016/j.cogsc.2022.100626, doi:10.1016/j.cogsc.2022.100626.
310. Shanti, R.; Hadi, A.N.; Salim, Y.S.; Chee, S.Y.; Ramesh, S.; Ramesh, K. Degradation of ultra-high molecular weight poly(methyl methacrylate-co-butyl acrylate-co-acrylic acid) under ultra violet irradiation. *RSC Advances* **2017**, *7*, 112-120, doi:10.1039/c6ra25313j.
311. Wei, L.; McDonald, A.G. Accelerated weathering studies on the bioplastic, poly(3-hydroxybutyrate-co-3hydroxyvalerate). *Polymer Degradation and Stability* **2016**, *126*, 93-100, doi:10.1016/j.polymdegradstab.2016.01.023.
312. Niaounakis, M. 2. Properties. In *Biopolymers: Applications and Trends*, Jackson, D., Ed. William Andrew Publishing: Oxford, 2015; 10.1016/b978-0-323-35399-1.00002-8pp. 91-138.
313. Peutzfeldt, A.; Asmussen, E. The effect of postcuring on quantity of remaining double bonds, mechanical properties, and in vitro wear of two resin composite. *Journal of Dentistry* **2000**, *28*, 447–452, doi:10.1016/S0300-5712(00)00021-X.
314. Štaffová, M.; Ondreáš, F.; Svatík, J.; Zbončák, M.; Jančář, J.; Lepcio, P. 3D printing and post-curing optimization of photopolymerized structures: Basic concepts and effective tools for improved thermomechanical properties. *Polymer Testing* **2022**, *108*, doi:10.1016/j.polymertesting.2022.107499.
315. Krauklis, A.E.; Echtermeyer, A.T. Mechanism of Yellowing: Carbonyl Formation during Hygrothermal Aging in a Common Amine Epoxy. *Polymers (Basel)* **2018**, *10*, doi:10.3390/polym10091017.
316. Hetnarski, R.B. *Encyclopedia of Thermal Stresses*; 2014; 10.1007/978-94-007-2739-7.
317. Lei, Z.; Xing, W.; Wu, J.; Huang, G.; Wang, X.; Zhao, L. The proper glass transition temperature of amorphous polymers on dynamic mechanical spectra. *Journal of Thermal Analysis and Calorimetry* **2013**, *116*, 447-453, doi:10.1007/s10973-013-3526-0.
318. Yong, A.X.H.; Sims, G.D.; Gnaniah, S.J.P.; Ogin, S.L.; Smith, P.A. Heating rate effects on thermal analysis measurement ofTgin composite materials. *Advanced Manufacturing: Polymer & Composites Science* **2017**, *3*, 43-51, doi:10.1080/20550340.2017.1315908.

319. Patel, S.R.; Case, S.W. Durability of hygrothermally aged graphite/epoxy woven composite under combined hygrothermal conditions. *International Journal of Fatigue 24*, 1295-1301, doi:10.1016/S0142-1123(02)00044-0.
320. Rocha, I.B.C.M.; Raijmaekers, S.; Nijssen, R.P.L.; van der Meer, F.P.; Sluys, L.J. Hygrothermal ageing behaviour of a glass/epoxy composite used in wind turbine blades. *Composite Structures* **2017**, *174*, 110-122, doi:10.1016/j.compstruct.2017.04.028.
321. Oliveira, M.S.; da Luz, F.S.; da Costa Garcia Filho, F.; Pereira, A.C.; de Oliveira Aguiar, V.; Lopera, H.A.C.; Monteiro, S.N. Dynamic Mechanical Analysis of Thermally Aged Fique Fabric-Reinforced Epoxy Composites. *Polymers (Basel)* **2021**, *13*, doi:10.3390/polym13224037.
322. Roszowska-Jarosz, M.; Masiewicz, J.; Kostrzewa, M.; Kucharczyk, W.; Żurowski, W.; Kucińska-Lipka, J.; Przybyłek, P. Mechanical Properties of Bio-Composites Based on Epoxy Resin and Nanocellulose Fibres. *Materials* **2021**, *14*, doi:10.3390/ma14133576.
323. Shi, H.; Ni, Y.; Guo, H.; Liu, Y. Chemical Structure and Microscopic Morphology Changes of Dyed Wood Holocellulose Exposed to UV Irradiation. *Polymers (Basel)* **2023**, *15*, doi:10.3390/polym15051125.
324. Yu, T.; Zhang, Z.; Song, S.; Bai, Y.; Wu, D. Tensile and flexural behaviors of additively manufactured continuous carbon fiber-reinforced polymer composites. *Composite Structures* **2019**, *225*, doi:10.1016/j.compstruct.2019.111147.
325. Nandanwar R.A; Chaudhari A.R; J.D, E. Nitrobenzene Oxidation for Isolation of Value Added Products from Industrial Waste Lignin. *Journal of Chemical, Biological and Physical Sciences* **2016**, *6*, 13.
326. Španić, N.; Jambreković, V.; Šernek, M.; Medved, S. Influence of Natural Fillers on Thermal and Mechanical Properties and Surface Morphology of Cellulose Acetate-Based Biocomposites. *International Journal of Polymer Science* **2019**, *2019*, 1-17, doi:10.1155/2019/1065024.
327. Nassar, M.M.A.; Tarboush, B.J.A.; Alzebdeh, K.I.; Al-Hinai, N.; Pervez, T. New Synthesis Routes toward Improvement of Natural Filler/Synthetic Polymer Interfacial Crosslinking. *Polymers (Basel)* **2022**, *14*, doi:10.3390/polym14030629.
328. Bhagia, S.; Ďurkovič, J.; Lagaňa, R.; Kardošová, M.; Kačík, F.; Cernescu, A.; Schäfer, P.; Yoo, C.G.; Ragauskas, A.J. Nanoscale FTIR and Mechanical Mapping of Plant Cell Walls for Understanding Biomass Deconstruction. *ACS Sustainable Chemistry & Engineering* **2022**, *10*, 3016-3026, doi:10.1021/acssuschemeng.1c08163.
329. P. K. Adapa; L. G. Tabil; G. J. Schoenau; Canam, T.; Dumonceaux, T. Quantitative Analysis of Lignocellulosic Components of Non-Treated and Steam Exploded Barley, Canola, Oat and Wheat Straw Using Fourier Transform Infrared Spectroscopy. *Journal of Agricultural Science and Technology B 1* **2011**, *12*, 12.
330. Agustin-Salazar, S.; Cerruti, P.; Medina-Juarez, L.A.; Scarinzi, G.; Malinconico, M.; Soto-Valdez, H.; Gamez-Meza, N. Lignin and holocellulose from pecan nutshell as reinforcing fillers in poly (lactic acid) biocomposites. *International Journal of Biological Macromolecules* **2018**, *115*, 727-736, doi:10.1016/j.ijbiomac.2018.04.120.
331. Lopez Serna, D.; Elizondo Martinez, P.; Reyes Gonzalez, M.A.; Zaldivar Cadena, A.A.; Zaragoza Contreras, E.A.; Sanchez Anguiano, M.G. Synthesis and Characterization of a Lignin-Styrene-Butyl Acrylate Based Composite. *Polymers (Basel)* **2019**, *11*, doi:10.3390/polym11061080.
332. Rashid, T.; Kait, C.F.; Murugesan, T. A “Fourier Transformed Infrared” Compound Study of Lignin Recovered from a Formic Acid Process. *Procedia Engineering* **2016**, *148*, 1312-1319, doi:10.1016/j.proeng.2016.06.547.

333. Piccinino, D.; Capecchi, E.; Botta, L.; Bollella, P.; Antiochia, R.; Crucianelli, M.; Saladino, R. Layer by layer supported laccase on lignin nanoparticles catalyzes the selective oxidation of alcohols to aldehydes. *Catalysis Science and Technology* **2019**, *9*, 4125-4134, doi:10.1039/c9cy00962k.
334. Lun, L.W.; Gunny, A.A.N.; Kasim, F.H.; Arbain, D. Fourier transform infrared spectroscopy (FTIR) analysis of paddy straw pulp treated using deep eutectic solvent.
335. Flórez Pardo, L.M.; González Córdoba, A.; López Galán, J.E. Characterization of hemicelluloses from leaves and tops of the CC 8475, CC 8592, and V 7151 varieties of sugarcane (Saccharum officinarum L. *Dyna* **2019**, *86*, 98-107, doi:10.15446/dyna.v86n210.75757.
336. Ho, Y.H.; Parthiban, A.; Thian, M.C.; Ban, Z.H.; Siwayanan, P.; Lai, J.-Y. Acrylated Biopolymers Derived via Epoxidation and Subsequent Acrylation of Vegetable Oils. *International Journal of Polymer Science* **2022**, *2022*, 1-12, doi:10.1155/2022/6210128.
337. Narewska, J.; Lassila, L.; Fardim, P. Preparation and characterization of new mouldable cellulose-AESO biocomposites. *Cellulose* **2014**, *21*, 1769-1780, doi:10.1007/s10570-013-0157-3.
338. Goncalves, F.A.; Costa, C.S.; Fabela, I.G.; Farinha, D.; Faneca, H.; Simoes, P.N.; Serra, A.C.; Bartolo, P.J.; Coelho, J.F. 3D printing of new biobased unsaturated polyesters by microstereo-thermallithography. *Biofabrication* **2014**, *6*, 035024, doi:10.1088/1758-5082/6/3/035024.
339. Li, X.; Wang, D.; Zhao, L.; Hou, X.; Liu, L.; Feng, B.; Li, M.; Zheng, P.; Zhao, X.; Wei, S. UV LED curable epoxy soybean-oil-based waterborne PUA resin for wood coatings. *Progress in Organic Coatings* **2021**, *151*, doi:10.1016/j.porgcoat.2020.105942.
340. Yang, R. Chapter 7 - Polymer degradation and stability. In *Polymer Science and Nanotechnology*, Narain, R., Ed. Elsevier: 2020; https://doi.org/10.1016/B978-0-12-816806-6.00007-8pp. 125-148.

5. SUPPLEMENTARY

Supplementary 1.

FTIR spectra of HDDA and TMPTA reactive diluents before and after curing at different UV-irradiation times.

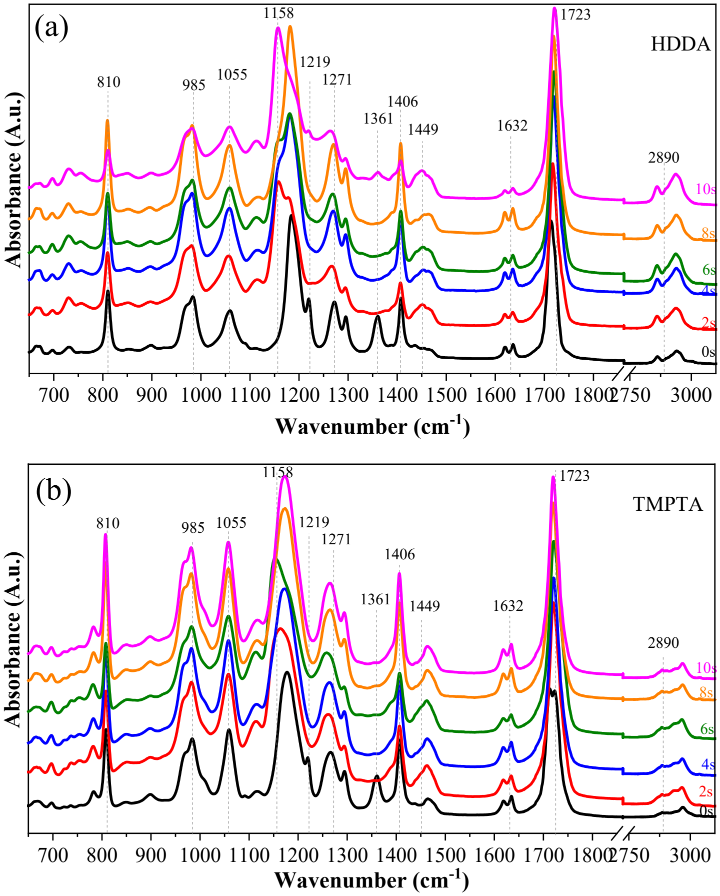

Supplementary 2.

FTIR spectra of resins and cured compositions of VO and 5 wt% compositions (a). FTIR spectra of cured 0 wt%, and 20 and 30 wt% C and F nanocomposites (b). The curing time was 10 s.

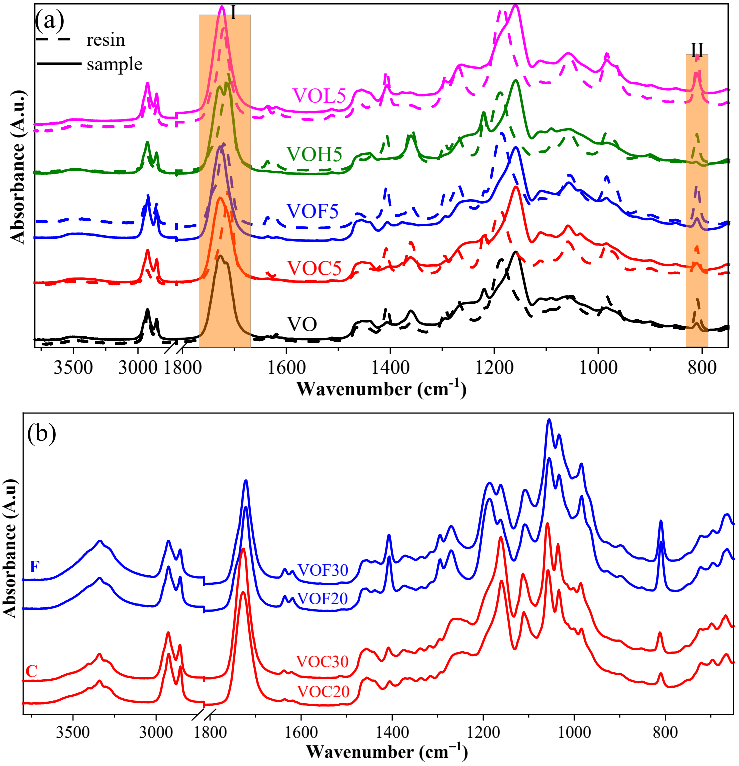

Supplementary 3.

FTIR spectra cured VO composition CNC, CNF, L fillers and HC diluent.

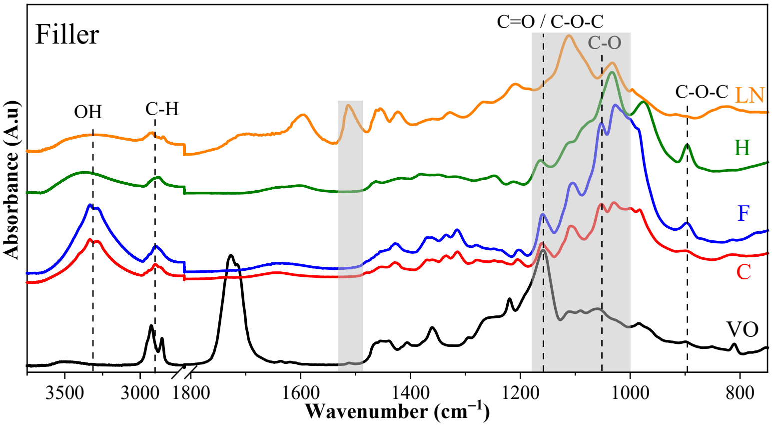

Supplementary 4.

The characteristic absorption peaks attributed to the polymer matrix and lignocellulose component structural groups

Absorption peak, cm^{-1}	Functional group				Ref.
	Absorption peaks of F	Absorption peaks of C	Absorption peaks of H	Absorption peaks of LN	
826				Represents aromatic C-H out of plane deformation	[325]
897	C-O-C asymmetric stretching at β-glycosidic linkages of amorphous cellulose		C-H deformation in cellulose	-	[216,223,326]
996			972 cm^{-1} rocking and symmetric bending vibration modes of CH_3 groups	C−OH stretching of C6	[327,328]
1030	Characteristic C-O stretching of the pyranose ring skeletal vibration		1035 cm^{-1} -C-O, C=C and C-C-O vibrational stretching	1033 cm^{-1} C-O-C, C-O by ring vibrations of carbohydrates	[328-330]
1055			-	-	
1107			1111 cm^{-1} asymmetric in phase ring vibrations	1110 cm^{-1} C-O-C, C-O by ring vibrations of carbohydrates	
1160	C-O-C asymmetrical stretching at β-glycosidic linkage		C-O-C vibrations	-	[216,326]
1209	-		1213 cm^{-1} C-O stretching	C-O in G ring	[329,331]
1246	-		C-O stretch in hemicellulose)	-	[326]
1268	-		-	Guaiacyl ring breathing	[332]
1316	-CH_2- wagging at C6		-CH_2- wagging at C6	1328 cm^{-1}	[216]

1328			Syringyl ring breathing with CO stretching	[328,331]
1348		$C-H_2$ bending	-OH	[328,331]
1381		Rocking and symmetric bending vibration modes of CH_3 groups	Phenolic OH and aliphatic C–H in methyl groups	[223,327,332]
1430	$-CH_2-$ symmetric bending	-	1423 cm^{-1} in plane bending in C-H group ($C=CH_2$)	[218]
1455		1461 cm^{-1} C-H deformation (methyl and methylene)	C-H deformation asymmetric in $-CH_3$ and $-CH_2-$	[329,332]
1513			Aromatic skeletal vibrations, G>S	[223,332]
1595			Aromatic skeletal vibrations plus C=O stretch	[223,332,333]
1636	Water adsorbed into the cellulose fibrils	Absorbed water	1630 cm^{-1} stretching of the C=C and C=O lignin aromatic ring	[326,334]
1701			C=O stretch in unconjugated ketones carbonyls and in ester groups	[325,331,333]
2888	$-CH_2-$ stretching	$-CH_2-$ stretching	2847/2914 cm^{-1} $-CH_2-$, $-CH_3$, C-H stretch	[218,333]
3338	O-H stretching	3372 cm^{-1} O-H stretching	3311 cm^{-1} -OH stretching	[216,217,335]
	Absorption peaks of AESO			
810	C=C out of plane deformation			[199,215]
985	$CH_2=CH-R$ asymmetric band			[170]
1055	C-H asymmetric stretching			[20]
1160	C-O-C			[336]
1185	C-O-C stretching vibrations			[336,337]
1268, 1294	O=C-O			[20]
1409	$CH_2=CH$ scissoring band for terminal alkene			[206,215]
1460	CH scissoring band in $-CH_2-$			[336]

1629	$CH_2=CH$	[215]
1716	C=O stretching of carbonyl groups of acrylates	[215,337,338]
1727	C=O stretching of carbonyl groups of the triglyceride	[215]
2850, 2920	$-CH_2-$, $-CH_3$ groups C-H stretching (saturated fatty acid backbone stretching band)	[199,339]
3499	-OH stretching	[199,206]

Supplementary 5.

Double bond conversion rate % (DBC%) for 5, 20, and 30 wt% compositions.

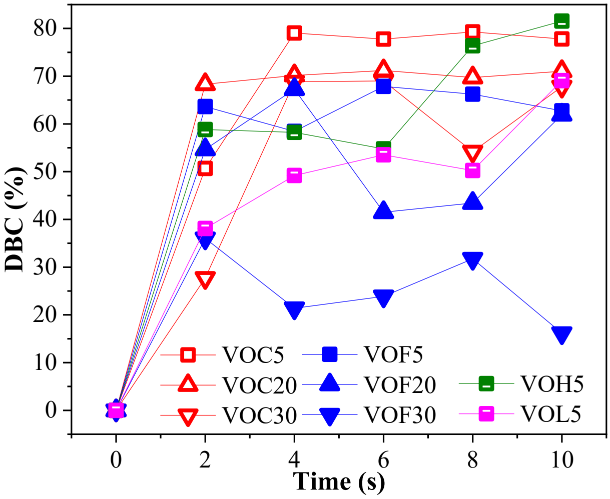

Supplementary 6.

FTIR spectra of C=O group for VO resin (black dashed line) and cured compositions (black solid line), 5 wt% compositions (dashed lines – theoretical spectra obtained with Lambert-Beer's equation and solid lines – experimental spectra), and lignocellulose components (dotted lines) (a) and FTIR spectra of uncured (dashed lines) and cured (solid lines) VOC30 and VOF30 compositions.

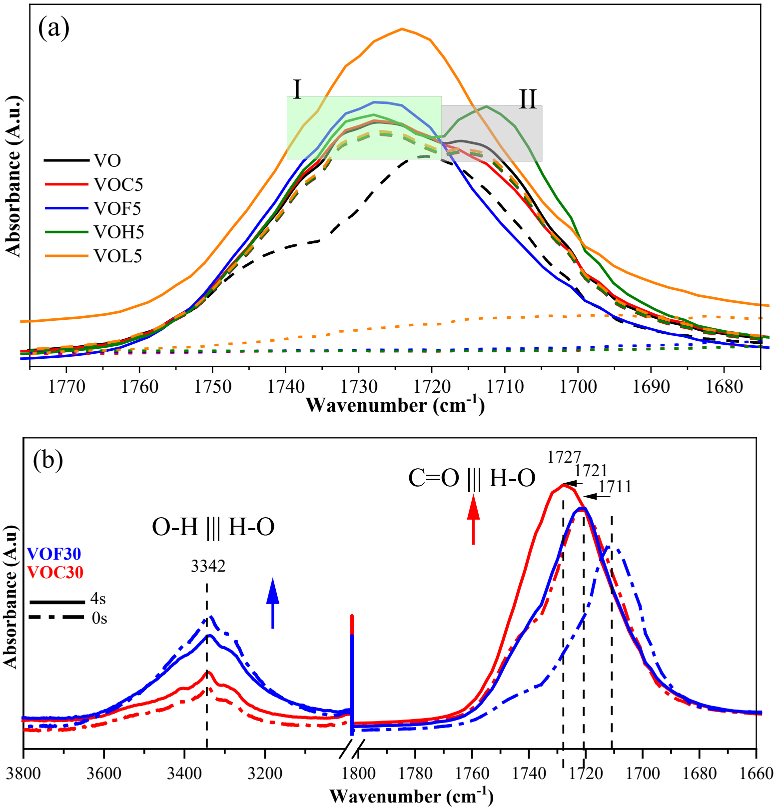

Supplementary 7.

Thermal stability of the VO and 5 wt% compositions (a) and thermal stability of C and F loaded nanocomposites: TG weight loss (b), (d), and DTG derivative (c), (e).

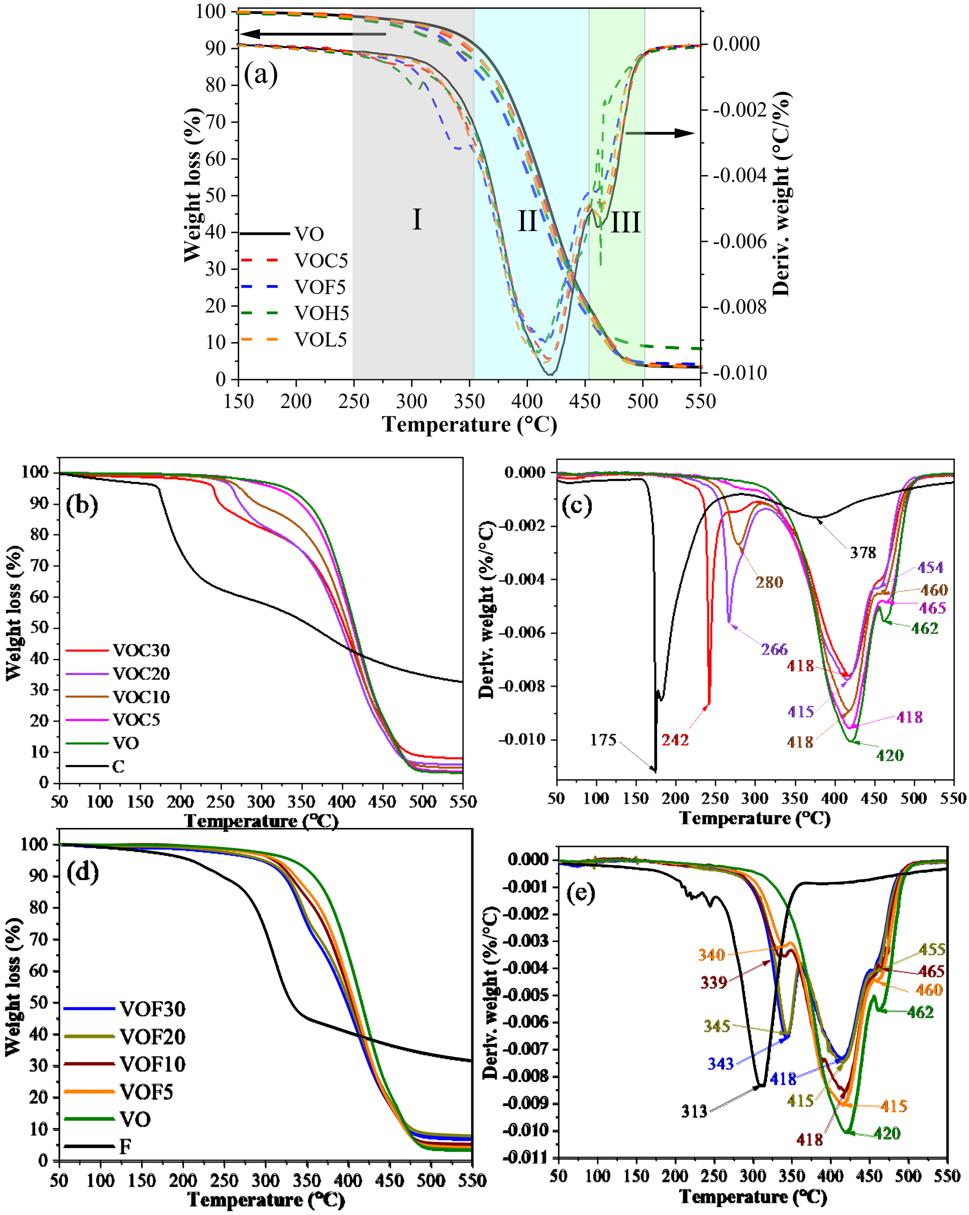

Supplementary 8.

Storage modulus (a), loss modulus (b), and loss factor tanδ (c) of the VO and 5 wt% compositions and VOC20, VOF20, VOC30, and VOF30 compositions **s**torage modulus (**d**), loss modulus (**e**), and loss factor tanδ (**f**).

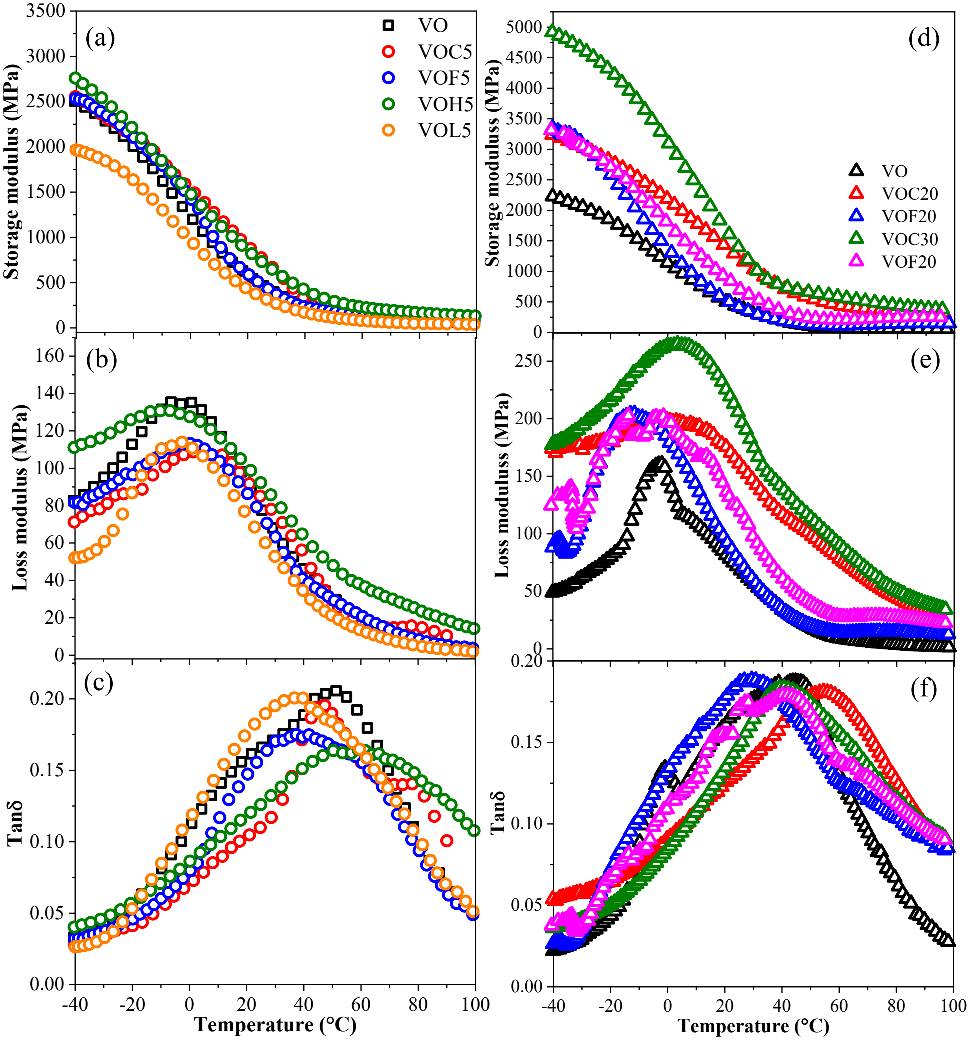

Supplementary 9.

Water contact angle for C2F3H1 (a), C1F1H1 (b), and C2F1H3 (c) sample surfaces.

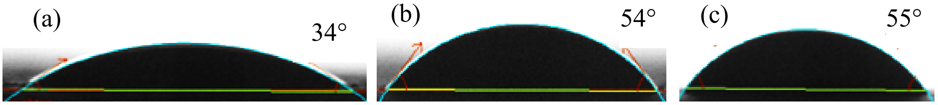

Supplementary 10.

A summary of the VO matrix and single filler composites properties

Sample	T_{max}, (°C)	Char yield, (wt%)	T_{g1}, (°C)*	T_{g2}, (°C)*
VO	420	3	9	52
C	174	27	-	-
F	312	28	-	-
H	273	28	-	-
LN	328	42	-	-
VOC5	418	4	32	46
VOC10	418	5	9	51
VOF5	418	4	35	69
VOF10	418	5	41	-
VOH5	408	8	-	57
VOH10	404	9	23	74
VOL5	414	3	37	-
VOL10	402	9	33	-

T_{g1} and T_{g2} are obtained from tanδ peaks after deconvolution

Supplementary 11.

Thermal stability of C2F3H1 (a) and C2F1H3 (b) at different heating rates and C2F3H1 (c) and C2F1H3 (d) composition plots of Ln(d α/dt) versus 1/T from 5 % to 90 %.

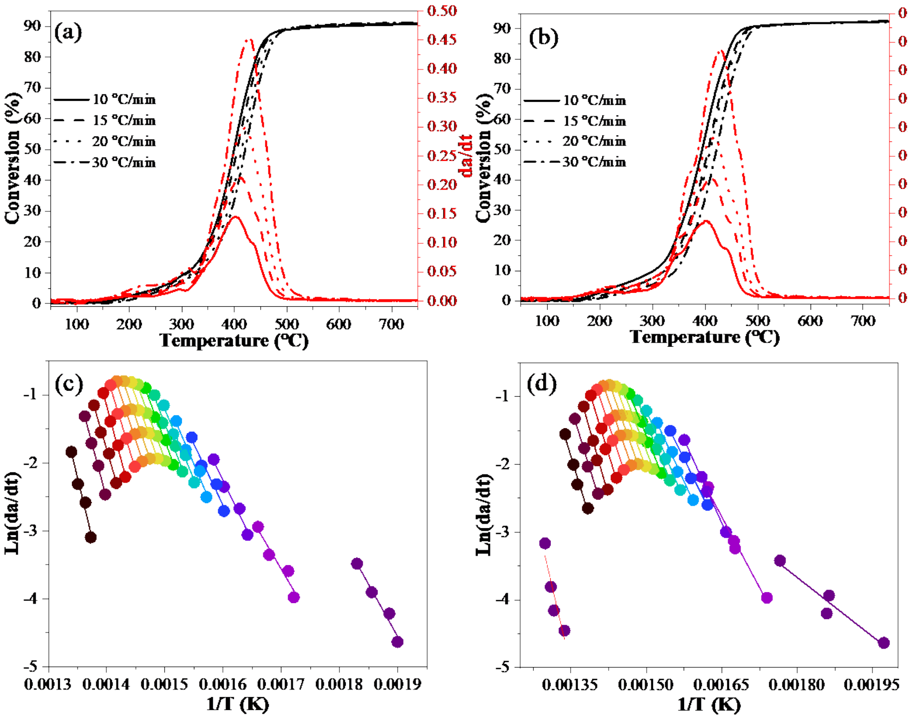

Supplementary 12.

The 3D surface graph for the FTIR spectra of the evolved gases produced by C2F3H1 (a) and C2F1H3 (b) composition, and C2F3H1 (c) and C2F1H3 (d) composition spectra at different temperatures.

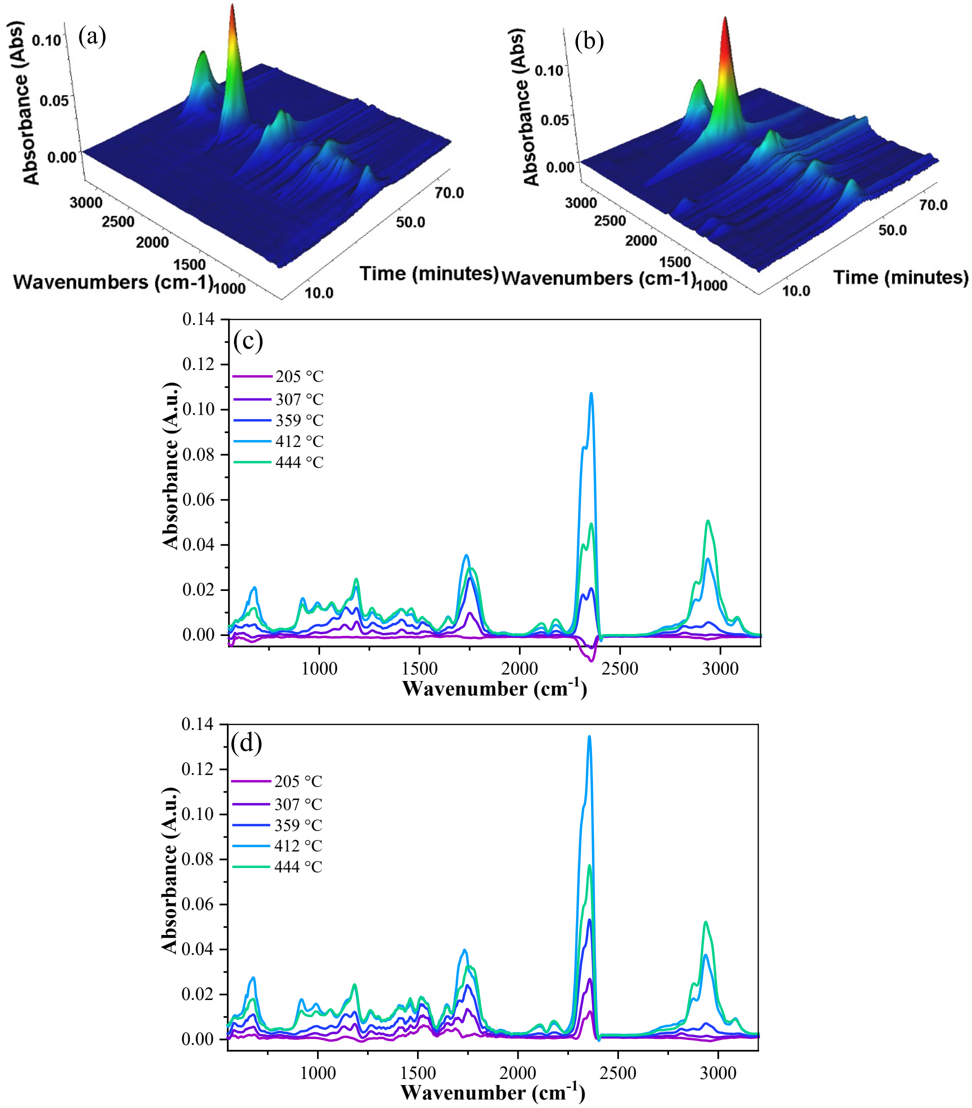

Supplementary 13.

UV-VIS spectra and images of the 3D printed samples; samples from left to right: VO, VO/NF, VO/NFA, VO/NC, and VO/NCI.

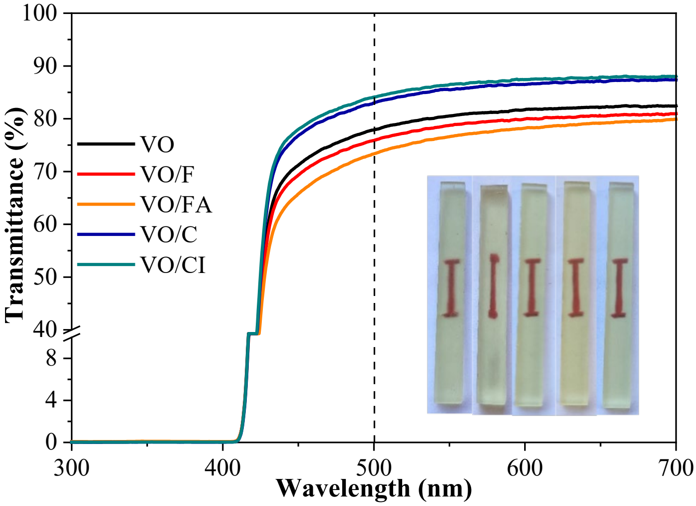

Supplementary 14.

FTIR spectra of resins (dashed lines) and printed (solid lines) samples (a) and FTIR spectra of C=C (b) and C=O (c) bonds used for DBC% calculation of raw resins (dashed lines) and printed (solid lines) samples.

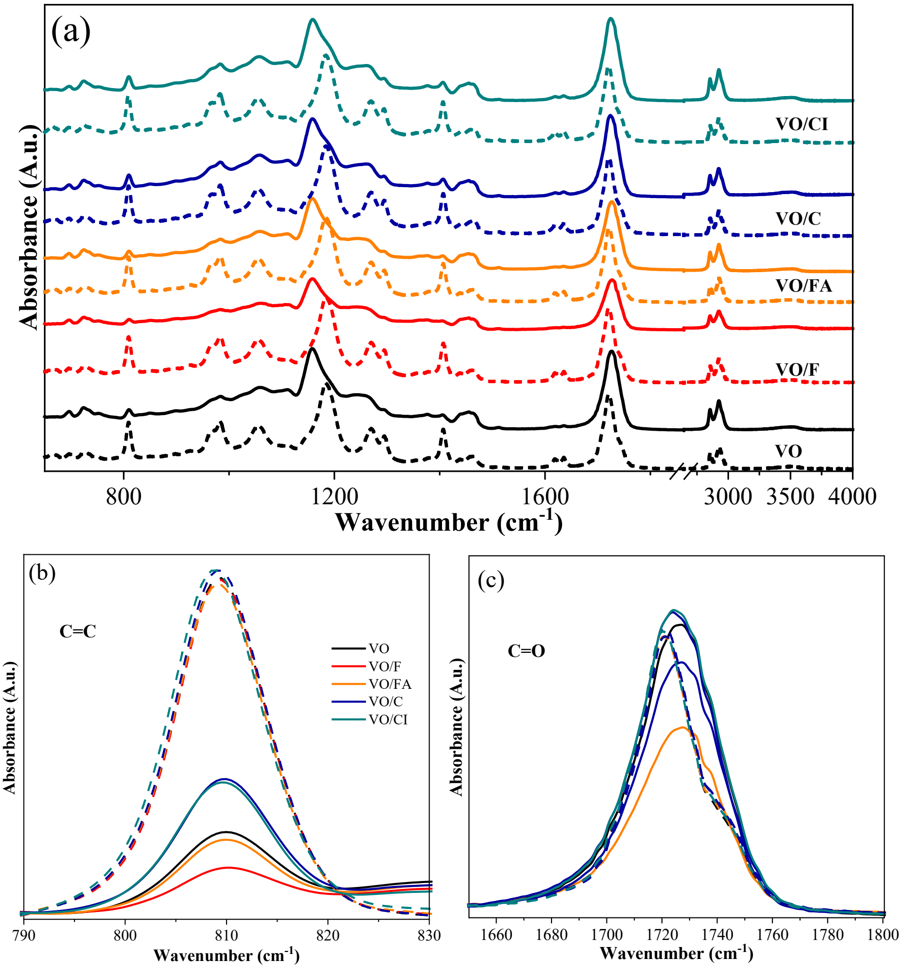

Thermal analysis.

All samples demonstrated a two-step decomposition process (Supplementary 15). The first step concerns AESO degradation, while the second relates to the other monomers used [20]. The associated temperatures (defined by peaks in derivative weight curves) remained fixed at ~419 ± 2 °C for the first degradation step and ~458 ± 3 °C for the second step. The addition of pF did not affect the initial mass loss temperature (Supplementary 16) of the neat VO, whereas the addition of pFA increased the temperature by 7 °C. Covalent bonding between the pFA and the polymer matrix likely accounts for the slight improvement in thermal stability [340]. The increased char yield (Supplementary 16) of the VO/pFA can be explained in the same way. VO/pC and VO/pCI followed similar initial decomposition temperature tendencies and have slightly lower thermal stability. A decrease in the initial mass loss temperature in the pC-based composites is explained by the lower thermal stability of the pC vs. the pF and the larger initial mass losses observed in the former vs. the latter, as shown previously in Figure 3.36.

TGA weight loss and thermal stability curves of 3D printed samples (in nitrogen).

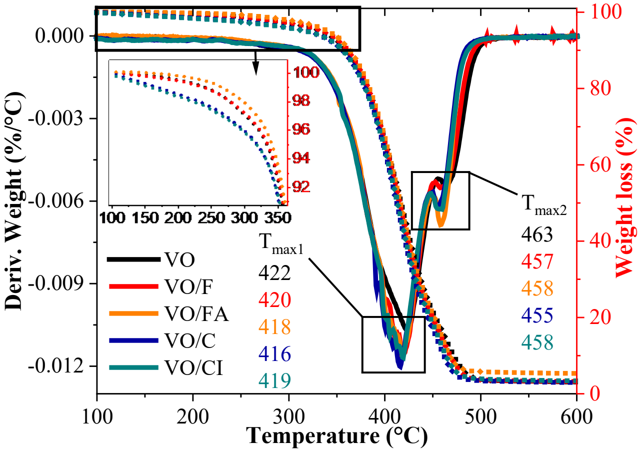

Supplementary 16.

Thermal degradation parameters of 3D printed samples

Sample	$T_{5\%}$, °C	Char yield, wt%
VO	333	3.0
VO/F	334	3.2
VO/FA	341	5.3
VO/C	318	2.9
VO/CI	317	3.4

Supplementary 17.

The glass transition temperatures of 3D printed samples

Sample	Temperature (°C)		
	T_{g1}	T_{g2}	T_{g3}
VO	-	-	46
VO/F	21	39	74
VO/FA	26	44	71
VO/C	21	-	57
VO/CI	25	-	68

T_{g1}, T_{g2}, and T_{g3} are obtained from tanδ peaks after deconvolution in Figure 3.38

Supplementary 18.

UV-Vis reflectance and transmittance spectra of the samples at 0 h (a), 250 h (b), 500 h (c), 750 h (d), and 1000 h (e) UV weathering

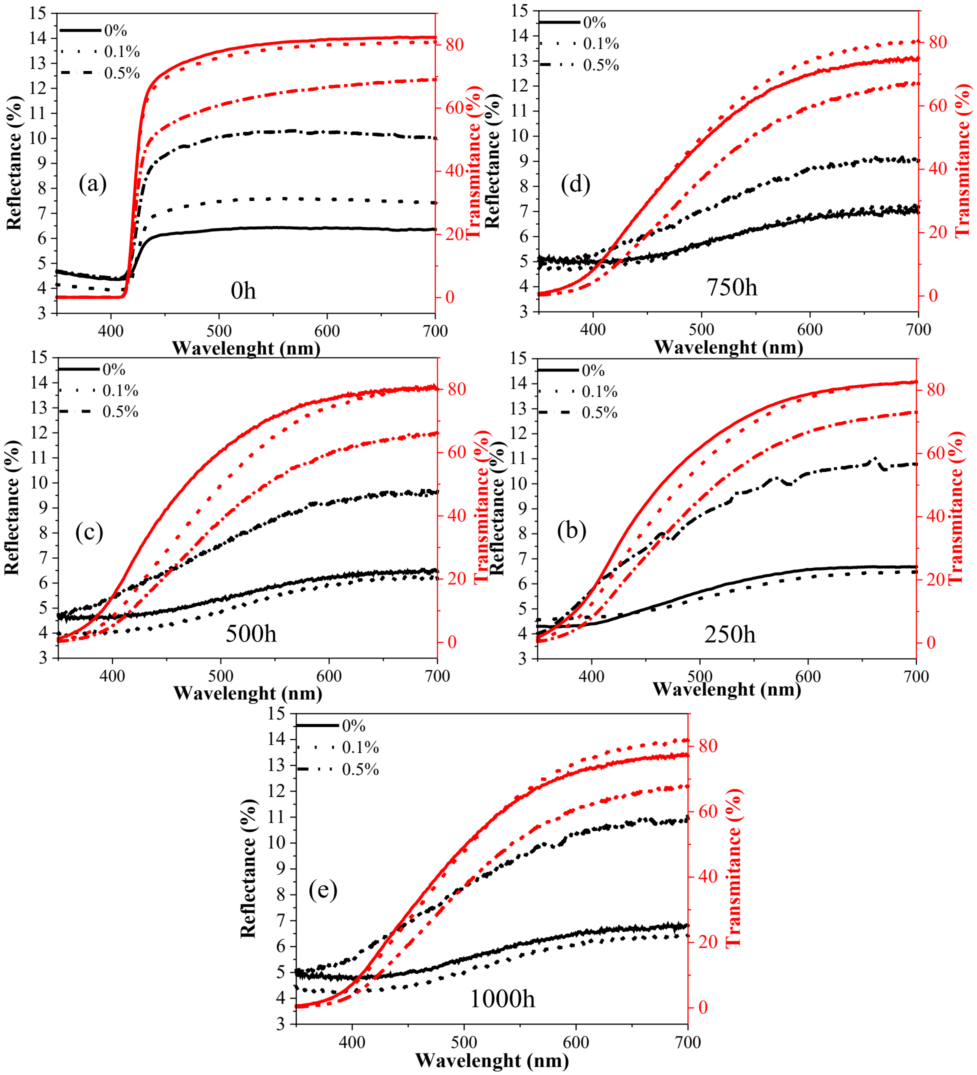

Supplementary 19

UV-Vis measurement data at 500 nm

Time	0%			pF0.1%			pF0.5%		
	T, %	R, %	S, %	T, %	R, %	S, %	T, %	R, %	S, %
0 h	78.0	6.3	15.7	76.0	7.5	16.5	60.5	10.0	29.5
250 h	62.0	5.7	32.3	56.0	5.0	39.0	45.5	8.7	45.8
500 h	60.6	5.3	34.1	49.8	4.8	45.4	38.6	7.5	53.9
750 h	48.3	5.7	46.0	50.0	5.7	42.3	36.8	7.0	56.2
1000 h	49.0	5.5	45.5	47.8	5.0	47.2	37.0	8.2	54.8

Supplementary 20.

FTIR spectra of 0% sample resin and TPO photoinitiator.

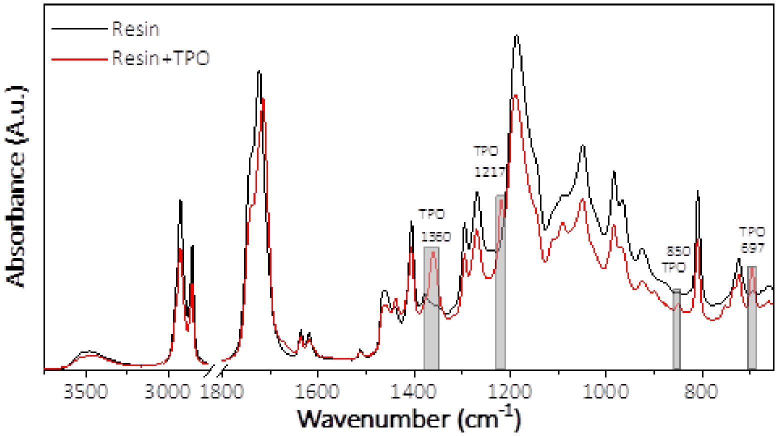

Supplementary 21.

Photodegradation chemical changes evaluation: pF0.1% sample FTIR spectra (a), and peak intensity ratios (b) and pF0.5% sample FTIR spectra (c), and peak intensity ratios (d) during UV weathering.

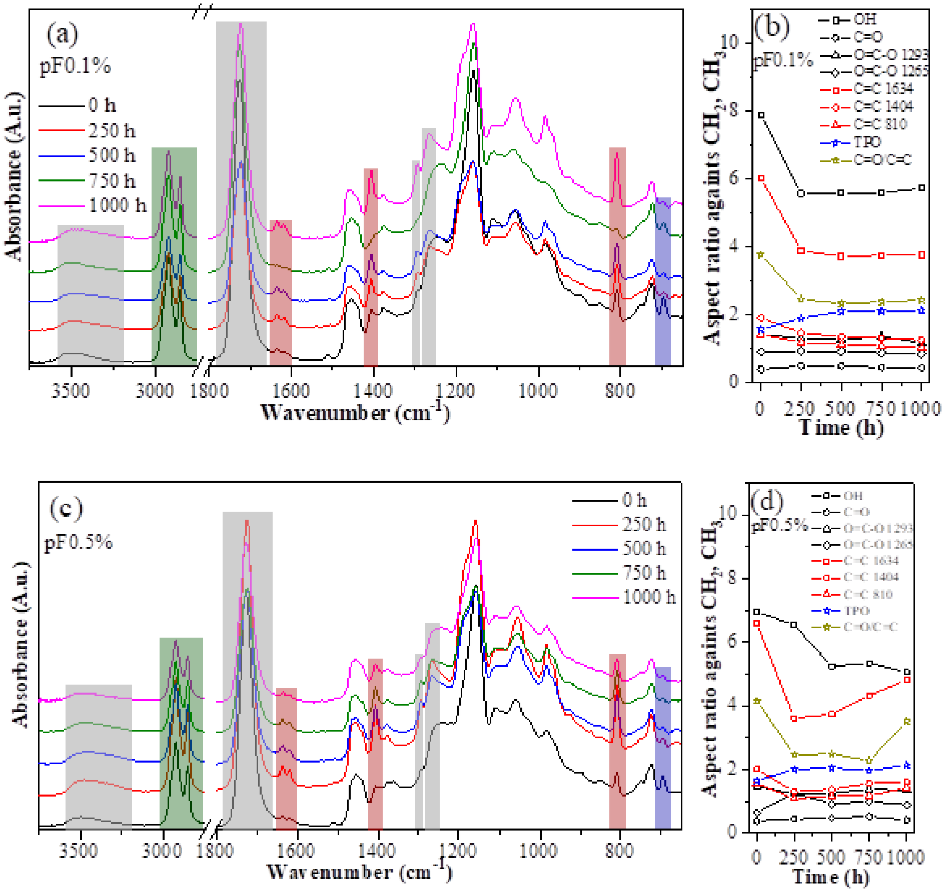

Anda Barkāne was born in 1994 in Riga. She obtained a Bachelor's degree in Chemical Technology (2018) and a Master's degree in Nanotechnologies (2020) from Riga Technical University (RTU). Since 2018, she has been a scientific assistant at the Polymer Materials Institute of the Faculty of Material Science and Applied Chemistry of RTU and since 2020, a researcher. Currently, she is a researcher at the Institute of Chemistry and Chemical Technology of the Faculty of Natural Sciences and Technologies, of RTU and Head of the RTU Doctoral School. Parallel to her bachelor's studies, Anda was actively involved in the Student Parliament of RTU, where she was head of the Science Department and the coordinator of the Latvian Student Association's Science Fund. During her bachelor's studies, Anda completed an internship at Sakret Plus JSC.

She has participated in several research projects and has received RTU Doctoral Grants, a grant for PhD students and academic personnel of Riga Technical University and BA School of Business and Finance in the strategic fields of specialization. Anda is a laureate of the L'Oréal-UNESCO For Women in Science Young Talents Program – Baltic, with the support of the Latvian National Commission for UNESCO and the Latvian Academy of Sciences award. She has supervised the development of four bachelor's theses and has been actively involved in academic work, teaching various courses.

Anda specializes in photopolymer synthesis, working on resin formulation, photopolymerization studies, composite development, and 3D printing technologies. Her research focuses on the development of bio-based resin formulations and lignocellulose as fillers.